Numerical simulations of natural or mixed convection in vertical channels : comparisons of level-set numerical schemes for the modeling of immiscible incompressible fluid flows

Ru Li

Université PARIS-EST

École doctorale : Sciences, Ingénierie et Environnement

THÈSE

pour obtenir le grade de

Docteur de l'Université PARIS-EST

Spécialité : Energétique et Génie des Procédés

Ru LI

Numerical simulations of natural or mixed convection in vertical channels
—
Comparisons of Level-Set numerical schemes for the modeling of immiscible incompressible fluid flows

Thèse dirigée par Guy LAURIAT

Soutenance le 14 décembre 2012

MEMBRES DU JURY :

J.-P. Caltagirone	Professeur	Univ. Bordeaux 1	Rapporteur
S. Xin	Professeur	INSA Lyon	Rapporteur
B. Guerrier	Directrice CNRS	Lab. FAST Orsay	Examinateur
M.-C. Duluc	M. de Conférence, HDR	CNAM Paris	Examinateur
E. Chénier	M. de Conférence	Univ. Paris-Est MLV	Examinateur
G. Lauriat	Professeur	Univ. Paris-Est MLV	Directeur de thèse

Acknowledgements

I owe my deepest gratitude to my tutors, Mr. Guy LAURIAT, Professor of University of Paris-est for the continuous support of my PhD study and research, for their encouragement, patience, and profound knowledge. And Mr. Eric CHENIER expertly guided me through my thesis. His unwavering enthusiasm kept me constantly engaged with my research. He's the one of the smartest people I know. I hope that I could be as lively, enthusiastic, and energetic as him and to someday be able to command an audience as well as he can. I must say, without them, this dissertation would not have been possible.

Besides, I'm heartily thankful to my colleague Mr. Xavier NICOLAS, who always kindly help me with many kinds of technical problems. And Mr. Hua SUN and Ms. Chahinez TCHEKIKEN always provided insightful discussions about the research.

I especially thank my jury members, Béatrice GUERRIER , Directeur de Recherche CNRS, Marie-Christine DULUC in University of Paris-Sud, Mr. Jean-Paul Caltagirone, Professor in University Bordeaux 1 and Shihe XIN, Professor in INSA Lyon, accepted my request of graduation and gave me valuable advices.

My sincere thinks also extend to my friends in laboratory MSME, Ms. Yunmei LUO, Ms. Sandra JEREZ, Ms. Thu Huong TRAN, Mr. Thanh-Long VU, Mr. Minh Tan HOANG, Mr. Carmelo CAGGEGI, Mr. Manh Tu NGUYEN who helped sustain a positive atmosphere in which to do science.

Last but not least, I am extremely grateful to my family, I appreciate the understanding and help from my parents through all these years along, the great support from my husband and the endless inner strength from my lovely daughter Louise. They are my motivation to fight when times are rough. I dedicate this dissertation to them for their unconditional love.

Contents

Introduction

Whereas heat transfer in solids happens only by conduction of which the origin comes from vibrations of atoms constituting the matter, the motion which is authorized by the fluid medium can improve significantly the heat exchange. The transport of heat by the fluid flow is called convection and its efficiency versus the conduction depends greatly on the fluid velocity but also on the thermal properties of the medium. Roughly speaking, we can distinguish two kinds of heat convection according to the internal or external nature of forces applied in order to produce the fluid flow. On the one hand, the origin of the motion may be related to forces engendered inside the fluid itself. For example, this is the case of body forces created by the gravity acceleration. This convection is called *natural* because it occurs without the addition of any external mechanical device. On the other hand, we have *forced* convection for which the fluid flows thanks to outer mechanisms which may produce pressure drops, imposed velocities or flow rates, for instance. At last, if both internal and external forces have approximately the same intensity, we talk about *mixed* convection.

From the industrial point of view, the natural convection is very interesting to heat or cool systems by using the buoyancy forces induced by gravity, because the cost of this heat transfer is completely free. Unfortunately, its energetic efficiency is sometimes insufficient and mechanical devices (such as pumps, fans, $\cdots$) must be bought and installed to improve heat exchanges. Obviously, the aim of industrialists is to take advantage of natural convection as much as possible, and eventually to buy and install the cheapest equipments which are necessary to achieve the expected heat transfer performances.

Heat transfers by natural, mixed or forced convections are widely studied for single phase fluids with one component, only. However, numerous physical problems involve heat transfer in mixtures of liquids, gases or solids. In particular case of immiscible fluid flows, an interface appears between the different fluid media and this interface acts significantly on flow dynamics and subsequently on heat transfer. The unbalance of the molecular van der Waals forces on both sides of the interface creates a resulting force by unit length, the surface tension. This surface tension produces pressure jumps which are proportional to the local curvatures of the interface. Its numerical value depends on the nature of the fluids in contact, but also on the local temperature. When the interface is non-isotherm, it results a natural convective flow, the Marangoni convection, in which the fluid moves along the interface, usually from hot to cold regions; by viscosity, the fluid in the core region is dragged along.

To accurately take into account these new physical phenomena associated with the occurrence of an interface, specific numerical method must be developed.

The aim of my research was twofold. To emphasize both aspects of my work, my report is divided into two parts.

I first contributed to the study of natural and mixed convections of a single fluid flowing through vertical heated channels. To this end, I developed a numerical scheme suitable

for the simulation of laminar convection for small or large temperature differences. My motivation concerning this subject relies on the delicate issue of choosing the boundary conditions for open cavities, and this, despite the relative plenty of numerical works available in the scientific literature. Indeed for thermal natural and mixed convections, the distribution of the total heat fluxes entering and exiting through open boundaries depends on heat transferred at walls. Furthermore, the fluid flowing into this channel comes from and emerges outside. It results a close coupling between the dynamic and thermodynamic variables inside and outside the channel. Thus, the thermal and kinematic inlet/outlet boundary conditions cannot be a priori prescribed without accounting for the surrounding conditions.

In order to extend the study of natural and mixed convections to immiscible fluid flows, I investigated, in a second step, the numerical methods devoted to the treatment of the interface problems. Amongst the jungle of methods, the Level-Set method has retained my attention. This approach seems quite easy to implement and allows treating very complex configurations where the interfaces may break and merge. Whereas the Level-Set method is theoretically well defined, its implementation demands a particular attention. And that is the reason why numerous schemes have been developed to achieve a good accuracy. Since each of these techniques is often considered by their authors as the more efficient, I decided to perform my own tests to establish my own judgment.

Part I

Numerical simulations of natural or mixed convection in vertical channels

Outlines

The first three chapters introduce the governing heat and fluid flow equations, their discretizations, to end by a validation step.

In *chapter 1*, continuity, momentum and energy equations are derived from three fundamental physical principles: the mass conservation, the Newton's second law and the energy conservation. Then, the low Mach number approximation is briefly presented. With this approximation, the compressible governing equations are simplified by considering a small value for the Mach number. It results a decoupling between the thermodynamical pressure, which satisfies a gas law relation, and the dynamical pressure which only acts to ensure the mass conservation during the fluid flow. When the variations of the thermodynamical variables are small enough, the low Mach number approximation is reduced to the Boussinesq approximation which consists in keeping all physical properties constant, except the density in the buoyancy force.

Chapter 2 focuses on the discrete numerical scheme for the continuity, the momentum and the energy equations. The backward second order Euler scheme is used for time discretization and a finite volume method is applied to express the spatial derivatives on control volumes. The pressure and velocity coupling is ensured by a fractional time stepping algorithm. The mesh must fulfill some specific requirements about the locations of the adjacent cell centers with respect to their common edge. The classical structured grids, made of rectangles or parallelepipeds, and also unstructured triangular cells, provided that the triangulation is of Delaunay type, satisfy these conditions. All variables are expressed on the same set of cell centers; they are qualified as collocated. The spurious oscillations of the pressure field arising from the collocated arrangement are suppressed by altering the pressure equation. The discrete operators are mainly defined by a weak formulation with the aim of mimicking at the discrete level the continuous kinetic energy balance and the continuous quadratic form of the temperature evolution. For fluid flowing into enclosures with large temperature gaps (low Mach number approximation), the coupling between the thermodynamic pressure and the temperature is solved with an approximated Newton method.

Chapter 3 aims at presenting a validation of the numerical scheme on rectangular grids. Firstly, comparisons with analytical solutions are proposed in order to check the spatial and temporal orders of convergence of the numerical scheme. The isotherm decaying vortex of the Taylor-Green problem is considered, and then the low Mach number scheme is tested. To ascertain the convergence properties of the solutions with large temperature differences, we chose continuous velocity, pressure and temperature fields satisfying the mass conservation equation. Then, discrete source terms are defined and added to the momentum and energy equations so that the numerical approximations converge towards their continuous counterparts. Secondly, natural convection flows in differentially heated enclosures are calculated. Both steady state solutions under low Mach number approximation and unsteady

solution under Boussinesq approximation are compared with benchmark solutions.

The last three chapters provide applications of the numerical method described in this report for fluid flowing through heated vertical channels.

In *chapter 4*, numerical simulations of mixed convection of air between vertical isothermal surfaces were conducted in order to determine the optimum spacing corresponding to the peak heat flux transferred from an array of isothermal, parallel plates cooled by mixed convection. Comparisons between approximate analytical solutions for natural and forced convection are first discussed. From the computations carried out for aiding mixed convection by assuming a pressure drop at the outlet section rather than a constant flow rate, it is numerically predicted that the optimum spacing is smaller than those for pure natural or pure forced convection. This spacing is determined according to the pressure drop. As a sample, we considered an array of 10 cm-height, isothermal surfaces at temperature $T_h = 340\ K$ with air as the working fluid entering into the channels at $T_0 = 300\ K$. The increases in heat flux corresponding to the optimal spacing are discussed for outlet pressure drops ranging from $-0.1\ Pa$ to $-1\ Pa$. Such a range covers the entire laminar mixed convection regime for this specific application.

The aim of *chapter 5* is at showing that to prescribe a flow rate at the inlet section of a vertical channel with heated walls leads to surprising and counterintuitive physical solutions, especially when the problem is modeled as elliptical. Such an approach can give rise to the onset of recirculation cells in the entry region while the heat transfer is slightly increased under the influence of the buoyancy force. We suggest an alternative model based on more realistic boundary conditions based on a prescribed total pressure at the inlet and a fixed pressure at the outlet sections. In this case, the pressure and buoyancy forces act effectively in the same direction and, the concept of buoyancy aiding convection makes sense. The numerical results emphasize the large differences between solutions based on prescribed inlet velocity and those obtained with the present pressure-based boundary conditions.

Chapter 6 reports numerical solutions on the influence of surface radiation on the laminar air flow induced by natural convection in vertical, asymmetrically-heated channels. Variable property effects are accounted for in a full-elliptic mathematical formulation. The density variation is determined from the state equation for ideal gas. The experimental design and data reported in Webb et Hill [161] are taken as the base cases for carrying out the computations. The occurrence of flow reversals is first considered and revisited for pure natural convection, and the Nusselt number correlations derived from the numerical results are favorably compared with those reported in [161]. It is shown that the general effect of surface radiation is to delete the onset of pocketlike recirculations at the top part of the channel, to reduce the heated wall temperatures, and to increase the facing wall temperatures. Comparisons with usual methods used for decoupling the surface radiation effects are discussed. In the range of parameters investigated, increases in differences between inlet and maximum wall temperatures up to $200\ K$ are shown to have small influences on the flow field and negligible effects on heat transfer performances.

Chapter 1

Governing flow equations

1.1 Generalities

Continuity, momentum and energy equations are mathematical statements of three fundamental physical principles: mass conservation; Newton's second law and energy conservation. They are widely used as mathematical models to describe physical phenomena and valid only for continuous fluids. To explain clearly continuous fluids, it's better to have an overview about different categories of fluid flows.

The Knudsen number Kn, ratio of mean free path to the characteristic length scale, is used as the parameter to distinguish the fluid regime [170] which is an average distance covered by a moving particle between successive impacts.

- when $Kn \leq 0.001$, the fluid flows in a continuous regime. The characteristic length scale of fluid is much greater than the mean free path, the fluid flow is considered as a continuous medium;

- when $Kn > 10$, the fluid flows in a free molecule regime. Molecules have a greater chance to collide with walls than between themselves. Under this condition, the fluid medium cannot be viewed as a continuous medium;

- when $0.001 < Kn \leq 0.1$, the fluids flows in a slip flow regime. Here, the fluid is considered as continuous but a slippery effect at walls should be applied;

- when $0.1 < Kn < 10$, the fluid flows in a transition regime. The fluid is in a state between continuous and free molecule regimes.

Continuity, momentum and energy equations are appropriate for $Kn \leq 0.1$, when the characteristic length scale of fluid flow is much greater than the mean free path. Most of common fluid flows satisfy this assumption. The problems in which we are interested can also be attributed to the continuum regime. The purpose of this chapter is to derive continuous equations from three fundamental physical principles.

In deriving continuous equations, two forms of these equations are introduced, the conservative form and the convective form. In principle, both forms are equivalent. However, for Computational Fluid Dynamics (CFD), applying one form leads to success, while another may result in unphysical oscillations in the numerical results, or even produce a divergence of the solution provided by the numerical scheme. Therefore, for CFD, the

different forms of equations are of great interests [2]. According to whether the governing equations are established by considering a fixed control volume or a control volume which moves with the fluid particles, we obtain the conservative or convective forms. The presentation of governing equations is the subject of the section 1.2.

The low Mach number approximation proposed by Paolucci [125] is briefly presented in section 1.3. This method is based on series expansion in Mach number for the velocity, the pressure, the temperature and the density. The equations are then reduced by considering a small value for the Mach number. It results in a decoupling between the thermodynamical pressure, which satisfies a gas law relation, and the dynamical pressure which only acts to ensure the mass conservation during the fluid flow. Thus, the sound waves are removed to allow us to set the numerical time step, not on the acoustic time but on the characteristic time of the fluid motion. When the thermodynamical variables are small enough, the low Mach number approximation reduces into the Boussinesq approximation. This latter approximation consists in keeping all physical properties constant, except the density in the buoyancy force. The density may therefore be linearized as a function of temperature.

1.2 Fluid flow equations

1.2.1 Mass conservation

If we choose an infinitesimal fluid element which moves with the fluid flow, the mass δm of this element is constant. It writes $\delta m = \rho \delta V$, with δV the volume of the fluid element and ρ its density. Since the mass is conserved, we can state that the time rate of mass change for a fluid element is zero along the flow path:

$$\frac{D(\delta m)}{Dt} = 0$$

where $(D/Dt)(.) \equiv (\partial/\partial t + (\vec{v} \cdot \nabla))(.)$ is the particular derivative, with $\vec{v}$ the local flow velocity. Substituting δm by its definition, we have

$$\frac{D\rho}{Dt} + \rho \left[\frac{1}{\delta V} \frac{D\delta V}{Dt} \right] = 0$$

with $\left[\frac{1}{\delta V} \frac{D\delta V}{Dt} \right]$ the time rate of relative volume change which is equal to $\nabla \cdot \vec{v}$. The continuity equation in its non-conservative form then writes:

$$\frac{D\rho}{Dt} + \rho \nabla \cdot \vec{v} = 0 \tag{1.1}$$

To obtain the continuity equation in its conservative form, we have to consider a fixed control volume. The sum over the control volume of the growth rate of the fluid density, plus the net mass flow rate leaving the control volume is zero. Per unit volume, we then have:

$$\frac{\partial \rho}{\partial t} + \nabla \cdot (\rho \vec{v}) = 0 \tag{1.2}$$

Let us note that equations (1.1) and (1.2) are obviously fully equivalent. For example, starting from Eq. (1.2), we obtain

$$\frac{\partial \rho}{\partial t} + \vec{v} \cdot \nabla \rho + \rho \nabla \cdot \vec{v} = 0$$

$$\left(\frac{\partial \rho}{\partial t} + \vec{v} \cdot \nabla \rho \right) + \rho \nabla \cdot \vec{v} = 0$$

$$\frac{D\rho}{Dt} + \rho \nabla \cdot \vec{v} = 0$$

1.2.2 Momentum equation

The Newton's second law provides the momentum equation for the fluid flow. Let us consider a fixed control volume. The net increase in the fluid momentum (temporal derivative plus the transport contribution through the control surface) is balanced by the sum of surface (mechanical stress) and volume (weight) forces applied on the fluid control volume [29]. The resulting differential expression writes:

$$\frac{\partial \rho \vec{v}}{\partial t} + \nabla \cdot (\rho \vec{v} \otimes \vec{v}) = \nabla \cdot \overline{\overline{\sigma}} + \rho \vec{g}$$

with $\vec{g} = -g\vec{e}_z$ the gravitational acceleration vector and $\vec{e}_z$ the unit vertical vector pointing upward. The mechanical stress tensor $\overline{\overline{\sigma}}$ is split into two terms. The first term represents the thermodynamical pressure which appears in static problems whereas the second one contains the viscous contributions coming from the fluid motion:

$$\overline{\overline{\sigma}} = -p\overline{\overline{\delta}} + \overline{\overline{\tau}}$$

with $\overline{\overline{\tau}}$ the molecular viscous shear stress tensor, p the thermodynamic pressure and $\overline{\overline{\delta}}$ is the second order Kronecker tensor whose components δ_{ij} are set to 1 if $i = j$ and 0 otherwise. We then find:

$$\frac{\partial \rho \vec{v}}{\partial t} + \nabla \cdot (\rho \vec{v} \otimes \vec{v}) = -\nabla p + \nabla \cdot \overline{\overline{\tau}} + \rho \vec{g} \tag{1.3}$$

For Newtonian fluid flows, the viscous shear stress is proportional to the velocity gradients:

$$\overline{\overline{\tau}} = \mu(\nabla \vec{v} + (\nabla \vec{v})^t) + \eta(\nabla \cdot \vec{v})\overline{\overline{\delta}} \tag{1.4}$$

where μ is the dynamic viscosity and η is the volume viscosity. The bulk viscosity $(2\mu/3 + \eta)$ gives the difference between the "mechanical pressure", defined as the mean mechanical stress, and the thermodynamic pressure p_{th} due to the rate of volume expansion $\nabla \cdot \vec{v}$, namely,

$$p_m \equiv -\frac{1}{3}\overline{\overline{\delta}} : (-p\overline{\overline{\delta}} + \overline{\overline{\tau}}) = p - \left(\frac{2}{3}\mu + \eta\right)\nabla \cdot \vec{v}$$

and measures the dissipation of energy in the fluid upon expansion. If the fluid is incompressible, $\nabla \cdot \vec{v} = 0$, then the mechanical and thermodynamic pressures are equivalent and the former is known to an arbitrary constant; only the dynamical pressure ∇p enters the momentum balance. When $\nabla \cdot \vec{v} \neq 0$, Stokes' assumption states that the bulk viscosity is zero and thus $\eta = -2\mu/3$. In this work, this approximation is always assumed valid.

The non-conservative expression of Eq. (1.3) simply writes:

$$\rho \frac{D\vec{v}}{Dt} = -\nabla p + \nabla \cdot \overline{\overline{\tau}} - \rho g \vec{e}_z \tag{1.5}$$

1.2.3 Energy equations

1.2.3.1 First principle of thermodynamics

According to the first principle of thermodynamics, the total energy variation of a fluid element per unit time (including the internal energy U and the kinetic energy K) is equal to the power gained through heat $\dot{Q}$ and mechanical works $\dot{W}$ along its path [29]:

$$\frac{D(U + K)}{Dt} = \dot{Q} + \dot{W} \tag{1.6}$$

Let us note $\hat{u}$ the internal energy per mass unit. If we divide the mechanical contributions into volume (weight) and surface (mechanical stress) forces and by introducing the Fourier's law to model the heat transfer by conduction, we obtain the differential relation

$$\frac{\partial}{\partial t}\left(\rho\hat{u} + \frac{1}{2}\rho\vec{v}^2\right) + \nabla\cdot\left(\left(\rho\hat{u} + \frac{1}{2}\rho\vec{v}^2\right)\vec{v}\right) \equiv \rho\frac{D}{Dt}\left(\hat{u} + \frac{1}{2}\vec{v}^2\right) = \nabla\cdot(k\nabla T) + \rho\vec{g}\cdot\vec{v} + \nabla\cdot(\overline{\overline{\sigma}}\cdot\vec{v})$$

(1.7)

where k is the thermal conductivity, T the temperature

1.2.3.2 Internal energy equation

We get the kinetic energy equation by applying to each side of Eq. (1.3) the scalar product by $\vec{v}$:

$$\frac{\partial}{\partial t}\left(\frac{1}{2}\rho\vec{v}^2\right) + \nabla\cdot\left(\frac{1}{2}\rho\vec{v}^2\vec{v}\right) = -\vec{v}\cdot\nabla p + \vec{v}\cdot(\nabla\cdot\overline{\overline{\tau}}) + \rho\vec{g}\cdot\vec{v}$$

By using $(\nabla\cdot\overline{\overline{\tau}})\cdot\vec{v} = \nabla\cdot(\overline{\overline{\tau}}\cdot\vec{v}) - \overline{\overline{\tau}}:\nabla\vec{v}$,

$$\frac{\partial}{\partial t}\left(\frac{1}{2}\rho\vec{v}^2\right) + \nabla\cdot\left(\frac{1}{2}\rho\vec{v}^2\vec{v}\right) = -\vec{v}\cdot\nabla p + \nabla\cdot(\overline{\overline{\tau}}\cdot\vec{v}) - \overline{\overline{\tau}}:\nabla\vec{v} + \rho\vec{g}\cdot\vec{v}$$

(1.8)

Subtracting Eq. (1.8) from Eq. (1.7), we get:

$$\frac{\partial\rho\hat{u}}{\partial t} + \nabla\cdot(\rho\hat{u}\vec{v}) = \nabla\cdot(k\nabla T) + \nabla\cdot(\overline{\overline{\sigma}}\cdot\vec{v}) + \vec{v}\cdot\nabla p - \nabla\cdot(\overline{\overline{\tau}}\cdot\vec{v}) + \overline{\overline{\tau}}:\nabla\vec{v}$$

By writing $\nabla\cdot(\overline{\overline{\sigma}}\cdot\vec{v}) = -p\nabla\cdot\vec{v} - \vec{v}\cdot\nabla p + \nabla\cdot(\overline{\overline{\tau}}\cdot\vec{v})$, we obtain

$$\frac{\partial\rho\hat{u}}{\partial t} + \nabla\cdot(\rho\hat{u}\vec{v}) \equiv \rho\frac{D\hat{u}}{Dt} = \nabla\cdot(k\nabla T) - p\nabla\cdot\vec{v} + \overline{\overline{\tau}}:\nabla\vec{v}$$

(1.9)

1.2.3.3 Enthalpy equation

Starting from Eq. (1.9), the energy equation can also be written as:

$$\frac{\partial(\rho\hat{u} + p)}{\partial t} + \nabla\cdot((\rho\hat{u} + p)\vec{v}) = \nabla\cdot(k\nabla T) + \overline{\overline{\tau}}:\nabla\vec{v} + \frac{Dp}{Dt}$$

(1.10)

with the relationship between the internal energy and enthalpy $\hat{h} = \hat{u} + \frac{p}{\rho}$. The enthalpy equation is then:

$$\frac{\partial(\rho\hat{h})}{\partial t} + \nabla\cdot(\rho\hat{h}\vec{v}) \equiv \rho\frac{D\hat{h}}{Dt} = \nabla\cdot(k\nabla T) + \overline{\overline{\tau}}:\nabla\vec{v} + \frac{Dp}{Dt}$$

(1.11)

From the derivative of enthalpy per mass unit $\hat{h}(T, p)$

$$\frac{D\hat{h}}{Dt} = \left(\frac{\partial\hat{h}}{\partial T}\right)_p\frac{DT}{Dt} + \left(\frac{\partial\hat{h}}{\partial p}\right)_T\frac{Dp}{Dt}$$

(1.12)

with

$$\left.\frac{\partial\hat{h}}{\partial T}\right|_p = c_p$$

(1.13)

$$\left.\frac{\partial\hat{h}}{\partial p}\right|_T = \frac{1}{\rho}(1 - \beta T)$$

(1.14)

10

and $\beta = -\frac{1}{\rho} \left.\frac{\partial \rho}{\partial T}\right|_p$.

Therefore, we have reduced the enthalpy equation in an equation dealing with the temperature variable:

$$c_p \frac{\partial(\rho T)}{\partial t} + c_p \nabla \cdot (\rho T \vec{v}) \equiv \rho c_p \frac{DT}{Dt} = \nabla \cdot (k\nabla T) + \overline{\overline{\tau}} : \nabla \vec{v} + \beta T \frac{Dp}{Dt} \qquad (1.15)$$

1.2.4 Ideal gas properties

To express the relationships between macroscopic variables and movements of microscopic molecules, we have to introduce an equation of state for the fluid. When the fluid is a gas, the simplest equation of state is the ideal gas law. This hypothetical ideal gas neglects both molecular size and intermolecular attractions. This assumption is most accurate for monatomic gases even at high temperatures and low pressures [160]. Under these conditions, most of gases can be treated as an ideal gas with negligible errors. With this assumption, complicate gas properties can be greatly reduced.

1.2.4.1 Ideal gas law

At relatively high temperature and sufficiently low pressure, most substances behave as a single-phase fluid, in which the interactions between its molecules are generally negligible. The equation of state can be expressed as

$$p = \rho r T \qquad (1.16)$$

where r stands for a constant for a given substance. Its value is defined by $r = R/\mathcal{M}$ with $R = 8.31\,J \cdot K^{-1} \cdot mol^{-1}$ the universal ideal gas constant and $\mathcal{M}$ the molecular mass of the gas $(kg \cdot mol^{-1})$. The ideal gas law can be rewritten using the volume per mass unit $v = 1/\rho$:

$$pv = rT$$

1.2.4.2 Internal energy

For a real gas, according to [160], the internal energy per volume unit is:

$$d\hat{u} = c_v dT + (T \left.\frac{\partial p}{\partial T}\right|_v - p)dv \qquad (1.17)$$

For the ideal gas, $T \left.\frac{\partial p}{\partial T}\right|_v = \rho r T = p$. We obtain the definition of internal energy for ideal gas:

$$d\hat{u} = c_v dT \qquad (1.18)$$

where c_v is constant.

1.2.4.3 Enthalpy

For a real gas, according to [160], the enthalpy per mass unit is:

$$d\hat{h} = c_p dT + (v - T \left.\frac{\partial v}{\partial T}\right|_P)dp \qquad (1.19)$$

For the ideal gas, $v - T \left.\frac{\partial v}{\partial T}\right|_P = v - \frac{rT}{p} = 0$, enthalpy at constant pressure is:

$$d\hat{h} = c_p dT \qquad (1.20)$$

where c_p is constant.

1.2.4.4 Thermodynamical coefficients

By using the ideal gas equation, thermodynamical coefficients can be determined.

$$\beta(T,p) = -\frac{1}{\rho}\left.\frac{\partial \rho}{\partial T}\right|_p = \frac{1}{T} \tag{1.21}$$

Starting from the enthalpy relation, we have

$$
\begin{aligned}
d\hat{h} &= c_p dT \\
d(\hat{u} + pv) &= c_p dT \\
d\hat{u} + r dT &= c_p dT
\end{aligned}
$$

Accounting to $d\hat{u} = c_v dT$, we then obtain $c_p - c_v = r$. By noticing $\gamma = c_p/c_v$, we obtain the specific heat at constant pressure

$$c_p(T,p) = \frac{\gamma r}{\gamma - 1} \tag{1.22}$$

For monatomic gas, $c_p = 5r/2$, and for diatomic gas, $c_p = 7r/2$.

1.3 Low Mach number approximation

1.3.1 From compressible to incompressible models

Equations described in Sec. 1.2 are general for Newtonian fluids. In the framework of fluid mechanics, we usually distinguish compressible and incompressible fluid flows. For compressible flows, the local pressure appears in the state equation to influence the mass conservation by density; also the pressure contributes to the momentum balance, velocity, density and it's highly coupled. When variations of velocity caused by variations of density are relatively small. Flows can be considered as incompressible flow and the density is often assumed constant.

To distinguish regimes of compressible and incompressible flow, the Mach number (Ma) is used as an independent dimensionless parameter which is defined through the ratio between the characteristic velocity u_c and the sound speed c, $Ma = u_c/c$ (in ideal gas and isentropic evolutions $c^2 = \gamma p/\rho$ with $\gamma = c_p/c_v$). The threshold between both flow regimes is usually set to $Ma_c = 0.2$. With Mach number less than this threshold, compressible effects in the flow become negligible, and the density is uncorrelated to the local pressure variations.

However for $Ma < 0.2$, there still exits situations in which the density cannot assume to be constant. Such typical cases concern the convection in atmosphere which originates in the sensitivity of the density with height, the circulation of the oceans driving by salinity and temperature gradients and flows in fuel/air combustors open fires. One way to solve these flows is to use a full compressible model, abiding by the limitations associated to the numerical scheme [128, 145]. Indeed, the acoustic wave cannot travel more than one computational cell length in one time increment, the pressure forces cannot be transmitted more than one cell each time step [125]. If a large time increment is chosen, sound waves should travel more than one cell. It yields large pressure gradients which lead to excessive cell compressions or expansions and considerable reversed pressure gradient which try to reverse the previous excesses. The process repeats itself and oscillations are

rapidly strengthened by superposition of waves, thus leading to a catastrophic numerical instability. For low Mach number fluid flow, the acoustic wave contains very few energy in comparison with the part transferred by the flow field. Therefore, the governing equations for compressible flows can be simplified by removing the acoustic waves, which allows to substantially relax the time step constraint associated with the compressible scheme.

A classic simplification of Navier-Stokes equations is due to Boussinesq [33]. Let's assume that density variations are induced by thermal gradients. Then, this approximation mainly relies on a first-order series expansion of density as a function of temperature field, only the leading contributions are conserved in the resulting equations. Other physical properties being assumed constant. It consists in setting the density constant in the mass, momentum and energy equations, except in the gravity term where the first-order term which is originated the flow motion must be kept. It makes the mathematics and physics simpler. A very strict limitation for this approximation is that the density variations must remain small enough, viz for a relative temperature difference less than 10% [69]. Otherwise, an intermediate model between the Boussinesq approximation and the full compressible flow model must be employed. This consists in the low Mach number approximation which is now presented.

1.3.2 Low Mach number Model

1.3.2.1 Equations

The low Mach number approximation relies on a decoupling between the acoustic speed and the flow velocity. We consider an enclosed container and a fixed time interval, the acoustic waves have ample time to reflect several times on walls before the gas travels a small distance. Thus, the small fluctuating pressures equilibrate almost instantaneously in comparison with the characteristic time of the fluid flow. And the same occurs for open systems where the pressure equilibrium is quickly restored to the outer pressure. The low Mach approximation is now described following the method presented by Paolucci [125]. Let T_0, ρ_0 and p_0 be the scales for the temperature, the density and the pressure expressed at the reference gravitational potential line. The velocity scale is based on the sound speed c_0 evaluated at T_0, ρ_0 and p_0. The dynamic viscosity, the thermal conductivity, the specific heats at constant pressure and volume are also normalized by their values at T_0, p_0 and ρ_0, namely μ_0, k_0, $c_{p,0}$ and $c_{v,0}$. Finally, the length and time scales are referenced by l and l/U where l is a characteristic length and U is a representative fluid flow velocity. Notice that p_0 measures the thermodynamic pressure unlike to the quantity $\rho_0 U^2$ which scales the dynamic pressure only. Adopting the above mentioned normalization leads to the appearance of five independent dimensionless parameters corresponding to the Mach number Ma, the Reynolds number Re, the Froude number Fr, the Péclet number Pe and the ratio of specific heats γ:

$$Ma = \frac{U}{c_0}, \quad Re = \frac{\rho_0 U l}{\mu_0}, \quad Fr = \frac{U^2}{g_0 l}, \quad Pe = \frac{\rho_0 c_{p,0} U l}{k_0}, \quad \gamma = \frac{c_{p,0}}{c_{v,0}} \tag{1.23}$$

To prevent overloaded notations, the dimensionless variables are written as their dimensional counterparts. Using the perfect gas law, the Navier-Stokes and energy equations write:

$$\frac{\partial \rho}{\partial t} + \frac{1}{Ma} \nabla \cdot (\rho \vec{v}) = 0 \tag{1.24a}$$

$$\frac{\partial \rho \vec{v}}{\partial t} + \frac{1}{Ma} \nabla \cdot (\rho \vec{v} \otimes \vec{v}) = -\frac{1}{\gamma Ma} \nabla p + \frac{Ma}{Fr} \rho \vec{g} + \frac{1}{Re} \nabla \cdot \bar{\bar{\tau}} \tag{1.24b}$$

$$c_p \left(\frac{\partial \rho T}{\partial t} + \frac{1}{Ma} \nabla \cdot (\rho \vec{v} T) \right) = \frac{\gamma - 1}{\gamma} \left(\frac{\partial p}{\partial t} + \frac{1}{Ma} \vec{v} \cdot \nabla p \right) + \frac{1}{Pe} \nabla \cdot (k \nabla T) + \frac{\gamma - 1}{Re} \bar{\bar{\tau}} : \nabla \vec{v}$$

(1.24c)

with

$$\bar{\bar{\tau}} = \mu (\nabla \vec{v} + (\nabla \vec{v})^t) - \frac{2}{3} \mu (\nabla \cdot \vec{v}) \bar{\bar{\delta}}$$

and

$$\frac{\gamma - 1}{\gamma} = \frac{p_0}{\rho_0 c_{p,0} T_0}, \qquad p = \rho T$$

The velocity field is rescaled to reflect its true magnitude, and, with the thermodynamic variables, is expanded in a small parameter Ma as follows:

$$\vec{v} = Ma[\vec{v}^{(0)} + Ma^2 \vec{v}^{(1)} + o(Ma^2)], \tag{1.25a}$$

$$T = T^{(0)} + Ma^2 T^{(1)} + o(Ma^2), \tag{1.25b}$$

$$p = p^{(0)} + Ma^2 p^{(1)} + o(Ma^2), \tag{1.25c}$$

$$\rho = \rho^{(0)} + Ma^2 \rho^{(1)} + o(Ma^2), \tag{1.25d}$$

Physical properties μ, λ, k and c_p can be expanded in a similar way.

With the expansions above, we write down the $O(1)$ and $O(Ma^2)$ conservation equations:

Mass
- $O(1)$:

$$\frac{\partial \rho^{(0)}}{\partial t} + \nabla \cdot (\rho^{(0)} \vec{v}^{(0)}) = 0 \tag{1.26a}$$

- $O(Ma^2)$:

$$\frac{\partial \rho^{(1)}}{\partial t} + \nabla \cdot (\rho^{(1)} \vec{v}^{(0)} + \rho^{(0)} \vec{v}^{(1)}) = 0 \tag{1.26b}$$

Momentum
- $O(1)$:

$$0 = -\frac{1}{\gamma} \nabla p^{(0)} + \frac{Ma^2}{Fr} \rho^{(0)} \vec{g} \tag{1.27a}$$

- $O(Ma^2)$:

$$\frac{\partial \rho^{(0)} \vec{v}^{(0)}}{\partial t} + \nabla \cdot (\rho^{(0)} \vec{v}^{(0)} \otimes \vec{v}^{(0)}) = -\frac{1}{\gamma} \nabla p^{(1)} + \frac{Ma^2}{Fr} \rho^{(1)} \vec{g} + \frac{1}{Re} \nabla \cdot \bar{\bar{\tau}}^{(0)} \tag{1.27b}$$

Energy
- $O(1)$:

$$c_p^{(0)} \left(\frac{\partial \rho^{(0)} T^{(0)}}{\partial t} + \nabla (\rho^{(0)} \vec{v}^{(0)} T^{(0)}) \right) =$$

$$\frac{\gamma - 1}{\gamma} \left(\frac{\partial p^{(0)}}{\partial t} + \vec{v}^{(0)} \cdot \nabla p^{(0)} \right) + \frac{1}{Pe} \nabla \cdot (k^{(0)} \nabla T^{(0)}) \tag{1.28a}$$

14

– $O(Ma^2)$:

$$c_p^{(0)} \left(\frac{\partial \rho^{(1)} T^{(0)}}{\partial t} + \nabla \cdot (\rho^{(1)} \vec{v}^{(0)} T^{(0)}) + \frac{\partial \rho^{(0)} T^{(1)}}{\partial t} + \nabla \cdot (\rho^{(0)} \vec{v}^{(0)} T^{(1)}) \right) +$$

$$c_p^{(1)} \left(\frac{\partial \rho^{(0)} T^{(0)}}{\partial t} + \nabla \cdot (\rho^{(0)} \vec{v}^{(0)} T^{(0)}) \right) + c_p^{(0)} \nabla \cdot (\rho^{(0)} \vec{v}^{(1)} T^{(0)}) =$$

$$\frac{\gamma - 1}{\gamma} \left(\frac{\partial p^{(1)}}{\partial t} + \vec{v}^{(0)} \nabla p^{(1)} + \vec{v}^{(1)} \nabla p^{(0)} \right) +$$

$$\frac{1}{Pe} \left(\nabla \cdot (k^{(0)} \nabla T^{(1)}) + \nabla \cdot (k^{(1)} \nabla T^{(0)}) \right) +$$

$$\frac{\gamma - 1}{Re} \bar{\bar{\tau}}^{(0)} : \nabla \vec{v}^{(0)} \quad (1.28b)$$

Perfect gas law

– $O(1)$:

$$p^{(0)} = \rho^{(0)} T^{(0)} \quad (1.29a)$$

– $O(Ma^2)$:

$$\frac{p^{(1)}}{p^{(0)}} = \frac{\rho^{(1)}}{\rho^{(0)}} + \frac{T^{(1)}}{T^{(0)}} \quad (1.29b)$$

with

$$\bar{\bar{\tau}}^{(0)} = \mu^{(0)} \left((\nabla \vec{v}^{(0)} + (\nabla \vec{v}^{(0)})^t) - \frac{2}{3} (\nabla \cdot \vec{v}^{(0)}) \bar{\bar{\delta}} \right)$$

These equations make sense if $Ma^2/Re << O(1)$ in Eqs. (1.27b) and (1.28b) and $Ma^2/Fr = O(1)$ in Eqs. (1.27a) and (1.27b). Approximating the kinematic viscosity by $\nu \approx c\Lambda$, with Λ the mean free path of fluid, the first dimensional group is reduced to $Ma^2/Re \approx Ma \times \Lambda/l$, and thus it is very small, like it has been assumed. The second assumption deserves a closer scrutiny. It requires $gl/c_0^2 = O(1)$ or g and/or l to be large as in the atmospheric or stellar problems. In that case, to avoid acoustic waves, we require an additional assumption $\rho^{(0)}(\vec{x}, t) = f(\vec{v} \cdot \vec{g}, t)$, viz the leading term in the density expansion only depends on direction collinear to the gravity acceleration. But in numerous problems, $Fr \gtrsim O(1)$ so that the term $Ma^2/Fr \times \rho^{(0)} \vec{g}$ in Eq. (1.27a) is of order $O(Ma^2)$ and $Ma^2/Fr \times \rho^{(1)} \vec{g}$ in Eq. (1.27b) becomes $O(Ma^4)$. With such an assumption, we have

$$\nabla p^{(0)} = 0 \quad (1.30)$$

The leading part of the pressure then depends on time only. Then, the motion-induced spatial variations in pressure $p^{(1)} = O(\rho U^2)$ are extremely small and does not exceed the total static variation $p^{(0)}(t)$.

After dropping the zero superscripts, neglecting the $O(Ma^2)$-terms in the mass and energy equations, reintroducing the different scales for the variables and expressing the pressure as the sum of the thermodynamic pressure $\bar{P}(t)$ and the dynamical pressure $\Pi(\vec{x}, t)$

$$p(\vec{x}, t) = \bar{P}(t) + \Pi(\vec{x}, t) \quad (1.31)$$

the remaining leading order of the governing equations become:

Continuity equation

$$\frac{\partial \rho}{\partial t} + \nabla \cdot (\rho \vec{v}) = 0 \quad (1.32a)$$

Momentum equations

$$\frac{\partial \rho \vec{v}}{\partial t} + \nabla \cdot (\rho \vec{v} \otimes \vec{v}) = -\nabla (\Pi - \rho_0 \vec{x} \cdot \vec{g}) + (\rho - \rho_0)\vec{g} + \nabla \cdot \overline{\overline{\tau}} \qquad (1.32\text{b})$$

Energy equation

$$c_p \left(\frac{\partial \rho T}{\partial t} + \nabla \cdot (\rho \vec{v} T) \right) = \beta T \frac{d\bar{P}}{dt} + \nabla \cdot (k \nabla T) \qquad (1.32\text{c})$$

State equation – the perfect gas law

$$\bar{P}(t) = \rho(\vec{x}, t) r T(\vec{x}, t) \qquad (1.32\text{d})$$

1.3.2.2 Mass conservation in closed system

The splitting of the pressure into a thermodynamic part $\bar{P}$ and a dynamic contribution Π introduces a new unknown variable in the system. An extra equation is then needed to determine the state pressure $\bar{P}$.

In an open system, $\bar{P}$ equilibrates instantaneously with the ambient pressure. Therefore, the pressure time derivative simply vanishes in Eq. (1.32c).

In an enclosure of volume Ω, we can establish another relationship from the mass and energy conservation equations.

From the mass conservation equation The ideal gas law acts as a constraint enforced by the thermodynamic pressure:

$$\rho = \frac{\bar{P}}{rT}$$

Let $m_0 = \int_\Omega \frac{\bar{P}(\vec{x}, t_0)}{rT(\vec{x}, t_0)} d\vec{x}$ be the mass contained in the enclosure at time $t = t_0$. Without any sink or source of mass, we then have:

$$\int_\Omega \rho(\vec{x}, t) d\vec{x} \equiv \int_\Omega \frac{\bar{P}(t)}{rT(\vec{x}, t)} d\vec{x} = m_0$$

We then deduce

$$\bar{P}(t) = m_0 \frac{r}{\displaystyle\int_\Omega \frac{1}{T(\vec{x}, t)} d\vec{x}}$$

and the time derivative gives

$$\frac{d\bar{P}}{dt} = m_0 \frac{r \displaystyle\int_\Omega \frac{1}{T^2} \frac{\partial T}{\partial t} d\vec{x}}{\left(\displaystyle\int_\Omega \frac{1}{T(\vec{x}, t)} d\vec{x} \right)^2} \qquad (1.33)$$

From the energy conservation equation Substituting ρT in (1.32c) by $\bar{P}/r$ leads to

$$\frac{c_p}{r} \left(\frac{d\bar{P}}{dt} + \nabla \cdot (\bar{P} \vec{v}) \right) = \beta T \frac{d\bar{P}}{dt} + \nabla \cdot (k \nabla T)$$

Taking into account that the thermodynamic pressure depends only on time, we get:

$$\frac{c_p}{r} \left(\frac{d\bar{P}}{dt} + \bar{P} \nabla \cdot \vec{v} \right) = \beta T \frac{d\bar{P}}{dt} + \nabla \cdot (k \nabla T)$$

The velocity divergence can then be express by

$$\nabla \cdot \vec{v} = \frac{r}{\bar{P} c_p} \left(\nabla \cdot (k \nabla T) + \left(\beta T - \frac{c_p}{r} \right) \frac{d\bar{P}}{dt} \right) \tag{1.34}$$

Integrating over the flow domain Ω and using impervious boundary conditions, Eq.(1.34) becomes:

$$0 = \int_\Omega \frac{r}{\bar{P} c_p} \nabla \cdot (k \nabla T) \, d\vec{x} + \frac{d\bar{P}}{dt} \int_\Omega \frac{r}{\bar{P} c_p} \left(\beta T - \frac{c_p}{r} \right) d\vec{x}$$

After simplification by $\bar{P}$ and r, we have:

$$\frac{d\bar{P}}{dt} = \frac{\displaystyle\int_\Omega \frac{1}{c_p} \nabla \cdot (k \nabla T) \, d\vec{x}}{\displaystyle\int_\Omega \frac{1}{c_p} \left(\frac{c_p}{r} - \beta T \right) d\vec{x}}$$

$$= \frac{\displaystyle\int_\Omega \left(\nabla \cdot \left(\frac{k}{c_p} \nabla T \right) - (k \nabla T) \cdot \nabla \left(\frac{1}{c_p} \right) \right) d\vec{x}}{\displaystyle\int_\Omega \left(\frac{1}{r} - \frac{\beta T}{c_p} \right) d\vec{x}}$$

$$= \frac{\displaystyle\int_\Omega \left(\nabla \cdot \left(\frac{k}{c_p} \nabla T \right) + \frac{1}{c_p^2} (k \nabla T) \cdot \nabla c_p \right) d\vec{x}}{\displaystyle\int_\Omega \left(\frac{1}{r} - \frac{\beta T}{c_p} \right) d\vec{x}}$$

Applying the divergence theorem, we obtain

$$\frac{d\bar{P}}{dt} = \frac{\displaystyle\int_{\delta\Omega} \frac{k}{c_p} \nabla T \cdot \vec{n} \, d\vec{x} + \int_\Omega \frac{1}{c_p^2} (k \nabla T) \cdot \nabla c_p \, d\vec{x}}{\displaystyle\int_\Omega \left(\frac{1}{r} - \frac{\beta T}{c_p} \right) d\vec{x}} \tag{1.35}$$

where $\delta\Omega$ and denotes $\vec{n}$ the boundary of the domain Ω and the unit normal vector pointing outwards Ω. The rate of change of the thermodynamic pressure is affected by heat transferred through the boundary of the domain, the heat capacity and its gradient but also by the product βT.

For a perfect gas, $\beta = 1/T$ and $c_p = \gamma r/(\gamma - 1)$ then

$$\frac{d\bar{P}}{dt} = (\gamma - 1) \int_{\delta\Omega} k \nabla T \cdot \vec{n} \, d\vec{x}$$

1.4   Boussinesq approximation

The Boussinesq approximation proposed by Oberbeck (1873) and Boussinesq (1903) [33] considers a weak variation for the density while preserving the incompressible assumption for the mass equation. This model can be viewed as a simplification of the low Mach number approximation Eq. (1.32) when the relative variation of temperature is not too large, namely smaller than 0.1 [69].

The physical properties are assumed constant and the thermodynamic variables are expressed as small fluctuations about a stationary and uniform reference state:

$$
\begin{aligned}
\rho(\vec{x}, t) &= \rho_0 + \rho'(\vec{x}, t) \\
T(\vec{x}, t) &= T_0 + T'(\vec{x}, t) \\
p(\vec{x}, t) &= \bar{P}_0 + p'(\vec{x}, t)
\end{aligned}
$$

Using the definition of the pressure Eq. (1.31), we identify $\bar{P}(t) = \bar{P}_0$ and $\Pi(\vec{x}, t) = p'(\vec{x}, t)$. Keeping the leading order only, this leads to:

$$
\nabla \cdot \vec{v} = 0 \tag{1.36a}
$$

$$
\frac{\partial \rho_0 \vec{v}}{\partial t} + \nabla \cdot (\rho_0 \vec{v} \otimes \vec{v}) = -\nabla(p' - \rho_0 \vec{x} \cdot \vec{g}) + \rho' \vec{g} + \nabla \cdot \bar{\bar{\tau}} \tag{1.36b}
$$

$$
c_p \left(\frac{\partial \rho_0 T}{\partial t} + \nabla \cdot (\rho_0 \vec{v} T) \right) = \nabla \cdot (k \nabla T) \tag{1.36c}
$$

$$
0 = \rho' r T_0 + \rho_0 r T' \tag{1.36d}
$$

From Eq. (1.36d), we deduce the expression of the density fluctuation as a function of the departure of the temperature with its reference value:

$$
\rho' = -\rho_0 \frac{T'}{T_0} = -\rho_0 \frac{T - T_0}{T_0}
$$

Introducing the isobaric volume expansion coefficient $\beta = 1/\rho_0 \times (\partial \rho)/(\partial T))_{T_0} = 1/T_0$, we recover the usual density relation

$$
\rho' = -\rho_0 \beta (T - T_0) \tag{1.37}
$$

It is worth to point out that the density fluctuation in Eq. (1.36b), and expressed by Eq. (1.37), cannot be neglected for natural convection flows, otherwise no motion could occur.

Chapter 2

Numerical scheme

2.1 Temporal discretization

2.1.1 Initial value problem

We consider the initial value problem

$$\frac{d\phi(t)}{dt} = f(t, \phi(t)), \qquad \phi(t = 0) = \phi^{(0)}$$

with ϕ^0 the initial condition. By integrating the differential equation in time, from 0 to $T > 0$, we obtain

$$\phi(T) - \phi^{(0)} = \int_0^T f(t, \phi(t)) \, dt \tag{2.1}$$

The exact solution $\phi(t)$ being unknown, the right-hand side of this equation must be approximated. The idea is firstly to split the time interval $[0, T]$ into small successive intervals such that $T = \sum_{m=0}^n \Delta t_m$, $\Delta t_m = t_{m+1} - t_m$ with $t_0 = 0$ and $t_{n+1} = T$. We also assume the time steps Δt_m are of same order, $\Delta t_n = O(\Delta t)$. Then, Eq. (2.1) reads:

$$\phi(t_{n+1}) - \phi^{(0)} = \sum_{m=0}^n \int_{t_m}^{t_{m+1}} f(t, \phi(t)) \, dt \tag{2.2}$$

and subtracting $\phi(t_{n+1})$ to $\phi(t_n)$ leads to:

$$\phi(t_{n+1}) - \phi(t_n) = \int_{t_n}^{t_{n+1}} f(t, \phi(t)) \, dt \tag{2.3}$$

The issue is now to express an approximation of the right-hand side of (2.3). The approximation $\phi(t_i)$ is now noted $\phi^{(i)}$.

Different classical methods presented are based on Taylor expansions of the integrand of Eq. (2.3).

Forward Euler The function $f(t, \phi(t))$ is expressed starting from t_n:

$$f(t, \phi(t)) = f(t_n, \phi^{(n)}) + (t - t_n) \Big(\frac{\partial f(t, \phi(t))}{\partial t} + \frac{\partial f(t, \phi(t))}{\partial \phi} \frac{d\phi}{dt} \Big)_{t_n} + O((t - t_n)^2)$$

Substituting this expression in Eq. (2.3) leads to

$$
\begin{aligned}
\phi^{(n+1)} - \phi^{(n)} &= f(t_n, \phi^{(n)}) \Delta t_n + \frac{\Delta t_n^2}{2} \Big(\frac{\partial f(t, \phi(t))}{\partial t} + \frac{\partial f(t, \phi(t))}{\partial \phi} \frac{d\phi}{dt} \Big)_{t_n} + O(\Delta t_n)^3 \\
&\approx f(t_n, \phi^{(n)}) \Delta t_n
\end{aligned}
$$

This method is referenced as an explicit Euler scheme because it only uses known variables. This approximation introduces an error of order $O(\Delta t_n)^2$ respectively to Eq. (2.3) and a cumulative error $O(\Delta t)$ when starting from the initial condition (Eq. (2.2)). This explicit Euler scheme is then first order accurate.

Backward Euler The function $f(t, \phi(t))$ is expressed starting from t_{n+1}:

$$f(t, \phi(t)) = f(t_{n+1}, \phi^{(n+1)}) +$$
$$(t - t_{n+1})\Big(\frac{\partial f(t, \phi(t))}{\partial t} + \frac{\partial f(t, \phi(t))}{\partial \phi}\frac{d\phi}{dt}\Big)_{t_{n+1}} + O((t - t_{n+1})^2)$$

Substituting this expression in Eq. (2.3) gives

$$
\begin{aligned}
\phi^{(n+1)} - \phi^{(n)} &= f(t_{n+1}, \phi^{(n+1)})\Delta t_n + \frac{\Delta t_n^2}{2}\Big(\frac{\partial f(t, \phi(t))}{\partial t} + \frac{\partial f(t, \phi(t))}{\partial \phi}\frac{d\phi}{dt}\Big)_{t_{n+1}} + O(\Delta t_n)^3 \\
&\approx f(t_{n+1}, \phi^{(n+1)})\Delta t_n
\end{aligned}
$$

This approach leads to an implicit Euler scheme because the right-hand side is unknown at time $t = t^{(n+1)}$. The global accuracy of this scheme is first order.

Midpoint rule – Crank-Nicolson method The function $f(t, \phi(t))$ is expressed starting from $t_{n+1/2} = (t_n + t_{n+1})/2$:

$$f(t, \phi(t)) = f(t_{n+1/2}, \phi^{(n+1/2)}) +$$
$$(t - t_{n+1/2})\Big(\frac{\partial f(t, \phi(t))}{\partial t} + \frac{\partial f(t, \phi(t))}{\partial \phi}\frac{d\phi}{dt}\Big)_{t_{n+1/2}} + O((t - t_{n+1/2})^2)$$

Integrating this relation between t_n and t_{n+1} cancels the term involving the partial derivatives. Eq. (2.3) writes:

$$
\begin{aligned}
\phi^{(n+1)} - \phi^{(n)} &= f(t_{n+1/2}, \phi^{(n+1/2)})\Delta t_n + O(\Delta t_n)^3 \\
&\approx \Big(\frac{f(t_n, \phi^{(n)}) + f(t_{n+1}, \phi^{(n+1)})}{2} + O(\Delta t_n)^2\Big)\Delta t_n + O(\Delta t_n)^3 \\
&\approx \frac{f(t_n, \phi^{(n)}) + f(t_{n+1}, \phi^{(n+1)})}{2}\Delta t_n
\end{aligned}
$$

This approximation is then third order accurate on one time step Δt_n, but simply of second order when starting from initial condition (Eq. (2.2)).

Backward second order Euler scheme We suppose $\Delta t_n = \Delta t_{n-1} = \Delta t$. To improve the order of accuracy of the backward Euler scheme, we consider the two following expressions, $\phi(t_{n+1}) - \phi(t_n)$ (Eq. (2.3))

$$\phi(t_{n+1}) - \phi(t_n) = \int_{t_n}^{t_{n+1}} f(t, \phi(t))\, dt$$

and $\phi(t_{n+1}) - \phi(t_{n-1})$

$$\phi(t_{n+1}) - \phi(t_{n-1}) = \int_{t_{n-1}}^{t_{n+1}} f(t, \phi(t))\, dt$$

Using the backward Euler scheme, we obtain

$$\phi^{(n+1)} - \phi^{(n)} = f(t_{n+1}, \phi^{(n+1)})\Delta t +$$
$$\frac{\Delta t^2}{2}\Big(\frac{\partial f(t, \phi(t))}{\partial t} + \frac{\partial f(t, \phi(t))}{\partial \phi}\frac{d\phi}{dt}\Big)_{t_{n+1}} + O(\Delta t)^3 \quad (2.4)$$

and

$$\phi^{(n+1)} - \phi^{(n-1)} = f(t_{n+1}, \phi^{(n+1)})(2\Delta t)+$$
$$\frac{(2\Delta t)^2}{2}\left(\frac{\partial f(t, \phi(t))}{\partial t} + \frac{\partial f(t, \phi(t))}{\partial \phi}\frac{d\phi}{dt}\right)_{t_{n+1}} + O(\Delta t)^3 \quad (2.5)$$

The term weighted by Δt^2 is eliminated by the linear combination $4 \times$ (Eq. (2.4)) − (Eq. (2.5)) to provide:

$$3\phi^{(n+1)} - 4\phi^{(n)} + \phi^{(n-1)} \approx 2f(t_{n+1}, \phi^{(n+1)})\Delta t \quad (2.6)$$

This local approximation is third order but it reduces to second order when we consider the full time integration starting from $t = 0$. It must be noticed that similar expressions can also be written if $\Delta t_n \neq \Delta t_{n-1}$.

The orders of accuracy of these methods make sense only if the schemes are stable during the temporal iterations. Therefore, it may result restriction conditions on the time step Δt_n. It can be proved that whatever the time step is, if $(\partial f(t, \phi))/(\partial \phi) < 0$, the implicit Euler and Crank-Nicolson schemes are unconditionally stable. The stability of the explicit Euler method requires

$$\left|1 + \Delta t_n \left.\frac{\partial f(t, \phi)}{\partial \phi}\right|_{t=t_n}\right| < 1$$

and thus an upper bound for the time step. If $f(t, \phi)$ represents a 1D-diffusion contribution ($f(t, \phi) = (\partial^2 \phi)/(\partial x^2)$) in an unbounded x-domain, $(\partial f(t, \phi))/(\partial \phi)$ writes $-k^2$ in the Fourier space, with $k \in \mathbf{R}$ the wavenumber in x-direction. In this example, the implicit Euler and Crank-Nicolson schemes are then unconditionally stable (energy norm) whereas the wavenumber k is stable for the explicit Euler method only if $\Delta t < 2/k^2$. In physical space, this inequality reduces to classical relation $\Delta x^2/\Delta t < 1/2$ with Δx the smallest admissible wave length corresponding, for example, to the smallest spatial grid size.

2.1.2 Governing fluid flow equations

The mass and momentum equations are expressed in their conservative form whereas the energy equation is written in convective form. This latter choice is explained by the following remarks. In the conservative form, the temperature equation exhibits the product of the density by the temperature. But in the low Mach number approximation, this product is equal to the thermodynamic pressure which does not depend any more on space. It results a temperature equation of which the numerical solution proves to be unstable. Although the convective form of the temperature equation is preferred, the convective fluxes remains conservative at the numerical level (see Sec. 2.2.3.3).

The low Mach approximation (1.32) writes:

$$\frac{\partial \rho}{\partial t} + \nabla \cdot (\rho \vec{v}) = 0 \quad (2.7a)$$

$$\frac{\partial \rho \vec{v}}{\partial t} + \nabla \cdot (\rho \vec{v} \otimes \vec{v}) = -\nabla \Pi_g + \nabla \cdot \bar{\bar{\tau}} + (\rho - \rho_0)\vec{g} \quad (2.7b)$$

with $\Pi_g = \Pi - \rho_0 \vec{x} \cdot \vec{g}$ the departure from the hydrostatic pressure

$$\rho c_p \left(\frac{\partial T}{\partial t} + (\vec{v} \cdot \nabla)T\right) = \frac{d\bar{P}}{dt} + \nabla \cdot (k\nabla T) \quad (2.7c)$$

An extra equation is needed to compute the new variable $\bar{P}(t)$.

Low Mach number – Open system The thermodynamic pressure equilibrates instantaneously with the outer pressure $\bar{P}_{out}$. We then get

$$\bar{P}(t) = P_{out}, \qquad \left(\text{and then } \frac{d\bar{P}}{dt} = 0\right) \tag{2.7d}$$

with $\rho = \bar{P}_{out}/(rT(\vec{x},t))$ the equation of state for the gas.

Low Mach number – Enclosure The thermodynamic pressure equilibrates instantaneously to satisfy the global mass conservation (Sec. (1.3.2.2)):

$$\bar{P}(t) = \frac{m_0}{\displaystyle\int_\Omega \frac{1}{rT(\vec{x},t)}\, d\vec{x}} \tag{2.7e}$$

with $\rho = \bar{P}(t)/(rT(\vec{x},t))$ the equation of state for the gas.

Boussinesq approximation The thermodynamic pressure is kept constant, then

$$\frac{d\bar{P}}{dt} = 0 \tag{2.7f}$$

with $\rho = \rho_0$ except in the gravity contribution (Eq. (2.7b)) where the density is a linear function of the temperature.

We now focus on the low Mach number approximation for fluid flows inside closed cavities. The set of equations (2.7a)-(2.7c), plus equation (2.7e), are discretized in time with the second order backward Euler scheme:

$$\frac{3\rho^{(n+1)} - 4\rho^{(n)} + \rho^{(n-1)}}{2\Delta t} + \nabla \cdot (\rho^{(n+1)}\vec{v}^{(n+1)}) = 0 \tag{2.8a}$$

$$\frac{3\rho^{(n+1)}\vec{v}^{(n+1)} - 4\rho^{(n)}\vec{v}^{(n)} + \rho^{(n-1)}\vec{v}^{(n-1)}}{2\Delta t} + (\nabla \cdot (\rho\vec{v} \otimes \vec{v}))^{(n+1)AB} = -(\nabla\Pi_g)^{(n+1)} +$$
$$\nabla \cdot \left(\mu^{(n+1)}\left(\nabla\vec{v}^{(n+1)} + (\nabla\vec{v}^{(n+1)AB})^t - \frac{2}{3}\nabla \cdot \vec{v}^{(n+1)AB}\bar{\bar{\delta}}\right)\right) + (\rho^{(n+1)} - \rho_0)\vec{g} \tag{2.8b}$$

$$c_p^{(n+1)AB}\left(\rho^{(n+1)AB}\frac{3T^{(n+1)} - 4T^{(n)} + T^{(n-1)}}{\Delta t} + ((\rho\vec{v} \cdot \nabla)T)^{(n+1)AB}\right) =$$
$$\frac{3\bar{P}^{(n+1)} - 4\bar{P}^{(n)} + \bar{P}^{(n-1)}}{\Delta t} + \nabla \cdot (k^{(n+1)AB}\nabla T^{(n+1)}) \tag{2.8c}$$

$$\bar{P}^{(n+1)} = \frac{m_0}{\displaystyle\int_\Omega \frac{1}{rT^{(n+1)}(\vec{x})}\, d\vec{x}} \tag{2.8d}$$

In this set of equations, all variables are evaluated at $t = (n+1)\Delta t$, but in different ways:
– the superscript $^{(n+1)}$ refers to implicit value;
– the superscript $^{(n+1)AB}$ indicates second order extrapolation using Adams-Bashforth scheme: $X^{(n+1)AB} = 2X^{(n+1)} - X^{(n)}$.

The set of Eqs. (2.8) are solved iteratively as follows:

1. The energy equation (2.8c) is first considered, with $\bar{P}^{(n+1)}$ and $T^{(n+1)}$ unknown;

2. The temperature field being computed at time $(n+1)\Delta t$, the momentum (Eq. (2.8b)) and mass (Eq. (2.8a)) equations are solved using a time splitting method. Pressure and velocity fields are updated at the new time step $(n+1)$.

2.1.3 Energy equation

For a low Mach number approximation of a fluid flowing in an enclosure, T^{n+1} and $\bar{P}^{n+1}$ are non-linearly coupled in Eqs. (2.8c) and (2.8d). Solutions are then obtained using the Newton-Raphson method.

2.1.3.1 Newton-Raphson method – Principle

To find the root of a single algebraic equation $f(x) = 0$, we use Taylor series to linearize this function with an estimated value x_k:

$$f(x) \approx f(x_k) + f'(x_k)(x - x_k)$$

Setting the linearized function to zero provides a new estimate of the root:

$$x_{k+1} = x_k - \frac{f(x_k)}{f'(x_k)} \tag{2.9}$$

Iterations are carried on till the error between x_k and x_{k+1} is as small as desired. The speed of convergence to the root $\bar{x}$ is second order, namely there exists a finite positive real β such that

$$\lim_{k \to \infty} \frac{|x_{k+1} - \bar{x}|}{|x_k - \bar{x}|^2} = \beta$$

If the initial estimate x_0 is close enough of the root, less than three iterations are usually necessary to converge.

2.1.3.2 Newton-Raphson method – Application

We aim to solve the non-linear equation $f(\bar{P}^{(n+1)}, T^{(n+1)}(\bar{P}^{(n+1)})) = 0$ with

$$f(\bar{P}, T(\bar{P})) = \bar{P} - \frac{m_0}{\displaystyle\int_\Omega \frac{1}{rT(\vec{x})} \, d\vec{x}}$$

with $T(\bar{P})$ provided by Eq. (2.8c):

$$\left(\frac{3c_p^{(n+1)AB} \rho^{(n+1)AB}}{\Delta t} - \nabla \cdot (k^{(n+1)AB} \nabla) \right) T = \frac{3\bar{P} - 4\bar{P}^{(n)} + \bar{P}^{(n-1)}}{\Delta t} +$$

$$c_p^{(n+1)AB} \left(\rho^{(n+1)AB} \frac{4T^{(n)} - T^{(n-1)}}{\Delta t} - ((\rho\vec{v} \cdot \nabla)T)^{(n+1)AB} \right) \tag{2.10}$$

The Newton-Raphson method requires the computation of the derivative of f with respect to its variable $\bar{P}$ (Eq. (2.9)). Because this expression is a bit difficult to establish, we substitute its exact value by an approximation defined as follows:

$$\frac{df}{d\bar{P}} \approx \frac{f(\bar{P} + \delta\bar{P}, T(\bar{P} + \delta\bar{P})) - f(\bar{P}, T(\bar{P}))}{\delta\bar{P}}$$

with $\delta\bar{P} \ll \bar{P}$.

The Newton-Raphson algorithm writes:

1. Set $\bar{P}_0 = \bar{P}^{(n+1)AB}$ an estimated value at the initial iteration,

2. for $k \geq 0$, do

(a) Compute the temperature field $T_{k,1}(\bar{P}_k)$ using Eq. (2.10),

(b) Compute the temperature field $T_{k,2}(\bar{P}_k + \delta\bar{P})$ using Eq. (2.10),

(c) Define $\bar{P}_{k+1}$ as follows:

$$\bar{P}_{k+1} = \bar{P}_k - f(P_k, T_{k,1})\frac{\delta\bar{P}}{f(\bar{P}+\delta\bar{P}, T_{k,2}) - f(\bar{P}, T_{k,1})}$$

(d) if $(\bar{P}_{k+1} - \bar{P}_k)/P_k < 10^{-12}$, exit.

3. $\bar{P}^{(n+1)} = \bar{P}_{k+1}$, stop.

Once again, notice that iterative procedure is useful for closed systems only. In the other cases, the thermodynamic pressure is kept constant and then $d\bar{P}/dt$ disappears. Therefore, only one solving of Eq. (2.10) cleared of the pressure terms is needed.

2.1.4 Navier-Stokes equations – Fractional-time step method

For fluid flows governed by incompressible Navier-Stokes equations, the main numerical difficulty relies on the coupling between the pressure used in the momentum equation and the mass equation. Indeed, whereas the spatio-temporal pressure evolution is directly linked to local mass fluxes in compressible flows, this coupling disappears when Boussinesq or low Mach number approximations are used. It results that the scaling of the pressure in the momentum equation is no more based on the thermodynamic pressure (or static pressure), but on the dynamic pressure. Another consequence is the local pressure must adapt instantaneously in order to fulfill the mass constraint. The relaxation of this coupling may lead to numerical instabilities.

The fractional-time step method is an efficient algorithm developed for incompressible Navier-Stokes equations to maintain the coupling between the pressure and velocity while the mass and the momentum equations are solved separately [89]. This method was firstly proposed by Chorin [48] and Teman [154] independently. Based on these precursory works, Kim and Moin [89] improved this method in conjunction with the approximate-factorization technique [20] and with appropriate boundary conditions for the intermediate velocity field [100]. Despite the efficiency of this approach in terms of computational time and memory storage, this method introduces a numerical boundary layer on both the pressure field and the velocity field [162].

The energy equation being solved at first, the temperature field and the thermodynamic pressure are evaluated at the new time $(n+1)\Delta t$. Consequently, the density $\rho^{(n+1)}$ and the dynamical viscosity $\mu^{(n+1)}$ become also known functions. For sake of simplicity, we gather all known terms into a single vector noted $\vec{f}$ such that

$$\vec{f} = \frac{4\rho^{(n)}\vec{v}^{(n)} - \rho^{(n-1)}\vec{v}^{(n-1)}}{2\Delta t} - (\nabla \cdot (\rho\vec{v}\otimes\vec{v}))^{(n+1)AB} +$$
$$\nabla \cdot \left(\mu^{(n+1)}\left((\nabla\vec{v}^{(n+1)AB})^t - \frac{2}{3}\nabla\cdot\vec{v}^{(n+1)AB}\bar{\bar{\delta}}\right)\right) + (\rho^{(n+1)} - \rho_0)\vec{g} \quad (2.11)$$

The discrete Navier-Stokes equations (2.8b) and (2.8a) then writes:

$$\begin{cases} \dfrac{3\rho^{(n+1)}\vec{v}^{(n+1)}}{2\Delta t} - \nabla \cdot \left(\mu^{(n+1)}\nabla\vec{v}^{(n+1)}\right) = -(\nabla\Pi_g)^{(n+1)} + \vec{f} & (2.12a) \\[2mm] \dfrac{3\rho^{(n+1)} - 4\rho^{(n)} + \rho^{(n-1)}}{2\Delta t} + \nabla \cdot (\rho^{(n+1)}\vec{v}^{(n+1)}) = 0 & (2.12b) \end{cases}$$

The method initially developed for constant density [89] is extended to low Mach number approximation. It consists of three successive steps:

1. Find the intermediate velocity $\vec{v}^{(n+1)^*}$ solution of the momentum equation (2.12a), provided the pressure at time $(n+1)\Delta t$ is substituted by the pressure at $t = n\Delta t$:

$$\frac{3\rho^{(n+1)}\vec{v}^{(n+1)^*}}{2\Delta t} - \nabla \cdot \left(\mu^{(n+1)}\nabla\vec{v}^{(n+1)^*}\right) = -(\nabla\Pi_g)^{(n)} + \vec{f} \qquad (2.13)$$

with the same boundary conditions as $\vec{v}^{(n+1)}$,

2. Define the velocity at the new time step as the sum of the intermediate velocity and the gradient of a scalar variable $\Phi^{(n+1)}$:

$$\vec{v}^{(n+1)} = \vec{v}^{(n+1)^*} - \frac{2\Delta t}{3\rho^{(n+1)}}\nabla\Phi^{(n+1)} \qquad (2.14)$$

such that the mass equation (2.12b) is satisfied:

$$\frac{3\rho^{(n+1)} - 4\rho^{(n)} + \rho^{(n-1)}}{2\Delta t} + \nabla \cdot \left(\rho^{(n+1)}\vec{v}^{(n+1)^*}\right) = \frac{2\Delta t}{3}\nabla \cdot \nabla\Phi^{(n+1)} \qquad (2.15)$$

This Poisson equation requires boundary conditions. Two cases have to be considered:

– The velocity normal to the boundary $\vec{v} \cdot \vec{n}$ is prescribed, as for example along solid walls. Accounting for the boundary conditions on $\vec{v}^*$ and the relation between the new velocity and the intermediate velocity (Eq. (2.14)), we find

$$\nabla\Phi^{(n+1)} \cdot \vec{n} = 0$$

– The normal derivative of the normal component of the velocity $\nabla(\vec{v} \cdot \vec{n}) \cdot \vec{n}$ is prescribed to $h(\vec{x}, t)$, as for instance at open boundaries. In that specific case, the pressure must also be known in order the solution exists. Let us note $k(\vec{x}, t)$ the pressure, then

$$\Phi^{(n+1)} = k(\vec{x}, t^{(n+1)}) - \Pi^{(n)}$$

It is interesting to notice that the boundary condition associated to the normal component to the boundary then becomes

$$\frac{\partial(\vec{v}^{(n+1)} \cdot \vec{n})}{\partial\vec{n}} = h(\vec{x}, t^{(n+1)}) - \frac{2\Delta t}{3\rho^{(n+1)}}\frac{\partial}{\partial\vec{n}}(\nabla\Phi^{(n+1)} \cdot \vec{n}) \qquad (2.16)$$

Then in the general case, only the intermediate velocity satisfy the boundary condition when the pressure is prescribed. However, it is worth to notice that the boundary condition $\nabla(\vec{v}^{(n+1)} \cdot \vec{n}) \cdot \vec{n} = h(\vec{x}, t^{(n+1)})$ is recovered when $\Delta t \to 0$, and also when the solution converge toward a stationary solution since $\Phi \equiv \Pi_g^{(n+1)} - \Pi_g^{(n)} \to 0$.

3. The velocity is updated using Eq. (2.14), and the new pressure writes

$$\Pi_g^{(n+1)} = \Pi_g^{(n)} + \Phi^{(n+1)} \qquad (2.17)$$

The pressure correction step (Eq. (2.17)) shows that $\Phi^{(n+1)} = \Pi_g^{(n+1)} - \Pi_g^{(n)} \equiv O(\Delta t)$. Thus, both the velocity decomposition (Eq. (2.14)) and the boundary conditions (Eq. (2.16)) are consistent in time to second order.

2.2 Spatial discretization

2.2.1 Discrete formulation of the equations

The partial differential equations are discretized in space using the finite volume method. The principle of the finite volume method is now briefly described.

First, this consists in subdividing the physical domain into a finite number of contiguous control volumes or cells. This subdivision may differ according to the variable considered. The equations, expressed in their conservative form, are then integrated on the whole geometry. Using the divergence (or Ostrogradsky) formula, volume integrals defined on each cell are substituted by surface integrals. And one key point of the finite volume method relies on the discrete approximation of the surface integrals. They must satisfy the following conservation property: the sum of the discrete fluxes leaving two adjacent cells through their common surface must be zero. To achieve the discrete scheme, the variables are assumed constant on each control volume. Interpolation procedures are used to express the variable on cell faces and algebraic relations are used to provide approximations of spatial derivatives. It results a large linear (or non-linear) algebraic system at each time step, coupling the variables on the different cells, which is solved numerically.

In our implementation of the finite volume scheme, we used only one set of control volume. In that case, the scalar variables and the components of the velocity are approximated on the same representative point on the cell: this approach is known as a collocated scheme. For convenience, this specific point is called *center* of the cell, even if it is not necessary the centroid of the control volume. We denote by K any cell of the mesh and $\vec{x}_K$ the coordinate of its center. To differentiate the continuous operators to their discrete counterpart expressed on K, the subscript K is added.

Any continuous variable $\phi(\vec{x}) \in \{u, v, w, p, T\}$ expressed at the cell center $\vec{x}_K$, $K \in \mathcal{M}$, is approximated by ϕ_K, viz $\phi(\vec{x}_K) \approx \phi_K$. The same is worth for the values evaluated on the boundary of the domain $\sigma \in \varepsilon_{out}$: $\phi(\vec{x}_\sigma) \approx \phi_\sigma$. The discrete variables ϕ_K are unknown whereas ϕ_σ are either known if Dirichlet boundary conditions are prescribed or can be expressed as a function of the inner variables defined on cell centers.

2.2.1.1 Pressure oscillations and stabilization method

It is well known that the discretization spaces for the velocity components and the pressure must differ to fulfill the Babuška-Brezzi inf-sup condition [14, 35]. But for collocated variables, this condition is not satisfied and spurious oscillations may appear into the numerical solution. To avoid such problems, the equation (2.15) dealing with the pressure correction must be stabilized. Let us rewrite this equation in its discrete form:

$$\frac{3\rho_K^{(n+1)} - 4\rho_K^{(n)} + \rho_K^{(n-1)}}{2\Delta t} + \nabla_K \cdot \left(\rho^{(n+1)} \vec{v}^{(n+1)*} \right) = \frac{2\Delta t}{3} \nabla_K \cdot \widetilde{\nabla}_K \Phi^{(n+1)} \qquad (2.18)$$

where $\widetilde{\nabla}_K$ and $\nabla_K \cdot$ denote the discrete gradient used for the pressure variable and the discrete divergence, both expressed on cell K.

To explain the appearance of oscillations, let us consider a one dimensional problem gridded with a regular space step $\Delta x = x_{i+1} - x_i$ and let us note Φ_i, the correction pressure at the cell centroid x_i. The divergence of a vector $\vec{v} = u\vec{e}_x$ and the gradient on

cell $K =]x_i - \Delta x/2; x_i + \Delta x/2[$ simply write:

$$\begin{cases} \nabla_K \cdot \vec{v} \equiv \dfrac{\frac{u_{i+1}+u_i}{2} - \frac{u_i+u_{i-1}}{2}}{\Delta x} = \dfrac{u_{i+1} - u_{i-1}}{2\Delta x} \\ \widetilde{\nabla}_K \Phi \equiv \dfrac{\Phi_{i+1} - \Phi_{i-1}}{2\Delta x} \vec{e}_x \end{cases}$$

Therefore the discrete Laplacian expressed on cell $K =]x_i - \Delta x/2; x_i + \Delta x/2[$

$$\nabla_K \cdot \widetilde{\nabla}_K \Phi = \dfrac{\frac{\Phi_{i+2}-\Phi_i}{2\Delta x} - \frac{\Phi_i-\Phi_{i-2}}{2\Delta x}}{2\Delta x} = \dfrac{\Phi_{i+2} - 2\Phi_i + \Phi_{i-2}}{(2\Delta x)^2}$$

does not depend on neighboring cells $]x_{i-1} - \Delta x/2; x_{i-1} + \Delta x/2[$ and $]x_{i+1} - \Delta x/2; x_{i+1} + \Delta x/2[$. It results a decoupling of odd and even cell values, and a birth of spurious oscillations which are organized into checkerboards for two-dimensional problems. One way to suppress these non-physical oscillations is to substitute $\nabla_K \cdot \widetilde{\nabla}_K$ by a true Laplacian operator build on one grid size [131].

$$\nabla_K^2 \phi \equiv (\nabla \cdot \nabla \Phi)_K = \dfrac{\Phi_{i+1} - 2\Phi_i + \Phi_{i-1}}{\Delta x^2}$$

This substitution introduces a residual contribution $R \equiv (\nabla \cdot \nabla \Phi)_K - \nabla_K \cdot \widetilde{\nabla}_K \Phi$ which is consistent to $O(\Delta x^2)$ for a regular mesh (or for a grid slightly non-uniform), and then it tends to zero with the grid size. Mathematically, it consists in replacing the collocated divergence and gradient operators by their staggered versions with the normal components of vectors (velocity and pressure gradient) expressed on cell faces.

Finally, equation (2.18) is rewritten as follows:

$$\dfrac{3\rho_K^{(n+1)} - 4\rho_K^{(n)} + \rho_K^{(n-1)}}{2\Delta t} + \nabla_K \cdot \left(\rho^{(n+1)} \vec{v}^{(n+1)*}\right) = \dfrac{2\Delta t}{3} \left(\nabla \cdot \nabla \Phi^{(n+1)}\right)_K \qquad (2.19)$$

2.2.1.2 Discrete equations

The discrete formulation of the energy equation (2.8c) (or Eq. (2.10)) and the discrete Navier-Stokes equations expressed with the fractional-time step method (Eq. (2.13) for the diffusion step and Eq. (2.15) for the pressure correction) write:

$$c_{p_K}^{(n+1)AB} \left(\rho_K^{(n+1)AB} \dfrac{3T_K^{(n+1)} - 4T_K^{(n)} + T_K^{(n-1)}}{\Delta t} + \left(((\rho\vec{v}) \cdot \nabla)T \right)_K^{(n+1)AB} \right) =$$

$$\dfrac{3\bar{P}_K^{(n+1)} - 4\bar{P}_K^{(n)} + \bar{P}_K^{(n-1)}}{\Delta t} + \left(\nabla \cdot (k^{(n+1)AB} \nabla T^{(n+1)}) \right)_K \quad (2.20)$$

$$\begin{cases} \dfrac{3\rho_K^{(n+1)} \vec{v}_K^{(n+1)*}}{2\Delta t} - \left(\nabla \cdot \left(\mu^{(n+1)} \nabla \vec{v}^{(n+1)*} \right) \right)_K = - \left(\widetilde{\nabla}_K \Pi_g \right)^{(n)} + \vec{f}_K & (2.21a) \\ \dfrac{3\rho_K^{(n+1)} - 4\rho_K^{(n)} + \rho_K^{(n-1)}}{2\Delta t} + \nabla_K \cdot \left(\rho^{(n+1)} \vec{v}^{(n+1)*} \right) = \dfrac{2\Delta t}{3} \left(\nabla \cdot \nabla \Phi^{(n+1)} \right)_K & (2.21b) \end{cases}$$

with

$$\vec{f}_K = \dfrac{4\rho_K^{(n)} \vec{v}_K^{(n)} - \rho_K^{(n-1)} \vec{v}_K^{(n-1)}}{2\Delta t} - \left(\nabla \cdot \left((\rho\vec{v}) \otimes \vec{v} \right) \right)_K^{(n+1)AB} +$$

$$\widehat{\nabla_K \cdot} \left(\mu^{(n+1)} \left((\nabla_K \vec{v}^{(n+1)AB})^t - \dfrac{2}{3} \nabla_K \cdot \vec{v}^{(n+1)AB} \bar{\bar{\delta}} \right) \right) + (\rho_K^{(n+1)} - \rho_{0_K})\vec{g} \quad (2.22)$$

27

The updated velocity and pressure on cell K write:

$$\vec{v}_K^{(n+1)} = \vec{v}_K^{(n+1)*} - \frac{2\Delta t}{3\rho_K^{(n+1)}} \widetilde{\nabla}_K \Phi^{(n+1)} \tag{2.23}$$

$$\Pi_{gK}^{(n+1)} = \Pi_{gK}^{(n)} + \Phi_K^{(n+1)} \tag{2.24}$$

2.2.2 Discretization space, notations and geometrical requirements

The discretization space is defined by $\mathcal{D} = (\mathcal{M}, \varepsilon, \mathcal{P})$ with $\mathcal{M}$ the set of control volumes, ε the set of faces bounding the control volumes and $\mathcal{P}$ the set of points coordinates where the variables are approximated.

The set of faces ε is divided into two disjoint subsets ε_{in} and ε_{out} such that $\varepsilon = \varepsilon_{in} \cup \varepsilon_{out}$. The subset ε_{in} contains faces between adjacent control volumes whereas ε_{out} gathers faces located on the boundary of the computational domain. The set of faces making up of the control volume $K \in \mathcal{M}$ is noted ε_K.

For each control volume $K \in \mathcal{M}$, we denote by
  – m_K its volume in $3D$ (or its area in $2D$);
  – $\vec{x}_K \in \mathcal{P}$ the coordinates of its cell center.

For a face $\sigma \in \varepsilon$, we define
  – $\sigma \in \varepsilon_K \cap \varepsilon_L$ the common face in $3D$ (or edge in $2D$) between adjacent cells $K \in \mathcal{M}$ and $L \in \mathcal{M}$;
  – $\sigma \in \varepsilon_K \cap \varepsilon_{out}$ the common face in $3D$ (or edge in $2D$) between the cell $K \in \mathcal{M}$ and the boundary of the domain;
  – $\vec{x}_\sigma$ the centroid of σ;
  – m_σ the surface in $3D$ (or length in $2D$) of σ;
  – d_{KL} the distance between $\vec{x}_K$ and $\vec{x}_L$;
  – $d_{K\sigma}$ the distance between $\vec{x}_K$ and $\vec{x}_\sigma$;
  – $\vec{n}_{K\sigma}$ the unit normal vector to σ, pointing outside K.

We also define two algebraic quantities which correspond to the algebraic contributions of the reduced distances between the cell centers $\vec{x}_K$ and $\vec{x}_L$ to the centroid $\vec{x}_\sigma$, in the normal direction $\vec{n}_{K\sigma}$ of the interface $\sigma \in \varepsilon_K \cap \varepsilon_L$:

$$\alpha_K = \frac{\overrightarrow{x_\sigma x_L} \cdot \vec{n}_{K\sigma}}{d_{KL}}, \tag{2.25a}$$

$$\alpha_L = \frac{\overrightarrow{x_K x_\sigma} \cdot \vec{n}_{K\sigma}}{d_{KL}}. \tag{2.25b}$$

The mesh must also fulfill some requirements:

1. The straight line joining the centers of two adjacent cells K and L must be orthogonal to the common face $\sigma \in \varepsilon_K \cap \varepsilon_L$ ($\overrightarrow{x_K x_L} \wedge \vec{n}_{K\sigma} = \vec{0}$);

2. The cell centers must satisfy the order relation: $\overrightarrow{x_K x_L} \cdot \vec{n}_{K\sigma} > 0$;

3. The straight line joining the centers of two adjacent cells K and L must intersect the common face $\sigma \in \varepsilon_K \cap \varepsilon_L$ at its centroid $\vec{x}_\sigma$.

By taking the geometry requirements into account, the two coefficients α_K and α_L (Eqs. (2.25)) satisfy the vectorial relations

$$\alpha_K \vec{n}_{K\sigma} = \frac{1}{d_{KL}} \overrightarrow{x_\sigma x_L}, \tag{2.26a}$$

$$\alpha_L \vec{n}_{K\sigma} = \frac{1}{d_{KL}} \overrightarrow{x_K x_\sigma}. \tag{2.26b}$$

with $\alpha_K + \alpha_L = 1$.

These conditions are verified for orthogonal structured grids which consist of rectangles or parallelepipeds. For general two-dimensional problems, the domain can be covered by unstructured control volumes triangle-shaped (Fig. 2.1). To fulfill the geometrical re-
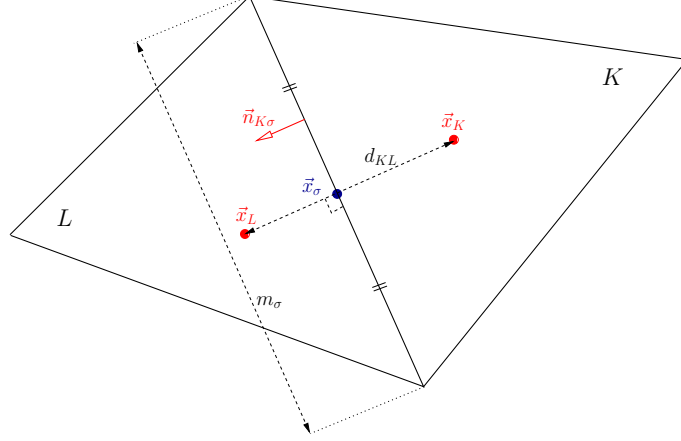
Figure 2.1 – Control volume and notations

quirements given here above, the triangles must be Delaunay [54]. Delaunay triangulation maximizes the minimum angle of all the angles of the triangles in the the mesh; this tends to avoid skinny triangles. The center $\vec{x}_K$ of the cell K is the circumcenter, point where the perpendicular bisectors of the sides intersect. The triangle is Delaunay if no other circumcenter is located inside the circumcircle of K.

2.2.3 Discrete operators

The discrete approximations of the continuous spatial operators are based on previous works [46, 47, 155]. One key point of the spatial discretization is that the discrete velocity and pressure aim also to satisfy a discrete kinetic energy equation which mimics its continuous counterpart; the same yields for the thermal equation. To achieve such a requirement, weak formulations are often invoked, either explicitly or implicitly. The different discretizations are reminded in the next subsections.

2.2.3.1 Diffusion contribution $(\nabla \cdot (\kappa \nabla \phi))_K$

The general expression of the discrete diffusion term can be given by $(\nabla \cdot (\kappa \nabla \phi))_K$. In the momentum equation (2.21a), κ and ϕ stand for the dynamic viscosity μ and any of the components of the velocity. Concerning the thermal equation (2.20), κ corresponds to the thermal conductivity k and ϕ represents the temperature T. And finally, $\kappa \equiv 1$ and $\phi \equiv \Phi$ in the pressure correction equation (2.21b).

The discrete operator is defined in order to mimic the continuous divergence formula

$$\int_K \nabla \cdot (\kappa(\vec{x}) \nabla \phi(\vec{x})) \, d\vec{x} = \sum_{\sigma \in \varepsilon_K} \int_\sigma \kappa(\vec{x}) \nabla \phi(\vec{x}) \cdot \vec{n}_{K\sigma} \, d\vec{x}$$

Using the consistent flux approximation on $\sigma \in \varepsilon_K \cap \varepsilon_L$, the common face between cells K and L,

$$\int_\sigma \kappa(\vec{x}) \nabla \phi(\vec{x}) \cdot \vec{n}_{K\sigma} \, d\vec{x} \approx \kappa_\sigma \frac{m_\sigma}{d_{KL}} (\phi_L - \phi_K)$$

and approximating $\nabla \cdot (\kappa \nabla \phi)$ by its mean value $(\nabla \cdot (\kappa \nabla \phi))_K$ on cell K, we obtain:

$$m_K \ (\nabla \cdot (\kappa \nabla \phi))_K = \sum_{\sigma \in \varepsilon_K \cap \varepsilon_L} \kappa_\sigma \frac{m_\sigma}{d_{KL}} (\phi_L - \phi_K) + \sum_{\sigma \in \varepsilon_K \cap \varepsilon_{out}} \kappa_\sigma \frac{m_\sigma}{d_{K\sigma}} (\phi_\sigma - \phi_K) \qquad (2.27)$$

We deduce the approximation of diffusion term on cell K:

$$(\nabla \cdot (\kappa \nabla \phi))_K = \frac{1}{m_K} \left(\sum_{\sigma \in \varepsilon_K \cap \varepsilon_L} \kappa_\sigma \frac{m_\sigma}{d_{KL}} (\phi_L - \phi_K) + \sum_{\sigma \in \varepsilon_K \cap \varepsilon_{out}} \kappa_\sigma \frac{m_\sigma}{d_{K\sigma}} (\phi_\sigma - \phi_K) \right) \qquad (2.28)$$

The diffusion coefficient k_σ on face σ is expressed using the harmonic mean. For general grids, this writes

$$\kappa_\sigma = \frac{1}{\frac{\alpha_K}{\kappa_K} + \frac{\alpha_L}{\kappa_L}}$$

This expression has the advantage of being exact when the diffusion coefficients κ_K and κ_L are constant on cells K and L (basic assumption for the finite volume approximation). If the face is located at mid-length of centers $\vec{x}_K$ and $\vec{x}_L$ ($\alpha_K = \alpha_L = 1/2$), we recover the usual relation

$$\kappa_\sigma = \frac{2\kappa_K \kappa_L}{\kappa_K + \kappa_L}$$

2.2.3.2 Divergence $\nabla_K \cdot \vec{w}$ for the mass contribution

The discrete divergence operator appears in the pressure correction equation of the fractional-time step method (2.21b) as $\nabla_K \cdot (\rho \vec{v})$.

Let us note $\vec{w}(\vec{x})$ a velocity vector. The divergence of the velocity $\vec{w}$ satisfied the continuous relation:

$$\int_K \nabla \cdot (\vec{w}(\vec{x})) \ d\vec{x} = \sum_{\sigma \in \varepsilon_K} \int_\sigma \vec{w}(\vec{x}) \cdot \vec{n}_{K\sigma} \, d\vec{x} \qquad (2.29)$$

Considering the common face σ between cells K and L, $\sigma \in \varepsilon_K \cap \varepsilon_L$, the integral contribution of the right-hand side of this equation is consistently approximated by

$$\int_\sigma \vec{w}(\vec{x}) \cdot \vec{n}_{K,\sigma} \, d\vec{x} \approx m_\sigma \left(\alpha_K \vec{w}_K + \alpha_L \vec{w}_L \right) \cdot \vec{n}_{K\sigma}$$

Let $\nabla_K \cdot \vec{w}$ be an approximation of the mean value of $\nabla \cdot \vec{w}(\vec{x})$ on cell K, then the continuous relation is approximated by

$$m_\sigma \nabla_K \cdot \vec{w} = \sum_{\sigma \in \varepsilon_K \cap \varepsilon_L} m_\sigma \left(\alpha_K \vec{w}_K + \alpha_L \vec{w}_L \right) \cdot \vec{n}_{K\sigma} + \sum_{\sigma \in \varepsilon_K \cap \varepsilon_{out}} m_\sigma \vec{w}_\sigma \cdot \vec{n}_{K\sigma}$$

and then:

$$\nabla_K \cdot \vec{w} = \frac{1}{m_K} \left(\sum_{\sigma \in \varepsilon_K \cap \varepsilon_L} m_\sigma \left(\alpha_K \vec{w}_K + \alpha_L \vec{w}_L \right) \cdot \vec{n}_{K\sigma} + \sum_{\sigma \in \varepsilon_K \cap \varepsilon_{out}} m_\sigma \vec{w}_\sigma \cdot \vec{n}_{K\sigma} \right) \qquad (2.30)$$

2.2.3.3 Transport contributions $\left(\nabla \cdot (\phi \rho \vec{v}) \right)_K$ and $\left(\rho \vec{v} \cdot \nabla \phi \right)_K$

The differential operator involved in the conservative expression of the transport term is the divergence. Similarly to the previous subsection dealing with the discrete operator "$\nabla_K \cdot$", the conservative form of the transport terms satisfies:

$$\int_K \nabla \cdot (\phi(\vec{x}) \rho(\vec{x}) \vec{v}(\vec{x})) \ d\vec{x} = \sum_{\sigma \in \varepsilon_K} \int_\sigma \phi(\vec{x}) \rho(\vec{x}) \vec{v}(\vec{x}) \cdot \vec{n}_{K\sigma} \, d\vec{x} \qquad (2.31)$$

A first idea could consist in using "$\nabla_K\cdot$" defined by (2.30), but the drawback of this expression is that the convective and conservative expressions of the transport contribution are not equivalent any more. To satisfy the continuous identity

$$\nabla \cdot (\phi\rho\vec{v}) = \rho\vec{v}\cdot\nabla\phi + \phi\nabla\cdot(\rho\vec{v}) \tag{2.32}$$

another expression for the divergence must be considered.

To construct the discrete operator, we must first examine carefully the relation (2.32). The last term $\nabla\cdot(\rho\vec{v})$ is related to the mass equation which is handled by the fractional-time step method (2.21b). From the numerical point of view, this writes in discrete form:

$$m_K\frac{3\rho_K^{(n+1)} - 4\rho_K^{(n)} + \rho_K^{(n-1)}}{2\Delta t}+$$
$$\sum_{\sigma\in\varepsilon_K\cap\varepsilon_L} m_\sigma\left(\alpha_K\rho_K\vec{v}_K^{(n+1)*} + \alpha_L\rho_L\vec{v}_L^{(n+1)*}\right)\cdot\vec{n}_{K\sigma} + \sum_{\sigma\in\varepsilon_K\cap\varepsilon_{out}} m_\sigma\rho_\sigma\vec{v}_\sigma^{(n+1)*}\cdot\vec{n}_{K\sigma} =$$
$$\frac{2\Delta t}{3}\left(\sum_{\sigma\in\varepsilon_K\cap\varepsilon_L}\frac{m_\sigma}{d_{KL}}(\Phi_L^{(n+1)} - \Phi_K^{(n+1)}) + \sum_{\sigma\in\varepsilon_K\cap\varepsilon_{out}}\frac{m_\sigma}{d_{K\sigma}}(\Phi_\sigma^{(n+1)} - \Phi_K^{(n+1)})\right) \tag{2.33}$$

Let us define de mass flux
  – $\dot{m}_{KL}^{(n+1)}$ through the face $\sigma\in\varepsilon_K\cap\varepsilon_L$

$$\dot{m}_{KL}^{(n+1)} \equiv m_\sigma\left(\alpha_K\rho_K\vec{v}_K^{(n+1)*} + \alpha_L\rho_L\vec{v}_L^{(n+1)*}\right)\cdot\vec{n}_{K\sigma} - \frac{2\Delta t}{3}m_\sigma\left(\frac{\Phi_L^{(n+1)} - \Phi_K^{(n+1)}}{d_{KL}}\right) \tag{2.34}$$

  – $\dot{m}_{K\sigma}^{(n+1)}$ through the face $\sigma\in\varepsilon_K\cap\varepsilon_{out}$

$$\dot{m}_{K\sigma}^{(n+1)} \equiv m_\sigma\left(\rho_\sigma\vec{v}_\sigma^{(n+1)*}\right)\cdot\vec{n}_{K\sigma} - \frac{2\Delta t}{3}m_\sigma\left(\frac{\Phi_\sigma^{(n+1)} - \Phi_K^{(n+1)}}{d_{K\sigma}}\right) \tag{2.35}$$

Using the new variables, relation (2.33) then is reduced to

$$m_K\frac{3\rho_K^{(n+1)} - 4\rho_K^{(n)} + \rho_K^{(n-1)}}{2\Delta t} + \sum_{\sigma\in\varepsilon_K\cap\varepsilon_L}\dot{m}_{KL}^{(n+1)} + \sum_{\sigma\in\varepsilon_K\cap\varepsilon_{out}}\dot{m}_{K\sigma}^{(n+1)} = 0 \tag{2.36}$$

This equation is the true mass equation solved by the fractional-time step method. Therefore, to mimic the continuous equality (2.32) at the discrete level, the discrete conservative transport operator must be based on $\dot{m}_{KL}$ and $\dot{m}_{K\sigma}$.

Assuming $\left(\nabla\cdot(\phi\rho\vec{v})\right)_K$ is an approximation of the mean value of $\nabla\cdot(\phi(\vec{x})\rho(\vec{x})\vec{v}(\vec{x}))$ on cell K, the discrete counterpart of equality (2.31) writes

$$m_K\left(\nabla\cdot(\phi\rho\vec{v})\right)_K = \sum_{\sigma\in\varepsilon_K\cap\varepsilon_L}\dot{m}_{KL}\frac{\phi_K + \phi_L}{2} + \sum_{\sigma\in\varepsilon_K\cap\varepsilon_{out}}\dot{m}_{K\sigma}\phi_\sigma$$

or

$$\left(\nabla\cdot(\phi\rho\vec{v})\right)_K = \frac{1}{m_K}\left(\sum_{\sigma\in\varepsilon_K\cap\varepsilon_L}\dot{m}_{KL}\frac{\phi_K + \phi_L}{2} + \sum_{\sigma\in\varepsilon_K\cap\varepsilon_{out}}\dot{m}_{K\sigma}\phi_\sigma\right) \tag{2.37}$$

with definitions (2.34) and (2.35).

The discrete contribution for the convective transport term must satisfy the discrete counterpart of relation (2.32) integrated on cell K:

$$\int_K \rho(\vec{x})\vec{v}(\vec{x}) \cdot \nabla\phi(\vec{x})\, d\vec{x} = \int_K \nabla \cdot (\phi(\vec{x})\rho(\vec{x})\vec{v}(\vec{x}))\, d\vec{x} - \int_K \phi(\vec{x})\nabla \cdot (\rho(\vec{x})\vec{v}(\vec{x}))\, d\vec{x} \quad (2.38)$$

Approximating $\rho(\vec{x})\vec{v}(\vec{x})\cdot\nabla\phi(\vec{x})$ on cell K by the mean value $\left(\rho\vec{v}\cdot\nabla\phi\right)_K$, using the discrete conservative transport expression (2.37) and the mass flux balance on cell K (Eq. (2.36)), we obtain

$$m_K\left(\rho\vec{v} \cdot \nabla\phi\right)_K = \sum_{\sigma\in\varepsilon_K\cap\varepsilon_L} \dot{m}_{KL}\frac{\phi_K + \phi_L}{2} + \sum_{\sigma\in\varepsilon_K\cap\varepsilon_{out}} \dot{m}_{K\sigma}\phi_\sigma -$$

$$\phi_K\left(\sum_{\sigma\in\varepsilon_K\cap\varepsilon_L} \dot{m}_{KL} + \sum_{\sigma\in\varepsilon_K\cap\varepsilon_{out}} \dot{m}_{K\sigma}\right)$$

After some simplifications, we find:

$$\left(\rho\vec{v} \cdot \nabla\phi\right)_K = \frac{1}{m_K}\left(\sum_{\sigma\in\varepsilon_K\cap\varepsilon_L} \dot{m}_{KL}\frac{\phi_L - \phi_K}{2} + \sum_{\sigma\in\varepsilon_K\cap\varepsilon_{out}} \dot{m}_{K\sigma}(\phi_\sigma - \phi_K)\right) \quad (2.39)$$

Thus, both $\left(\nabla \cdot (\phi\rho\vec{v})\right)_K$ and $\left(\rho\vec{v}\cdot\nabla\phi\right)_K$ are conservative approximations of the transport terms.

It is intersecting to notice that the conservative expression of the transport (2.37), and consequently the convective form (2.39) also, are based on the centered approximation of ϕ on cell face $\phi_\sigma = (\phi_K + \phi_L)/2$, and not a more general linear interpolation $\phi_\sigma = \alpha_K\phi_K + \alpha_L\phi_L$. The reason of such a choice lies in the mean kinetic energy balance (and mean quadratic balance of the temperature field) over the whole computational domain. In that case and for an impervious domain, the discrete contribution of the transport terms into the energy balances must be zero, as requested by the continuous equations. This requirement may introduces a slight error in the transport terms of the momentum and energy equations, but the convergence order is not affected provided that the grid size evolves slowly. Obviously, if the face is located at mid-distance of the two adjacent centers, the linear approximation and the centered approximation are identical ($\alpha_K = \alpha_L = 1/2$). When the mesh size evolves quickly, the linear interpolation $\phi_\sigma = \alpha_K\phi_K + \alpha_L\phi_L$ may be preferred to $\phi_\sigma = (\phi_K + \phi_L)/2$ so as to improve the accuracy of the solution, but at the cost of the energy balance. This change may also be applied to the convective form of the transport term (2.39). This consistent interpolation method has been used for the momentum equation in Sec. 3.2.

2.2.3.4 Pressure gradient $\widetilde{\nabla}_K\Pi_g^{(n)}$ and $\widetilde{\nabla}_K\Phi^{(n+1)}$

The discrete pressure gradient $\widetilde{\nabla}_K\Pi_g^{(n)}$ and $\widetilde{\nabla}_K\Phi^{(n+1)}$ involved in the momentum equation (2.21a) and in the velocity correction (2.23) must satisfy at the discrete level the duality between the pressure gradient and the velocity divergence. Let $\vec{w}$ be any test vector and consider the integral of its product by the pressure gradient over the computation domain Ω, then the weak form of the pressure gradient writes

$$\int_\Omega \vec{w} \cdot \nabla p\, d\vec{x} = \int_\Omega \nabla \cdot (p\vec{w})\, d\vec{x} - \int_\Omega p(\nabla \cdot \vec{w})\, d\vec{x}$$

$$= \int_{\partial\Omega} p\vec{w} \cdot \vec{n}\, d\vec{x} - \int_\Omega p(\nabla \cdot \vec{w})d\vec{x} \quad (2.40)$$

We assume that "$\widetilde{\nabla}_L$" is the discrete approximation on cell L of the pressure gradient "∇". Since the approximation of the velocity divergence is provided by Eq. (2.30) then the discrete form of Eq. (2.40) writes

$$\sum_{L\in\mathcal{M}} m_L \left(\vec{w}_L \cdot (\widetilde{\nabla}_L p) \right) = \left(\sum_{L\in\mathcal{M}} \sum_{\sigma\in\varepsilon_L\cap\varepsilon_{out}} m_\sigma p_\sigma \vec{w}_\sigma \cdot \vec{n}_{L\sigma} \right) -$$
$$\left(\sum_{L\in\mathcal{M}} p_L \left(\sum_{\sigma\in\varepsilon_L\cap\varepsilon_M} m_\sigma(\alpha_L\vec{w}_L + \alpha_M\vec{w}_M) \cdot \vec{n}_{L\sigma} + \sum_{\sigma\in\varepsilon_L\cap\varepsilon_{out}} m_\sigma\vec{w}_\sigma \cdot \vec{n}_{L\sigma} \right) \right) \quad (2.41)$$

By gathering the contributions on the boundary of the domain, we obtain

$$\sum_{L\in\mathcal{M}} m_L \left(\vec{w}_L \cdot (\widetilde{\nabla}_L p) \right) = \left(\sum_{L\in\mathcal{M}} \sum_{\sigma\in\varepsilon_L\cap\varepsilon_{out}} m_\sigma(p_\sigma - p_L)\vec{w}_\sigma \cdot \vec{n}_{L\sigma} \right) -$$
$$\left(\sum_{L\in\mathcal{M}} p_L \left(\sum_{\sigma\in\varepsilon_L\cap\varepsilon_M} m_\sigma(\alpha_L\vec{w}_L + \alpha_M\vec{w}_M) \cdot \vec{n}_{L\sigma} \right) \right) \quad (2.42)$$

For the finite volume scheme, the discrete test function is constant on each cell. To obtain the ith component of the pressure gradient on cell K, $\widetilde{\nabla}_K^i p \equiv \widetilde{\nabla}_K p \cdot \vec{e}_i$, the test function $\vec{w}_L = \sum_{j=1}^d w_L^j \vec{e}_j$, $L \in \mathcal{M}$, is chosen such that $w_L^j = \delta_{K,L}\delta_{i,j}$, namely
  – $w_K^i = 1$,
  – $w_K^j = 0$, for all $j \neq i$,
  – $w_L^j = 0$, for all j and for all $L \neq K$.
We then find:

$$m_K \widetilde{\nabla}_K^i p = \left(\sum_{\sigma\in\varepsilon_K\cap\varepsilon_{out}} m_\sigma(p_\sigma - p_K)w_\sigma^i \vec{e}_i \cdot \vec{n}_{K\sigma} \right) -$$
$$\left(p_K \left(\sum_{\sigma\in\varepsilon_K\cap\varepsilon_L} m_\sigma\alpha_K n_{K\sigma}^i \right) + p_L \left(\sum_{\sigma\in\varepsilon_L\cap\varepsilon_K} m_\sigma\alpha_K n_{L\sigma}^i \right) \right) \quad (2.43)$$

with $\vec{n}_{L\sigma} = \sum_{i=1}^d n_{L\sigma}^i \vec{e}_i$. After some simplifications, we obtain

$$m_K \widetilde{\nabla}_K^i p = \left(\sum_{\sigma\in\varepsilon_K\cap\varepsilon_{out}} m_\sigma(p_\sigma - p_K)w_\sigma^i n_{K\sigma}^i \right) + \left(\sum_{\sigma\in\varepsilon_K\cap\varepsilon_L} m_\sigma\alpha_K(p_L - p_K)n_{K\sigma}^i \right) \quad (2.44a)$$

This latter expression depends on the normal contribution to the interface of $w_\sigma^i \vec{e}_i$, namely $w_\sigma^i n_{K\sigma}^i$. The boundary conditions associated with the test function can be seen as a perturbation of the velocity boundary conditions:
  – if $\vec{v}_\sigma$ is prescribed, $\vec{w}_\sigma = \vec{0}$. Since $w_\sigma^i = 0$ then Eq. (2.44a) writes

$$\widetilde{\nabla}_K p \equiv \sum_{i=1}^d (\widetilde{\nabla}_K^i p)\,\vec{e}_i = \frac{1}{m_K} \sum_{\sigma\in\varepsilon_K\cap\varepsilon_L} m_\sigma\alpha_K(p_L - p_K)\vec{n}_{K\sigma} \quad (2.44b)$$

  – If we assume Newman boundary conditions for the normal velocity to face $\sigma \in \varepsilon_K \cap \varepsilon_{out}$, $\nabla(\vec{v} \cdot \vec{n}_{K\sigma}) \cdot \vec{n}_{K\sigma} = f(\vec{x})$, then the discrete test function satisfies the same kind of relation, but with a homogeneous right-hand side: $\nabla(\vec{w} \cdot \vec{n}_{K\sigma}) \cdot \vec{n}_{K\sigma} = 0$, that is

$$\vec{w}_\sigma \cdot \vec{n}_{K\sigma} = \vec{w}_K \cdot \vec{n}_{K\sigma}$$

Since $\vec{w}_K = \delta_{ij}\vec{e}_j$ then $w^i_\sigma n^i_{K\sigma} = n^i_{K\sigma}$ and from Eq. (2.44a) we finally get

$$\widetilde{\nabla}_K p \equiv \sum_{i=1}^{d}(\widetilde{\nabla}^i_K p)\,\vec{e}_i = \frac{1}{m_K}\left(\sum_{\sigma\in\varepsilon_K\cap\varepsilon_{out}} m_\sigma(p_\sigma - p_K)\vec{n}_{K\sigma} + \sum_{\sigma\in\varepsilon_K\cap\varepsilon_L} m_\sigma\alpha_K(p_L - p_K)\vec{n}_{K\sigma}\right)$$
$$(2.44c)$$

2.2.3.5   Discrete consistent gradient operator $\nabla_K\phi$

The gradient "$\widetilde{\nabla}_K$" presented in section 2.2.3.4 is not defined strongly, but weakly, that is to say it satisfies the duality between the pressure gradient and the velocity divergence (Eq. (2.40)). The definition of a consistent discrete gradient operator "∇_K" is also essential to express the full viscous tensor which will be presented in the next section.

To establish the discrete gradient on cell K, we start from the identity:

$$\int_K \nabla\big(\vec{w}_K\cdot(\vec{x}-\vec{x}_K)\big)\,d\vec{x} = \sum_{\sigma\in\varepsilon_K\cap\varepsilon_L}\int_\sigma \big(\vec{w}_K\cdot(\vec{x}-\vec{x}_K)\big)\vec{n}_{K\sigma}\,d\vec{x} + \sum_{\sigma\in\varepsilon_K\cap\varepsilon_{out}}\int_\sigma \big(\vec{w}_K\cdot(\vec{x}-\vec{x}_K)\big)\vec{n}_{K\sigma}\,d\vec{x}$$

with $\vec{x} = \sum_{i=1}^{3} x^i\vec{e}_i$ and $\vec{w}_K$ a vector constant on cell K. Calculations can be pursued to give:

$$m_K\vec{w}_K = \sum_{\sigma\in\varepsilon_K\cap\varepsilon_L} m_\sigma\big(\vec{w}_K\cdot(\vec{x}_\sigma - \vec{x}_K)\big)\vec{n}_{K\sigma} + \sum_{\sigma\in\varepsilon_K\cap\varepsilon_{out}} m_\sigma\big(\vec{w}_K\cdot(\vec{x}_\sigma - \vec{x}_K)\big)\vec{n}_{K\sigma}$$

Let $\vec{w}_K \equiv \nabla_K\phi$ the discrete gradient of ϕ on cell K, then

$$m_K\nabla_K\phi = \sum_{\sigma\in\varepsilon_K\cap\varepsilon_L} m_\sigma\big(\nabla_K\phi\cdot(\vec{x}_\sigma-\vec{x}_K)\big)\vec{n}_{K\sigma} + \sum_{\sigma\in\varepsilon_K\cap\varepsilon_{out}} m_\sigma\big(\nabla_K\phi\cdot(\vec{x}_\sigma-\vec{x}_K)\big)\vec{n}_{K\sigma} \quad (2.45)$$

Since $\vec{x}_\sigma - \vec{x}_K$ and $\vec{n}_{K\sigma}$ are collinear, we have

$$\big(\nabla_K\phi\cdot(\vec{x}_\sigma - \vec{x}_K)\big)\vec{n}_{K\sigma} = \nabla_K\phi\cdot\vec{n}_{K\sigma}\,(\vec{x}_\sigma - \vec{x}_K)$$

The normal gradients are approximated as follows:

$$\nabla_K\phi\cdot\vec{n}_{K\sigma} = \frac{\phi_L - \phi_K}{d_{KL}}, \quad \sigma\in\varepsilon_K\cap\varepsilon_L$$

$$\nabla_K\phi\cdot\vec{n}_{K\sigma} = \frac{\phi_\sigma - \phi_K}{d_{K\sigma}}, \quad \sigma\in\varepsilon_K\cap\varepsilon_{out}$$

Substituting in relation (2.45) we obtain the discrete gradient:

$$m_K\nabla_K\phi = \sum_{\sigma\in\varepsilon_K\cap\varepsilon_L} m_\sigma\frac{\phi_L - \phi_K}{d_{KL}}(\vec{x}_\sigma - \vec{x}_K) + \sum_{\sigma\in\varepsilon_K\cap\varepsilon_{out}} m_\sigma\frac{\phi_\sigma - \phi_K}{d_{K\sigma}}(\vec{x}_\sigma - \vec{x}_K)$$

or

$$\nabla_K\phi = \frac{1}{m_K}\left(\sum_{\sigma\in\varepsilon_K\cap\varepsilon_L} m_\sigma\frac{\phi_L - \phi_K}{d_{KL}}(\vec{x}_\sigma - \vec{x}_K) + \sum_{\sigma\in\varepsilon_K\cap\varepsilon_{out}} m_\sigma\frac{\phi_\sigma - \phi_K}{d_{K\sigma}}(\vec{x}_\sigma - \vec{x}_K)\right) \quad (2.46)$$

2.2.3.6 Viscous stress tensor contribution $\widehat{\nabla_K \cdot}\left(\mu(\nabla_K \vec{v})^t - \frac{2}{3}\mu(\nabla_K \cdot \vec{v})\overline{\overline{\delta}}\right)$

The full viscous stress $\overline{\overline{\tau}} \equiv \mu\left(\nabla \vec{v} + (\nabla \vec{v})^t\right) - \frac{2}{3}\mu(\nabla \cdot \vec{v})\overline{\overline{\delta}}$ tensor is divided into two parts.

The divergence of the first term, $\nabla \cdot (\mu \nabla \vec{v})$, was already discretized in section 2.2.3.1. Its finite volume approximation on cell K writes $\left(\nabla \cdot (\mu \nabla \vec{v})\right)_K$ (see Eq. (2.28)):

$$(\nabla \cdot (\mu \nabla \vec{v}))_K = \frac{1}{m_K}\left(\sum_{\sigma \in \varepsilon_K \cap \varepsilon_L} \mu_\sigma \frac{m_\sigma}{d_{KL}}(\vec{v}_L - \vec{v}_K) + \sum_{\sigma \in \varepsilon_K \cap \varepsilon_{out}} \mu_\sigma \frac{m_\sigma}{d_{K\sigma}}(\vec{v}_\sigma - \vec{v}_K)\right)$$

This expression differs substantially from $\nabla_K \cdot (\nabla_K \vec{v})$ with "$\nabla_K \cdot$" and "∇_K" expressed by equations (2.30) and (2.46). Indeed, the discrete operator "$\nabla_K \cdot (\nabla_K)$" may be not invertible (or at least very badly conditioned) contrary to $\left(\nabla \cdot (\mu \nabla \vec{v})\right)_K$ defined here-above.

The divergence of the second part of the viscous stress tensor $\overline{\overline{\tau}}' \equiv \mu(\nabla \vec{v})^t - \frac{2}{3}\mu(\nabla \cdot \vec{v})\overline{\overline{\delta}}$, namely $\nabla \cdot \overline{\overline{\tau}}'$ is now detailed. In order the discrete solution satisfies a kinetic energy balance similar to that of the continuous equations, "$\widehat{\nabla_K \cdot}$" must differ from "$\nabla_K \cdot$" (Eq. (2.30)). As for the pressure gradient term, the discretisation of $\nabla \cdot \overline{\overline{\tau}}'$ is defined by its weak form. In a continuous formalism, we define a vectorial test function $\vec{w}(\vec{x})$ such that

$$\int_\Omega \vec{w}(\vec{x}) \cdot \left(\nabla \cdot \overline{\overline{\tau}}'\right) d\vec{x} = \int_{\delta\Omega}\left(\vec{w}(\vec{x}) \cdot \overline{\overline{\tau}}'\right) \cdot \vec{n}\, d\vec{x} - \int_\Omega \nabla \vec{w}(\vec{x}) : \overline{\overline{\tau}}'\, d\vec{x}$$

We assume that "$\widehat{\nabla_L \cdot}$" is the discrete approximation on cell L of "$\nabla \cdot$". The discrete version of the preceding equation then writes:

$$\sum_{L \in \mathcal{M}} m_L \vec{w}_L \cdot \left(\widehat{\nabla_L \cdot}\overline{\overline{\tau}}'\right) = \left(\sum_{L \in \mathcal{M}} \sum_{\sigma \in \varepsilon_L \cap \varepsilon_{out}} m_\sigma \left(\vec{w}_\sigma \cdot \overline{\overline{\tau}}'_\sigma\right) \cdot \vec{n}_{L\sigma}\right) - \left(\sum_{L \in \mathcal{M}} m_L \nabla_L \vec{w} : \overline{\overline{\tau}}'_L\right)$$

Substituting $\nabla_L \vec{w}$ by Eq. (2.46),

$$\sum_{L \in \mathcal{M}} m_L \vec{w}_L \cdot \left(\widehat{\nabla_L \cdot}\overline{\overline{\tau}}'\right) = \left(\sum_{L \in \mathcal{M}} \sum_{\sigma \in \varepsilon_L \cap \varepsilon_{out}} m_\sigma \left(\vec{w}_\sigma \cdot \overline{\overline{\tau}}'_\sigma\right) \cdot \vec{n}_{L\sigma}\right) -$$
$$\left(\sum_{L \in \mathcal{M}}\left(\sum_{\sigma \in \varepsilon_L \cap \varepsilon_M} m_\sigma \frac{\vec{w}_M - \vec{w}_L}{d_{LM}} \otimes (\vec{x}_\sigma - \vec{x}_L) + \sum_{\sigma \in \varepsilon_L \cap \varepsilon_{out}} m_\sigma \frac{\vec{w}_\sigma - \vec{w}_L}{d_{L\sigma}} \otimes (\vec{x}_\sigma - \vec{x}_L)\right) : \overline{\overline{\tau}}'_L\right)$$

and then collecting the boundary terms we get:

$$\sum_{L \in \mathcal{M}} m_L \vec{w}_L \cdot \left(\widehat{\nabla_L \cdot}\overline{\overline{\tau}}'\right) =$$
$$\left(\sum_{L \in \mathcal{M}} \sum_{\sigma \in \varepsilon_L \cap \varepsilon_{out}} m_\sigma \left(\left(\vec{w}_\sigma \cdot \overline{\overline{\tau}}'_\sigma\right) \cdot \vec{n}_{L\sigma} - \left(\frac{\vec{w}_\sigma - \vec{w}_L}{d_{L\sigma}} \otimes (\vec{x}_\sigma - \vec{x}_L)\right) : \overline{\overline{\tau}}'_L\right)\right) -$$
$$\left(\sum_{L \in \mathcal{M}}\left(\sum_{\sigma \in \varepsilon_L \cap \varepsilon_M} m_\sigma \frac{\vec{w}_M - \vec{w}_L}{d_{LM}} \otimes (\vec{x}_\sigma - \vec{x}_L)\right) : \overline{\overline{\tau}}'_L\right)$$

Taking the notations $(\vec{x}_\sigma - \vec{x}_L)/d_{LM} = \alpha_M \vec{n}_{L\sigma}$ with $\sigma \in \varepsilon_L \cap \varepsilon_M$ (Eq. (2.26a)) into account,

and $(\vec{x}_\sigma - \vec{x}_L)/d_{L\sigma} = \vec{n}_{L\sigma}$, we find:

$$
\sum_{L\in\mathcal{M}} m_L \vec{w}_L \cdot \left(\widehat{\nabla_L \cdot \overline{\overline{\tau}}'}\right) =
$$

$$
\left(\sum_{L\in\mathcal{M}} \sum_{\sigma\in\varepsilon_L\cap\varepsilon_{out}} m_\sigma \left(\left(\vec{w}_\sigma \cdot \overline{\overline{\tau}}'_\sigma \right) \cdot \vec{n}_{L\sigma} - \left((\vec{w}_\sigma - \vec{w}_L) \otimes \vec{n}_{L\sigma} \right) : \overline{\overline{\tau}}'_L \right) \right) -
$$

$$
\left(\sum_{L\in\mathcal{M}} \left(\sum_{\sigma\in\varepsilon_L\cap\varepsilon_M} m_\sigma \alpha_M (\vec{w}_M - \vec{w}_L) \otimes \vec{n}_{L\sigma} \right) : \overline{\overline{\tau}}'_L \right) \quad (2.47)
$$

For the finite volume scheme, the discrete test function is constant on each cell. To find the ith component of the divergence of the tensor $\overline{\overline{\tau}}'$ on cell K, $\left(\widehat{\nabla_K \cdot \overline{\overline{\tau}}'}\right)^i \equiv \left(\widehat{\nabla_K \cdot \overline{\overline{\tau}}'}\right) \cdot \vec{e}_i$, the test function $\vec{w}_L = \sum_{j=1}^d w_L^j \vec{e}_j$, $L \in \mathcal{M}$, is chosen such that $w_L^j = \delta_{K,L}\delta_{i,j}$, namely
  – $w_K^i = 1$,
  – $w_K^j = 0$, for all $j \neq i$,
  – $w_L^j = 0$, for all j and for all $L \neq K$.
Equation (2.47) then writes

$$
m_K \left(\widehat{\nabla_K \cdot \overline{\overline{\tau}}'}\right)^i =
$$

$$
\left(\sum_{\sigma\in\varepsilon_K\cap\varepsilon_{out}} m_\sigma \left(\left(w_\sigma^i \vec{e}_i \cdot \overline{\overline{\tau}}'_\sigma \right) \cdot \vec{n}_{K\sigma} - \left((w_\sigma^i - 1)\vec{e}_i \otimes \vec{n}_{K\sigma} \right) : \overline{\overline{\tau}}'_K \right) \right) -
$$

$$
\left(\sum_{\sigma\in\varepsilon_K\cap\varepsilon_L} (-m_\sigma \alpha_L \vec{e}_i \otimes \vec{n}_{K\sigma}) : \overline{\overline{\tau}}'_K - \left(\sum_{\sigma\in\varepsilon_K\cap\varepsilon_L} m_\sigma \alpha_K \vec{e}_i \otimes \vec{n}_{K\sigma} \right) : \overline{\overline{\tau}}'_L \right)
$$

After some simplifications, we get

$$
m_K \left(\widehat{\nabla_K \cdot \overline{\overline{\tau}}'}\right)^i =
$$

$$
\left(\sum_{\sigma\in\varepsilon_K\cap\varepsilon_{out}} m_\sigma \left(w_\sigma^i \left(\overline{\overline{\tau}}'_\sigma \cdot \vec{n}_{K\sigma} \right)^i - (w_\sigma^i - 1)\left(\vec{n}_{K\sigma} \cdot \overline{\overline{\tau}}'_K \right)^i \right) \right) +
$$

$$
\left(\sum_{\sigma\in\varepsilon_K\cap\varepsilon_L} \left(m_\sigma \left(\alpha_L \left(\vec{n}_{K\sigma} \cdot \overline{\overline{\tau}}'_K \right)^i + \alpha_K \left(\vec{n}_{K\sigma} \cdot \overline{\overline{\tau}}'_L \right)^i \right) \right) \right) \quad (2.48a)
$$

To simplify further, we need to introduce the boundary conditions for the discrete test function $\vec{w}$. The test function fulfills the homogeneous counterpart of the velocity boundary conditions.
  – If $\vec{v}_\sigma$ is prescribed then $\vec{w}_\sigma = \vec{0}$, and consequently $w_\sigma^i = 0$. Eq. (2.48a) then writes:

$$
m_K \left(\widehat{\nabla_K \cdot \overline{\overline{\tau}}'}\right)^i = \left(\sum_{\sigma\in\varepsilon_K\cap\varepsilon_{out}} \left(m_\sigma \left(\vec{n}_{K\sigma} \cdot \overline{\overline{\tau}}'_K \right)^i \right) \right) +
$$

$$
\left(\sum_{\sigma\in\varepsilon_K\cap\varepsilon_L} \left(m_\sigma \left(\alpha_L \left(\vec{n}_{K\sigma} \cdot \overline{\overline{\tau}}'_K \right)^i + \alpha_K \left((\vec{n}_{K\sigma} \cdot \overline{\overline{\tau}}'_L)^i \right) \right) \right) \right) \quad (2.48b)
$$

  – If the normal derivative to $\sigma \in \varepsilon_K \cap \varepsilon_{out}$ of the ith velocity component $\partial v^i/\partial \vec{n}$ is prescribed then $\partial w^i/\partial \vec{n} = 0$. Since the discrete expression writes $w_\sigma^i = w_K^i = 1$, Eq.

(2.48a) becomes:

$$
m_K \left(\widehat{\nabla_K \cdot \overline{\overline{\tau}}'} \right)^i = \left(\sum_{\sigma \in \varepsilon_K \cap \varepsilon_{out}} \left(m_\sigma \left(\overline{\overline{\tau}}'_\sigma \cdot \vec{n}_{K\sigma} \right)^i \right) \right) +
$$

$$
\left(\sum_{\sigma \in \varepsilon_K \cap \varepsilon_L} \left(m_\sigma \left(\alpha_L \left(\vec{n}_{K\sigma} \cdot \overline{\overline{\tau}}'_K \right)^i + \alpha_K \left(\left(\vec{n}_{K\sigma} \cdot \overline{\overline{\tau}}'_L \right)^i \right) \right) \right) \right) \quad (2.48c)
$$

To end this subsection, we have to define the discrete viscous tensor arising in Eqs. (2.48), both on cell K and on the boundary $\sigma \in \varepsilon_K \cap \varepsilon_{out}$.

The components of the tensor $\overline{\overline{\tau}}'_K$ writes:

$$
\overline{\overline{\tau}}'_K{}^{ij} = \mu_K \left(\nabla^i_K v^j_K - \sum_{k=1}^d \left(\frac{2}{3} \nabla^k_K v^k_K \right) \delta_{ij} \right)
$$

where the expression "∇^m_K" of any discrete variable ϕ is deduced from Eq. (2.46) and is expressed as follows

$$
\nabla^m_K \phi = \frac{1}{m_K} \left(\sum_{\sigma \in \varepsilon_K \cap \varepsilon_L} m_\sigma \frac{\phi_L - \phi_K}{d_{KL}} (x^m_\sigma - x^m_K) + \sum_{\sigma \in \varepsilon_K \cap \varepsilon_{out}} m_\sigma \frac{\phi_\sigma - \phi_K}{d_{K\sigma}} (x^m_\sigma - x^m_K) \right)
$$

The approximation in Eq. (2.48c) of the tensor $\overline{\overline{\tau}}'$ at the face boundary $\sigma \in \varepsilon_K \cap \varepsilon_{out}$ is a bit difficult in the framework of the finite volume method because this term is not define on a control volume. On way to overcome this difficulty is to simply approximate the value on the face $\sigma \in \varepsilon_K \cap \varepsilon_{out}$ by its value on the neighboring cell K: $\overline{\overline{\tau}}'_\sigma = \overline{\overline{\tau}}'_K$.

Chapter 3

Validation

This chapter aims to present a validation of the numerical scheme on rectangular grids. This relies on two complementary approaches. First, comparisons with analytical solutions are proposed. This enables to check the order of convergence of the scheme, both spatially and temporally. Secondly, comparisons with benchmark solutions will be led.

3.1 Spatial and temporal convergence – Analytical tests

To measure the accuracy of the numerical scheme; we define the relative error based on the discrete L2-norm:

$$
e(f) = \sqrt{\frac{\sum\limits_{K \in \mathcal{M}} m_K (f_K^{(n)} - f(\vec{x}_K, t^{(n)}))^2}{\sum\limits_{K \in \mathcal{M}} m_K f(\vec{x}_K, t^{(n)})^2}}, \qquad f \in \{u, v, T, p\}
$$

with $f_K^{(n)}$ the discrete approximation of the exact solution $f(\vec{x}_K, t^{(n)})$.

3.1.1 Incompressible flow – Taylor-Green problem

The dimensionless Taylor-Green problem consists in the time evolution of a vortex in an incompressible fluid flow. In a square domain $(x, y) \in [-\pi/2, \pi/2] \times [-\pi/2, \pi/2]$, the vortex solution writes:

$$
u(x, y, t) = -\cos(x) \sin(y) \exp(-2t/Re)
$$
$$
v(x, y, t) = \sin(x) \cos(y) \exp(-2t/Re)
$$
$$
\Pi_g(x, y, t) = \frac{\cos(2x) + \sin(2y)}{4} \exp(-4t/Re)
$$

with Re the Reynolds number.

The initial and boundary conditions for the discrete velocity components are set to the exact values. The normal velocity being known at the boundary of the domain, no boundary conditions are required for the pressure. The discrete pressure is initialized to zero. Computations are carried out for a Reynolds number $Re = 100$, with uniform square cells. Errors are presented for the horizontal component of the velocity and for the pressure. The behavior of the vertical component of the velocity is similar to the horizontal one.

3.1.1.1 Spatial convergence

The time step is chosen equal to $\Delta t = 0.001$, a value small enough to keep the temporal error negligible with respect to the spatial one. The number of control volumes in each direction ranges from 5 to 640 and consequently the mesh size h extend from $\pi/640$ to $\pi/5$.

Fig. 3.1(a) shows that the relative spatial error for the velocity converges with a second

(a) Velocity

(b) Pressure
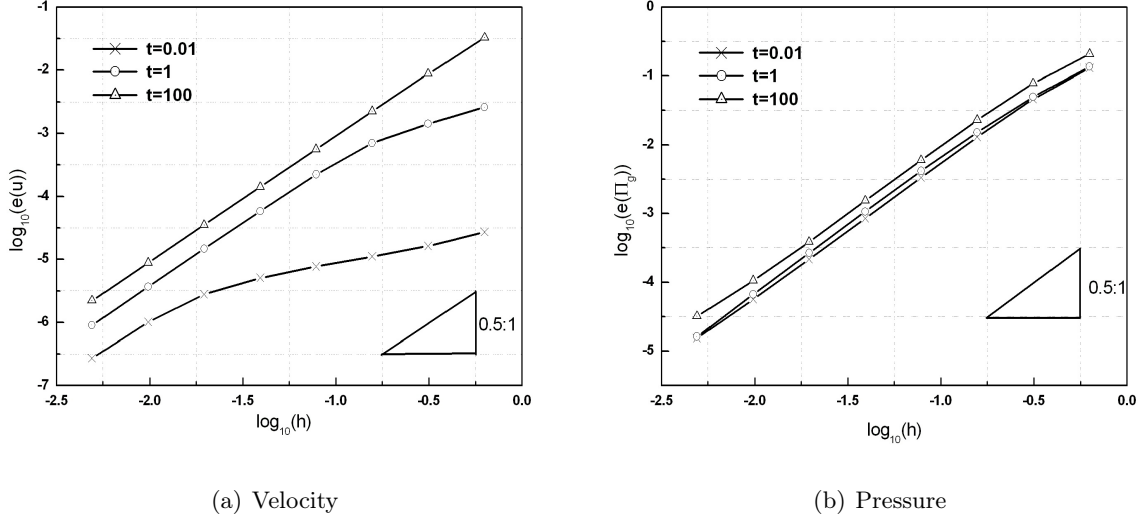
Figure 3.1 – Variations of relative spatial error as a function of the grid size h at different time.

order accuracy from the moment that the mesh size is smaller than a threshold value h_c. This threshold value is about $h_c = \pi/160$ for $t = 0.01$ and $h_c = \pi/20$ for $t = 1$. And for the largest integration time $t = 100$, the second order accuracy is recovered from the coarsest grid. Since the initial condition is analytic, the accuracy decreases with time increase when the mesh size is fixed. Thus for a very short time $t = 0.01$ and $h > h_c$, the solution retains values close to the exact initial value: the spatial error is then negligible and reducing the mesh size does not modify substantially $e(u)$. But beyond h_c, the error of discretization becomes dominant and finally control the convergence order of the numerical scheme.

Concerning the pressure (Fig. 3.1(b)), since its initialization is not set to the exact value, the spacial error is always dominant: the spatial convergence is then always second order, whatever the mesh size and time considered.

3.1.1.2 Temporal convergence

Figure 3.2 presents the variations of the temporal error as a function of four time steps, $\Delta t = 0.2$, 0.1, 0.05 and 0.025. Computations have been carried out for three grids, 20×20, 40×40 and 160×160.

The convergence properties of the velocity (Fig. 3.2(a)) and of the pressure (Fig. 3.2(b)) indicate second order accuracies for large time steps. Indeed, if Δt is too small, the error remains governed by the spatial accuracy. As a result, the range for which the second order is measured increases with the decrease in the mesh size. For the finest grid, both the

(a) Velocity   (b) Pressure
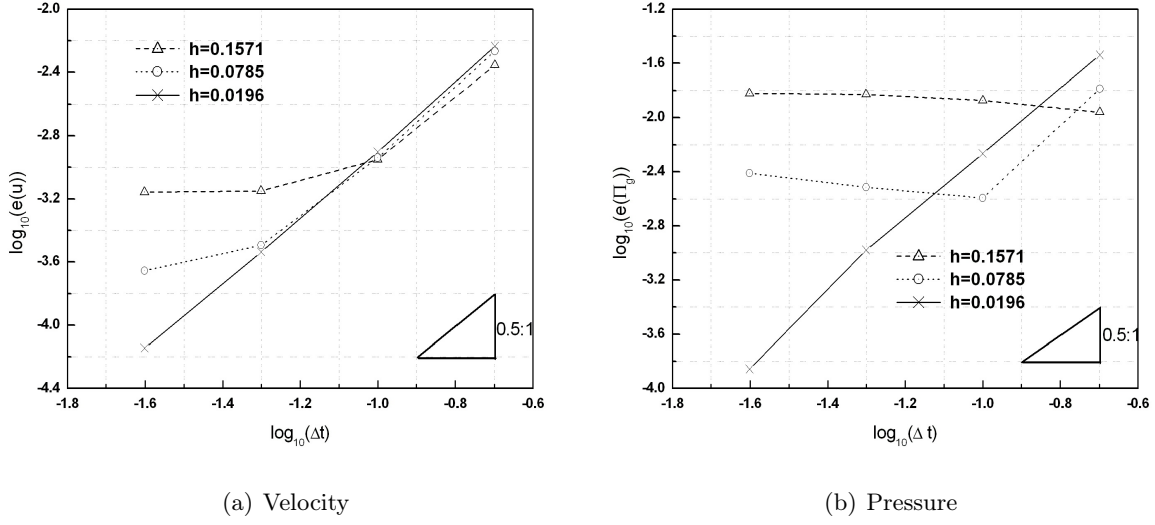
Figure 3.2 – Variation of the relative temporal error as a function of the time step Δt for different grid size h.

velocity and the pressure errors converge according to a straight line with a slope close to 2.

3.1.2   Low Mach number approximation

3.1.2.1   Convergence to a steady state

We consider the dimensional problem of air flowing in a $1\,m$-square domain, $(x,y) \in [0;1] \times [0;1]\,m^2$. We assume no-slip boundary conditions and the following temperature conditions:

$$T(0,y) = T(1,y) = 273\ [K]$$

$$k\frac{\partial T}{\partial y}\bigg|_{x,0} = k\frac{\partial T}{\partial y}\bigg|_{x,1} = 0\ [W/m^2]$$

The density, temperature and thermodynamic pressure fulfill the ideal gas law relation $\rho = \bar{P}/(rT)$. We assume a constant and uniform thermodynamic pressure $\bar{P} = 101\,325\,[Pa]$. To highlight the sensitivity of the fluid flow with temperature dependent properties, arbitrary relations have been used for the specific heat at constant pressure, the thermal conductivity and the dynamic viscosity:

$$\begin{aligned}
c_p(T) &= 100 - \exp{(T/200)}\ \ [J/(kg \cdot K)], \\
\mu(T) &= 100 + \exp{(T/100)}\ \ [kg/(m \cdot s)], \\
k(T) &= 100 + \exp{(T/100)}\ \ [W/(m \cdot K)]
\end{aligned} \tag{3.1}$$

The definition of an analytical vector field $\vec{v}$, satisfying the mass conservation $\nabla \cdot (\rho\vec{v}) = 0$, relies on the vectorial identity $\nabla \cdot (\nabla \wedge \vec{\varphi}) \equiv 0$, for all vectorial function $\vec{\varphi}(\vec{x})$. Then, the velocity field simply writes

$$\vec{v} = \frac{1}{\rho}(\nabla \wedge \vec{\varphi})$$

41

The chosen vectorial function $\vec{\varphi}(\vec{x})$ writes:

$$\vec{\varphi}(x,y) = [4x(x-1)]^3 [4y(y-1)]^4 \, \vec{e}_z \; [kg/(m \cdot s)] \qquad (3.2)$$

Then the velocity field

$$\vec{v}(x,y) = \frac{1}{\rho} \nabla \wedge \left([4x(x-1)]^3 [4y(y-1)]^4 \, \vec{e}_z \right) \; [m/s]$$

is a solution of the steady state mass conservation equation and cancels at the boundaries. The temperature and pressure fields are set to:

$$\Pi_g(x,y) = 10000 \times \cos(\pi x)\cos(\pi y) \, [Pa] \qquad (3.3)$$
$$T(x,y) = 273 \times (1 + 0.5 \times \sin(\pi x)\cos(\pi y)) \, [K] \qquad (3.4)$$

With this choice of temperature field, the specific heat at constant pressure ranges over $[92; 98] \, J/(kg \cdot K)$. The magnitude of the thermal conductivity and dynamic viscosity lies between 104 and 160 and the density ρ is bounded by $0.86 \, kg/m^3$ and $2.6 \, kg/m^3$.

Obviously, the temperature and the velocity field do not follow the energy and momentum equations. To ensure that the discrete solution converges to our solution, we need to introduce source terms. We define the residual to
  – the momentum equation

$$\vec{R}^{\text{residual}, \vec{v}}(\vec{x}) = \nabla \Pi_g + \nabla \cdot (\rho \vec{v} \otimes \vec{v}) - (\rho - \rho_0)\vec{g} - \nabla \cdot \overline{\overline{\tau}}$$

  – the temperature equation

$$R^{\text{residual}, T}(\vec{x}) = c_p \nabla \cdot (\rho \vec{v} T) - \nabla \cdot (k \nabla T)$$

These residuals expressed on cell K, $\left(R^{\text{residual}, T} \right)_K = R^{\text{residual}, T}(\vec{x}_K)$ and $\left(\vec{R}^{\text{residual}, \vec{v}} \right)_K = \vec{R}^{\text{residual}, \vec{v}}(\vec{x}_K)$, are then added to the right-hand sides of Eq. (2.20) and Eq. (2.21a), respectively.

Figure 3.3 shows the sensitivity of the spatial error to the uniform grid size $h/[m] \in \{1/10; 1/20; 1/40; 1/80; 1/160\}$, for the velocity components, the temperature and the pressure. The relative errors between numerical and exact solutions decrease with h with a slope of 2. The spatial accuracy of the low Mach number scheme is then second order.

3.1.2.2   Transient study – Temporal convergence

The definition of an analytical solution which would satisfy the unsteady mass conservation is a bit delicate. To answer this issue, we assume an uniform density so that the mass equation simplifies:

$$\frac{\partial \rho}{\partial t} + \rho \nabla \cdot \vec{v} = 0$$

With this assumption, $\nabla \cdot \vec{v}$ must not depend on spatial coordinates. To do this, we define the velocity as follows:

$$\vec{v}(\vec{x}, t) = \nabla \wedge \vec{\varphi}(\vec{x}) \cos(\omega t) + \begin{pmatrix} \alpha x \\ \beta y \\ \gamma z \end{pmatrix} \; [m/s]$$

42
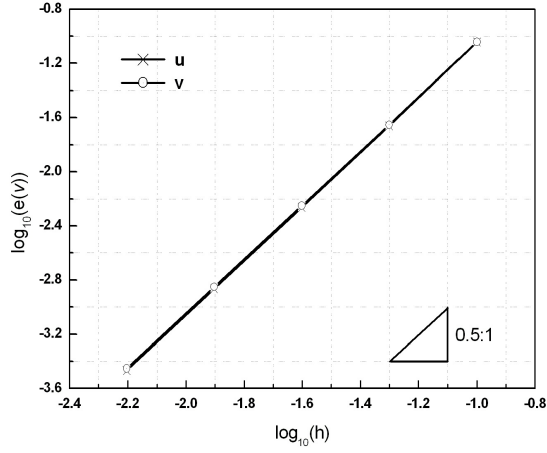
(a) Velocity
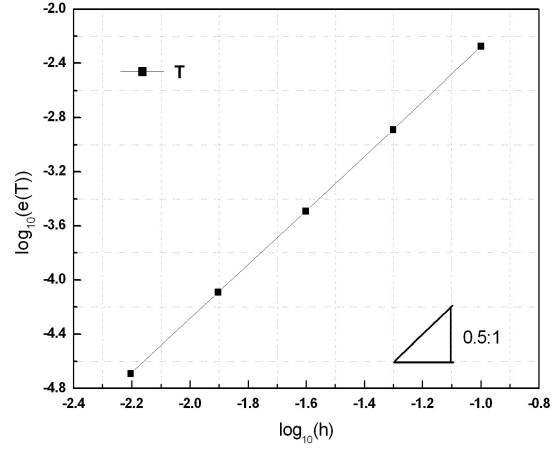
(b) Temperature
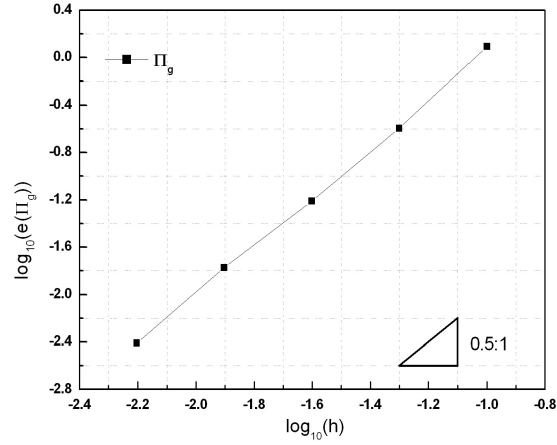
(c) Pressure

Figure 3.3 – Variations of relative spatial errors as a function of the grid size h

Substituting this expression into the mass equation leads to

$$\frac{d\rho}{dt} + \rho(\alpha + \beta + \gamma) = 0$$

that is to say

$$\rho(t) = \rho_0 \exp\left(-(\alpha + \beta + \gamma)t\right) \ [kg/m^3]$$

For the test problem, $\vec{\varphi}(x,y)$ and the density are defined by Eq. (3.2) and $\alpha = \beta = \gamma = 0.05$ with $\rho_0 = 1$. The spatial variation of the pressure $\Pi_g(x,y,t)$ and the temperature $T(x,y,t)$ are given by relations (3.3) and (3.4):

$$\Pi_g(x,y) = 10000 \times \cos(\pi x)\cos(\pi y) \times \cos(\omega t) \ [Pa]$$
$$T(x,y) = 273 \times (1 + 0.5 \times \sin(\pi x)\cos(\pi y)) \times \cos(\omega t) \ [K]$$

43

The physical properties are given by relations (3.1).

To converge toward the analytical solutions, we define the unsteady residuals for

– the momentum equation

$$\vec{R}^{\text{residual},\,\vec{v}}(\vec{x}, t) = \nabla \Pi_g + \nabla \cdot (\rho \vec{v} \otimes \vec{v}) - (\rho - \rho_0)\vec{g} - \nabla \cdot \bar{\bar{\tau}}$$

– the temperature equation

$$R^{\text{residual},\,T}(\vec{x}, t) = c_p \nabla \cdot (\rho \vec{v} T) - \nabla \cdot (k \nabla T)$$

These residuals expressed on cell K at time $t = (n+1)\Delta t$, $\left(R^{\text{residual},\,T}\right)_K^{(n+1)} = R^{\text{residual},\,T}(\vec{x}_K, (n+1)\Delta t)$ and $\left(\vec{R}^{\text{residual},\,\vec{v}}\right)_K^{(n+1)} = \vec{R}^{\text{residual},\,\vec{v}}(\vec{x}_K, (n+1)\Delta t)$, are then added to the right-hand sides of Eq. (2.20) and Eq. (2.21a), respectively.

Comparisons are carried out at time $t = 0.2\,s$ and for a uniform grid with a mesh size $h = 1/40\,m$. The selected time steps $\Delta t/[s]$ are 4×10^{-2}, 2×10^{-2}, 1×10^{-2}, 5×10^{-3}, 2.5×10^{-3} and 1.25×10^{-3}. Figure 3.4 shows the relative departure between the numerical

(a) Velocity

(b) Temperature
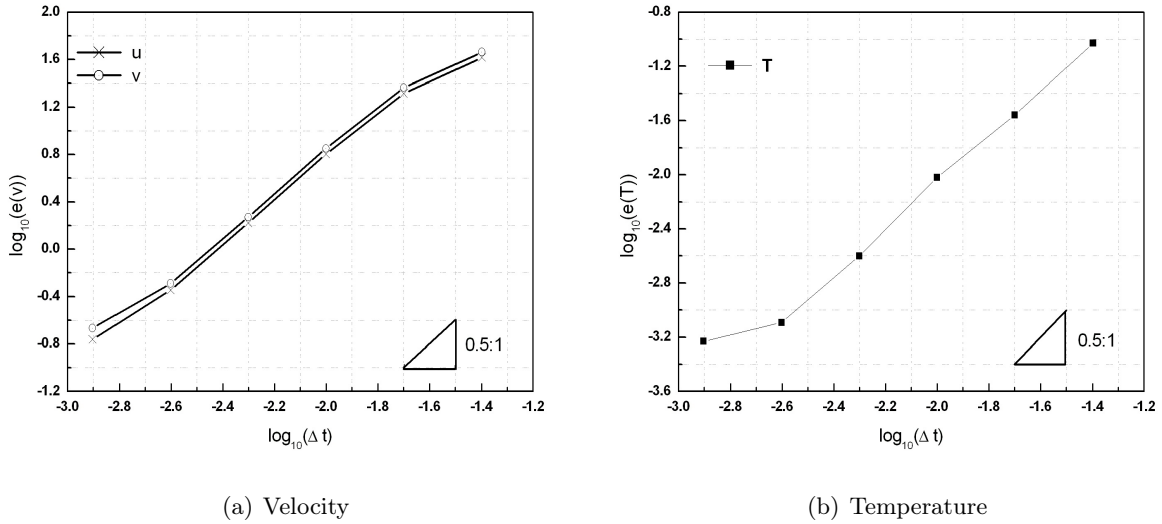
Figure 3.4 – Variation of the relative temporal error as a function of the time step step Δt.

and analytical solutions as a function of the time step. The second order accuracy is, by in large, recovered, except for the smallest time step where the spatial error becomes dominant.

3.2 Natural convection flows in differentially heated enclosures

This section deals with flows occurring in square (Fig. 3.5) or rectangular (Fig. 3.6) cavities differentially heated along the vertical walls. By heat conduction the fluid is either warmed up or cooled, and consequently, the local density of the fluid changes. Under unstable conditions, the light fluid rises up whereas the heavier one falls down, what generates a natural global motion whose the generic name is natural convection.

3.2.1 Low Mach number approximation – Steady state solutions

Since the precursory works of De Vahl Davis [53] in 1983, the thermally driven square (or rectangular) cavity with two different temperatures applied on vertical walls (Fig. 3.5) has been widely studied and becomes a reference problem for the numericist community
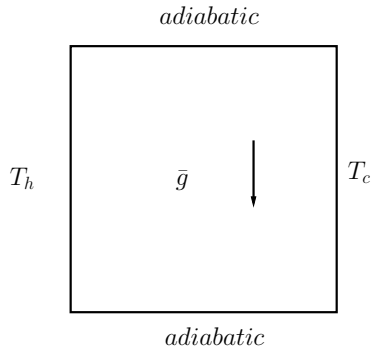
Figure 3.5 – Differently heating cavity

dealing with natural convection problems. First studied for small temperature differences with Boussinesq approximation (see for example [53, 73, 94–96, 126, 156]), this problem has been recently reconsidered for large temperature gaps and low Mach number approximation model, with the setting up of benchmark solutions [97, 124].

We consider the test case proposed in [97, 124]. It consists of the natural convection of air in a L-length square differentially heated cavity with a vertical hot wall at T_h facing a vertical cold wall at T_c. We assume the equation of state of air follows the ideal gas law ($r = 287\,J/(kg \cdot K)$). The dimensionless parameters are the Rayleigh number $Ra = g\beta_0 \Delta T L^3/(\nu_0\alpha_0) = 10^7$, the Prandtl number $Pr = \nu(T)/\alpha(T) = 0.71$, the relative temperature difference $\varepsilon_T = (T_h - T_c)/T_0 = 1.2$ and the isentropic exponent $\gamma = 1.4$ where the index 0 corresponds to the initial conditions. The reduced dynamic viscosity and thermal conductivity depend on temperature according to the same Sutherland law:

$$\frac{k(T)}{k^*} = \frac{\mu(T)}{\mu^*} = \left(\frac{T}{T^*}\right)^{\frac{3}{2}} \frac{T^* + S}{T + S}$$

with $T^* = 273\,K$, $S = 110.5\,K$, $\mu^* = 1.68 \times 10^{-5}\,kg/(m \cdot s)$ and $k^* = \mu^* \gamma\, r/((\gamma - 1)\,Pr)$.

For fluids flowing in enclosures with large relative temperature gaps, the thermodynamic initial conditions must be known. They are set to $T(\vec{x}, t = 0) = T_0 \equiv (T_h + T_c)/2$ and $\bar{P}(t = 0) = P_0 = 101325\,Pa$ ($\rho(\vec{x}, t = 0) = \rho_0 \equiv P_0/(rT_0)$); the fluid is initially at rest.

No slip boundary conditions are set on the vertical isothermal and horizontal adiabatic walls. The hot and cold temperatures are defined by $T_h = T_0(1 + \varepsilon_T/2)$ and $T_c = T_0(1 - \varepsilon_T/2)$. Results are essentially discussed in term of local and average Nusselt numbers computed on vertical walls, $x = 0$ or $x = 1$:

$$\mathrm{Nu}(x, y) = \frac{k(T)\left|\frac{\partial T}{\partial x}\right|}{k_0 \frac{T_h - T_c}{L}}$$

$$\overline{\mathrm{Nu}} = \frac{1}{L}\int_0^L Nu(x, y)\, dy$$

Some comparisons concerning the velocity are also proposed.

Computations have been carried out with a time step controlled by the Courant-Friedrichs-Lewy number (CFL number) set to 0.5. The solution is assumed steady if the maximum of the relative increments between two successive time steps for the velocity and temperature is smaller than 10^{-9}. To take the boundary layers along the walls into account, non-uniform grids were used, both in x- and y-directions. Faces of the control volume $K \equiv [x(i); x(i+1)] \times [y(j); y(j+1)]$ with $1 \leq i \leq N_x$ and $1 \leq j \leq N_y$ are defined by

$$\frac{x(i)}{L} = \frac{i-1}{N_x} - \frac{\xi_x}{2\pi} \sin\left(\frac{2\pi(i-1)}{N_x}\right) \tag{3.5a}$$

$$\frac{y(j)}{L} = \frac{j-1}{N_y} - \frac{\xi_y}{2\pi} \sin\left(\frac{2\pi(j-1)}{N_y}\right) \tag{3.5b}$$

with $\xi_x = \xi_y = 1$ and $N_x = N_y = 160$.

Relative errors on local and average Nusselt numbers between our results and those referenced in [97, 124] are presented in the table 3.1. The maximum error between us and

	Vierendeels [124]	Dabbene [124]	Kloczko [124]	Heuveline [124]	Le Quéré [97]	our solution
$\bar{N}u_0$	0%	0.086%	0.38%	0.006%	0%	16.241
$\bar{N}u_1$	0%	0.32%	0.005%	0.10%	0%	16.241
$Nu(0; 0.5)$	0.022%	2.6%	0.091%	-	-	13.192
$Nu(1; 0.5)$	0.026%	1.6%	0.85%	-	-	15.508
$\max_y(Nu(0; y))$	0.062%	0.34%	1.3%	0.12%	-	46.408
$\min_y(Nu(0; y))$	0.21%	0.069%	0.89%	0.14%	-	1.457
$\max_y(Nu(1; y))$	0.19%	1.99%	0.23%	0.51%	-	34.337
$\min_y(Nu(1; y))$	0.092%	0%	2.8%	0%	-	1.088
P/P_0	0.037%	0.076%	0.076%	0.076%	0.036%	0.9223
Number of control volumes	2048×2048 $\approx 4.2 \times 10^6$	160×160 $= 2.56 \times 10^4$	100×100 $= 10^4$	4×10^5	1024×1024 $\approx 1.05 \times 10^6$	160×160 $= 2.56 \times 10^4$

Table 3.1 – Low Mach number approximation, $Ra = 10^7$, $\delta_T = 1.2$ and Sutherland law. Relative discrepancies of our results with respect to corresponding references.

Vierendeels is 0.21% for the minimum local Nusselt on the left wall. The three important data, average Nusselt number on the left and right walls $\bar{N}u_0$, $\bar{N}u_1$ and the ratio between the thermodynamic pressure and initial pressure, agrees well with the references. Table 3.2 lists the maximum dimensionless vertical and horizontal components of the velocity in

	our results	[155]
$\max_y u(x = 0.5; y) \times \frac{L}{\alpha_0}$	165.48	167.98
y	0.825	0.826
$\max_x v(x; y = 0.5) \times \frac{L}{\alpha_0}$	716.38	724.64
x	0.030	0.031
Mesh	160×160	304×304

Table 3.2 – Comparison of dimensionless velocity components in cross-sections for $Ra = 10^7$, $\delta_T = 1.2$ and Sutherland law. The velocity scale is based on thermal diffusion.

the horizontal and vertical cross-section $y = 0.5$ and $x = 0.5$, as well as their locations. Relative errors for $\max_y u(0.5; y)$ and $\max_x v(x; 0.5)$ are 1.49% and 1.14% respectively.

3.2.2 Unsteady solution – Boussinesq approximation

This subsection aims to validate the numerical scheme once the natural convection flow became unsteady and converges to an oscillatory solution. This transition depends sensitively on the aspect ratio of the enclosure, on the Prandtl number of the fluid and on the thermal boundary conditions [95]. For air fluid ($Pr = 0.71$) flowing in a cavity of height eight times larger than its width (Fig. 3.6), three successive oscillatory modes are unstable
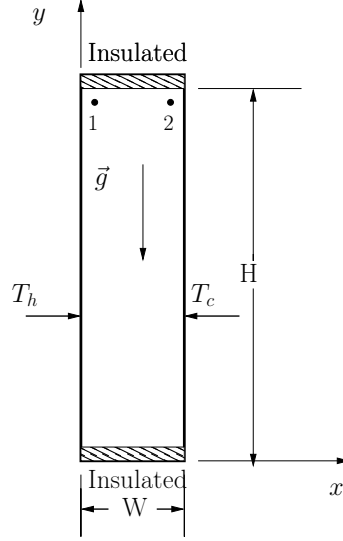

Figure 3.6 – Differentially heated cavity, $H/W = 8$. Coordinates of two probes: $(x_1, y_1) = (0.1810\,W; 7.3700\,W)$ and $(x_1, y_1) = (0.8190\,W; 7.3700\,W)$.

at $Ra_{crit_1} \approx 3.062 \times 10^5$, $Ra_{crit_2} \approx 3.112 \times 10^5$ and $Ra_{crit_3} \approx 3.339 \times 10^5$, provided that the temperature difference remains small enough to adopt Boussinesq approximation [164]. The first and third unstable modes have skew-symmetric patterns whereas the second one has the same symmetry as the steady basic flow. Theses perturbations travel around the cavity in the direction of the primary flow and their maximum amplitudes are located close to the side walls indicating a boundary layer type instability.

A comparison exercise has been carried out by Christon *et al.* [49] in 2002 to provide reference data on time-dependent natural convection flows in enclosures. According to the authors, identification of the "best" time-dependent solution was not clear cut, but they finally considered the contribution by Xin et Le Quéré [164] as a "truth" solution.

Comparisons are then performed for natural convection of air ($Pr = 0.71$), at a supercritical Rayleigh number ($Ra > Ra_{crit_3}$) equal to $Ra = 3.4 \times 10^5$ in a 8:1 aspect ratio cavity (see Fig. 3.6). Two probes are located at coordinates

$$\vec{x}_1 = (x_1, y_1) = (0.1810\,W; 7.3700\,W)$$
$$\vec{x}_2 = (x_2, y_2) = (0.8190\,W; 7.3700\,W)$$

where W denotes the width of the cavity. The fluid is initially at rest, at the average temperature of the vertical walls. Once the transient flow is completed, the solution is periodic (see Fig. 3.7). Then, average value $\bar{\phi}$ and oscillation magnitude ϕ' are computed
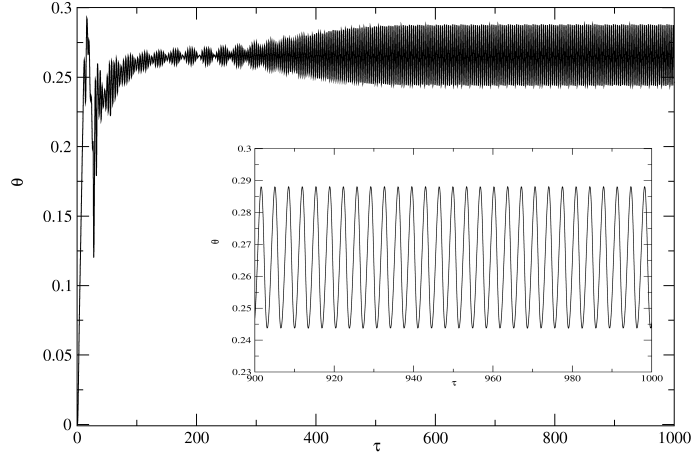
Figure 3.7 – Reduced temperature evolution $\theta = (T - (T_h + T_c)/2)/(T_h - T_c)$ at point 1 as a function of dimensionless time $\tau \equiv t\alpha_0/W^2$.

using the following relations

$$\bar{\phi} = \frac{1}{T} \int\limits_{t}^{t+T} \phi(t)\, dt \tag{3.6a}$$

$$\phi' = \max_{\tau \in [t;t+T]} \phi(\tau) - \min_{\tau \in [t;t+T]} \phi(\tau) \tag{3.6b}$$

with $\phi(t) \in \{u(\vec{x}_1, t), \theta(\vec{x}_1, t), \Delta\Pi_{g12}(t)\}$ with $\Delta\Pi_{g12}(t) \equiv \Pi_g(\vec{x}_1, t) - \Pi_g(\vec{x}_2, t)$.

We use the non-uniform grids defined by Eq. (3.5), and we fix the CFL number to 0.5. Non-uniform grid spacings are used to accurately model the boundary layers along the solid walls. By default, the expansion coefficients are set to $\xi_x = 0.6834$ and $\xi_y = 0.3070$. To avoid interpolation procedure to compute the solution on point $\vec{x}_1$ (and by symmetry on point $\vec{x}_2$), these coefficients are slightly modified in order the nearest cell center of $\vec{x}_1$ coincides exactly with $\vec{x}_1$. It results the following mesh coefficients $(\xi_x, \xi_y) = (0.6699, 0.3052)$ for $(N_x, N_y) = (100, 260)$, $(\xi_x, \xi_y) = (0.7033, 0.3175)$ for $(N_x, N_y) = (133, 346)$, $(\xi_x, \xi_y) = (0.6883, 0.3124)$ for $(N_x, N_y) = (200, 520)$ and $(\xi_x, \xi_y) = (0.6945, 0.3051)$ for $(N_x, N_y) = (300, 780)$.

Starting from rest, the fluid is set in motion by natural convection and the flow converges to periodic solution for a dimensionless time $\tau = t \times \alpha/W^2 \approx 500$ (Fig. 3.7). Results calculated at point 1 are compared with those of Xin and Le Quéré (2002) [164]. Table 3.3 gathers the average values (Eq. (3.6a)) and the fluctuations (Eq. (3.6b)) for
  – the horizontal component of the velocity rescaled by $\sqrt{g\beta(T_h - T_c)W}$, $u(\vec{x}_1)$;
  – the reduced temperature, $\theta(\vec{x}_1) = (T(\vec{x}_1) - (T_h + T_c)/2)/(T_h - T_c)$;
  – the difference of the dimensionless dynamic pressure between points $\vec{x}_1$ and $\vec{x}_2$, $\Delta\Pi_{g12}$;
  – the local Nusselt number, $Nu(\vec{x}_1)$.
The results are in excellent agreement with those of the reference, except $\overline{\Delta\Pi}_{g12}$ which departs from 10% for the finest grid; reducing the CFL number does not modify significantly $\overline{\Delta\Pi}_{g12}$. A deeper insight of the different solutions given by [49] shows a large dispersion of this average pressure difference. It can also be noticed that some of the participants provide values close to ours.

	$\overline{u}(\vec{x}_1)$	$u^{'}(\vec{x}_1)$	$\overline{\theta}(\vec{x}_1)$	$\theta^{'}(\vec{x}_1)$	$\overline{\Delta\Pi_{g_{12}}}$
100×260	0.054976	0.048864	0.265460	0.038310	0.001716
133×346	0.05550	0.051096	0.265471	0.039973	0.001715
200×520	0.055967	0.053211	0.26547	0.041541	0.002032
300×780	0.056174	0.054074	0.265474	0.042160	0.002045
48×180 [164]	0.056345	0.054768	0.265480	0.042690	0.001854
	$\Delta P^{'}_{1,2}$	$\overline{N}u(\vec{x}_1)$	$Nu^{'}(\vec{x}_1)$	Period	
100×260	0.018294	4.57900	0.006368	3.4245	
133×346	0.019082	4.57890	0.006704	3.4193	
200×520	0.01982	4.57920	0.006883	3.4150	
300×780	0.020108	4.57941	0.007017	3.413	
48×180 [164]	0.020355	4.57946	0.007092	3.4115	

Table 3.3 – Comparisons of solutions at the probe 1 in the case $Ra = 3.4 \times 10^5$, $Pr = 0.71$ et $H/W = 8$ (Fig. 3.6). The length and velocity are scaled by W, the width of the cavity, and $\sqrt{g\beta(T_h - T_c)W}$. The pressure is made dimensionless with $\rho_0(\alpha/W)^2$. The reduced temperature writes $\theta = (T - (T_h + T_c)/2)/(T_h - T_c)$.

Chapter 4

Optimal plate spacing for mixed convection from an array of vertical isothermal plates [150]

Nomenclature

a	thermal diffusivity $[m^2\ s^{-1}]$
A	aspect ratio, $A = H/D$
Be	pressure difference number, $Be = \Delta p H^2/a_o\mu_0$
c_p	specific heat $[J\ K^{-1}\ kg^{-1}]$
$\overline{\overline{d}}$	deformation velocity tensor $[s^{-1}]$
D	plate spacing [m]
D_h	hydraulic diameter, $D_h = 2D$ [m]
Fr	Froude number, $Fr = w_0^2/gD_h$
g	gravitational acceleration $[m\ s^{-2}]$
Gr_D	Grashof number based on D, $Gr_D = g\beta_0\Delta T D^3/\nu_0^2$)
G_v	volumetric flow rate, $G_v = w_0 S_c\ [m^3 s^{-1}]$
h	heat transfer coefficient $[W\ m^{-2}K^{-1}]$
H	channel height $[m]$
k	thermal conductivity $[W\ m^{-1}\ K^{-1}]$
L	channel length in the direction perpendicular to Fig. 4.1 $[m]$
$\dot{m}$	mass flow rate $[kg\ s^{-1}]$
n	number of channel
$\overline{Nu}_{2w}$	mean Nusselt number based on the wall heat fluxes
$\overline{Nu}_{en}$	mean Nusselt number based on the enthalpy flux
n_x, n_z	numbers of grid points in $x-$ and $z-$directions
p	pressure $[Pa]$
p_m	sum of static and hydrostatic pressures $[Pa]$
p_s	pressure at the outlet section $[Pa]$
p^*	dimensionless pressure, $P = p/(\rho_0 w_0^2)$
Pr	Prandtl number, $Pr = \nu_0/a_0$
Q	heat flux, $[W]$
Q_a, Q_b	analytical expressions for the heat flux, $[W]$
Q_{2w}	convective heat flux along the two vertical channel walls (Eq. 4.13), $[W]$
Q_{en}	enthalpy heat flux (Eq. 4.14), $[W]$
Q_{cond}	axial difusion flux (Eq. 4.16), $[W]$

Ra_H	Rayleigh number based on H, $Ra_H = g\beta\Delta T H^3/a_0\nu_0$
Re	Reynolds number based on D_h, $Re = w_0 D_h/\nu_0$
Ri	Richardson number, $Ri = Gr/Re^2$
S_c	area of the channel cross section, $S_c = DL$ $[m^2]$
S_T	area of the overall heated surfaces, $S_T = 2n(HL)$ $[m^2]$
t	time $[s]$
T	temperature $[K]$
u, w	velocity components $[m\ s^{-1}]$
v_{ref}	reference velocity for natural convection, $v_{ref} = \nu_0/D_h$ $[m\ s^{-1}]$
$\mathcal{W}_m$	pumping power $[W]$
x, z	coordinates $[m]$
Greeks	
α	order of consistency of the numerical scheme
β	thermal coefficient of volumetric expansion, $\beta = 1/T_0$ $[K^{-1}]$
ΔT	temperature difference, $\Delta T = (T_h - T_0)$ $[K]$
Δp	pressure difference, $\Delta p = -\frac{1}{2}\rho_0\overline{w}^2 - p_s$ $[Pa]$
η	efficiency (Eq. 4.44)
η_b	mixed convection group [26], $(Ra_H/Be)^{1/4}$
ν	kinematic viscosity $[m^2\ s^{-1}]$
ρ	density $[kg\ m^{-3}]$
θ	dimensionless temperature ratio, $\theta = (T - T_0)/\Delta T$
τ	dimensionless time, $\tau = w_0 t/(Re D_h)$
Subscripts	
$a,\ b$	analytical solutions
$cond$	conduction
en	enthalpy
h	hot wall
H	quantity based on channel height
nc	natural convection
opt	optimum
w	wall
0	inlet section
$2w$	two walls
Superscripts	
$-$	averaged quantity
$*$	dimensionless quantity

4.1   Introduction

Mixed convection occurs when both natural convection and forced convection heat transfer mechanisms interact. In vertical and inclined parallel-plate channels the bulk flow can be either upward or downward. The thermal and/or solutal buoyancy forces may be either assisting or opposing the forced flow according to the forced flow direction relative to gravity, and depending on the thermal and/or solutal conditions at both walls. The four important parameters are the channel aspect ratio, $A = H/D$, the Reynolds, Grashof and Prandtl numbers, Re, Gr and Pr, respectively. The relative contributions of forced and natural convection effects are often discussed in term of the Richardson number, Ri

$= Gr/Re^2$, or in term of $Ri\,Re = Gr/Re$. It should be noted here that the choice of the appropriate length scale for the buoyancy term (i.e. the length in the Grashof number) is not obvious while it should be the hydraulic diameter for the Reynolds number.

In the last three decades, mixed convection through parallel-plate channels and in ducts with various cross-sections has been extensively studied both for vertical and inclined configurations. However, reference results for mixed convection are relatively sparse in comparison with those for forced or natural convection flows in ducts. That is due to the large increase in the complexity and numbers of possible flow configurations occurring in practical applications: cooling of electronic equipment, solar energy collectors, compact heat exchangers and many others [17].

Most of the theoretical studies on laminar mixed convection in vertical, parallel-plate channels were for thermal conditions of uniform wall heat fluxes or uniform wall temperatures, the heating of the two walls being either identical or asymmetric. Analytical methods for fully developed flows were first derived by Aung and Worku [11–13]. This problem was revisited recently by Padet et al. [121–123] who determined relevant criteria for the transitions from natural to mixed convection and from mixed to forced convection. A combined perturbation and similarity approach was used by Yao [167] for solving the governing equations in the entry region for conditions of constant wall temperature and constant wall heat flux. Purely numerical solutions were obtained by Cheng et al. [44] who suggested modifications to the parabolic model (based on negligible streamwise diffusion terms in comparison with spanwise diffusion terms) and, a new algorithm for the analysis of buoyancy-induced flow reversal within vertical channels was introduced. Numerical solutions based on a fully elliptic formulation are only few. To our best knowledge, the first numerical study on mixed convection based on the full elliptic formulation was carried out by Jeng et al. [82] who showed the limitations of the parabolic model for low Reynolds number flows. Recently, flow reversal and flow recirculations were anew considered in details by Yang et al. [166] and by Desrayaud and Lauriat [56]. Only few numerical studies were conducted by using the elliptic formulation. The reason is that the writing of appropriate boundary conditions at the inlet and outlet sections is difficult to handle: it is the mathematical backbone of such approaches. The main interest in considering an elliptic formulation is that the axial conduction may be accounted for, which is of importance for low mass flow rate.

In this work, we are considering only mixed convection with buoyancy and pressure forces acting in the same direction: this case is generally termed as "assisting mixed convection". The first question to be raised is: which force assists the other? Most papers published in the current literature considers that natural convection assists forced convection, i.e. the flow rate is fixed and the effect of natural convection on the heat transfer rate is examined. We are solving the problem from a different viewpoint: forced convection generated by an additional pressure difference is aiding natural convection, as it is mostly the case for the cooling of electronic equipments or in the case of severe nuclear accident.

Amongst the difficulties underlying a general description of thermal mixed convection (the thermosolutal case [74, 92, 99] being out the scope of this work) are the occurrences of flow reversal and flow recirculations, the origins of which are fully different although there exists some confusion into the literature. On one hand, Aung and Worku [12] analytically demonstrated that flow reversal is impossible in the case of fully developed flow for symmetrically heated channels at constant temperature. On the other hand, Desrayaud and

Lauriat [56] showed numerically the occurrence of flow recirculations in the entrance region for the constant temperature case at relatively low Reynolds number. Linear stability analysis of laminar mixed convection in a vertical channel with constant heat flux imposed on the walls has been investigated by Chen and Chung [43]. They demonstrated that the fully developed flow is highly unstable, the critical Grashof number being strongly dependent on the Reynolds and Prandtl numbers. Non-linear local analysis [70] gave results in good agreement with those of Chen and Chung [43].

Flow reversals in vertical parallel-plate channels and in circular pipe have been quite extensively studied, both for developing and fully developed flows, experimentally as well as theoretically. The experimental works performed by Morton et al. [115] and Ingham et al. [81] for mixed-convection water flows in vertical pipes and relatively small Reynolds numbers have clearly shown the occurrence of flow reversal. Less experiments were devoted to parallel-plate channels. Flow reversal and its structure have been visualized by Gau and coworkers [63, 64, 79] for both assisted and opposed convection. Its occurrence originates from asymmetric heating conditions. Flow reversal can be easily predicted, just by using the simplest one-dimensional form of the governing equations [12, 123].

Flow recirculations are caused by an imposed flow rate and are predicted in the entrance section experimentally [27] as well as numerically when using an elliptical formulation [56]. The existence of a flow recirculation bubble is caused by increases in upstream velocities close to the heated walls. This increases is due the decrease in density in conjunction with the largest gravitational force that produces acceleration of the fluid in regions next to the walls where maximums of axial velocities are observed. To satisfy mass conservation, fluid is drawn downward from the centerline region when the flow rate is kept fixed, independently of the magnitude of the buoyancy force. These recirculations are thus directly linked to the inlet flow boundary conditions.

As depicted above, a general study of mixed convection is beyond the scope of this paper. Therefore, we are just concentrating on the optimal spacing between isothermal plates arranged in an array and cooled by mixed convection. The optimal spacing for the cooling of an array of heated surfaces by natural or by forced convection is a problem that has attracted many experimental and numerical studies since the famous work by Elenbass [57]. This spacing corresponds to the peak heat flux that can be transferred by providing the surface of n perfectly conducting fins.

When the parallel plates are cooled by natural convection, Bar-Cohen and Rohsenow [18] have demonstrated that the optimum spacing can be determined through an analytic optimization procedure based on maximizing the total heat transfer per unit volume. This method permits to find optimum spacings for various thermal boundary conditions at the walls. At the same time, Bejan [21], suggested that the optimal spacing can be determined by the intersection of two asymptotic solutions varying as D^{-1} or D^2 (the foundation of the theory of the intersection of asymptotes, followed by the Constructal Theory [22, 24]). The first solution is based on the assumption that the thicknesses of boundary layers growing on vertical surfaces are much lower than $D/2$ at the exit section ($z = H$). On the other hand, the second solution assumes that the temperature of the coolant is uniformly equal to the temperature of the walls at the exit section. Later on, the optimum plate spacing for natural convection between heated vertical parallel plates was numerically analysed by Anand et al. [1] for channels subjected to uniform wall temperature and uniform heat flux heating conditions. Boundary layers approximations were introduced and calculations were

conducted for various asymmetric heating parameters.

For forced convection Bejan and Scuibba [25] determined an optimal spacing, intersection of two asymptotic solutions in $D^{-2/3}$ when the distance between the walls is large enough and in D^2 when they are sufficiently close for the occurrence of a short thermal entry length. The optimal spacing of a stack of isothermal parallel boards cooled by forced convection was studied numerically and theoretically by Mereu et al. [110] according to the flow generation: fixed pressure drop (Δp), mass flow rate ($\dot{m}$), or pumping power. For each of these cases, the optimal spacing and maximum overall thermal conductance of the stack were correlated in dimensionless form. It was shown that neither the constant Δp model nor the constant $\dot{m}$ model is appropriate when the stack is cooled by a stream created by a fan or a pump. Campo [38] complemented the study conducted by Bejan and Scubbia [25] by proposing an order-of-magnitude analysis for channels with the plates heated with uniform heat fluxes. To this end, he introduced a new characteristic plate temperature based on the mean value of the axially variable temperature difference between plate and free-stream temperatures.

In many applications, especially for electronic components, cooling is performed by mixed convection in order to increase the efficiency of the fins while using low power fans. Laminar mixed convection between a series of parallel plates with planar heat sources was numerically investigated by Watson et al. [159] with conjugate conduction effects included. A fully elliptic formulation and extensions above the plates were considered for various plate-to-fluid conductivity ratios. The thermodynamic optimization of cooling techniques for heat generating devices were examined in Bejan and Ledezma [23] and da Silva et Bejan [52] by considering five models for applications above and below room temperature. They showed, in particular, that the minimum fan power requirement for forced convection is minimum when the heat transfer area is optimized according to the relation $A = 2A_f/St$, where St is the Stanton number and A_f the flow cross-sectional area. For natural convection cooling, this optimization rule determines the maximum possible heat generation rate.

A single correlation for optimal spacing and maximal heat transfer rate density for mixed convection as well as for natural and forced convection in stacks of isothermal parallel plates was derived by Bello-Ochende and Bejan [26]. The starting point of the numerical study was the expressions of the optimal spacings for pure natural convection (Bejan, [21]) and pure forced convection generated by a pressure difference (Bejan and Sciubba [18]). Their results, extended to the Prandtl number range [0.001, 100] for natural and forced convection, re-inforced the argument that the role of the pressure drop number (or Bejan number) in forced convection is analogous to that of the Rayleigh number in natural convection. The authors claimed that the success of the universal correlation derived in their study is due to the systematic manner it was developed. We will compare our results against these correlations with air as working fluid in the Result section of the present paper.

We present in this paper numerical results obtained when the pressure and buoyancy forces act in the same direction. It is shown that an optimal spacing still exists for mixed convection but its value depends strongly on the pressure difference between the inlet and outlet sections.

The paper is organized as follows. In section 4.2, we present the problem formulation both in dimensional form and in dimensionless form for the specific case of a vertical

flat-plate channel subjected to uniform and equal wall temperatures. The heat transfer characteristics are then discussed. Section 4.3 describes the numerical method used to solve the conservation equations and to satisfy the overall mass conservation. In section 4.4, results and discussion are presented successively for natural, forced and mixed convection.

4.2   Governing equations

We consider two-dimensional, incompressible and laminar buoyancy-assisting flows inside vertical parallel-plate channels, as shown in Fig. 4.1. The fluid enters the channel stack
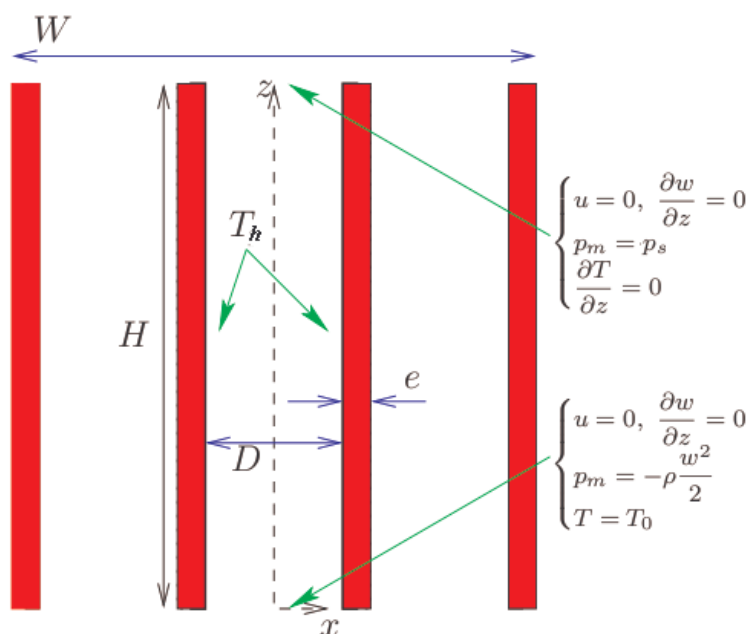

Figure 4.1 – Schematic of the array of vertical isothermal plates and boundary conditions.

of height H at ambient temperature and traverses upward, being heated by the hot walls at uniform temperature T_h. The fully developed region may be eventually reached at the outlet $(z = H)$, after a development length mainly depending on the value of the plate spacing for the problem under consideration. On account of the maximum temperature difference invoked, it is assumed that all physical properties are constant except for the density in the buoyancy force in the vertical direction (Boussinesq approximation). The reference temperature has been taken as the inlet temperature, as in most of the solutions reported in the current literature. However, this choice remains an open question, as discussed by Barletta and Zanchini [19], especially for fully developed mixed-convection. By assuming also that the inlet and outlet boundary conditions are the same for each of the channels, we are thus considering the flow in only one channel (periodicity of the flow in the horizontal direction). Owing to the stability results by Chen and Chung [43], the governing equations are written in transient form in order to capture possible transitions to unsteady flows. With the z-axis pointing upwards and the origin of coordinates placed at the center of the inlet section, the conservation equations based on a fully elliptic model are

$$\frac{\partial u}{\partial x} + \frac{\partial w}{\partial z} = 0 \tag{4.1}$$

$$\frac{\partial u}{\partial t} + u\frac{\partial u}{\partial x} + w\frac{\partial u}{\partial z} = -\frac{1}{\rho_0}\frac{\partial p}{\partial x} + \nu_0\left(\frac{\partial^2 u}{\partial x^2} + \frac{\partial^2 u}{\partial z^2}\right) \tag{4.2}$$

$$\frac{\partial w}{\partial t} + u\frac{\partial w}{\partial x} + w\frac{\partial w}{\partial z} = -\frac{1}{\rho_0}\frac{\partial(p + \rho_o gz)}{\partial z} + \nu_0\left(\frac{\partial^2 w}{\partial x^2} + \frac{\partial^2 w}{\partial z^2}\right) + g\beta_0(T - T_0) \tag{4.3}$$

$$\frac{\partial T}{\partial t} + u\frac{\partial T}{\partial x} + w\frac{\partial T}{\partial z} = a_0\left(\frac{\partial^2 T}{\partial x^2} + \frac{\partial^2 T}{\partial z^2}\right) \tag{4.4}$$

4.2.1 Boundary and initial conditions

The boundary conditions are written:

$$u = w = 0, \quad T = T_h \quad \text{at } x = \pm D/2 \text{ and for } 0 < z < H$$
$$u = 0, \quad \frac{\partial w}{\partial z} = 0, \quad p = -\rho_0 w^2/2, \quad T = T_0 \quad \text{for } -D/2 < x < D/2 \text{ and at } z = 0$$
$$u = 0, \quad \frac{\partial w}{\partial z} = 0, \quad p + \rho_0 gH = p_s, \quad \frac{\partial T}{\partial z} = 0 \quad \text{for } -D/2 < x < D/2 \text{ and at } z = H \tag{4.5}$$

The initial condition is a fluid at rest at uniform temperature T_0.

For natural convection $p_s = 0$ while the buoyancy force is neglected in Eq. 4.3 (i. e. $g\beta_0(T - T_0) = 0$) for forced convection.

For forced and mixed convection, a fall in pressure is prescribed at the outlet section (it could be as well an increase in pressure at the inlet section). Therefore, the prescribed boundary conditions are inlet temperature and outlet pressure, zero z-derivative for the vertical velocity component and zero horizontal velocity-component. It should be emphasized that these flow B.C. differ somehow from those used in most of previous works.

4.2.2 Dimensionless form

4.2.2.1 Natural convection

Three velocity scales v_{ref} are commonly used for natural convection: either $v_{ref} = \nu_0/D$, or equivalently for gas flows $v_{ref} = a_0/D$, or $v_{ref} = (g\beta\Delta TH/Pr)^{1/2}$ which appears to be more appropriate for boundary layer type flows.

4.2.2.2 Forced or mixed convection

The velocity scale for forced convection with a prescribed volumetric flow rate is generally the inlet velocity, w_0. With the present model, this velocity scale is not *a priori* known. We set thus $v_{ref} = w_0 = (-p_s/\rho_0)^{1/2}$, the maximal possible mean velocity corresponding to a non-viscous fluid.

As suggested in Jeng et al. [82], we introduce the following set of dimensionless quantities:

$$x^* = \frac{x}{D_h}, \quad z^* = \frac{z}{D_h Re}, \quad \tau = \frac{w_0\, t}{D_h Re}, \quad u^* = \frac{uD_h}{\nu_0}, \quad w^* = \frac{w}{w_0}, \quad p^* = \frac{p}{\rho_0 w_0^2}, \quad \theta = \frac{T - T_0}{T_h - T_0} \tag{4.6}$$

where $D_h = 2D$ denotes the hydraulic diameter of the channel. The dimensionless governing equations are as follows

$$\frac{\partial u^*}{\partial x^*} + \frac{\partial w^*}{\partial z^*} = 0 \tag{4.7}$$

$$\frac{\partial u^*}{\partial \tau} + u^* \frac{\partial u^*}{\partial x^*} + w^* \frac{\partial u^*}{\partial z^*} = -Re^2 \frac{\partial p_m^*}{\partial x^*} + \frac{\partial^2 u^*}{\partial x^{*2}} + \frac{1}{Re^2} \frac{\partial^2 u^*}{\partial z^{*2}} \tag{4.8}$$

$$\frac{\partial w^*}{\partial \tau} + u^* \frac{\partial w^*}{\partial x^*} + w^* \frac{\partial w^*}{\partial z^*} = -\frac{\partial p_m^*}{\partial z^*} + \frac{\partial^2 w^*}{\partial x^{*2}} + \frac{1}{Re^2} \frac{\partial^2 w^*}{\partial z^{*2}} + \frac{Gr}{8Re} \theta \tag{4.9}$$

$$\frac{\partial \theta}{\partial \tau} + u^* \frac{\partial \theta}{\partial x^*} + w^* \frac{\partial \theta}{\partial z^*} = \frac{1}{Pr} \left(\frac{\partial^2 \theta}{\partial x^{*2}} + \frac{1}{Re^2} \frac{\partial^2 \theta}{\partial z^{*2}} \right) \tag{4.10}$$

where

$$Gr_D = \frac{g\beta_0 D^3 \Delta T}{\nu_0^2} \ , \quad Pr = \frac{\nu_0}{a_0} \ , \quad Re = \frac{w_0 D_h}{\nu_0}$$

The dimensionless expression p_m^*, associated with the sum of static and hydrostatic pressures, can be calculated by the following equation

$$p_m^* = p^* + (\frac{Re}{Fr})z^*$$

where $Fr = \frac{w_0^2}{gD_h}$ is the Froude number. If $w_0 \to \infty$, $Re/Fr \to 0$, and the x^*-momentum equation shows that p_m^* becomes constant within a channel cross section. When $Re >> 1$, the axial diffusion terms in the momentum and energy equations becomes negligibly small in comparison with the transverse terms: a parabolic model is then relevant. For a fully established regime ($u^* = 0$, $\theta = 1$), the only dimensionless parameter is thus Gr/Re (see Aung and Worku [12, 13] or Padet et al. [122, 123]).

4.2.2.3   Boundary and initial conditions

$$u^* = w^* = 0, \quad \theta = 1 \ \text{ at } x^* = \pm 1/4 \text{ and for } \ 0 < z^* < \frac{A}{Re}$$

$$u^* = 0, \quad \frac{\partial w^*}{\partial z^*} = 0, \quad p_m^* = -w^{*^2}/2, \quad \theta = 0 \ \text{ for } -1/4 < x^* < 1/4 \ \text{ and at } \ z^* = 0$$

$$u^* = 0, \quad \frac{\partial w^*}{\partial z^*} = 0, \quad p_m^* = p_s^*, \quad \frac{\partial \theta}{\partial z^*} = 0 \ \text{ for } -1/4 < x^* < 1/4 \ \text{ and at } \ z^* = \frac{A}{Re} \tag{4.11}$$

where $A = H/D_h$ is the height to spacing ratio of the channel.

$$u^* = w^* = 0, \quad \theta = 0 \ \text{ at } \tau = 0 \quad \forall \ x^*, z^* \tag{4.12}$$

The dimensionless forms of the governing equations and boundary conditions show that the problem solution depends on five dimensionless parameters: A, Fr, Gr, Pr and Re. The relative importance of the buoyancy force is characterized by the ratio $Gr/8Re$. For pure natural convection, w_0 may be changed into $v_{ref} = \nu_0/D_h$. Therefore, it is found that $Re = 1$ and $Re/Fr = gD_h^2/(\nu_0/D_h)$.

4.2.3 Heat transfer

The total heat transfer rate released by two walls of depth L and height H, denoted as Q_{2w}, is calculated as follows:

$$Q_{2w} = 2Lk_0 \int_0^H \left. \frac{\partial T}{\partial x} \right|_{x=D/2} dz = 2\overline{h}(LH)(T_h - T_0) \qquad (W) \qquad (4.13)$$

where $\overline{h}$ is the mean heat transfer coefficient defined by right-hand side of equality (4.13). For natural or mixed convection, a mean Nusselt number expressed by $\overline{Nu}_{2w} = Q_{2w}/[2(LH)(k_0\Delta T/D)]$ may be introduced [18]. The enthalpy flux removed from the two heated surfaces by the stream is

$$Q_{en} = \rho_0 c_p S_c [(\overline{wT})_H - (\overline{wT})_0] \qquad (W) \qquad (4.14)$$

where $(\overline{wT})_z$ is the cross-section averaged (wT) over one channel of cross-section area $S_c = DL$ defined as

$$(\overline{wT})_z = \frac{1}{D} \int_{-D/2}^{D/2} w(x,z)T(x,z)dx \qquad (4.15)$$

By using again $2(LH)(k_0\Delta T/D)$ as a reference heat flux, we can define a Nusselt number $\overline{Nu}_{en} = Q_{en}/[2(LH)(k_0\Delta T/D)]$.

It should be emphasized that Q_{2w} is always greater than Q_{en} because heat lost by axial diffusion at the channel inlet is not included into the definition of Q_{en}. When the wall temperatures are kept fixed, Q_{2w} and Q_{en} merge provided that the Reynolds number is large enough for assuming that axial diffusion is negligibly small compared with Q_{2w} and Q_{en}, as shown by Eqs. 4.8-4.10. The difference $Q_{cond} = Q_{2w} - Q_{en}$ yields the effect of axial diffusion which can be written according to Eq. 4.5 as

$$Q_{cond} = k_0 L \int_{-D/2}^{D/2} \left. \frac{\partial T}{\partial z} \right|_{z=0} dx = 2k_0 L \int_0^H \left. \frac{\partial T}{\partial x} \right|_{x=D/2} dz - \rho_0 c_p L \int_{-D/2}^{D/2} [w(x,H)T(x,H) - w(x,0)T_0]dx$$
$$(4.16)$$

For negligible axial heat diffusion, equation 4.16 reads:

$$2k_0 L \int_0^H \left. \frac{\partial T}{\partial x} \right|_{x=D/2} dz = 2\overline{h}(HL)(T_h - T_0) = \rho_0 c_p S_c [(\overline{wT})_H - (\overline{wT})_0] \qquad (4.17)$$

Such an approximation is one of the foundations introduced for establishing the analytical solutions reported in Ref. [18, 22, 25].

4.3 Numerical method and validation

4.3.1 Numerical scheme

The conservation equations were spatially discretized to second order by the finite volume method on a structured grid with variables co-localized at the center of the mesh. Centered approximations were used for the transport terms. A second-order Euler scheme was adopted for time derivatives at time $t = (n+1)\Delta t$, with an implicit treatment of the diffusion terms and an Adams-Bashforth extrapolation procedure for the transport terms. The velocity-pressure decoupling was handled by a projection method. The resolution of the Poisson problem with an appropriate source term f, $\nabla \cdot (\nabla \Phi) = f$, for calculating the pressure correction $\Phi = P^{n+1} - P^n$ is known to produce checkerboard oscillations when $\nabla \cdot (.)$

and $\nabla(.)$ are the collocated divergence and gradient respectively. To stabilize the pressure correction term, the Poisson equation has been substituted by $\widetilde{\nabla}^2\Phi = f - (\nabla \cdot (\nabla\widehat{\Phi}) - \widetilde{\nabla}^2\widehat{\Phi})$ where $\widetilde{\nabla}^2\Phi$ denotes the 5-points diffusion operator classically used on staggered meshes and $\widehat{\Phi}$ is an explicit approximation for Φ at time $t = (n+1)\Delta t$.

The solutions of Helmholtz problems for the components of velocity, temperature field and pressure correction, solution of the modified Poisson problem presented here-above, were obtained by the Bi-Conjugate Gradient Stabilized (BCGS) method, preconditioned by an incomplete LU decomposition. Owing to the axial symmetry of the flow, the problem was solved on the half-width of the channel. The faces of the mesh x_i^f and z_k^f are defined as follows:

$$\frac{x_i^f}{D/2} = \frac{i}{n_x} - \frac{c_x}{2\pi} \sin\left(\frac{i}{n_x}\pi\right), \quad 0 \leq i \leq n_x \tag{4.18}$$

$$\frac{z_k^f}{H} = \frac{\tanh\left(c_z\left(\frac{k}{n_z} - 1\right)\right)}{\tanh(c_z)} + 1, \quad 0 \leq k \leq n_z \tag{4.19}$$

The coefficients c_x and c_z define the mesh refinements in the entrance region and along the isothermal wall. The time integration was performed with the Courant-Friedrich-Levy number kept fixed to $CFL = 0.5$. The stationary solution is reached when $E^{n,n+1} < 10^{-4}$ with

$$E^{n,n+1} = \max_{X\in\{u,w,T\}} \left(\frac{\|X^{(n+1)} - X^{(n)}\|}{\|X^{(n+1)}\|\Delta t}\right) \tag{4.20}$$

where $\|.\|_2$ is the discrete L_2-norm.

The asymptotic behavior of the numerical solution was investigated using a Richardson extrapolation on two or three sets of three meshes defined by $n_x \in \{10, 20, 40\}$, $n_x \in \{20, 40, 80\}$ and $n_x \in \{40, 80, 160\}$ with, in all cases, $n_z = 50n_x$. This method leads to the extrapolated value of f which is written:

$$f_{extrap} = f_{n_x} + \frac{c_{n_x}}{(n_x)^\alpha} \tag{4.21}$$

where c_{n_x} is a coefficient depending on n_x and f_{n_x} is the numerical result on grid $n_x \times n_z$. For sufficiently fine meshes, the value of α must tend towards the order of consistency of the numerical scheme (i.e. $\alpha = 2$), f_{extrap} must then become independent of the mesh. The preliminary study carried out for validating the numerical procedure used the refinement coefficients $c_x = 1$ and $c_z = 1.5$.

4.3.2 Heat flux convergence

For small spacings, the transport of enthalpy may be negligibly small compared to thermal diffusion for natural convection or for forced convection when a small pressure difference is applied. It may therefore be assumed that heat transfer reduces to pure heat conduction in a rectangular $(x \times z)$-domain with $T(\pm D/2, z) = T_w(z)$ in $0 \leq z \leq H$, $T(x, 0) = T_0$ at $z = 0$ in $0 < x < D/2$ and, adiabatic conditions at $z = H$ in $0 < x < D/2$. By using the method of separation of variables for solving the 2D-heat conduction equation subjected to the above boundary conditions, the analytical solution writes :

$$T(x, z) = T_0 + \Delta T \sum_{n=0}^{\infty} \frac{E_n}{\cosh(\lambda_n \frac{D}{2})} \cosh(\lambda_n x) \sin(\lambda_n z) \tag{4.22}$$

where $\lambda_n = (2n+1)\pi/(2H)$. The coefficients of the series are as follows

$$E_n = \frac{2}{H\,\Delta T} \int_0^H (T_w(z) - T_0)sin(\lambda_n z)dz \qquad (4.23)$$

The conductive flux transfered from the side walls of depth L at $x = \pm D/2$ writes:

$$Q_{cond} = 2L \int_0^H k \left. \frac{\partial T}{\partial x}\right|_{x=D/2} dz = 2Lk\Delta T \sum_{n=0}^{\infty} E_n \tanh(\lambda_n \frac{D}{2}) \qquad (4.24)$$

Owing to the adiabatic conditions at $x = 0$ and at $z = H$, the conductive heat flux at surface $z = 0$ equals Q_{cond}. It can be readily shown that the Q_{cond}-expression for $T_w(z) = T_h$, i.e.

$$Q_{cond} = \frac{8Lk\Delta T}{\pi} \sum_{n=0}^{\infty} \frac{1}{2n+1} \tanh\left[\frac{(2n+1)\pi}{4} \left(\frac{D}{H} \right) \right] \qquad (4.25)$$

is a non-convergent series. Therefore, the numerical scheme cannot converge, as it can be seen from the results reported in Table 4.1 for $D = 6\ 10^{-3}\,m$, $H = 0.1\ m$, $L = 1\ m$ and

n_x	10	20	40	80	160	α	Extrap.
Q_{cond}	-6.78347	-7.73104	-8.66075			$2.74585\ 10^{-2}$	53.5420
		-7.73104	-8.66075	-9.58505		$8.41087\ 10^{-3}$	-167.667
			-8.66075	-9.58505	-10.50776	$2.48607\ 10^{-3}$	-545.507

Table 4.1 – Pure conductive wall heat flux Q_{cond} (W) for $D = 6\,10^{-3}m$, $H = 0.1\ m$, $L = 1\ m$ and $\Delta T = 40\ K$ according to the mesh refinement ($n_z = 50n_x$). Order α of convergence of the numerical scheme and Richardson-extrapolated values.

$\Delta T = 40\,K$. Despite the use of quite fine meshes, the order of consistency is found very different from $\alpha = 2$ and the extrapolated values with the three sets of grids differ accordingly. This behavior shows the non-convergence of the numerical scheme for the wall heat fluxes. That is directly linked to the temperature discontinuity at $(x, z) = (\pm D/2, 0)$ into the continuous problem formulation. Such a non-convergent behavior obviously exists for convective heat transfer but it is almost hidden when considering large enough flow rates (or Re) because axial diffusion becomes negligible.

For natural convection ($Pr = 0.71$, $Ra_H = 3.76 \times 10^6$), the values of the average velocity $\overline{w}$, the enthalpy flux, Q_{en}, and the convective flux, Q_{2w}, reported in Table 4.2, show that Richardson extrapolation indicates a very good convergence for $\overline{w}$ and Q_{en} ($\overline{w} = 0.14716\,m/s$, $Q_{en} = 40.246\,W$). However, Q_{2w} (and thus by conservation of fluxes, $Q_{cond} = Q_{2w} - Q_{en}$) gives no indication about spatial convergence. The question of ill-formulated boundary conditions has been investigated by Sadat and Salagnac [137] : the present discussion corroborates their very relevant study about the right methods for solving problems with singularities at the boundaries.

The conclusion is that the total heat transfer at the isothermal wall cannot be accurately calculated, except if axial conduction (refer to Eq. 4.16) is negligibly small: in that case Q_{en} may be considered as a relevant approximation of Q_{2w}.

n_x	10	20	40	80	α	Extrap.
Q_{2w}	-43.4100	-44.2962	-45.2092		$-4.29693\ 10^{-2}$	-14.0963
Q_{2w}		-44.2962	-45.2092	-46.1288	$-1.04261\ 10^{-2}$	81.5836
Q_{en}	40.3414	40.2699	40.2520		1.99095	40.2459
Q_{en}		40.2699	40.2520	40.2477	2.07492	40.2464
$\bar{w}$	0.147638	0.147280	0.147190		1.99445	0.147160
$\bar{w}$		0.147280	0.147190	0.147168	2.01678	0.147160

Table 4.2 – Natural convection for $D = 6\,10^{-3}m$, $H = 0.1\ m$, $L = 1\ m$ and $\Delta T = 40\ K$ ($n_z = 50n_x$). Convective flux at the isothermal wall, $Q_{2w}\ (W)$, enthalpy flux, $Q_{en}\ (W)$, and average velocity, $\bar{w}\ (m/s)$. Order α of convergence of the numerical scheme and Richardson-extrapolated values.

Possible attempts for solving this problem are the use of channel extensions as it was suggested in many previous numerical studies that we will briefly review in what follows for closely related flow configurations.

Naylor et al. [116] solved the full elliptic forms of the governing equations for pure natural convection using inlet flow boundary conditions based on the Jeffrey-Hamel flow in order to represent more realistically the entrance flow. Their solutions validated the inlet pressure approximation ($p = -\rho_0 w^2/2$) commonly used in parabolic formulations. Their predictions of fluid separation at the channel inlet is not agreement with most of the elliptic solutions published so far, and appear to be caused by the shape of the extension. The optimization of plate separation of an open, vertical, parallel-plate channel that is cooled by natural convection of air with the plates symmetrically heated by uniform heat flux has been studied by Morrone et al. [114] by solving the full elliptic conservation equations in a I-shaped computational domain. Correlations for the dimensionless flow rate and optimal values of the spacing were derived and compared with the predictions of Bar-Cohen and Rohsenow [18] and Anand et al. [1]. The deviations at small values of the Grashof number were attributed to the importance of diffusive effects.

The problem of natural convection involving the buoyancy-driven interaction of the fluid motion in a semi-confined space (including horizontal channels open at both ends) with the flow in a large external space was extensively studied, both theoretically and numerically. This problem was reconsidered in a recent paper by Boetcher and Sparrow [31]. One of the two goals of this paper was to examine the impact of the size of the extended domain, boundary conditions on its surfaces, and the mesh density required to achieve high accuracy. As in Desrayaud and Lauriat [55], it was shown that the opening boundary condition must permit the fluid to enter and leave across a boundary in accordance with the dynamics of the situation, unlike it was suggested in most of the previous numerical studies. Khanafer and Vafai ([86]-[87]) showed that an accurate set of effective boundary conditions at the aperture plane for two-dimensional open-ended structures can be obtained from previous computations carried out when using an extended domain.

Natural convection of air in channel-chimney systems was studied experimentally [7], and numerically by using the stream function-vorticity approach and the control volume method by Manca et al. ([4, 5]) for vertical channels heated symmetrically at uniform heat flux and with adiabatic extensions. Results obtained showed how and why the chimney

effect worsens, and provide guidelines to determine if the channel-chimney system is in critical condition related to flow reattachment or separation.

Closely related to what we are considering here is the paper by Bello-Ochende and Bejan [26]: the channel was fitted with upstream and downstream extensions whose lengths were selected based on accuracy tests. For the downstream extension domain, free slip and no penetration were specified at one side and zero stress at the other side in order to nullify the chimney effect. From our point of view, this procedure leads to unrealistic outflow fields for a periodic array of vertical channels.

Based on the work by Sadat and Salagnac [137], we are therefore suggesting an alternative approach to those based on channel extensions.

4.3.3   Regularization of thermal conditions at the inlet corner

Since the problem of convergence of the wall heat flux has been identified as linked to the temperature discontinuity in $(x, z) = (\pm D/2, 0)$, we have modified the temperature profile along the walls using the relationship:

$$T(\pm D/2, z) = T_w(z) = T_0 + (T_h - T_0)\tanh(5000z) \tag{4.26}$$

Therefore the sum of the following series

$$Q_{cond} = 2L\Delta T \sum_{n=0}^{\infty} E_n \tanh(\lambda_n D) \quad \text{with} \quad E_n = \frac{2}{H} \int_0^H \tanh(5000z)\sin(\lambda_n z)dz \tag{4.27}$$

converges to $Q_{cond} = -5.0136\,(W)$ for $D = 6\,10^{-3}m$, $H = 0.1\,m$, $L = 1\,m$ and $\Delta T = 40\,K$. It should be noted that the relative temperature difference $(T_w(z) - T_0)/(T_h - T_0)$ increases from 50% for $z = 0.11\,mm$ to 99% for $z = 0.53\,mm$ and up to 99.9% for $z = 0.76\,mm$. This regularization is thus very steep, and we expect it has little effect on the average velocity, and hence on the enthalpy heat flux.

Taking up the problem of heat conduction with the wall temperature corrected as $T_w(z)$, we see that the extrapolations (Tab. 4.3) give a value rounded to five significant

n_x	10	20	40	80	160	α	Extrap.
Q_{cond}	−4.87969	−4.97384	−5.00314			1.68449	−5.01636
		−4.97384	−5.00314	−5.01110		1.87876	−5.01407
			−5.00314	−5.01110	−5.01314	1.96323	−5.01385

Table 4.3 – Pure conductive wall heat flux Q_{cond} (W) for $D = 6\,10^{-3}m$, $H = 0.1\,m$, $L = 1\,m$ and $\Delta T = 40\,K$ with a regularized temperature distribution (Eq. 4.26) according to the mesh refinement ($n_z = 50n_x$). Order α of convergence of the numerical scheme and Richardson-extrapolated values.

digits for the heat flux equal to $Q_{cond} = -5.0138\,W$. This regularization modifies very slightly the convective transfer as shown in Fig. 4.2 in which are drawn the enthalpy flux and convective flux on the isothermal wall for the problem of natural convection with or without the regularized temperature. By comparing the values of the average velocity and enthalpy flux with or without regularization we found that these values are identical to
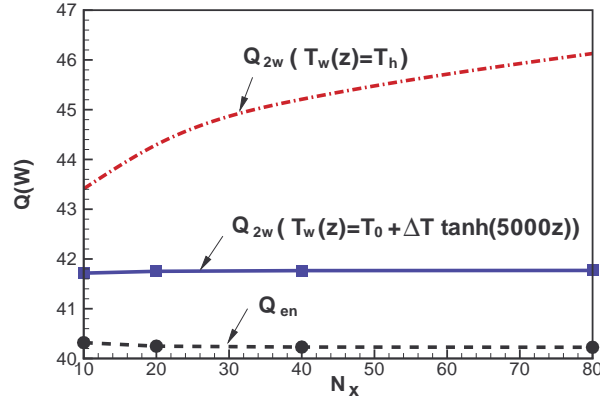
Figure 4.2 – Natural convection: variations of heat flux versus the number of grid points in the x-direction ($n_z = 50n_x$) for $D = 6\ mm$, $H = 0.1\ m$, $L = 1\ m$, $\Delta T = 40\ K$. Q_{2w} is the wall heat flux for non-regularized wall temperature (Eq. 4.25) or for regularized wall temperature (Eq. 4.27). Q_{en} is the enthalpy flux (Eq. 4.14).

three significant digits : $\bar{w} = 0.147\ m/s$ and $Q_{en} = 40.2\ W$.

In conclusion, the regularization method adopted allows to calculate the solution with a very good accuracy and to study the axial conduction, dominant for low axial velocities (or $Pe \ll 1$).

The study of the mesh convergence of numerical solutions was made in the case of natural convection with a regularized temperature at the inlet corner. In addition to computations carried out for $D = 6\ mm$, we also considered the two spacings $D = 1\ mm$ and $D = 10\ mm$ which correspond to the smallest and largest value of D considered in this study.

Once the reference solutions are established using the Richardson extrapolation method, we sought the irregular coarsest mesh which provides accurate numerical solutions to 3 significant digits, for all considered plate spacings. The retained mesh is composed of 40×1000 control volumes covering a half-channel, the mesh being finer along the isothermal wall and close to the entrance region by setting $c_x = 1.64$ and $c_z = 1.82$. The ratio between the smallest and largest length of a rectangular control volume is, for each direction of space, about 10. Rounded to 3 significant digits, we obtain for $L = 1\ m$:
$Q_{2w} = 2.85\ W$, $Q_{en} = 0.326\ W$ and $\bar{w} = 6.89 \cdot 10^{-3}\ m/s$ for $D = 1\ mm$,
$Q_{2w} = 41.8\ W$, $Q_{en} = 40.2\ W$ and $\bar{w} = 0.147\ m/s$ for $D = 6\ mm$,
$Q_{2w} = 57.0\ W$, $Q_{en} = 55.6\ W$ and $\bar{w} = 0.172\ m/s$ for $D = 10\ mm$.

4.4   Results and discussions

Although the conservation equations were presented in their transient form, only the steady-state solutions are discussed here. The height and depth of the isothermal plates at $T_h = 340\ K$ are set as $H = 0.1\ m$ and $L = 1\ m$, and the thermophysical properties of air evaluated at the inlet fluid temperature, $T_0 = 300\ K$, are set as: $\rho_0 = 1.176\ kg.m^{-3}$, $\mu_0 = 1.85\ 10^{-5} Pa.s$, $c_{p,0} = 1006\ J.kg^{-1}.K^{-1}$, $k_0 = 0.0261\ W.m^{-1}.K^{-1}$. The two main

parameters of the problem are the plate spacing, D, and the outlet pressure, p_s. The plate spacing is varied from $D = 10^{-3}m$ to $D = 10^{-2}m$ ($10 \leq A \leq 100$, $5.29 \leq Gr_D \leq 5.29 \, 10^3$) and, p_s is varied from $p_s = -0.1 \, Pa$ to $p_s = -1 \, Pa$.

4.4.1 Natural convection

For air flowing by natural convection in a channel of height $H = 10 \, cm$ and subject to a temperature difference $\Delta T = 40 \, K$, the Rayleigh number based on H is $Ra_H = Gr_D \, Pr \, A^3 = 3.76 \times 10^6$. Two mean Nusselt numbers may be deduced from the overall heat fluxes defined by equations 4.13 and 4.14: $\overline{Nu}_{2w} = 4.79DQ_{2w}$ or $\overline{Nu}_{en} = 4.79DQ_{en}$.

The asymptotic heat transfer correlations reported in Bejan [22] for small or large spacings may be combined for deriving a $\overline{Nu}$-correlation valid whatever the spacing is [18]. However, these predictions assume that the axial heat conduction is negligibly small despite that the temperature at the inlet section is kept fixed at the ambient temperature for all flow rates. The assumption of constant inlet temperature is also used in the present study (see Eq. 4.5). Nevertheless, the elliptic formulation allows comparisons between the total heat transfer rate released by the two walls and the change in the enthalpy flux between the inlet and outlet sections, denoted in dimensionless form as $\overline{Nu}_{2w}$ and $\overline{Nu}_{en}$ (Table 4.4).

D (mm)	Nu_a		Nu_{en}	Nu_{2w}
1	0.0016		0.0016	0.014
3	0.125		0.120	0.151
5	0.782		0.711	0.751
7	1.638		1.591	1.642
9	2.280		2.338	2.402
10	2.563		2.658	2.729

Table 4.4 – Natural convection: comparisons between the mean Nusselt number defined by Eq. 4.28 and the numerical values Nu_{2w} and Nu_{en} based on Eqs. 4.13 and 4.14.

In terms of the present dimensionless variables, the composite heat transfer correlation given by Bar-Cohen and Rohsenow [18] for symmetric, isothermal plates may be written as

$$\overline{Nu}_a = \frac{1}{A} \left[\frac{576A^6}{Ra_H^2} + \frac{2.873}{Ra_H^{1/2}} \right]^{-1/2} \tag{4.28}$$

The first term in Eq. 4.28 dominates for small spacings while the second term dominates for large spacings since it is based on boundary-layer type correlations. Equation 4.28 allows calculations of the wall heat fluxes provided that the axial thermal diffusion is negligibly small (i.e. $Q_{2w} \approx Q_{en}$) and, therefore, an approximate analytical expression for the mean flow velocity, $\overline{w}_a$, is obtained as:

$$Q_{2w,a} = \rho c_{p,0}(LD)\overline{w}_a\Delta T = (2LH)k_0 \left(\frac{\Delta T}{D} \right) \overline{Nu}_a \quad \Rightarrow \quad \overline{w}_a = 2 \left(\frac{a_0}{D} \right) A \, \overline{Nu}_a \tag{4.29}$$

It should be noted that Eq. 4.29 is valid if the outlet bulk temperature is equal, or very close, to that of the walls since it is assumed that $T_b(H) = T_h$ when deriving this equation.

Table 4.4 shows that the agreement between $\overline{Nu}_a$ and $\overline{Nu}_{en}$ is fairly good for all spacings considered while large discrepancies between $\overline{Nu}_a$ and $\overline{Nu}_{2w}$ are reported for

$D < 4\,mm$ owing to the small flow rates. Figure 4.3 shows that the analytical and numerical
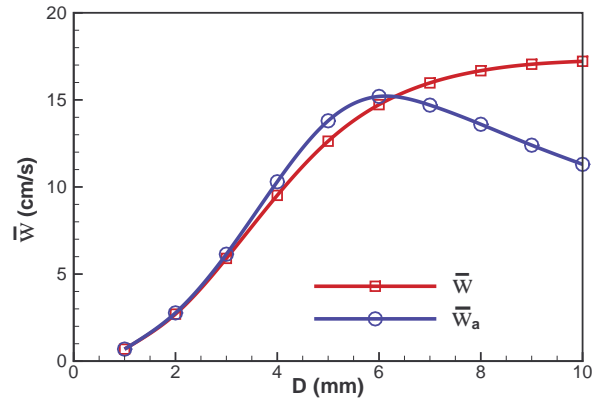
Figure 4.3 – Natural convection: comparison between the analytical ($\overline{w}_a$, Eq. 4.29) and numerical ($\overline{w}$) solutions of the mean flow velocity versus the plate spacing.

predictions for $\overline{w}$ are in good agreement up to $D \approx 7\,mm$. For larger spacings, the boundary layer-type solution (Eq. 4.29) is inappropriate for predicting the flow rate because the outlet velocity profiles calculated numerically are fully different from those for two separate boundary layers : in that case, the temperature along the channel axis (i.e. $T(0, z)$) should be equal to the inlet temperature. From Fig. 4.4 showing the temperature profile at the
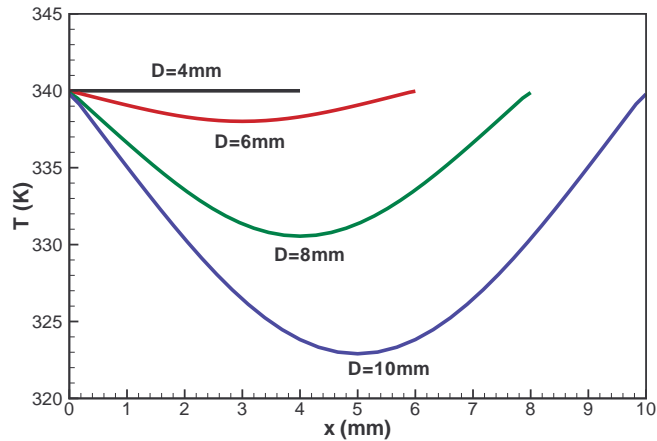
Figure 4.4 – Natural convection: temperature profile at the outlet section for various plate spacings.

outlet section for various spacings, it can be deduced that the axial temperature at the outlet section is much higher than the inlet temperature. On the other hand, the decreases in the relative importance of axial conduction when increasing the spacing leads to smaller differences between $\overline{Nu}_a$ and $\overline{Nu}_{2w}$ (Table 4.4).

Optimal spacing : D_{opt}

The optimal spacing D_{opt} corresponds to the maximum heat flux that is possible to trans-

fer between an ambient fluid flowing between $2n$ isothermal surfaces ($n+1$ plates) forming a stack of n channels of total width W (Fig. 4.1). Such a spacing is just a compromise between overall heat transfer area, $S_t = 2n \times H \times L$, and heat transfer in each of the n channels, $Q_{2w}(D)$ or $Q_{en}(D)$. The optimal spacing for natural convection may be approximately determined from the asymptotic analysis presented in Bejan [22] or by using the $\overline{Nu}$-correlation by Bar-Cohen and Rohsenow [18]. As a result, the ratio $Q_{en}(D)/D$ varies between a value close to zero (corresponding to a very small plate-spacing such as $\overline{w} \approx 0$) and the value for $D = W$, in between there exists an optimum spacing, $D = D_{opt}$, at which $Q_{en}(D)/D$ reaches a maximum value.

D_{opt} can be estimated from the intersection of two curves corresponding to asymptotic solutions [22] or by using the correlation proposed in [18]. The solution given in [22],[26] is $D_{opt} \cong 2.3\ H \times Ra_H^{-1/4}$, i.e. $D_{opt} \cong 5.22\ mm$ for the configuration considered here. The optimization procedure suggested by Bar-Cohen and Rohsenow [18] leads to $D_{opt} = 2.714\ H \times Ra_H^{-1/4}$, i.e. $D_{opt} = 6.16\ mm$.

Figure 4.5 shows the variation of Q/D (W/m) as a function of D, Q_a/D and Q_b/D
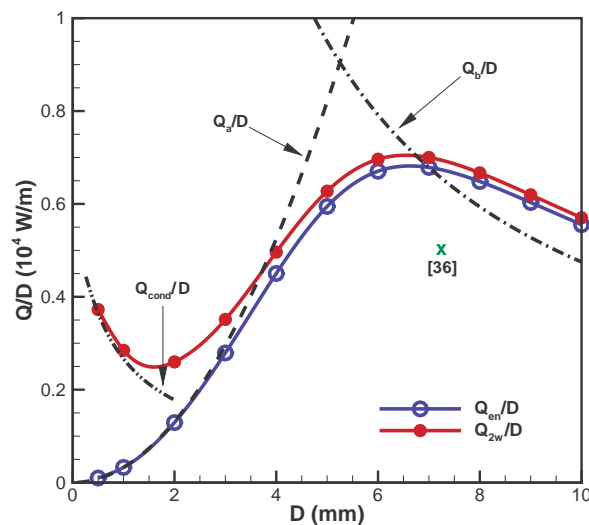
Figure 4.5 – Natural convection: variations of the ratios Q/D with the plate spacing. Q_a and Q_b are the asymptotic analytical solutions (Eq. 4.30), Q_{2w} and Q_{en} are given by Eqs. 4.13 and 4.14, and Q_{cond} by Eq. 4.27. The cross symbol is for D_{opt} and Q_{max}/D_{opt} based on Eq. 4.32.

being calculated by using the following correlations [22]

$$Q_a/D = \frac{k_0 L \Delta T}{12} Ra_H \frac{D^2}{H^3} = 0.327\ 10^9 D^2 \quad \text{and} \quad Q_b/D = \frac{2k_0 L \Delta T}{D} 0.517 Ra_H^{1/4} = \frac{47.54}{D} \tag{4.30}$$

In Fig. 4.5, D_{opt} corresponds to the maximum value of Q_{2w}/D. Figure 4.5 shows that Q_{2w}/D and Q_{en}/D differ significantly for $D < 4\ mm$. The reason is that Q_{en}/D systematically tends towards zero as $D \to 0$ because $\overline{w} \to 0$. On the other hand, Q_{2w} decreases less quickly than D because the problem turns into a pure conductive heat transfer problem as

depicted in section III. As a result Q_{2w}/D increases sharply as $D \to 0$ and tends towards Q_{cond}/D, the exact analytical solution for regularized hot-wall temperatures (Eq. 4.27). The difference $Q_{2w}/D - Q_{en}/D$ is thus the conductive heat flux lost by the fluid at the inlet section, as given by Eq. 4.16. This result raises obviously the problem of the classical choice of the temperature boundary condition at the inlet. Solving this question is out of the scope of the present study.

It can also be seen in Fig. 4.5 that the numerical solution for Q_{en}/D is in excellent agreement with the asymptotic prediction for small spacings, i.e. for low fluid velocities while it starts diverging from Q_a/D when $D \geq 4 \; mm$. For large spacings, the numerical solution does not agree well with the asymptotic solution for boundary-layer type flows, as discussed previously (Fig. 4.4): the Q_b-solution (Eq. 4.30) is not an upper bound for the heat flux. On the other hand, the agreement with the Bar-Cohen and Rohsenow correlation [18] is much better, as displayed in Fig. 4.6. Q_c/D is calculated as follows
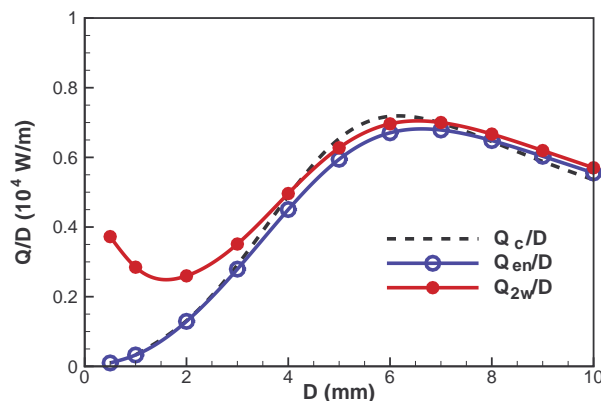
Figure 4.6 – Natural convection: variations of the ratios Q/D with the plate spacing. Q_c is the analytical solution (Eq. 4.31), Q_{2w} and Q_{en} are given by Eqs. 4.13 and 4.14.

$$Q_c/D = (2LH)k_0 \left(\frac{\Delta T}{D^2} \right) \overline{Nu}_a \quad \Rightarrow \quad Q_c/D = 2.09[4.068 \times 10^{-17} D^{-5} + 1.481 \times 10^{-3} D]^{-1/2}$$

(4.31)

From the present numerical results, D_{opt} is found to be $D_{opt} = 6.52 \; mm$ or $D_{opt} = 6.62 \; mm$ by considering either the maximum in Q_{en}/D or in Q_{2w}/D. These values are in good agreement with the maximum of Q_c/D located at $D_{opt} = 6.16 \; mm$ [18]. Figure 4.7 shows axial velocity profiles and temperature distributions at various height of the channel for $D_{opt} = 6.62 \; mm$. In that case , $Q_{2w} = 48.5 \; W$ while $Q_b = 47.3 \; W$ (Eq. 4.30) and $Q_c = 47.04 \; W$ (Eq. 4.31). The discrepancies are therefore very small. However, Figure 4.7 shows that the velocity and temperature profiles are far to be like those for a boundary layer-type flow : they resemble more or less the profiles for an established channel flow. Bello-Ochende and Bejan [26] suggested to take into account the Prandtl effect on D_{opt} and maximum heat transfer density Q_{max}/D, obtained by substituting D by D_{opt} in Eq. 4.30, as

$$D_{opt} \cong 0.0104 A(Pr) \; H \; Ra_H^{-1/4} \quad \Longrightarrow \quad Q_{max}/D_{opt} \leq 0.028 B(Pr) \left(\frac{k_0 \Delta T}{H} \right) Ra_H^{1/2}$$

(4.32)
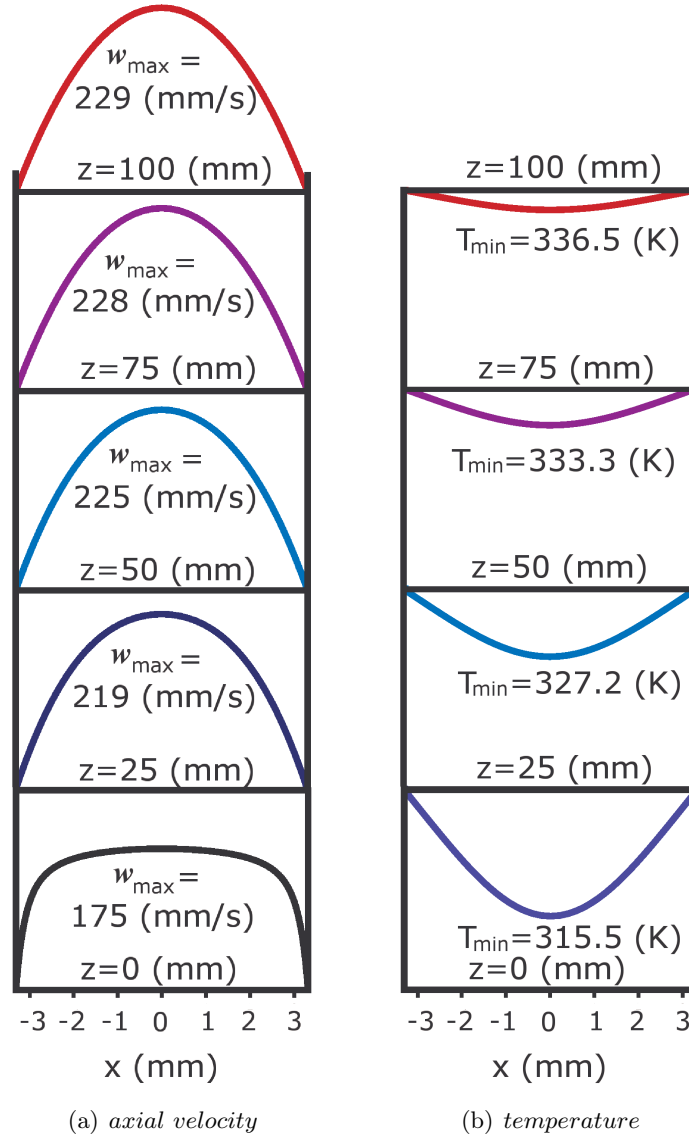
Figure 4.7 – Natural convection: axial velocity and temperature profiles at various heights for the optimal spacing, $D_{opt} = 6.62$ mm.

where $A(Pr) = [263^{0.52} + (2.83Pr^{0.667})^{0.52}]^{1/0.52}$ and $B(Pr) = [15.5^{-0.51} + (181Pr^{0.81})^{-0.51}]^{-1/0.51}$. These correlations are assumed valid in the range $10^5 \leq Ra_H \leq 10^7$ and $10^{-3} \leq Pr \leq 10^2$. The result for $Pr = 0.71$ and $Ra_H = 3.76 \times 10^6$ is reported on Fig. 4.5. As can be seen, there is a large discrepancy with the present results, both on D_{opt} and Q_{max}/D_{opt} which stands much below our predictions.

4.4.2 Forced convection

The asymptotic analysis presented in Bejan et Sciubba [25] leads to the following results:
- if the flow regime may be assumed dynamically and thermally established over the most

part of the height of a vertical channel, the enthalpy flux may approximated as

$$Q_a/D = \frac{D^2}{12\nu_0} \left(\frac{\Delta p}{H}\right) c_{p,0}\Delta T \tag{4.33}$$

- on the other hand, the boundary layer limit approximation leads to

$$Q_b/D = 1.208 k_0 \Delta T \left(\frac{(PrH\Delta p)^{1/3}}{\rho_0^{1/3}\nu_0^{2/3}D^{2/3}}\right) \tag{4.34}$$

Equation 4.34 is based on the Blasius solution for forced flows over a flat plate and by assuming that the velocity along the channel axis, keeping a constant value, is created by a pressure difference Δp.

Based on these two limits, the optimum spacing results from the equality $Q_a = Q_b$. It can be readily shown that [25][26]

$$D_{opt,a} \cong 2.726 H^{1/2} \left(\frac{a_0\mu_0}{\Delta p}\right)^{1/4} \cong 2.726H \ Be^{-1/4} \tag{4.35}$$

where $Be = \frac{\Delta p H^2}{a_o\mu_0}$ is the pressure difference number or Bejan number. With the present set of data, $D_{opt,a}$ can be rewritten as $D_{opt,a} \cong 3.88 \ 10^{-3}\Delta p^{-1/4}$.
The order of magnitude of the maximum heat flux that corresponds to D_{opt} is obtained by combining Eq. 4.33 and Eq. 4.35:

$$Q_{max} \cong 0.62 D_{opt} \left(\frac{\rho_0\Delta p}{Pr}\right)^{1/2} c_{p,0}\Delta T = 0.62 Be^{1/2} D_{opt} \left(\frac{k_0\Delta T}{H}\right) \qquad (W) \qquad (4.36)$$

With the present set of data, Q_{max} can be rewritten as $Q_{max} \cong 124.4\Delta p^{1/4}$. Similarly to what has been done for natural convection, equations 4.35 and 4.36 were reformulated in [26] in order to correlate the Pr effect as

$$D_{opt} \cong 0.0114 A(Pr) H \ Be^{-1/4} \quad \text{and} \quad Q_{max}/D_{opt} \cong 0.035 B(Pr) \left(\frac{k_0\Delta T}{H}\right) Be^{1/2} \tag{4.37}$$

where $A(Pr)$ and $B(Pr)$ are the same as the ones for natural convection.

It should be noted that equations 4.35 and 4.36 cannot be directly applied if the fluid flow is created by a pressure drop at the outlet section because the inlet pressure depends on the inlet velocity through the Bernoulli relationship. On other hand, it is straightforward to calculate $D_{opt,a}$ and $Q_{opt,a}$ if the inlet pressure is fixed while assuming $p_s = 0$. With the model used in the present study, the mass flow rate, $\dot{m} = \rho_0(DL)\overline{w}$, as well as the inlet pressure, $p(x,0)$, result from solving the conservation equations (4.7)-(4.10) with the boundary conditions given by Eq. (4.11). Therefore, we applied Eq. 4.33 to Eq. 4.37 through calculations of the pressure difference as $\Delta p = \overline{p}(0) - p_s = -\frac{1}{2}\rho\overline{w}^2(0) - p_s$, where $\overline{w}$ depends on p_s and D. The mean velocity for D_{opt} and various p_s is reported in Table 4.5. It can be deduced that the Reynolds number based on the hydraulic diameter ranges within $171 \leq Re \leq 309$ when $0.1 \ Pa \leq |p_s| \leq 1 \ Pa$.

The ratios Q_{2w}/D and Q_{en}/D are shown in Fig. 4.8a and 4.8b for $p_s = -0.1 \ Pa$ and $p_s = -1 \ Pa$, the asymptotic solutions Q_a/D and Q_b/D being drawn in dashed lines. As

p_s (Pa)	-0.1	-0.2	-0.4	-0.8	-1.0
$\overline{w}_{opt}$ (m/s)	0.178	0.252	0.357	0.504	0.566
$\Delta p = [\overline{p}(0) - p_s]_{opt}$ (Pa)	0.081	0.161	0.323	0.646	0.807
$D_{opt,a}$ $(Eq.\ 4.35)$	7.28	6.13	5.15	4.33	4.10
$D_{opt}(present)$	7.57	6.38	5.38	4.52	4.29
Q_{max}/D_{opt} $(Eq.\ 4.36)$	$0.91\ 10^4$	$1.29\ 10^4$	$1.82\ 10^4$	$2.58\ 10^4$	$2.88\ 10^4$
Q_{2w}/D_{opt} $(present)$	$0.70\ 10^4$	$0.99\ 10^4$	$1.39\ 10^4$	$1.97\ 10^4$	$2.21\ 10^4$

Table 4.5 – Forced convection: comparisons between analytical solutions ($D_{opt,a}$ and Q_{max}/D_{opt}, Eq. 4.35 and 4.36) and numerical solutions: D_{opt} (mm) and Q_{2w}/D_{opt} (W/m).

(a) $p_s = -0.1\,Pa$ (b) $p_s = -1\,Pa$
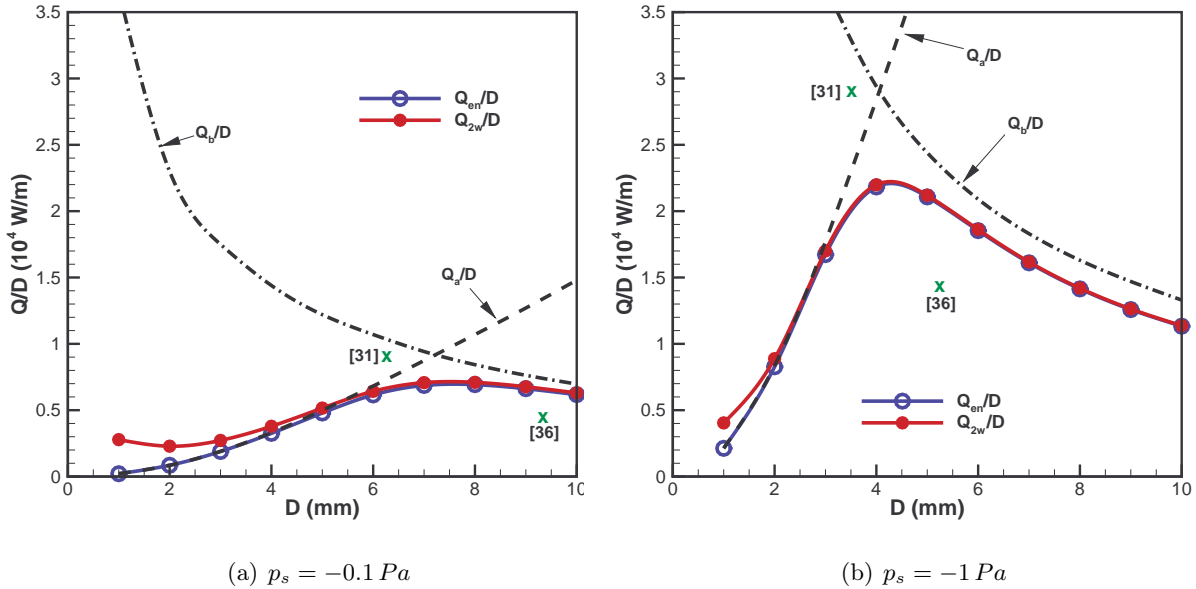
Figure 4.8 – Forced convection: variations of the ratios Q/D with the plate spacing for $p_s = -0.1\,Pa$ and for $p_s = -1\,Pa$ (Q_a and Q_b are the asymptotic analytical solutions, Q_{2w}, Q_{en} are given by Eqs. 4.13 and 4.14, respectively). The cross symbols are for the analytical solutions given by Eq. 4.37 [26] and Eq. 4.38 [110].

can be seen, the agreement between the numerical solution (maximum of Q_{2w}/D) and analytical solution (intersection of Q_a/D and Q_b/D) for D_{opt} is better than for natural convection. On the other hand, the optimal plate-spacing calculated using Eq. 4.37 [26] does not agree neither with our computations nor with Eq. 4.35.

Table 4.5 shows comparisons between the analytical (Eq. 4.35) and numerical values of D_{opt} as a function of p_s: the agreement is satisfactory. The analytical solution (Eq. 4.36) slightly overestimates the peak in Q_{2w}/D_{opt} as shown from comparisons between the last two lines of Table 4.5. Therefore, that can be assumed as a rather good approximation of the maximum of Q_{2w}/D (within 20%) for the range of p_s considered in the present study ($0.1\,Pa \leq |p_s| \leq 1\,Pa$).

In Figs. 4.8a and 8b, the effect of axial conduction is exhibited through the discrepancy between Q_{2w}/D and Q_{2n}/D. It is clearly shown that the effect of axial conduction decreases either as $|p_s|$ or as D are increased. It may be also noted that the differences between Q_{2w}/D and Q_{en}/D are less than for natural convection, except for small spacing (D less than $\approx 2\ mm$) at which the flow rate is strongly reduced, whatever p_s in the range considered. Therefore, we plotted only the variations of Q_{2w}/D as function of D for various p_s in Fig. 4.9. As expected, this figure shows that the heat flux increases sharply
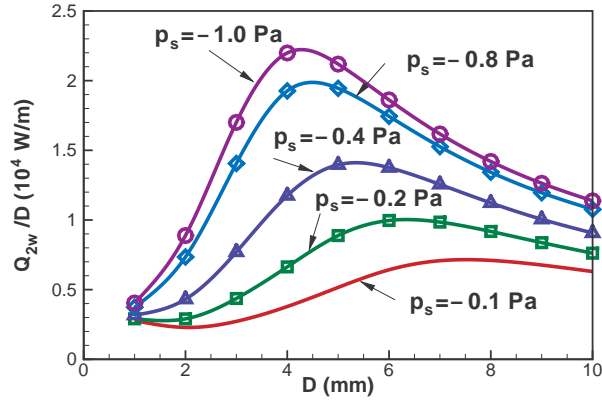
Figure 4.9 – Forced convection: variations of the ratio Q_{2w}/D versus the plate spacing for various p_s.

when decreasing p_s while D_{opt} decreases. The variations of the mean flow velocity versus D for various p_s reported in Fig. 4.10 explain the increase in heat flux and decrease in
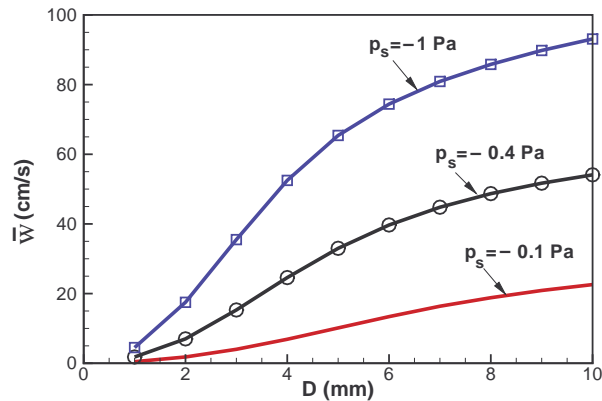
Figure 4.10 – Forced convection: variations of the mean flow velocity versus the plate spacing for various p_s.

axial conduction which may be considered negligible when $Pe_D > 100$, or $D \geq 9\ mm$, $\geq 5.5\ mm$ and $\geq 4\ mm$ for $p_s = -0.1\ Pa$, $-0.4\ Pa$ and $-1\ Pa$, respectively.

Mereu et al. [110] investigated the optimal geometry of packages with fixed pumping

power, i.e. when the flow is created by a fan or a pump. By denoting $\mathcal{W}_m = G_v|p_s|$ the pumping power for one channel ($G_v = \overline{w}(D_{opt}L)$ being the volumetric flow rate), the relations given in [110] for D_{opt} and Q_{max} can be rewritten as follows for negligible plate thickness ($e << D$):

$$D_{opt} \cong \mathbf{C}\mathcal{W}_m^{-1/5} \quad \text{and} \quad Q_{max}/D_{opt} \le \mathbf{C}\mathbf{C}'^{-1/3}\mathcal{W}_m^{2/5} \tag{4.38}$$

where $\mathbf{C} = 2.26^{6/5}Pr^{-60/135}(\mu H)^{3/5}/\rho^{2/5}$ and $\mathbf{C}' = 0.65k_0\Delta T Pr^{17/27}\rho^{2/3}/\mu$.

Using the set of physical data fixed in the present study, we obtain $\mathbf{C} = 1.05 \ 10^{-3}$ and $\mathbf{C}\mathbf{C}'^{-1/3} = 3.24 \ 10^5$. Therefore, comparisons between our predictions and those based on Eq. 4.38 can be made. To this end, the results reported in Table 4.6 were correlated as

p_s (Pa)	-0.1	-0.2	-0.4	-0.8	-1.0
D_{opt} (mm)	7.57	6.38	5.38	4.52	4.29
Q_{2w}/D_{opt} (W/m)	$0.70 \ 10^4$	$0.99 \ 10^4$	$1.39 \ 10^4$	$1.97 \ 10^4$	$2.21 \ 10^4$
$G_v = [\overline{w}(DL)]_{opt}$ (m^3/s)	$1.35 \ 10^{-3}$	$1.61 \ 10^{-3}$	$1.92 \ 10^{-3}$	$2.28 \ 10^{-3}$	$2.43 \ 10^{-3}$
$\mathcal{W}_m$ (W)	$1.35 \ 10^{-4}$	$3.22 \ 10^{-4}$	$7.69 \ 10^{-4}$	$1.83 \ 10^{-3}$	$2.43 \ 10^{-3}$

Table 4.6 – Forced convection: optimal plate-spacing, maximum heat flux, volumetric flow rate and pumping power for various pressure drops at the outlet section.

$D_{opt} = \alpha \mathcal{W}_m^{n_1}$ and $Q_{2w}/D_{opt} = \beta \mathcal{W}_m^{n_2}$. We found for D_{opt}: $\alpha = 1.31 \ 10^{-3}$, $n_1 = -0.197$, and for Q_{2w}/D_{opt}: $\beta = 2.35 \ 10^5$, $n_2 = 0.394$. The exponents are thus in excellent agreement with those in Eq. 4.38 while the discrepancies on both coefficients are quite large but of same order of magnitude. In conclusion, the overall discrepancies between our results and those based on Eq. 4.38 can be estimated to be about 20%. The values corresponding to the theoretical solution (Eq. 4.38) are reported in Fig. 4.8a and 4.8b for $p_s = -0.1 \ Pa$ and $p_s = -1 \ Pa$, respectively. In comparison with the numerical solution, D_{opt} is underestimated while Q_{2w}/D_{opt} is overestimated.

4.4.3 Mixed convection

Since comparisons between the results obtained for mixed convection with $|p_s| < 0.1 \ Pa$ does not differ significantly from those for natural convection (Fig. 4.5), and since the results for forced convection with $|p_s| > 1 \ Pa$ show that natural convection has a weak effect, we consider now the domain $|p_s| \in [0.1 \ Pa, 1 \ Pa]$ in which natural and forced convection have comparable strengths.

It should be emphasized that the pressure boundary conditions used in the present study lead automatically to an increase of the mass flow rate when considering mixed convection instead of natural or forced convection. According to the usual terminology, we are thus considering "aiding-buoyancy" flows only, for which any recirculating flow may appear in the channel entrance region owing to the pressure boundary conditions applied. As it is well established, reverse flows never occur for identical temperature of the channel

walls.

Variations of Q_{2w}/D as function of D for $p_s = -0.2\ Pa$ and $p_s = -1\ Pa$ are shown in Figs. 4.11a and 4.11b. These figures indicate that :

(a) $p_s = -0.2\ Pa$ (b) $p_s = -1\ Pa$
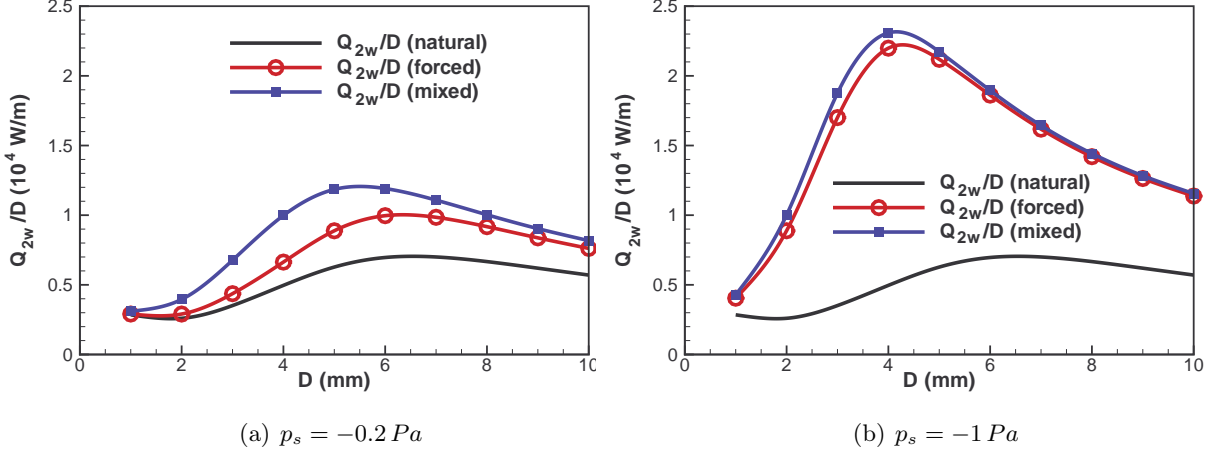
Figure 4.11 – Mixed convection : variations of the ratio Q_{2w}/D versus the plate spacing for forced and mixed convection.

- first, the effect of natural convection is significant for $p_s = -0.2\ Pa$ since the differences between $Q_{2w,mixed}/D$ and $Q_{2w,forced}/D$ are large. On the other hand, this difference is rather small for $p_s = -1\ Pa$. Therefore, it is not relevant to perform computations for $p_s < -1\ Pa$ in the configuration studied.
- second, as expected D_{opt} is the smallest for mixed convection. However, the difference between the values for forced and mixed convection decreases as $|p_s|$ is increased as can be seen by comparing Tables 4.5 and 4.7.

$p_s\ (Pa)$	-0.1	-0.2	-0.4	-0.8	-1.0
D_{opt}	5.95	5.52	4.95	4.33	4.14
Q_{2w}/D_{opt}	$0.98\ 10^4$	$1.21\ 10^4$	$1.56\ 10^4$	$2.10\ 10^4$	$2.32\ 10^4$

Table 4.7 – Mixed convection: effect of p_s on $D_{opt}\ (mm)$ and $Q_{2w}/D_{opt}\ (W/m)$.

A single correlation for natural, mixed and forced convection domains was developed by Bello-Ochende and Bejan [26]. Its range of application is $10^{-3} \leq Pr \leq 10^2$, $10^5 \leq Ra_H \leq 10^7$ and $10^5 \leq Be \leq 10^7$. It can be written as

$$D_{opt} = 1.76\ 10^{-4}A(Pr)C(\eta_b)H\ Be^{-1/4} \quad Q_{max}/D_{opt} = 0.0011B(Pr)E(\eta_b)\left(\frac{k_0\Delta T}{H}\right)Be^{1/2}$$
$$(4.39)$$

where $A(Pr)$ and $B(Pr)$ are as in Eq. 4.32 and $\eta_b = (Ra_H/Be)^{1/4}$. $C(\eta_b)$ and $E(\eta_b)$ are given by

$$C(\eta_b) = [17.69^{-2.08} + (28.27/\eta_b)^{-2.08}]^{-1/2.08} \quad E(\eta_b) = [511^{0.9} + (110.5\eta_b^2)^{0.9}]^{1/0.9} \quad (4.40)$$

For the set of physical data fixed in the present study, we obtain $A(Pr) = 307.2$, $B(Pr) = 8.875$, $\eta_b = 44.03\ Be^{-1/4}$ and $Be \approx 2.45\ 10^7\Delta p$ (Δp in Pa). From our computations,

$\Delta p = -\frac{1}{2}\rho_0 \overline{w}_0^2 - p_s$ varies between 6.8 10^{-2} Pa and 7.96 10^{-1} Pa for D_{opt} when 0.1 $Pa \leq |p_s| \leq 1$ Pa. We conclude that 1.67 $10^6 \leq Be \leq 1.95$ 10^7 and, $0.663 \leq \eta_b \leq 1.226$ in that range of p_s. Therefore, forced convection and natural convection are of same order of magnitude in our domain of computations. Unfortunately, application of Eq. 4.39 leads to completely different results from those reported in Table 4.7.

From Eq. 4.37 and Eq. 4.39 it is readily found that

$$D_{opt,mixed}/D_{opt,forced} = 0.0154 C(\eta_b) \qquad \text{with} \quad C(\eta_b) < 17.69 \tag{4.41}$$

If natural and forced convection strengths are of same order ($\eta_b = 1$), Eq. 4.41 indicates that $D_{opt,mixed} \approx 0.27 D_{opt,forced}$. Such a prediction does not agree with our results. For example, the present computations carried out for $p_s = -0.1$ Pa leads to $\eta_b = 1.226$. The correlation given by Eq. 4.40 yields $C(\eta_b) = 14.2$ and, $D_{opt,mixed} \approx 0.22 D_{opt,forced}$ while we found (see Tables 4.5 and 4.7) $D_{opt,forced} = 7.57$ mm and $D_{opt,mixed} = 5.95$ mm, i.e. $D_{opt,mixed} = 0.79 D_{opt,forced}$.

Figure 4.12a presents the D_{opt}-variations versus $|p_s|$, included is the natural convection

(a) D_{opt} (mm) (b) Q_{2w}/D_{opt} (W/m)
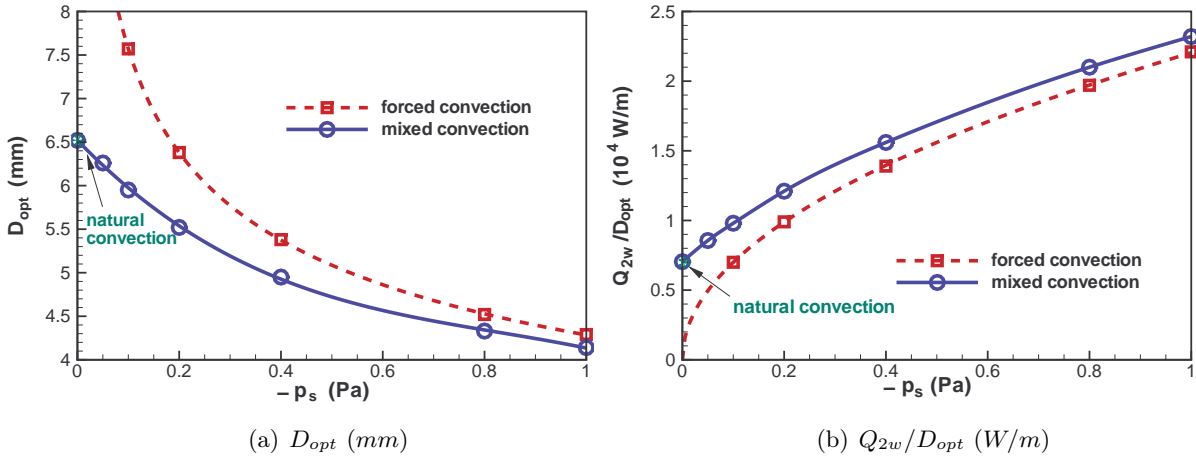
Figure 4.12 – Mixed convection : variations of D_{opt} and Q_{2w}/D_{opt} versus p_s for forced and mixed convection.

result corresponding to $p_s = 0$. Figure 4.12a shows that D_{opt} decreases when $|p_s|$ increases while Figure 4.12b shows that Q_{2w}/D_{opt} increases with $|p_s|$, the effect of buoyancy force being rather small for $p_s = -0.1$ Pa. Therefore, the last question to be considered is to look for a true optimal spacing by taking into account not only the increase of thermal efficiency but also the importance of mechanical load. To this end, it is convenient to make a distinction between thermal and overall efficiencies.

Efficiency

- *Thermal efficiency*

The design problem considered is a volume of width W cooled with a stack of n parallel, isothermal boards of thickness e, much smaller than the spacing D (Fig. 4.1). The total heat flux Q_T removed from the entire stack of heated surfaces having a total heat transfer

area $S_T = 2n(H \times L)$ is :

$$Q_T = nQ_{2w} = \left(\frac{W - e}{D + e}\right) Q_{2w} \qquad (W/m^2) \qquad (4.42)$$

The optimal spacing corresponds to the maximum of Q_T (or of $(W/D)Q_{2w}$ if the thickness of the plates is such as $e << D$).

• *Overall efficiency*
For forced or mixed convection, the pumping power required to create a flow or to increase the pure natural velocity can be deduced from a kinetic energy balance based on the conservation of mechanical energy.

The kinetic energy balance is obtained by multiplying the momentum equation by the velocity and then by integrating over the whole fluid domain. By taking into account the boundary conditions for pressure and velocity components used in the present work, the kinetic energy balance reduces to:

$$\underbrace{|p_s|G_v}_{(a)} = \underbrace{\int_{-D/2}^{D/2} \rho_0 \frac{w^3(x, H)}{2}\, dx}_{(b)} + \underbrace{\int_0^H \int_{-D/2}^{D/2} \frac{1}{2}\overline{\overline{\tau}} : \overline{\overline{d}}\, dx dz}_{(c)}$$

$$- \underbrace{\int_0^H \int_{-D/2}^{D/2} \rho_0 g\beta(T(x, z) - T_0)w(x, z)\, dx dz}_{(d)} \quad (4.43)$$

where $G_v = \overline{w}(DL)$ is the volumetric flow rate, $\overline{\overline{\tau}} = 2\mu\overline{\overline{d}}$ is the viscous stress tensor and $\overline{\overline{d}}$ the deformation velocity tensor. The term (a) in Eq. (4.43) represents the mechanical power supplied by a device to the fluid. In the case of fins, this device could be a fan, for example. In the natural convection framework, (a) is zero and it becomes positive in mixed convection. This power is balanced by two dissipation terms and one production term. Contribution (b) represents the kinetic power lost by the fluid at the outlet section and (c) denotes the power irreversibly lost by viscous friction. Note that (c) is negligibly small in the energy equation, and has been neglected, whereas it must introduced in order to properly balance the kinetic energy equation. The last contribution (d) corresponds to the production term of energy which must be accounted for in natural or mixed convection, when its contribution is significant. From a numerical point of view, the balance of kinetic energy (Eq. 4.43) is satisfied within less than 1% for the meshes used in the present study.

Therefore, the pumping power $\mathcal{W}_m$ for the entire stack of n boards can be written as $\mathcal{W}_m = n|p_s|G_v = n|p_s|\overline{w}(DL)$. For a given value of p_s, the effect of natural convection is to increase the inlet velocity corresponding to forced convection (a result which cannot be found by prescribing a pressure difference or an inlet velocity, as it has been assumed in most of the studies on mixed convection). Consequently, the pumping power is necessarily higher for mixed convection than for forced convection since $\overline{w}$ increases. However, the total heat flux Q_T is also increased. Table 4.8 allows comparisons between the increases in heat fluxes and in pumping powers for various pressure drops in the case $D = 5\ mm$. As can be seen, the increase in heat flux is more than four orders in magnitude larger than the increase in $\mathcal{W}_m$. The overall efficiency of a vertical stack of isothermal plates (mixed convection) is thus automatically better than that for an horizontal stack (forced

p_s (Pa)	-0.1	-0.2	-0.4	-0.6	-0.8	-1.0
$Q_{2w,mixed} - Q_{2w,forced}$ (W)	20.920	14.848	8.041	5.064	3.570	2.719
$|p_s|DL(\overline{w}_{mixed} - \overline{w}_{forced})$ (10^{-4} W)	0.483	0.778	1.116	1.308	1.439	1.540

Table 4.8 – Comparison between the increases in heat flux and in pumping power versus the pressure drop ($D = 5\ mm$, $L = 1\ m$)

convection) provided that buoyancy assisted flows are considered.

When considering mixed convection, it can be expected that the increase in mechanical power expense is compensated by a significant increase in heat transfer rate in comparison with natural convection. The efficiency of the system may be thus evaluated as

$$\eta(p_s) = \frac{(n_{opt}Q_{2w})_{mixed} - (n_{opt}Q_{2w})_{natural}}{|p_s|L((nD)_{opt}\overline{w})_{mixed}} \tag{4.44}$$

where n_{opt}, function of p_s and H, is the number of channels for a stack of width W working in optimal conditions (n_{opt} is the integer lying in the interval $[(W-e)/(D_{opt}+e)\pm0.5]$).

Let us consider a practical application by assuming that $W = 100\ mm$ and $e = 1\ mm$ (air as the working fluid, $\Delta T = 40\ K$, channel height $H = 0.1\ m$, unit spanwise depth $L = 1\ m$). For natural convection, it has been found that $D_{opt} = 6.52\ mm$ and $Q_{2w} = 46\ W$: therefore, $(n_{opt}Q_{2w})_{natural} \approx 600\ W$. For mixed convection, the values of D_{opt} are reported in Table 4.7. Since D_{opt} decreases as $|p_s|$ increases, n_{opt} is maximum for $|p_s| = 1\ Pa$. When $|p_s| > 1\ Pa$, n_{opt} should increase as $\Delta p_s^{1/4}$ according to Eq. 4.35 owing to the negligible effect of natural convection. The augmentation with the pressure drop both in n_{opt} and in the heat flux transferred along each of the channel result in large increases in the overall heat flux, Q_T. However, the pumping power augments more quickly than Q_T. As a result, the efficiency as defined in Eq. 4.44 decreases. $\eta(p_s)$ is plotted in Fig. 4.13 versus p_s by
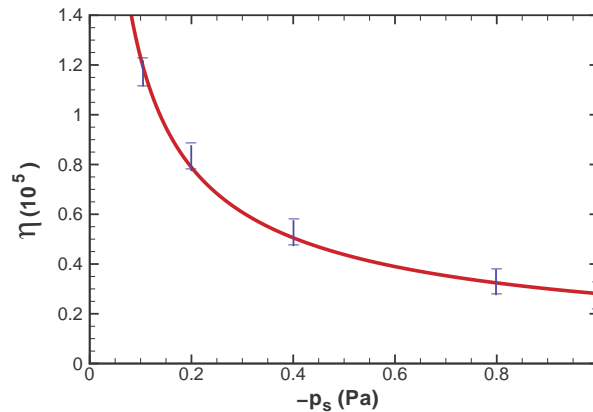
Figure 4.13 – Variations of overall efficiency η versus p_s for mixed convection.

taking into account the various approximations introduced in its definition. The high value of $\eta(p_s)$ (of the order of 10^5) exhibits a decrease as $\approx p_s^{-2/3}$ for the largest values of $|p_s|$, in rather good agreement with what could be easily found by using the analysis by Bejan

and Scubbia [25].

Chapter 5

On the modeling of aiding mixed convection in vertical channels [149]

Nomenclature

a	thermal diffusivity $[m^2\ s^{-1}]$
A	aspect ratio, $A = H/D$
c_p	specific heat $[J\ K^{-1}\ kg^{-1}]$
c_x, c_z	stretching parameters, Eq. 5.13
D	plate spacing [m]
D_h	hydraulic diameter, $D_h = 2D$ [m]
g	gravitational acceleration $[m\ s^{-2}]$
Gr_H	Grashof number based on H, $Gr_H = g\beta_0 \Delta T H^3/\nu_0^2$
h	heat transfer coefficient $[W\ m^{-2}K^{-1}]$
H	channel height $[m]$
k	thermal conductivity $[W\ m^{-1}\ K^{-1}]$
L	channel length in the spanwise direction $[m]$
$\dot{m}$	mass flow rate $[kg\ s^{-1}]$
n_x, n_z	numbers of grid points in $x-$ and $z-$directions
p	pressure $[Pa]$
p_s	pressure at the outlet section $[Pa]$
Pr	Prandtl number, $Pr = \nu_0/a_0$
Q	heat flux, $[W]$
Q_{en}	enthalpy heat flux, $[W]$
Q_{2w}	convective heat flux along the two channel walls, $[W]$
Re	Reynolds number based on D_h, $Re = w_0 D_h/\nu_0$
Ri	Richardson number, $Ri = Gr/Re^2$
S_c	area of the channel cross section, $S_c = DL\ [m^2]$
t	time $[s]$
T	temperature $[K]$
u, w	velocity components $[m\ s^{-1}]$
x, z	coordinates $[m]$
Greeks	
β	coefficient of thermal expansion, $\beta = 1/T_0\ [K^{-1}]$
ΔT	temperature difference, $\Delta T = (T_h - T_0)\ [K]$
μ	dynamic viscosity $[Pa.s]$
ν	kinematic viscosity $[m^2\ s^{-1}]$

ρ	density [$kg\ m^{-3}$]
θ	dimensionless temperature ratio, $\theta = (T - T_0)/\Delta T$
τ	dimensionless time

Subscripts

$a,\ b$	analytical solutions
h	hot wall
H	quantity based on channel height
nc	natural convection
0	inlet section

Superscripts

$-$	averaged quantity
$*$	dimensionless quantity

5.1 Introduction

Mixed convection may be defined as heat transfer situations where both pressure and buoyancy forces interact. In vertical channels, the bulk fluid flow can be either upward or downward, and the solutal and thermal buoyancy forces may be either assisting or opposing the forced flow. As a result, several hundred of papers were published just for mixed convection flows in vertical ducts of various shapes and thermal conditions, including two phase flows with surface condensation or evaporation, and flows in porous filled ducts. Most studies considered buoyancy assisted flow, i.e. upward flows with heating or downward flows with cooling. Under these conditions, the axial velocities may increase near the channel walls and decrease within the core region, with possible occurrence of a flow recirculation in the entry region for large effects of the buoyancy force [56, 74, 81, 92] (not to be confused with flow reversal occurring close to the outlet section in asymmetrically heated channels [11, 12, 44, 63, 64, 166]). In these cases, it is generally expected that heat transfer for mixed convection is larger than for forced convection. This intuition is obviously well physically based. However, numerical solutions may lead to opposite effects, not owing to the numerical accuracy but because the boundary conditions are not well specified. This paper is focused on this issue.

The extensive interest borne upon mixed convection in ducts stems from its wide range of practical applications including the design of compact heat exchangers, cooling of electronic equipment and, solar energy collectors. Numerous theoretical and experimental investigations were reviewed in many textbooks, such as in Aung [9], Gebhart et al. [65] or Bejan [22]. The present study is focused on mixed convection of air as the working fluid for typical geometries used for active cooling from the back of vertical photovoltaic cell panels operating at high fluxes.

This work considers the effect of thermal buoyancy force only (the effect of solutal force being similar, provided it acts in the same direction as the thermal force), and in the case of upward forced or natural flow direction (symmetrically heated vertical channel), commonly termed as buoyancy aiding or assisting mixed convective flows.

Most of the analytical and numerical studies on mixed convection were based on approximate problem formulations in order to easily solve the governing equations thanks to parabolized forms (or boundary-layer type equations for external flows with the streamwise pressure gradient dropped out [42]) which allow not to prescribe boundary conditions at

the outlet duct section. On the other hand, the increasingly use of commercial computational fluid dynamics packages during the last decade has led to solve the problem when it is based on fully elliptic formulation, mostly by considering again prescribed inlet flow rate and outlet free boundary conditions. However, despite the large number of papers available in the current literature, the fundamental question of inlet/outlet flow conditions seems not to have been properly addressed because it appears that mixed convection with fixed inlet velocity (and thus Reynolds number) was very often considered as the relevant formulation for solving mixed convection.

The aim of this paper is at showing that the use of prescribed inlet velocity condition (constant flow rate whatever the importance of the buoyancy force) leads to completely different solutions in comparison with those obtained using prescribed total pressure inlet and pressure outlet conditions. For our viewpoint, such pressure boundary conditions appear to provide more realistic physical behaviors in practical applications, as it will be shown in what follows.

We are considering the practical case of air flowing in vertical flat-plate channels submitted to uniform wall temperatures, and maximum temperature differences compatible with the Boussinesq approximation. Although most of the results are presented in dimensional form, we also analyze the relevance of scaling predictions based on dimensionless parameters. It should be added that the extension of the present work to weakly compressible formulation (i.e. large temperature differences) is straightforward when using our in-house computational code, but the results obtained have shown that the main conclusions drawn in this paper remain unchanged.

5.2   Governing equations

We consider two-dimensional, incompressible and laminar buoyancy-assisting flows inside a vertical parallel-plate channel, as shown in Fig. 5.1. The fluid enters the channel
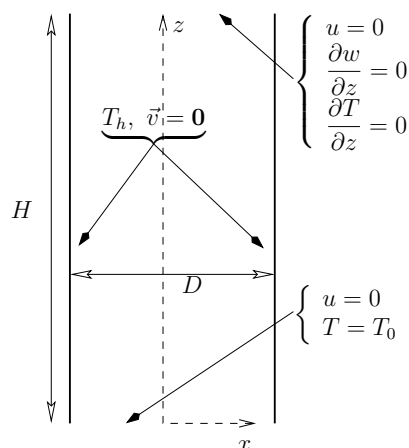
Figure 5.1 – The physical model of mixed convection in a vertical channel. The full boundary conditions are written in Eqs. (5.5-5.7) for the three cases investigated.

of height H at ambient temperature and traverses upward, being heated by the hot walls at uniform temperature T_h. The fully developed region may be eventually reached at the outlet ($z = H$), after a development length depending on the value of the plate spac-

ing as well as on importances of the pressure and buoyancy forces. On account of the maximum temperature difference invoked, it is assumed that all physical properties are constant except for the density in the buoyancy force in the vertical direction (Boussinesq approximation). The reference temperature has been taken to be the inlet temperature, T_0, like in most of the solutions reported in the current literature. However, this choice remains an open question, as discussed by Barletta et Zanchini [19], especially for fully developed mixed-convection. Owing to the stability results by Chen et Chung [43], the governing equations are written in transient form in order to capture possible transitions to unsteady flows. With the z-axis pointing upwards and the origin of coordinates placed at the center of the inlet section, the conservation equations based on a fully elliptic model are

$$\nabla.\vec{v} = 0 \tag{5.1}$$

$$\rho_0(\frac{\partial \vec{v}}{\partial t} + \nabla.(\vec{v} \otimes \vec{v})) = -\nabla(p + \rho_0 gz) + \mu_0 \nabla^2 \vec{v} + \rho_0 g\beta(T - T_0)\vec{e}_z \tag{5.2}$$

$$\frac{\partial T}{\partial t} + \nabla.(\vec{v}T) = a_0 \nabla^2 T \tag{5.3}$$

where ρ_0, μ_0 and a_0 are the fluid density, dynamic viscosity and thermal diffusivity evaluated at T_0.

Boundary and initial conditions
The initial condition is a fluid at rest at uniform temperature T_0.
The boundary conditions are written as follows:
   • Along the vertical isothermal walls:

$$\vec{v} = 0, \ T = T_h \text{ at } x = \pm D/2 \text{ and for } 0 < z < H \tag{5.4}$$

   where D and H are the channel width and height, respectively.
   • At the inlet ($z = 0$) and outlet ($z = H$) sections for $-D/2 < x < D/2$:
   (a) natural convection

$$u = 0, \ \frac{\partial w}{\partial z} = 0, \ p = -\rho_0\frac{w^2}{2}, \ T = T_0 \text{ at } z = 0$$
$$u = 0, \ \frac{\partial w}{\partial z} = 0, \ p + \rho_0 gH = 0, \ \frac{\partial T}{\partial z} = 0 \text{ at } z = H \tag{5.5}$$

   (b) forced or mixed convection
      b1 : fixed flow rate (w_0 prescribed)

$$u = 0, \ w = w_0, \ T = T_0 \text{ at } z = 0$$
$$u = 0, \ \frac{\partial w}{\partial z} = 0, \ p + \rho_0 gH = 0, \ \frac{\partial T}{\partial z} = 0 \text{ at } z = H \tag{5.6}$$

   b2 : fixed inlet total pressure and outlet pressure (p_s)

$$u = 0, \ \frac{\partial w}{\partial z} = 0, \ p = -\rho_0\frac{w^2}{2}, \ T = T_0 \text{ at } z = 0$$
$$u = 0, \ \frac{\partial w}{\partial z} = 0, \ p + \rho_0 gH = p_s, \ \frac{\partial T}{\partial z} = 0 \text{ at } z = H \tag{5.7}$$

With boundary conditions Eq. 5.7 applied to forced or mixed convection, a pressure drop ($p_s < 0$) is prescribed at the outlet section (it could be as well an increase in pressure at the inlet section). Therefore, the boundary conditions are inlet temperature and outlet

pressure, zero z-derivative for the vertical velocity component and zero horizontal velocity-component. It should be emphasized that these flow B.C. differ somehow from those used in most of previous works.

Let us emphasize that our results achieved using Eq. 5.6 or Eq. 5.7 are almost identical, provided the average velocities $\overline{w}(0)$ are the same. The choice of the particular boundary condition Eq. 5.6 may lead to wrong physical interpretations, because the imposed velocity w_0 is completely uncorrelated to the velocity induced by the natural convection flow. In contrast, the use of Eq. 5.7 preserves the coherence of the fluid flow with respect to free convection (Eq. 5.5) as it will be shown in what follows.

The governing equations are generally cast in dimensionless form by using either the set of dimensionless variables $X = x/D_h$, $Z = z/D_h$, $\theta = (T - T_0)/(T_h - T_0)$, $U = u/w_0$, $W = w/w_0$ and $P = p/\rho_0 w_0^2$ or the set X, $Z = z/(D_h Re)$, θ, $U = D_h u/(\nu_0)$, W and P where $D_h = 2D$ is the hydraulic diameter. It follows that the problem formulation depends on four parameters: $A = H/D$, $Re = w_0 D_h/\nu_0$, $Gr = g\beta(T_h - T_0)D_h^3/\nu_0^2 = 8Gr_H/A^3$ and $Pr = \nu_0/a_0$, the channel aspect ratio, the Reynolds, Grashof and Prandtl numbers, respectively. The relative strength of the buoyancy force is then characterized either by the Richardson number, $Ri = Gr/Re^2$, for the first set of dimensionless variables or by the product $Ri \times Re = Gr/Re$ for the second set. Some controversy still exist about the best pertinent parameter, e.g. Ri or $Ri \times Re$.

Heat transfer

The total heat transfer rate released by two walls of depth L and height H, denoted as Q_{2w}, is calculated as follows:

$$Q_{2w} = 2Lk_0 \int_0^H \left.\frac{\partial T}{\partial x}\right|_{x=D/2} dz = 2\overline{h}(LH)(T_h - T_0) \quad (W) \tag{5.8}$$

where L is the length of the channel in the y-direction, $\overline{h}$ is the mean heat transfer coefficient defined by the right equality in Eq. 5.8. For natural or mixed convection, a mean Nusselt number expressed by $\overline{Nu}_{2w} = Q_{2w}/[2(LH)(k_0\Delta T/D)]$ may be introduced [18].

The enthalpy flux removed from the two heated surfaces by the stream is

$$Q_{en} = \rho_0 c_p S_c[(\overline{wT})_H - (\overline{wT})_0] \qquad (W) \tag{5.9}$$

where $(\overline{wT})_z$ is the average of (wT) over the channel cross-section of area $S_c = DL$. By using again $2(LH)(k_0\Delta T/D)$ as a reference heat flux, we can define a Nusselt number $\overline{Nu}_{en} = Q_{en}/[2(LH)(k_0\Delta T/D)]$.

It should be emphasized that Q_{2w} is always greater than Q_{en} because the heat losses by axial diffusion through the channel inlet are not included into the definition of Q_{en}. When the wall temperatures are kept fixed, Q_{2w} and Q_{en} merge provided that the Reynolds number is large enough in order that axial diffusion may be assumed negligibly small. The difference $Q_{cond} = Q_{2w} - Q_{en}$ yields the effect of axial diffusion which can be written as

$$\begin{aligned} Q_{cond} &= k_0 \int_{-D/2}^{D/2} \left.\frac{\partial T}{\partial z}\right|_{z=0} dx \\ &= 2k_0 \int_0^H \left.\frac{\partial T}{\partial x}\right|_{x=D/2} dz - \rho_0 c_p \int_{-D/2}^{D/2} [w(x,H)T(x,H) - w(x,0)T_0]dx \end{aligned} \tag{5.10}$$

For negligible axial heat diffusion, equation (5.8) reads:

$$2k_0 L \int_0^H \frac{\partial T}{\partial x}\bigg|_{x=D/2} dz = 2\overline{h}(HL)(T_h - T_0) = \dot{m}c_p(T_b(H) - T_0) \qquad (5.11)$$

where $\dot{m} = \rho_0 \overline{w}_0 (DL)$ and $T_b(H) = (\overline{wT})_H / \overline{w}_0$ is the bulk temperature at the outlet section. Such an approximation is one of the foundations introduced for establishing the analytical solutions reported in Ref. [18, 22, 25].

5.3   Numerical method and validation

The mass, momentum and energy conservation equations were spatially discretized by using the collocated finite volume method presented in [47, 155], applied here for structured meshes. The key features of this method are:
  – the normal fluxes to cell faces are defined by a consistent two-points approximation,
  – the variables transported by the fluid flow are expressed on cell faces in a centered manner, not by using a linear interpolation at the faces,
  – the "pressure gradient" is defined by the dual expression of the velocity divergence and therefore, it can be non-consistent with a gradient.
An implicit second-order Euler scheme was adopted for time derivatives at time $t = (n + 1)\Delta t$, with an implicit treatment of the diffusion terms and an Adams-Bashforth extrapolation procedure for the transport terms. A stabilization method is necessary to prevent from the onset of checkerboard oscillations associated with collocated schemes. This is performed through the velocity-pressure decoupling which is handled by a projection method [68].

Attention was also paid to the temperature discontinuities at the corner of the inlet section (i.e. at $x = \pm D/2$, $z = 0$). In the case of pure conduction, the analytical heat fluxes along the vertical walls are indeed infinite. Therefore, the wall heat fluxes calculated numerically, Q_{2w}, cannot converge when refining the meshes (see [150] for details). To avoid this problem, it is then necessary to smooth the thermal boundary conditions in order to recover some regularity. To this end, we have substituted the uniform temperature imposed at the walls by a temperature distribution which decreases abruptly towards T_0 close to $z = 0$. The steep function retained in this work writes:

$$T_p(z) = T_0 + (T_h - T_0)\tanh(\Gamma \frac{z}{H}) \qquad (5.12)$$

For example, by choosing $\Gamma = 1000$, the wall temperature $T_p(z)$ for a channel height $H = 1\,m$ varies from $0.5T_h$ at $z \simeq 0.55\,mm$ to $0.9T_h$ at $z \simeq 1.5\,mm$ and then becomes larger than $0.99T_h$ for $z > 2.65\,mm$. We checked that such a steep variation in $T_p(z)$ does change significantly the temperature field while it allow second order convergence of the wall heat fluxes, Q_{2w}.

The velocity components, the temperature field and the pressure correction were calculated by using the Bi-Conjugate Gradient Stabilized (BCGS) method, preconditioned by an incomplete LU decomposition. Owing to the axial symmetry of the flow, the problem was solved on the half-width of the channel. The faces of the mesh x_i^f and z_k^f are defined

as follows:

$$\frac{x_i^f}{D/2} = \frac{i}{n_x} - \frac{c_x}{2\pi} \sin\left(\frac{i}{n_x}\pi\right), \quad 0 \le i \le n_x$$

$$\frac{z_k^f}{H} = \frac{\tanh\left(c_z\left(\frac{k}{n_z}-1\right)\right)}{\tanh(c_z)} + 1, \quad 0 \le k \le n_z \tag{5.13}$$

The coefficients c_x and c_z define the mesh refinements in the entrance region and along the isothermal wall. By choosing $c_x = 1$ and $c_z = 1.82$, the size ratios between the largest cell and the smallest cell are equal to 3 and 10 in horizontal and vertical directions, respectively. The time integration was performed with the Courant-Friedrich-Levy number kept fixed to $CFL = 0.5$.

The asymptotic behavior of the numerical solution was investigated using a Richardson extrapolation on one set of the three meshes defined by $n_x \in \{10, 20, 40\}$ with $n_z = 20n_x$. This method leads to the extrapolated value of f which is written

$$f_{\text{Extrap.}} = f_{n_x} + \frac{c_{n_x}}{(n_x)^s} \tag{5.14}$$

where c_{n_x} is a coefficient depending on n_x and f_{n_x} is the numerical result on grid $n_x \times n_z$. For sufficiently fine meshes, the value of s must tend towards the order of consistency of the numerical scheme (i.e. $s = 2$), $f_{\text{Extrap.}}$ must then become independent of the mesh. For natural convection flow, the mesh 20×400 defined for a half width of the channel provides accurate results within 3 digits (Tab. 5.1). This grid size is then retained for all computations.

n_x	10	20	40	s	$f_{\text{Extrap.}}$
Q_{2w} (W)	130.39	130.31	130.30	2.66	130.30
Q_{en} (W)	130.32	130.22	130.20	2.01	130.19
$\overline{w}_{nc}(m/s)$	0.3840	0.3833	0.3831	2.01	0.3830

Table 5.1 – Convective heat flux, enthalpy heat flux and mean velocity according to the mesh refinement ($n_z = 20n_x$), for $D/2 = 1\ cm$ and $H = 1\ m$. Order s of the numerical scheme and Richardson-extrapolated values (see Eq. 5.14).

5.4   Results

The influence of the dynamical boundary conditions at the inlet and outlet sections is discussed by considering air entering at $T_0 = 300\ K$ into a vertical channel with height walls $H = 1\ m$ at uniform hot temperature $T_h = 320\ K$ (or $H = 1.5\ m$, just for allowing comparisons with previously published works [56, 74]). The channel width was $D = 2\ cm$ or $D = 3\ cm$. With the air properties taken at $T_0 = 300\ K$ ($\rho_0 = 1.176\ kg.m^{-3}$, $\mu_0 = 1.85\ 10^{-5}Pa.s$, $c_{p,0} = 1006\ J.kg^{-1}.K^{-1}$, $k_0 = 0.0261\ W.m^{-1}.K^{-1}$) the Grashof number is then $Gr_H = 2.64\ 10^9 H^3$. Channel heights less than about two meters are thus considered as maximum in order to keep a laminar flow.

For pure natural convection (Tab. 5.1), the computations yield an average velocity $\overline{w}_{cn} = 0.38\ m/s$ and a pressure drop at the inlet section (Eq. 5.5) $\overline{p}_{cn,in} = -0.087\ Pa$. The heat flux transferred along one of the isothermal walls is $Q_{1w} = Q_{2w}/2 = 65.2\ W$ by unit of depth length (direction perpendicular to the plane of Fig. 1). These values are the basis

for the discussions of mixed convection results presented in what follows.

Before getting further into the result section, let us recall that flow solutions are similar provided that the average velocities, imposed or resulting from computation, are identical. However, when a constant flow rate is prescribed, counterintuitive results or surprising phenomena may arise. Such situations, developed in details in Sec.5.4.1, are now briefly exemplified. By using Eq. 5.6, astonishing flow recirculations are highlighted close to inlet section. Their occurrences are simply due to the incompatibility between the imposed flow rate and the necessity of feeding the dynamic boundary layers produced by the buoyancy along the vertical heated walls. Similarly from a purely thermal viewpoint, it is also expected that the buoyant force increases the velocities in the boundary layers and then improves the heat transfer at the solid walls. However this behavior is not observed when the inlet velocity is prescribed.

The next two subsections are then devoted to the detailed analysis of the fluid flows and heat transfers when using boundary conditions 5.6 and 5.7. For both sets of boundary conditions, comparisons between natural, forced and mixed convection flows are performed. These comparisons emphasize clearly that only the pressure boundary conditions make sense.

5.4.1 Constant flow rate

We are first considering prescribed inlet velocity in the range $0.1 \ m/s \leq w_0 \leq 1 \ m/s$ in order to satisfy the assumption of laminar flow ($Re = 2500$ for $w_0 = 1 \ m/s$). For pure forced convection, it results that the difference in pressure between the inlet and outlet sections is within $\Delta p = 0.061 \ Pa$ and $\Delta p = 0.96 \ Pa$.

The Δp-variations versus the inlet velocity are shown in Fig. 5.2 for forced convection and for mixed convection. Since the outlet pressure has been fixed to $p_s = 0$ (see Eq. 5.6), that implies $\Delta p = \overline{p}(0)$. For forced convection, the inlet pressure is always positive while it is negative for mixed convection if the inlet velocity is smaller than the inlet velocity corresponding to pure natural convection ($\overline{w}_{nc} = 0.38 \ m/s$). Therefore, the pressure and buoyancy forces are opposite if $w_0 < \overline{w}_{nc}$.

Let us now consider computations based on the dimensionless form of the governing equations. In most of the papers dealing with aiding mixed convection, the Reynolds and Grashof numbers were arbitrarily fixed: the relative importance of one convective mode was discussed by considering only the value of Ri or $Ri \times Re$ with the same length scale for Re and Gr. For the present computations ($D = 2 \ cm$), it is found that $Ri = 2.62 \ 10^{-2}/w_0^2$ (w_0 in m/s) and $Ri \times Re = 66.4/w_0$. Therefore, either the first or the second criterion (e.g $Ri > \mathcal{O}(1)$ [22] or $Ri \times Re > \mathcal{O}(10^3)$ [121]) leads to assume that natural convection dominates for w_0 less than about $0.15 \ m/s$, a value smaller than $\overline{w}_{cn} = 0.38 \ m/s$. For the practical case considered, the average velocity $0.15 \ m/s$ can only be reached for a negative pressure gradient (Fig. 5.2), namely for a "forced convection" opposing to the natural convection. Thus, concluding that natural convection is dominating has no physical meaning since the pressure gradient plays a dominant part into the flow rate.

The streamlines plotted in Fig. 5.3 shows another view of the results linked to a fixed flow rate smaller than the natural inlet flow rate. For this case, we consider a channel height $H = 1.5 \ m$ and a channel width $D = 3 \ cm$ in order to check that the present results
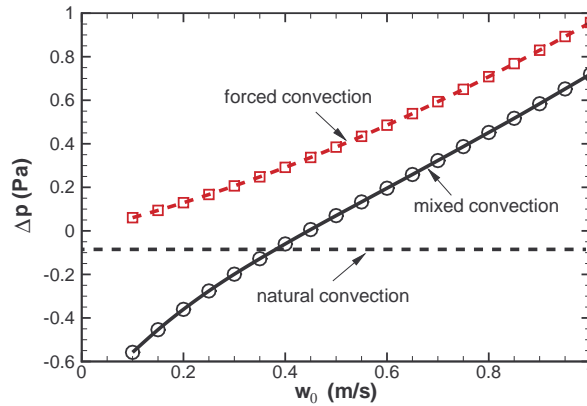
Figure 5.2 – Variations of the pressure difference between inlet and outlet sections according to the prescribed inlet velocity for forced, mixed and natural convection.

(a)   (b)
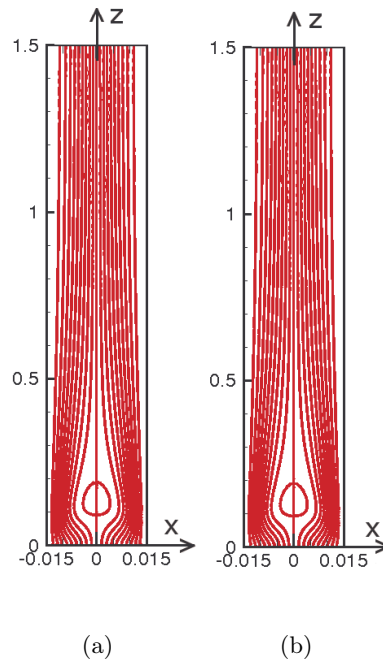
Figure 5.3 – Flow recirculation for mixed convection (a) prescribed inlet velocity , $w_0 = 0.05 \ m/s$ (b) overpressure at the outlet section $p_s = 1.4 \ Pa$ ($D = 3 \ cm$, $H = 1.5m$, $\Delta T = 20 \ K$).

are in full agreement with those published in [56, 74, 92].

Figure 5.3 raises obviously the question of the origin of existence of flow recirculations within the entry region for aiding mixed convection in vertical channels. As it is well established nowadays, the separation bubble (the axis of which being the channel axis) cannot be predicted when using parabolized formulations. On the other hand, elliptical models may lead to such flow topologies provided that the inlet velocity is prescribed without any

reference to the natural convection velocity. The case shown in Fig. 5.3 corresponds to a clear recirculating flow, easily reproducible by using the simulation conditions reported in the legend of this figure. The conclusion is that the flow field referenced as "buoyancy-assisted mixed flow" is similar to the flow predicted for "opposing mixed convection" with $p_s = 1.4 \ Pa \ (\Delta p < 0)$.

Figure 5.4 shows the variations of the vertical velocity component along the centerline
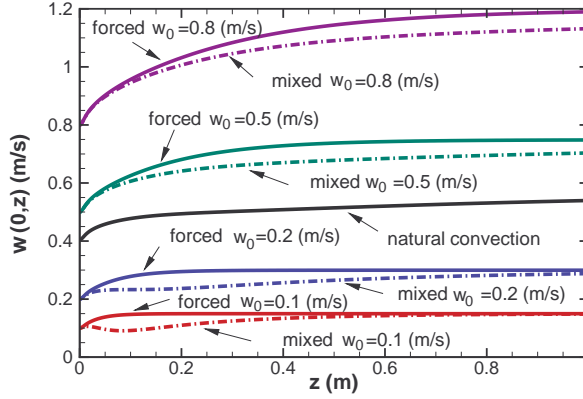
Figure 5.4 – Vertical velocity variations along the channel axis for forced and mixed convection according to the prescribed inlet velocity. The natural convection curve is also shown ($D = 2 \ cm$, $H = 1 \ m$, $\Delta T = 20 \ K$).

(e.g. $w(0, z)$) for the three convective modes. For forced convection, $w(0, z)$ is the maximum flow velocity at any z-section and it increases upstream until the flow regime is fully established (before $z = H$ if $w_0 < 0.2 \ m/s$ in the case considered). For mixed convection, the buoyancy force produces maximum in velocities near the walls. Therefore, $w(0, z)$ for mixed convection is lower than for forced convection when the flow rate is prescribed, the difference increasing upstream with w_0. If $w_0 < \overline{w}_{nc}$ ($\overline{w}_{nc}$ being the average velocity for natural convection) the decrease in $w(0, z)$ at the bottom of the channel indicates a possible onset of flow recirculation (see Fig. 5.3). For $w_0 = 0.1 \ m/s$ and $0.2 \ m/s$, a stagnant zone characterized by a decrease in the axial velocity spreads within the lower half-region. This stagnation zone becomes more and more confined close to the channel inlet as the difference between w_0 and the natural convection velocity increases.

Figure 5.5 displays the variation in the total heat flux transferred at one of the channel walls ($Q_{1w} = Q_{2w}/2$) as function of the inlet velocity, the horizontal dashed line being for pure natural convection. As can be seen, mixed convection with a prescribed inlet velocity lower than that for pure natural convection leads to a lower heat transfer rate. In addition, the very small differences between the results for forced and mixed convection clearly show that the buoyancy force does not assist significantly the pressure force. For the lowest inlet velocity considered here ($w_0 = 0.1 \ m/s$), the Péclet number is $Pe \approx 259$. Therefore, axial conduction is negligibly small ($Q_{cond} \ll Q_{2w}$, Eq. 5.8 and 5.10).
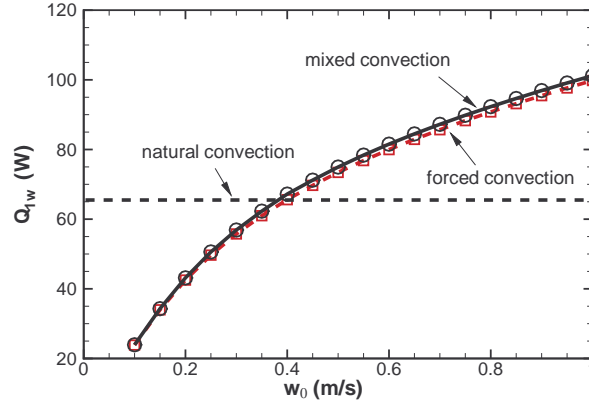
Figure 5.5 – Total heat flux transferred at one of the hot walls for forced and mixed convection according to the prescribed inlet velocity. The value for natural convection is also shown ($D = 2$ cm, $H = 1$ m, $\Delta T = 20$ K).

5.4.2 Pressure driven mixed convection

When a pressure drop is prescribed at the outlet section ($p_s < 0$), with an inlet total pressure fixed, the pressure and the velocity profile at the inlet as well as the flow rate are not *a priori* known. Therefore, it is not possible to calculate the Reynolds and Richardson numbers until the end of the computations. However, the flow rate is necessary greater than that for pure natural convection. For the practical case investigated ($H = 1$ m, $D = 2$ cm, $\Delta T = 20$ K), the maximum pressure (at the center of the inlet section) for natural convection is $p(0,0) = -0.143$ Pa. The inlet pressure for mixed convection should be lower than this value since the flow rate is assumed to increase ($\overline{p}(0) \approx -\rho_0\overline{w}^2/2$).

Figure 5.6 shows the axial variation of pressure along the channel axis. For natural
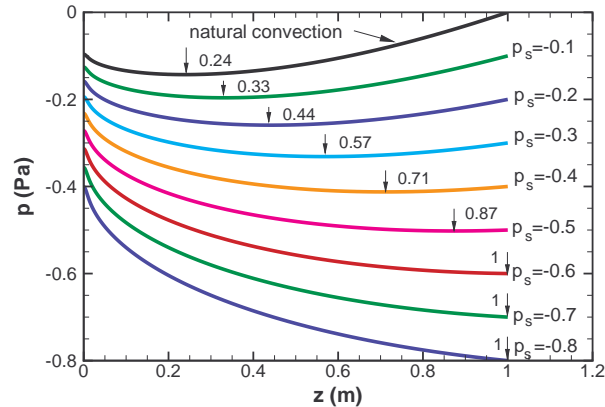
Figure 5.6 – Axial variation of pressure along the channel axis according to the outlet pressure drop ($D = 2$ cm, $H = 1$ m, $\Delta T = 20$ K). The arrows indicate the positions (in m) of the pressure minimum.

convection the pressure minimum is at $z = 0.24$ m while it is located at the outlet section

89

for forced convection. For mixed convection, the pressure curves exhibit a minimum, whose location is indicated by an arrow in Fig. 5.6. Therefore, $\partial p/\partial z$ is zero at this z-coordinate where the buoyancy force compensates viscosity and advection. When the pressure drop at the outlet section exceeds $0.6\ Pa$, the pressure decreases monotonously from the inlet to the outlet section, indicating the predominance of forced convection.

The average velocity is displayed in Fig 5.7 versus the outlet pressure drop. In contrast
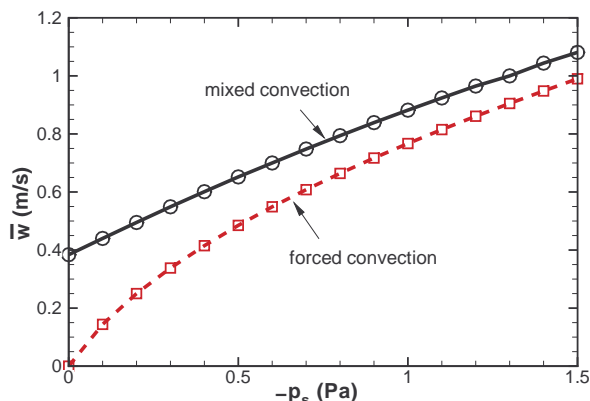
Figure 5.7 – Variations of the average velocity according to the pressure drop at the outlet section for forced and mixed convection ($D = 2\ cm$, $H = 1\ m$, $\Delta T = 20\ K$).

to what has been found for prescribed inlet velocity, $\overline{w}$ for mixed convection is systematically greater than for forced convection: buoyancy force assists thus the pressure force whatever $p_s < 0$ and, we can effectively speak in terms of "buoyancy assisted mixed convection". The results is obviously an increase in the heat flux transferred along the walls as can be seen in Fig 5.8. The computations were not pursued for $p_s < -1.5\ Pa$ owing to the large values of the Reynolds number involved ($Re = 2744$ for $p_s = -1.5\ Pa$). Figure 5.8 shows that natural convection dominates for the smallest values of $-p_s$ and that forced convection dominates for the largest values of $-p_s$. The comparison between Fig. 5.5 (B.C. 5.6) and Fig. 5.8 (B.C. 5.7) clearly exhibits the large differences in the wall heat flux according to the type of boundary conditions. It should be noted that the forced convection curve does not tend to zero as $p_s \to 0$ because the problem turns then into a pure conduction problem. From Eq. 5.10 it is found that $Q_{cond} = 4.8\ W$ for $p_s = 0$.

Let us now discuss the above results in terms of Ri or $Ri \times Re$ (Re and Gr being both based on the same length scale, i.e D_h). When increasing the pressure drop, Ri and $Ri \times Re$ decrease since the flow rate is increased. From $p_s = -0.1\ Pa$ to $p_s = -1.5\ Pa$, Ri decreases from 0.134 to 0.022 while $Ri \times Re$ decreases from about 151 to about 57. The criterion for the transition from dominant forced convection to dominant natural convection being $Ri > \mathcal{O}(1)$ [22] or $Ri \times Re > \mathcal{O}(10^3)$ [121], it could be assumed that natural convection plays a negligible role for the results discussed herein. In fact, the heat flux at one of the vertical walls is $Q_{1w} \approx 65\ W$ for pure natural convection. That substantially differs from $Q_{1w} \approx 75\ W$ for mixed convection when $p_s = -0.2\ Pa$ ($Q_{1w} \approx 50\ W$ for forced convection). Therefore, any of these two criteria based on approximate analyses appears to be relevant.
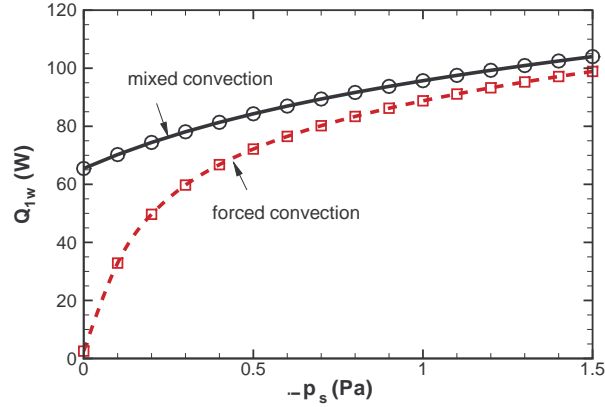
Figure 5.8 – Variations of the heat flux transferred at one of the walls according to the pressure drop at the outlet section for forced and mixed convection ($D = 2\ cm$, $H = 1\ m$, $\Delta T = 20\ K$).

The temperature distribution along the channel axis is plotted in Fig. 5.9 according
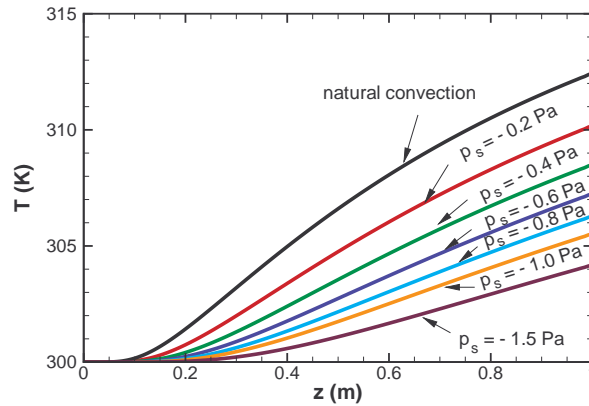
Figure 5.9 – Variations of the temperature along the channel axis according to the pressure drop at the outlet section for natural and mixed convection ($D = 2\ cm$, $H = 1\ m$, $\Delta T = 20\ K$).

to the pressure at the channel outlet section. Small increases in the axial temperature indicate that the channel flow regime turns into a boundary layer type regime. Asymptotic solutions for assisting mixed convection along a vertical isothermal plate may be thus useful. The present results show that it is not the case, at least for laminar flows (i.e. $|p_s| < 1.5\ Pa$). In addition, temperature as well as velocity profiles do not exhibit boundary layer-type behavior. When p_s is decreased from $p_s = 0$ (pure natural convection) to $p_s = -1.5\ Pa$ (dominant forced convection), Figure 5.9 indicates a significant decrease in the axial temperature which is closely linked to an increase in heat transfer at the walls. Since the temperature increases up to the outlet section, an established velocity field cannot be predicted, as shown in Fig. 5.10. This figure exhibits also that the dynamical entry length augments with the Reynolds number. However, the usual criterion for defining
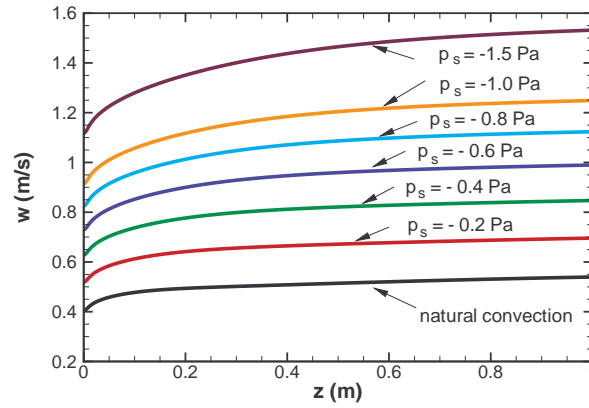
Figure 5.10 – Variations of the vertical velocity component along the channel axis according to the pressure drop at the outlet section for natural and mixed convection ($D = 2\ cm$, $H = 1\ m$, $\Delta T = 20\ K$).

the dynamical and thermal entry lengths for forced convection in a flat plate channel ($z_d \approx 4\ 10^{-4} Re_{D_h}$ and $z_t/D_h \approx 0.01 Re_{D_h} Pr$, respectively) are not met for the largest pressure drop considered.

Chapter 6

Effect of surface radiation on natural convective flows and onset of flow reversal in asymmetrically heated vertical channels [101]

Nomenclature

a	thermal diffusivity [$m^2\ s^{-1}$]
A	aspect ratio, $A = 2H/D$
B	radiosity [$W\ m^{-2}$]
c_p	specific heat [$J\ K^{-1}\ kg^{-1}$]
d_ψ	width of the recirculation [m], Eqs. 6.36 and 6.37
D	wall spacing [m]
g	gravitational acceleration [$m\ s^{-2}$]
G	irradiation or incoming radiative heat flux density [$W\ m^{-2}$]
Gr	modified Grashof number based on q_w, $Gr = g\beta_0 q_w D^4/\nu_0^2 k_0$
h	heat transfer coefficient [$W\ m^{-2}K^{-1}$]
H	half of the total channel height [m]
k	thermal conductivity [$W\ m^{-1}\ K^{-1}$]
K	kernel function (Eq. 6.10)
L_p	penetration length [m]
$\dot{m}$	mass flow rate [$kg\ m^{-1}\ s^{-1}$]
M_a	molecular weight [$kg\ kmol^{-1}$]
$\dot{m}_{in}$	mass flow rate in the entrance section, Eq. 6.34
$\dot{m}_{out}$	mass flow rate leaving the channel, Eq. 6.35
N_R	conduction-to-radiation parameter, $N_R = q_w/\sigma T_0^4$
$\overline{Nu}$	mean Nusselt number
n_x, n_z	numbers of grid points in $x-$ and $z-$directions
p	pressure [Pa]
p_m	sum of static and hydrostatic pressures [Pa]
p_s	pressure at the outlet section [Pa]
p^*	dimensionless pressure, $P = p/(\rho_0 w_0^2)$
Pr	Prandtl number, $Pr = \nu_0/a_0$
q	heat flux density [$W\ m^{-2}$]
R	ideal gas constant

Ra	modified Rayleigh number based on q_w, $Ra = g\beta_0 q_w D^4/a_0\nu_0 k_0$
Ra^*	channel Rayleigh number, $Ra^* = Ra(D/H)$
t	time $[s]$
T	temperature $[K]$
u, w	velocity components $[m\ s^{-1}]$
$\mathbf{v}$	velocity vector
x, z	coordinates $[m]$
Greeks	
α	order of consistency of the numerical scheme
β	thermal coefficient of volumetric expansion, $\beta = 1/T_0$ $[K^{-1}]$
ΔT	temperature difference $[K]$
ϵ	emissivity
γ	non-Boussinesq parameter, $\gamma = \Delta T/T_0$
μ	dynamic viscosity $[kg\ m^{-1}\ s^{-1}]$
ν	kinematic viscosity, $\nu = \mu/\rho$ $[m^2\ s^{-1}]$
ρ	density $[kg\ m^{-3}]$
σ	Stefan-Boltzmann constant, $\sigma = 5.67\,10^{-8}$ $[W\ m^{-2}\ K^{-4}]$
θ	dimensionless temperature, $\theta = (k_0(T - T_0)/q_w D$
τ	dimensionless time, $\tau = t(g\beta_0\Delta T D)^{1/2}/D$

Subscripts

H	quantity based on channel height
c, i	natural convection
max	maximum
r	radiative
w	wall
0	inlet section
t	total

Superscripts

$^-$	averaged quantity
$*$	dimensionless quantity

6.1 Introduction

Natural convection in vertical parallel-plate channel is relevant to a wide range of applications such as the cooling of electronic equipments in which circuit cards containing heat generating electronic devices are arrayed to form vertical channels, the design of solar panels, energy efficient buildings, heat removal in nuclear technology, and a host of others. The problem of natural convection in vertical channels has been the focus of extensive investigations since the pioneering work by Elenbass [57], resulting in numerous theoretical, numerical and experimental works. However, the number of studies reported on combined surface radiation and natural convection is very limited, despite radiative exchanges amongst surface plays a significant role for most practical applications.

Developing and fully developed laminar free convection between vertical flat plates with symmetric or asymmetric heating were reconsidered by Bodoia and Osterle [30], investigated analytically and experimentally by Aung [8], and Aung et al. [10]. These studies were the foundations for few others studies conducted later on. Amongst these, the experimental

work by Wirtz and Stutzman [163] on developing natural convection of air flowing between vertical parallel plates with uniform and symmetric heat fluxes is frequently quoted. An up to date review on the formulas for the calculation of the heat transfer and flow rate for two-dimensional natural convection between vertical plates having uniform wall temperature or uniform heat flux boundary conditions was presented by Olsson [117]. The recent experimental study conducted by Lu et al. [104] for channels with large aspect ratio and narrow gap, and with air as the working fluid, adds Nusselt number correlations for the case of symmetrical, uniformly heated vertical walls. Although high wall temperatures were measured (up to $\approx 600\,K$), the radiation effects may be considered as weak owing to the symmetrical heating, small size of the apertures and large aspect ratios.

Recently, laminar natural convection of air in parallel-plate vertical microchannels was investigated theoretically and numerically in the transient regime, with velocity slip and temperature jump boundary conditions at the walls, by Buonomo and Manca [36, 37]. The microchannels were asymmetrically or symmetrically heated at uniform heat flux, and the boundary layer assumption was invoked for various values of the Knudsen number over the range of the first-order model for the continuum slip flow regime. Results showed overshoots in the transient maximum wall temperature. A composite correlation was proposed to estimate average Nusselt numbers at steady state.

6.1.1 Flow reversals

The theory of flow reversal of fully developed, aiding mixed convection and numerical solutions for developing flows were presented by Aung and Worku [11, 12]. Since these early studies, many numerical works dealing with the buoyancy effect on the flow structure and heat transfer have been performed (see for example [44, 45, 82, 166]) while a limited number of experiments have been carried out.

The study of flow reversals in the case of pure natural convection in vertical channel was considered in only few works.

An experimental study for natural convection in a vertical channel with the heated wall maintained at uniform temperature and unheated facing wall was carried out with water as the working fluid by Sparrow et al. [144]. For the first time, the formation of pocket of recirculating flow at Rayleigh numbers exceeding a threshold value was revealed by flow visualizations. It was found that the recirculation, fed by fluid drawn into the outlet section of the channel adjacent to the adiabatic wall, has no effect on the heat transfer at the heated wall. As in the work by Bar-Cohen and Rohsenow [18], a new dimensionless group was introduced, the channel Rayleigh number $Ra^* = Ra_D(D/H)$, which has been shown to be the most convenient group for correlating the Nusselt number results. Since this pioneer work, the study of the flow reversals in natural convection has received only limited attention. The most salient studies are those by Kihm et al. [88] who identified the occurrence of the onset and penetration lengths of the flow reversal in natural convection of air through vertical isothermal channel walls, and the recent experimental study by Ospir et al. [120] on natural convection in an asymmetrically heated vertical plane channel with water as the working fluid. Flow visualization techniques based on laser tomography were used in [120] for investigating the flow structure in steady-state, boundary layer flow regime as well as in the early stage following the beginning of the heating. From the experiments carried out for several values of the modified Rayleigh number and channel aspect ratios, very new insights on the the reversed flow structures were revealed.

6.1.2 Coupled natural convection and radiation

The problem of combined radiation and natural convection was extensively studied, specially for closed cavities. It can be classified into two categories: one only with wall radiations, and the other with both wall and gas radiations. For cases including gas radiation combined with natural convection heat transfer, which is always important for combustion and engineering applications, numerous papers have been published. Yamada et al. [165], Colomer et al. [51] and, more recently, Mondal and Li [113], who used an improved lattice-Boltzmann method, presented relevant literature surveys on this subject. The present study encompasses only combined surface radiation and natural convection that arises when the working fluid is assumed transparent to infrared radiations.

6.1.2.1 Coupled natural convection and surface radiation in cavities

Numerical investigation of combined surface radiation and natural convection in a vertical square, differentially heated cavity were reported by Balaji and Venkateshan [15]. They showed that radiation has a dual effect of contributing to the overall heat transfer as well as decreasing the convective component. They underlined that simple formulae that account for radiation in an additive way are not adequate. In a subsequent study, Balaji and Venkateshan [16] proposed correlations for both convective and radiative heat transfers for air as the working fluid. These correlations were found in fair agreement with the results from an experimental study conducted by Ramesh and Venkateshan [130].

The impact of surface radiation on multiple solutions inside a square two-dimensional cavity heated from below was studied numerically by Ridouane et al. [133]. The emissivities of the isothermal horizontal walls were different from those of the vertical adiabatic walls and were set to $\epsilon = 0.05$ or to $\epsilon = 0.85$. Four combinations of wall emissivities were considered. In comparison with pure natural convection, it was shown that the ranges of the steady-state modes as well as the nature and magnitude of periodic solutions were highly affected by surface radiation.

This problem was reconsidered more recently by Ashish Gad and Balaji [62] for air-filled, rectangular cavities heated from below with surface radiation spanning six different aspect ratios (from $A = 1$ to $A = 10$). The critical Rayleigh number for the onset of convection was determined as function of two parameters: the emissivity of the adiabatic sidewalls and the aspect ratio for a cold top wall at $T_c = 303\ K$, the emissivity of the horizontal walls being set to $\varepsilon = 0.85$. It was shown that the onset of Rayleigh-Bénard convection is delayed with an increase in the emissivity of the sidewalls and, that the effect of surface radiation diminishes with an increase in the aspect ratio.

Natural convection for air in an open-ended cavity heated from above was experimentally studied by Manca and Nardini [106] in the case of high emissivity of the horizontal walls. They observed that surface radiation caused a temperature increase in the unheated lower plate, which could rise to secondary motions due to plumes inside the cavity. Correlations for average Nusselt numbers and maximum wall temperatures were proposed.

Studies on combined natural convection and surface radiation from a heated body inside a cavity are more scarse (for an overview of recent references, see Bouali et al. [32], Lauriat and Desrayaud [93], Mezrhab et al. [111]). In the paper by Mezrhab et al. [111], a differentially-heated cavity of square cross-section containing a conducting, centered square

body was numerically investigated. Amongst the conclusions drawn for this particular configuration, the effect of the inner body on the flow field and heat transfer was shown much important when surface radiation exchanges were taken into account. In the range of Rayleigh number considered, it was also shown that radiation augments the fluid velocities in comparison with those obtained for a cavity without an inner body. However, much of these conclusions are specific to the geometrical case considered, as underlined in Sun et al. [147].

6.1.2.2 Coupled natural convection and radiation in vertical parallel plate channels

The interaction of surface radiation with developing laminar natural convection in vertical parallel plate channels with asymmetric heating was numerically studied by Carpenter et al. [39]. A parabolic formulation of the governing equations was employed and the Boussinesq approximation invoked. They investigated the effects of the five dimensionless parameters involved in the dimensionless formulation (heat flux ratio, Rayleigh number, aspect ratio, emissivity, and radiation number), and showed that radiation significantly alters the pure natural convection results by reducing the wall temperatures, especially the maximum value.

The effect of surface radiation was reconsidered by Webb and Hill [161] in their paper reporting on experiments designed to determine local and average heat transfer characteristics for natural convection in a vertical parallel plate channel, one wall heated with uniform heat flux and the other thermally insulated. Local temperatures along both walls were collected for a wide range of heating rates and wall spacings corresponding to the high channel Rayleigh number regime (i.e. $503 \leq Ra^* \leq 1.75 \cdot 10^7$). Unheated entry and exit lengths ($H/2 = 7.62 \, cm$) were added to the heated section ($H = 15.2 \, cm$) to minimize radiation losses near the channel entrance and exit. The local radiative heat flux was determined from the temperature data by solving the system of equations describing the radiation exchanges for channel walls assumed gray and diffuse with an emissivity measured to $\varepsilon = 0.1$. The heating rate was then reduced by the calculated local radiation loss, and the corrected heat transfer results were used in all correlations presented in the paper. The results compared favorably with previous experimental data, and the importance of corrections for radiation and conduction losses as well as the use of local thermophysical properties in correlating the data were underlined.

The experimental design, wall spacings and heating rates described in [161] were numerically simulated, as accurately as possible, in the preparation of the present paper.

Combined natural convection and thermal radiation in vertical parallel plate channels was experimentally investigated by Manca and Naso [107]. The measurements showed that the effect of surface radiation is more important for asymmetric heating than for symmetric heating. In addition, it was emphasized that the flow patterns tend to those of symmetric heating for high wall emissivities, and reduce the Rayleigh number corresponding to the developing regime. Correlations between local Nusselt numbers at various emissivities have also been proposed.

Laminar natural convection and surface radiation between vertical parallel plates, a central, highly emissive ($\varepsilon = 0.85$) hot plate and two unheated polished plates ($\varepsilon = 0.05$),

was investigated experimentally by Krishnan et al. [91] for various plate spacings. The temperature measurements were introduced as boundary conditions into a numerical code in order to obtain the convective heat transfer rates. This study brought out the significance of radiation at room temperature. A correlation for the average convective wall heat transfer was derived.

6.1.3   Channel extensions

Amongst the attempts for solving natural convection at low channel Rayleigh number, is the use of channel extensions as it was suggested in many previous numerical studies that we briefly review in what follows.

Naylor et al. [116] solved the full elliptic forms of the governing equations for pure natural convection using inlet flow boundary conditions based on the Jeffrey-Hamel flow in order to represent more realistically the entrance flow. Their solutions validated the inlet pressure approximation ($p = -\rho_0 w^2/2$) commonly used in parabolic formulations. Their predictions of fluid separation at the channel inlet is not in agreement with most of the elliptic solutions published so far, and appear to be caused by the shape of the extension. The optimization of plate separation of an open, vertical, parallel-plate channel that is cooled by natural convection of air with the plates symmetrically heated by uniform heat flux has been studied by Morrone et al. [114] by solving the full elliptic conservation equations in a I-shaped computational domain. Correlations for the dimensionless flow rate and optimal values of the spacing were derived and compared with the predictions of Bar-Cohen and Rohsenow [18] and Anand et al. [1].

Natural convection of air in channel-chimney systems was studied experimentally [7], and numerically by using the stream function-vorticity approach and the control volume method by Andreozzi et al. [3, 4] for vertical channels heated symmetrically at uniform heat flux and with adiabatic extensions. Results obtained provide guidelines to determine if the channel-chimney system is in critical condition related to flow reattachment or separation.

Closely related to these approaches is the paper by Bello-Ochende and Bejan [26]: the channel was fitted with upstream and downstream extensions whose lengths were selected based on accuracy tests. For the downstream extension domain, free slip and no penetration were specified at one side and zero stress at the other side in order to nullify the chimney effect. From our point of view, this procedure leads to unrealistic outflow fields for a periodic array of vertical channels.

As shown in a recent paper by Sun et al. [150], the use of inlet channel extensions is not required, even for rather low channel Rayleigh numbers, since a regularization procedure allows to numerically solve the problem with a good accuracy. On the other hand, extensions are required for the very low Rayleigh numbers at which backward thermal diffusion dominates. Upper extensions lead obviously to other problems owing to superimposition of chimney effects.

6.1.4   Aim of the present study

This paper reports a numerical study of a combined radiation and natural convection problem between vertical plates with asymmetric heating. The present study differs from the aforementioned ones in the following issues:

-the problem formulation is based on a weakly compressible formulation in order to account for unpredictable maximum temperature difference for uniformly heated walls. Experimental studies reveal indeed surface-to-ambient temperature difference up to about $500\,K$ according to the heating rate and/or wall spacings when air is the working fluid [72, 104]. The dynamical inlet/outlet boundary conditions differ also,
-the flow reversal phenomenon for pure natural convection is revisited,
-the effects of surface radiation as well on the flow structure as on the heat transfer rate are investigated and supported through comparisons with the experimental study by Webb et Hill [161].

6.2 Problem statement

6.2.1 Dimensional form

The fluid flow and heat transfer are governed by the Navier-Stokes and energy equations for a two-dimensional, laminar flow of a Newtonian fluid. The viscous dissipation term in the energy equation is neglected and the fluid is assumed transparent to thermal radiation leaving the channel walls. The energy equation is coupled with the equation dealing with radiant interchanges amongst surfaces through the thermal boundary conditions. Since some calculations were carried out for maximum temperature differences larger than that possible for an accurate use of the Boussinesq approximation for ideal gases ($\Delta T_{max} \leq 0.1 T_0$, where T_0 is a reference temperature), a weakly compressible formulation was employed by assuming the pressure work in the energy equation as negligible and, by calculating the density field from the state equation with a uniform thermodynamic pressure within the channel.
The conservation equations are written as follows:

$$\frac{\partial \rho}{\partial t} + \nabla \cdot (\rho \vec{v}) = 0 \tag{6.1}$$

$$\frac{\partial (\rho \vec{v})}{\partial t} + \nabla \cdot (\rho \vec{v} \otimes \vec{v}) = -\nabla(p + \rho_0 g z) + \nabla \cdot \left[\mu \left(\nabla \vec{v} + \nabla^t \vec{v} \right) - \frac{2}{3} \nabla \cdot \vec{v} \right] + (\rho_0 - \rho) g \vec{e}_z \tag{6.2}$$

$$c_p \left(\frac{\partial (\rho T)}{\partial t} + \nabla \cdot (\rho \vec{v} T) \right) = \nabla \cdot (k \nabla T) \tag{6.3}$$

where ρ_0 in the momentum equation is the density at a reference temperature, chosen as the inlet fluid temperature and $\vec{e}_z$ is the unit vector along the z-axis, pointing upward. All thermophysical properties are considered as temperature dependent, i.e $\rho(T)$, $\mu(T)$, $c_p(T)$ and $k(T)$. For dry air, $c_p(T)$, $k(T)$ and $\mu(T)$ are calculated according to the polynomial relationships given by Lide and Kehiaian [102], valid in the range $[100\,K, 600\,K]$. These properties variations were used in [148] where the specific relationships employed herein can be found.

The system of conservation equations is completed by the ideal gas law used for the calculations of the density at any point $\mathbf{M}$:

$$\rho(\mathbf{M}, t) = \frac{\bar{P}_0 \, M_a}{R \, T(\mathbf{M}, t)} \tag{6.4}$$

$\bar{P}_0$ is the uniform thermodynamic pressure, equal the average hydrostatic pressure in the surroundings, $\bar{P}_0 = P(0) - \rho g \, H$.

6.2.1.1 Boundary conditions

– at the vertical walls:
   – $x = 0$, $0 < z < H/2$ and $3H/2 < z < 2H$,

$$\vec{v} = \mathbf{0}, \qquad q_r(z) - k\frac{\partial T}{\partial x} = 0 \tag{6.5}$$

where q_r is the net radiative heat flux density along the surface.

   – $x = 0$ and $H/2 < z < 3H/2$,

$$\vec{v} = \mathbf{0}, \quad q_r(z) - k\frac{\partial T}{\partial x} = q_w \tag{6.6}$$

   – $x = D$ and $0 < z < 2H$,

$$\vec{v} = \mathbf{0}, \qquad q_r(z) + k\frac{\partial T}{\partial x} = 0 \tag{6.7}$$

– at the inlet/outlet sections:
   – $0 < x < D$ and $z = 0$ or $z = 2H$,

$$u = 0, \ \frac{\partial w}{\partial z} = 0, \ \begin{cases} \text{if } \vec{v}\cdot\vec{n} < 0 \text{ (inlet condition)}, \ T = T_0, \ p_g = -\rho\frac{w^2}{2} \\ \text{if } \vec{v}\cdot\vec{n} \geq 0 \text{ (outlet condition)}, \ \frac{\partial T}{\partial z} = 0, \ p_g = 0 \end{cases} \tag{6.8}$$

where $p_g = p + \rho_0 gz$ is the departure of the pressure from the hydrostatic pressure and $\vec{n}$ is the unit normal vector pointing outward the computational domain. The inlet/outlet conditions (Eq. 6.8) for the velocity assume that the fluid enters or exits normally to the inlet/outlet sections.

The pressure and temperature boundary conditions at the bottom and top sections depend on whether the fluid enters or exits the channel:

$\star$ In the first case ($\vec{v}\cdot\vec{n} < 0$), the temperature equals the surroundings temperature and the static and hydrostatic pressure drops equilibrate the increase in kinetic energy for non-viscous fluids.

$\star$ In the second case ($\vec{v}\cdot\vec{n} \geq 0$), the heat diffusion normal to the inlet/outlet section is neglected and the fluid flow is assumed to behave as a jet with parallel streamlines. With the jet approximation, the sum of the static and hydrostatic pressures is kept constant at the outlet section and equal to its surrounding value which is arbitrary fixed to zero.

6.2.1.2 Radiative heat flux

The radiative exchanges amongst the surfaces were calculated by considering the channel as a two-dimensional enclosure consisting of four gray-diffuse, vertical surfaces (the three parts of the left-hand side wall and the adiabatic right-hand side wall) and two horizontal surfaces regarded as black radiators at an effective temperature T_0. Since the vertical walls have the same emissivity, ε, the temperature distributions are evaluated from

$$\sigma T_i^4(\mathbf{r}_i) = \frac{1-\varepsilon}{\varepsilon}q_w + B_i(\mathbf{r}_i) \tag{6.9}$$

The position vector $\mathbf{r}_i$ denotes the locations of elementary surfaces dS_i on surface S_i, and $B_i(\mathbf{r}_i)$ is the radiosity, which is the radiation heat flux density leaving surface S_i. The heat

fluxes are uniform along the vertical walls: $q_i = q_w$ on the heated surface and $q_i = 0$ on the three adiabatic surfaces. The radiosity distributions along the vertical walls are defined as

$$B_i(\mathbf{r}_i) = q_i(\mathbf{r}_i) + \sum_{j=1}^{6} \int_{S_j} B_j(\mathbf{r}_j) K(\mathbf{r}_i, \mathbf{r}_j) dS_j = q_i(\mathbf{r}_i) - G_i(\mathbf{r}_i) \tag{6.10}$$

The kernel function K reads $K(\mathbf{r}_i, \mathbf{r}_j) = cos(\theta_i)cos(\theta_j)/\pi r_{ij}^2$ [112]. For plane or convex surfaces, $K(\mathbf{r}_i, \mathbf{r}_i) = 0$. The term $G_i(\mathbf{r}_i)$ is the radiative heat flux density incident on surface S_i. At the channel apertures, $B_i(\mathbf{r}_i) = \sigma T_0^4$.

The preceding set of equations may be combined to yield a system of integral equations that relates temperatures and heat fluxes at the six surfaces. There follows

$$\sigma T_i^4(\mathbf{r}_i) - \frac{q_i(\mathbf{r}_i)}{\varepsilon_i} = \sum_{j=1}^{6} \int_{S_j} \sigma T_j^4(\mathbf{r}_j) K(\mathbf{r}_i, \mathbf{r}_j) dS_j - \sum_{j=1}^{6} \int_{S_j} \frac{1 - \varepsilon_j}{\varepsilon_j} q_j(\mathbf{r}_j) K(\mathbf{r}_i, \mathbf{r}_j) dS_j \quad 1 \leq i \leq 6 \tag{6.11}$$

The above system of six integral equations contains six unknown functions: the four distributions of temperature along the vertical walls and the two heat flux distributions at the channel apertures.

6.2.1.3 Wall heat fluxes and heat transfer coefficients

For an uniform heat flux density q_w prescribed at the heated surface, the local convective, $q_c(z)$ and radiative, $q_r(z)$ fluxes must balance q_w. Therefore

$$q_w = q_c(z) + q_r(z) = k(z)\frac{\partial T_w(z)}{\partial x}\vec{n} \cdot \vec{e}_x + B(z) - G(z) \tag{6.12}$$

where $G(z)$ is the local irradiation onto the heated surface (second right-hand side term in Eq. 6.10). The local convective heat transfer coefficient is determined using the relation (refer to [161]):

$$h(z) = \frac{q_w - q_r(z)}{T_w(z) - T_0} \tag{6.13}$$

while a local radiative heat transfer coefficient may be defined as

$$h_r(z) = \frac{q_r(z)}{T_w(z) - T_0} \tag{6.14}$$

The total heat transfer coefficient is thus $h_t(z) = h(z) + h_r(z)$. Average heat transfer coefficients over the heated surface ($x = 0$, $H/2 \leq z \leq 3H/2$) are calculated according to the relations

$$\overline{h}_{c,1} = \frac{1}{H} \int_{\frac{H}{2}}^{\frac{3H}{2}} h(z)\,dz \quad \text{and} \quad \overline{h}_{r,1} = \frac{1}{H} \int_{\frac{H}{2}}^{\frac{3H}{2}} h_r(z)\,dz \tag{6.15}$$

and $\overline{h}_{t,1} = \overline{h}_{c,1} + \overline{h}_{r,1}$.

The heat flux conservation at the heated surface may also be stated as:

$$q_w = \overline{q}_c + \overline{q}_r \tag{6.16}$$

Average heat fluxes are calculated by averaging $q_c(z)$ and $q_r(z)$. This leads to

$$\overline{q}_c = \frac{1}{H} \int_{\frac{H}{2}}^{\frac{3H}{2}} k(z)\frac{\partial T_w(z)}{\partial x}\vec{n} \cdot \vec{e}_x\,dz \quad \text{and} \quad \overline{q}_r = \frac{1}{H} \int_{\frac{H}{2}}^{\frac{3H}{2}} (B(z) - G(z))\,dz \tag{6.17}$$

It should be noted that two different average heat transfer coefficients may be also determined using the two following relations (refer to Bianco et al. [28]):

$$\overline{h}_{c,2} = \frac{\overline{q}_c}{\overline{T}_w - T_0} \quad \text{and} \quad \overline{h}_{r,2} = \frac{\overline{q}_r}{\overline{T}_w - T_0} \tag{6.18}$$

where $\overline{T}_w$ is the average temperature of the heated wall. The main advantage in using the above definitions is that a heat transfer correlation yields automatically $\overline{T}_w$ when the input is the wall heat flux.

As a result, if the wall temperatures are recorded from experiments, as in [91, 161], the radiative and total heat transfer coefficient can be calculated accurately, and the convective heat transfer coefficient can be deduced by using either Eq. 6.15 or Eq. 6.18. However, this convective heat transfer is meaningful in pure convection only if the surface radiation exchanges modify slightly the temperature distribution along the heated wall. This point will be examined in what follows.

6.2.2 Dimensionless form

The governing equations are cast in dimensionless form using the reference length scale D, time scale $D/(g\beta_0 \Delta T D)^{0.5}$ where $\beta_0 = 1/T_0$, the velocity scale $(g\beta_0 \Delta T D)^{0.5}$, the dynamic pressure scale $\rho_0 g \beta_0 \Delta T D$, the temperature difference scale $\Delta T = q_w D/k_0$, and the radiative heat flux scale σT_0^4. Note that these scales are those often used when invoking the Boussinesq approximation for boundary-layer type flows. The resulting set of governing equations reads:

$$\frac{\partial \rho^*}{\partial \tau} + \nabla \cdot (\rho^* \vec{v}^*) = 0 \tag{6.19}$$

$$\frac{\partial(\rho^*\vec{v}^*)}{\partial \tau} + \nabla \cdot (\rho^* \vec{v}^* \otimes \vec{v}^*) = -\nabla(p^* + \frac{1}{\gamma}z^*) + \sqrt{\frac{Pr}{Ra}} \nabla \cdot \left[\mu^* \left(\nabla \vec{v}^* + \nabla^t \vec{v}^* \right) - \frac{2}{3}\nabla \cdot \vec{v}^* \right) \right] + \frac{1}{\gamma}(1-\rho^*)\vec{e}_z \tag{6.20}$$

$$c_p^* \left(\frac{\partial(\rho^*\theta)}{\partial \tau} + \nabla \cdot (\rho^* \vec{v}^* \theta) \right) = \frac{1}{\sqrt{Ra\,Pr}} \nabla \cdot (k^* \nabla \theta) \tag{6.21}$$

$$\rho^* = \frac{1}{(\gamma\theta + 1)} \tag{6.22}$$

In the above equations, superscript * indicates dimensionless dependent quantities and dimensionless fluid properties with the reference properties being those at T_0. The dimensionless temperature difference is $\theta = (T - T_0)/\Delta T$. The three dimensionless parameters are the Prandtl and Rayleigh numbers and, the non-Boussinesq parameter, $\gamma = \Delta T/T_0$, that characterizes the departure from the Boussinesq approximation. The dimensionless form of Eq. 6.11 writes

$$\sigma T_i^{*4}(\mathbf{r}_i^*) - \frac{q_i^*(\mathbf{r}_i^*)}{\varepsilon_i} = \sum_{j=1}^{6} \int_{S_j^*} \sigma T_j^{*4}(\mathbf{r}_j^*) K(\mathbf{r}_i^*, \mathbf{r}_j^*) dS_j^* - \sum_{j=1}^{6} \int_{S_j^*} \frac{1-\varepsilon_j}{\varepsilon_j} q_j^*(\mathbf{r}_j^*) K(\mathbf{r}_i^*, \mathbf{r}_j^*) dS_j^* \quad 1 \le i \le 6 \tag{6.23}$$

where $T^* = \gamma\theta + 1$ and $q_{r,i}^* = q_{r,i}/\sigma T_0^4$.

6.2.2.1 Dimensionless form of the boundary conditions

– at the vertical walls:
  – $x^* = 0, \qquad 0 < z^* < A/4$ and $3A/4 < z^* < A$,

$$\vec{v}^* = \mathbf{0}, \qquad q_r^*(z^*) - N_R \, k^* \frac{\partial \theta}{\partial x^*} = 0 \tag{6.24}$$

  – $x^* = 0$ and $A/4 < z^* < 3A/4$,

$$\vec{v}^* = \mathbf{0}, \qquad q_r^*(z^*) - N_R \, k^* \frac{\partial \theta}{\partial x^*} = N_R \tag{6.25}$$

  – $x^* = 1$ and $0 < z^* < A$,

$$\vec{v}^* = \mathbf{0}, \qquad q_r^*(z^*) + N_R \, k^* \frac{\partial \theta}{\partial x^*} = 0 \tag{6.26}$$

– at the inlet/outlet sections:
  – $x^* = 1$ and $0 < z^* < A$,

$$u^* = 0, \; \frac{\partial w^*}{\partial z^*} = 0, \; \begin{cases} \text{if } \vec{v}^* \cdot \vec{n} < 0 \text{ (inlet condition), } \theta = 0, \; p_g^* = -\frac{w^{*2}}{2} \\ \text{if } \vec{v}^* \cdot \vec{n} \geq 0 \text{ (outlet condition), } \frac{\partial \theta}{\partial z^*} = 0, \; p_g^* = 0 \end{cases} \tag{6.27}$$

The additional dimensionless parameters involved in the boundary conditions are the channel aspect ratio, $A = 2H/D$, and $N_R = q_w/\sigma T_0^4$, usually called the conduction-to-radiation parameter for the effects of surface radiation without linearization of the radiative heat flux [112].

Finally, the above mathematical modeling shows that the problem of two-dimensional, laminar natural convection of a gas through a channel subjected to a prescribed heat flux at one section of the walls while the others are assumed adiabatic (or subjected to the same heat flux density), involves six dimensionless parameters (not accounted for is the reference temperature T_0 introduced in the relations used for modeling the temperature dependence of the thermophysical properties): A, Pr, Ra, γ, N_R and ε. The last three parameters account for variable properties and surface radiation effects.

Owing to this number of parameters, the derivation of a general Nusselt number correlation appears to be rather cumbersome. Note that the number of parameters is still 6 even if the maximum possible temperature difference is compatible with the validity of the Boussinesq approximation. This approximation makes sense *a priori* only if the maximum temperature difference is prescribed. A large class of practical applications, such as the cooling of electronic or lighting equipments (HB-LED, for example) does not match this requirement.

6.2.2.2 Correlations for average channel Nusselt numbers and maximum wall temperature

For pure natural convection, the flow and heat transfer are governed by the height to width ratio H/D, the Rayleigh number, the Prandtl number, and the non-Boussinesq parameter. For an asymmetric heating the following Rayleigh numbers are used:

$$Ra = \frac{g\beta_0 q_w D^4}{a_0 \nu_0 k_0} \text{ and } Ra^* = Ra\left(\frac{D}{H}\right) \text{ the modified or channel Rayleigh number} \tag{6.28}$$

As in many of the previous studies [104, 105, 161], we did not use local Rayleigh numbers in what follows for deriving Nusselt number or θ_{max} correlations. Correlation equations

were determined for the local Nusselt number at midheight of the heated plate, for average Nusselt numbers based either on Eq. 6.15 or 6.18, and for maximal heated wall temperature:

$$Nu_{\frac{1}{2}} = \frac{q_w D}{2k_0(T_{\frac{1}{2}} - T_0)} = a^* Ra^{*^m} \quad , \quad \overline{Nu} = b^* Ra^{*^n} \quad \text{and} \quad \theta_{max} = c^* Ra^{*^{-p}} \quad (6.29)$$

with $T_{\frac{1}{2}}$ the average of the two wall temperature at $z = H$ and $\theta_{max} = k_0(T_{max} - T_0)/q_w D$; the definition of $Nu_{\frac{1}{2}}$ refers to [10, 161]. The convective, radiative and total average Nusselt number are calculated according to the relations

$$\overline{Nu}_{c,i} = \frac{\bar{h}_{c,i}D}{k_0} \quad , \quad \overline{Nu}_{r,i} = \frac{\bar{h}_{r,i}D}{k_0} \quad , \quad \overline{Nu}_{t,i} = \overline{Nu}_{c,i} + \overline{Nu}_{r,i} \quad \text{for} \quad i = 1,2 \text{ (see Eqs. 6.15 and 6.18)}$$

$$(6.30)$$

It should be noted that the fluid thermal conductivity is that at the inlet temperature because, from a practical viewpoint, the only available data in the design of a uniformly heated, flat plate channel are the wall heat flux, the inlet temperature and the dimensions of the channel.

6.3   Numerical method

The equations for mass (Eq. 6.1), momentum (Eq. 6.2) and energy (Eq. 6.3) are discretized by a collocated finite volume scheme based on methods initially developed for incompressible fluid flows on unstructured meshes and for fully coupled velocity-pressure equations [47], and later on extended to the low Mach number approximation [155]. This latter method has been adapted to a velocity-pressure decoupling scheme and applied here for structured rectangular grids. Details on the numerical method can be found in chapter 2.

Some key points of the spatial discretization are briefly recalled. Variables are located at the center of the rectangular cells. The thermal diffusion and the viscous part $\nabla \cdot (\mu \nabla \vec{v})$ are discretized with the classical 5 points-scheme with fluxes evaluated on cell faces with a two-points approximation. In order to mimic as much as possible the kinetic energy balance (and the quadratic form of the thermal balance), additional conditions must be fulfilled. First, the discrete expression of the pressure gradient is the dual form of the discrete divergence of the velocity. Then, the mass flow rate acting in the transport contribution is the same as the one used in mass equation. Moreover, the convected quantities (the velocity components and the temperature) are evaluated on cell faces with a centered approximation, even if the mesh is irregular. Finally, the remaining viscous contributions $\nabla \cdot \left(\mu(\nabla\vec{v})^t - 2/3\,\mu(\nabla \cdot \vec{v})\overline{\overline{I}} \right)$, with $\overline{\overline{I}}$ the unit tensor, are expressed with a weak formulation. It is worth noticing that mimicking the energy balances is also a convenient way to ensure some numerical stability of the numerical solutions provided the scheme is fully implicit.

A second order implicit Euler scheme is used for diffusion, with Adams-Bashforth extrapolations in time for convective and advective terms, and for the viscous part $\nabla \cdot \left(\mu(\nabla\vec{v})^t - 2/3\,\mu(\nabla \cdot \vec{v})\overline{\overline{I}} \right)$. The velocity-pressure decoupling is provided by a projection method [68]. The pressure correction $\Phi^{n+1} = p^{n+1} - p^n$ is solution of the Poisson problem:

$$\nabla^2 \Phi^{n+1} = f \quad (6.31)$$

where f is an appropriate source term and $\nabla^2\Phi^{n+1} \equiv \nabla \cdot (\nabla\Phi^{n+1})$, with $\nabla \cdot (.)$ and $\nabla(.)$ the collocated divergence and gradient. The solution of such a problem is well known to

produce unrealistic checkerboard oscillations in the solution. To prevent this, the collocated Laplacian $\nabla^2(.)$ in (Eq. 6.31) is substituted by the stable 5-points Laplacian $\widetilde{\nabla}^2(.)$ defined on staggered grids:

$$\widetilde{\nabla}^2\Phi^{n+1} = f \tag{6.32}$$

The view factors between the elements of the discretized wall surfaces and of the inlet/outlet sections (facets) were calculated by Hottel's crossed-string method. The coupling between the discretized energy equation and radiosity equation was first handled by discretization of the integral term in Eq. 6.10 by using the 1-point Gauss method, leading to a linear system of equations. Then, starting from the known wall temperatures at time t^n, we calculate the radiative heat fluxes on each facet. The radiative heat fluxes are then introduced into the boundary conditions (Eq. 6.5-6.7) to get new temperatures at the time t^{n+1}.

The resolution of the linear system of radiosity equations was performed by the Gauss method with partial pivoting. Solutions of Helmholtz problems for both the components of velocity and the temperature field, and the solution of the pressure correction equation (Eq. 6.32) were obtained by the Bi-Conjugate Gradient Stabilized method, preconditioned by an incomplete LU-decomposition. The time step value was controlled by fixing the upper bound of the Courant-Friedrich-Levy number, for example $CFL = 0.5$. The stationary solution was assumed reached when $E^{n,n+1} < 10^{-6}$ with

$$E^{n,n+1} = \max \left(\frac{\|u^{n+1} - u^n\|_2}{\|u^{n+1}\|_2 \, \Delta t^n}, \frac{\|w^{n+1} - w^n\|_2}{\|w^{n+1}\|_2 \, \Delta t^n}, \frac{\|T^{n+1} - T^n\|_2}{\|T^{n+1}\|_2 \, \Delta t^n} \right) \tag{6.33}$$

where $\|.\|_2$ is the discrete norm L_2 and $\Delta t^n = t^{n+1} - t^n$.

Validation

A thorough check of the dependence of numerical solutions with the mesh size was conducted for the natural convection case, with $H = 15.2\,cm$ and two plate spacings, $D = 7.1\,cm$ and $D = 1.71\,cm$ (Tab. 6.1). The mesh consists of $n_x \times n_z$ cells uniformly

(a) $D = 7.1\,cm$, $q_w = 300\,W/m^2$, $Ra^* = 1.52 \cdot 10^7$

$n_x \times n_z$	$\dot{m}_{in}$ $[g/(m \cdot s)]$	$\dot{m}_{out}$ $[g/(m \cdot s)]$	$d_\psi(2H)$ $[cm]$	$d_\psi(3H/2)$ $[cm]$	$\overline{h}_{c,1}$ $[W/(m^2 \cdot K)]$	$\overline{h}_{c,2}$ $[W/(m^2 \cdot K)]$
80×800	1.379	2.747	6.606	6.532	6.479	6.179
120×1200	1.380	2.747	6.605	6.531	6.470	6.172
160×1600	1.381	2.748	6.604	6.530	6.467	6.170

(b) $D = 1.71\,cm$, $q_w = 300\,W/m^2$, $Ra^* = 1.24 \cdot 10^4$

$n_x \times n_z$	$\dot{m}_{in}$ $[g/(m \cdot s)]$	$\dot{m}_{out}$ $[g/(m \cdot s)]$	$d_\psi(2H)$ $[cm]$	$d_\psi(3H/2)$ $[cm]$	$\overline{h}_{c,1}$ $[W/(m^2 \cdot K)]$	$\overline{h}_{c,2}$ $[W/(m^2 \cdot K)]$
40×800	2.629	2.658	0.4652	0	7.292	6.751
80×1600	2.633	2.658	0.4530	0	7.294	6.750
160×3200	2.633	2.658	0.4523	0	7.294	6.750

Table 6.1 – Natural convection. Effect of the grid size for (a) $D = 7.1\,cm$, (b) $D = 1.71\,cm$ and $q_w = 300\,W/m^2$

distributed in the vertical direction. To accurately represent the dynamic and thermal boundary layers, the grid was refined in the horizontal direction with a ratio between the largest and smallest cells equal to 5. Table 6.1 provides:

– the mass flow rates in the entrance section,

$$\dot{m}_{in} = \int_0^D \rho(x,0)w(x,0)\,dx, \tag{6.34}$$

and leaving the channel (only the positive values of the vertical velocity are taken into account)

$$\dot{m}_{out} = \int_0^D \rho(x,2H)\frac{w(x,2H) + |w(x,2H)|}{2}\,dx, \tag{6.35}$$

– the widths of the recirculation at the outlet of the channel ($z = 2H$) and in the section of the outlet of the heated wall ($z = 3H/2$) are calculated from

$$d_\psi(2H) = D - x_1 \text{ with } \psi(x_1, 2H) = \psi_w \tag{6.36}$$

$$d_\psi(3H/2) = D - x_2 \text{ with } \psi(x_2, 3H/2) = \psi_w \tag{6.37}$$

with ψ_w the value of the stream function along the right plate, arbitrary set to zero,

– the two convective coefficients $\bar{h}_{c,1}$ and $\bar{h}_{c,2}$.

Some comparisons are also made with the results reported in [166] for mixed convection of air ($Pr = 0.71$). In that configuration, the aspect ratio of the whole vertical channel is $A = 12$, and flow reversal occurs for some set of Reynolds number, Re, and Richardson number $Ri = Gr/Re^2$. The entire left wall is subjected to a heat flux whereas the opposite plate is thermally isolated. The solid boundaries are perfectly reflecting surfaces ($\varepsilon = 0$). The inlet conditions (Eq. 6.8) at $z = 0$ are slightly modified in order to set a uniform velocity profile at the lower section of the channel. Because the velocity is now imposed, the pressure is set free in the lower section, such that $\partial p_g/\partial\vec{n} = 0$ (same condition implicitly set on solid walls). Note that imposing a velocity profile or the coupled pressure/velocity condition deduced from the Bernoulli relation (Eq. 6.8) in the entrance section of the channel for mixed convection was discussed in Sun *et al.* [149]. The depth of flow reversal is determined by the dimensionless length build on the hydraulic diameter of the channel and defined by $Z_r^* = (H - z_r)/(2D)$ where z_r designates the ordinate satisfying the condition $\partial w/\partial x|_{x=D} = 0$. In this section, the computations are performed with a 32×128 uniform grid, the same mesh as in reference [166]. Table 6.2 shows a good agreement with a maximal discrepancy of 5.3% for $Re = 400$ and $Ri = 100$.

(Re, Ri)	(200, 100)	(200, 400)	(400, 100)	(400, 400)
Z_r^*, present results	3.71	4.44	2.34	3.53
Z_r^*, [166]	3.8	4.5	2.47	3.6
Relative difference	2.4%	1.4%	5.3%	2.0%

Table 6.2 – Dimensionless length of the reversal flow Z_r^* as a function of the Reynolds number and Richardson number.

6.4 Results

6.4.1 Comparisons with the experimental results by Webb and Hill [161]

The experimental apparatus used by Webb and Hill [161] consisted in a vertical parallel plate channel of high $2H = 30.4\,cm$ formed by two walls, one heated and the other
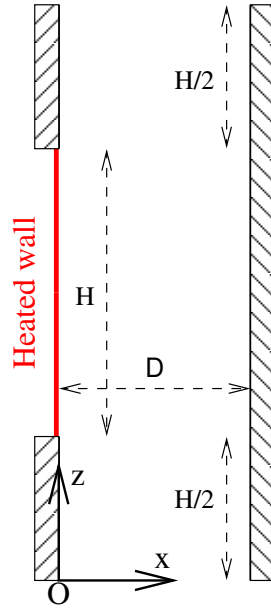
Figure 6.1 – Geometry of the parallel-plate channel.

adiabatic (Fig. 6.1). The length of the heated section was $H = 15.2\,cm$ and unheated $H/2 = 7.6\,cm$ entry and exit lengths were added to minimize radiation losses with the cold ambient environment. The three wall spacings ($D = 1.02\,cm$, $2.02\,cm$ and $3.8\,cm$), the three Ohmic dissipation fluxes at the heated wall ($q_w = 235\,W/m^2$, $300\,W/m^2$ and $375\,W/m^2$) considered in the present subsection are those used for preparing Fig. 6.2 and Fig. 6.3 displayed in [161]. The data reported in these figures were digitalized and are illustrated in the first two figures discussed below.

The first remark about the design of this experimental set-up, is that the upper extension has a significant effect on the flow, as it was demonstrated in others experimental or numerical works, [4, 7] for example.

The profiles of the temperature differences from the inlet temperature T_0 along the heated section are plotted in Fig. 6.2 for the three heating rates, a wall spacing of $D = 2.02\,cm$
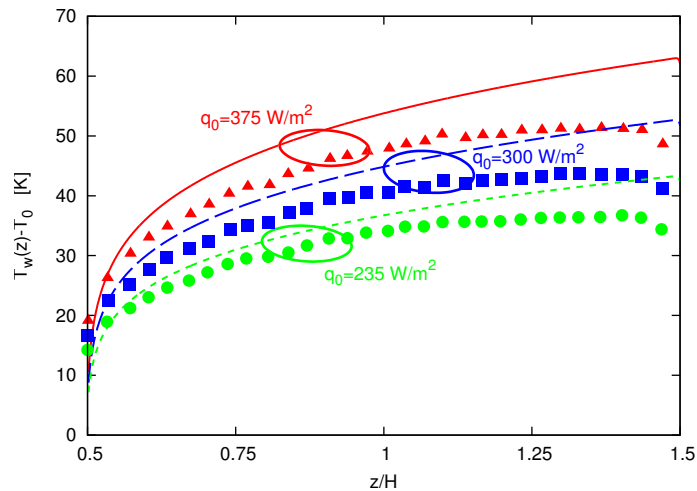
Figure 6.2 – Variations of the heated wall temperature versus z/H for the three heating rates studied by Webb et Hill [161], $D = 2.02\,cm$. Symbols are experimental data from [161].

and an emissivity of both vertical wall of $\epsilon = 0.1$, as it was assumed by Webb et Hill [161]. These fluxes are not corrected for the conduction losses, estimated less than 1.8 percent of the Ohmic heating [161]. Since the ambient air temperature was not specified in [161], an inlet temperature of $T_0 = 290\,K$ was retained. Note that lower T_0-values increase slightly the radiative heat losses from the heating section. However, computations carried out with $T_0 = 273\,K$ did not shown significant changes in the results reported in Fig. 6.2, owing to the small view factors between the heated section and the fictitious black surfaces, formed by the openings at the channel bottom and top provided that the channel aspect ratio is large enough. When the wall heat flux increases, the temperature differences along the walls increases, as expected. The maximum temperature is predicted at the top end of the heated wall, and it is followed by an abrupt temperature decrease along the adiabatic section. As can be seen, the temperature profile are similar to those reported in [161] while the present numerical results show higher temperatures, all the more since the wall heat flux is increased. These discrepancies are attributed to the conduction to the polystyrene insulation and to the conduction in the aluminum foil used for covering the adiabatic top section which acts as a fin. This point was mentioned in [161].

Figure 6.3 illustrates the ratio of radiative heat flux to the heat flux dissipated in the heated
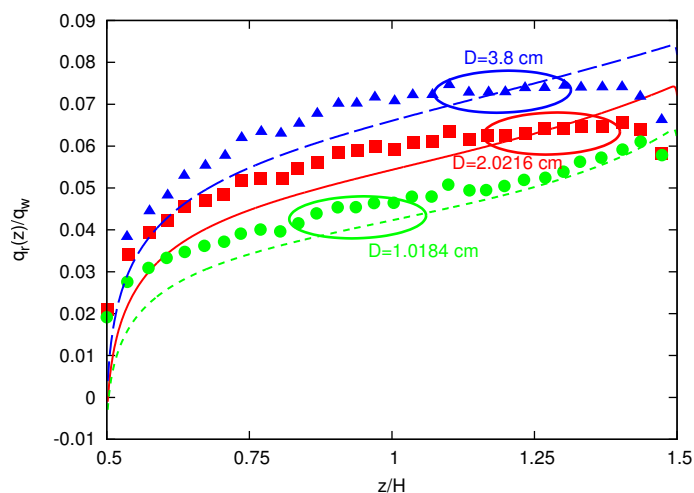
Figure 6.3 – Variations of the local radiative flux ($\epsilon = 0.1$) to the imposed wall heat flux for three wall spacings and $q_w = 300\,W/m^2$. Symbols are experimental data from [161].

section for $q_w = 300\,W/m^2$ and three plate spacings. The net radiative heat flux is positive (radiative heat losses) over the heated and adiabatic top sections of the left-hand side (LHS) wall while is it negative along both the bottom adiabatic section of the LHS-wall, and the facing unheated wall. The $q_r(z)/q_w$ profiles are closely similar to those reported in [161]. However, the discrepancies increase as the spacing increases. It should be noted that the values provided in [161] were calculated from the temperature measurements (Fig. 6.2) and, are therefore obviously smaller than those computed in the present study.

6.4.2   Pure natural convection

In order to show the importance of the effects on radiation, computations were firstly carried out for pure natural convection for various spacings and wall heat fluxes. The height of the one-sided heated vertical channel is the same as in the previous subsection [161]. The thermophysical properties of air at $T_0 = 290\,K$ are as follows: $\rho_0 = 1.2174\,kg/m^3$, $\mu_0 = 1.8058 \cdot 10^{-5}\,kg/(m \cdot s)$, $\beta_0 = 1/T_0\,K^{-1}$, $c_{p_0} = 1006.1\,J/(kg \cdot K)$, $k_0 = 0.025505\,W/(m \cdot K)$.

These properties were used for calculating the reference value of the channel Rayleigh number reported in subsequent Tables and Figures. Since the height of the heated section was set to $H = 0.152\,m$, it follows that $Ra^* = 2.825 \cdot 10^{10} q_w D^5$. Note that all computations were carried out for variable thermophysical properties based on the polynomial expressions given in [102].

At section $z = H/2$ (inlet of the heated section), the vertical velocity turns from a parabolic profile (developing flow) into an almost flat profile as the wall spacing increases, while the flow rate increases first with D and then decreases to, apparently, reaches an asymptotic value, as shown in Table 6.3.

$D\ [cm]$	1.02	1.23	1.40	1.71	2.02	2.30	3.80	7.10
Ra^*	945	$2.41 \cdot 10^3$	$4.60 \cdot 10^3$	$1.25 \cdot 10^4$	$2.88 \cdot 10^4$	$5.51 \cdot 10^4$	$6.78 \cdot 10^5$	$1.54 \cdot 10^7$
$\dot{m}_{in}\ [g/(m \cdot s)]$	1.84	2.23	2.44	2.63	2.59	2.43	1.70	1.38
$\dot{m}_{out}\ [g/(m \cdot s)]$	1.84	2.23	2.44	2.66	2.75	2.75	2.71	2.75

Table 6.3 – Mass flow rate as a function of the wall-spacing for $q_w = 300\,W/m^2$.

The vertical velocity and temperature profiles at the outlet of the heated section and at the outlet of the channel are plotted in Fig. 6.4-6.6. As soon as the fluid enters the heated section, the velocity profile for spacings larger than $D = 2.02\ cm$ exhibits a boundary layer structure, well established at the outlet section of the heated wall, as shown in Fig. 6.4(a), the maximum vertical velocity being almost independent of the spacing. On the

(a) Vertical velocity
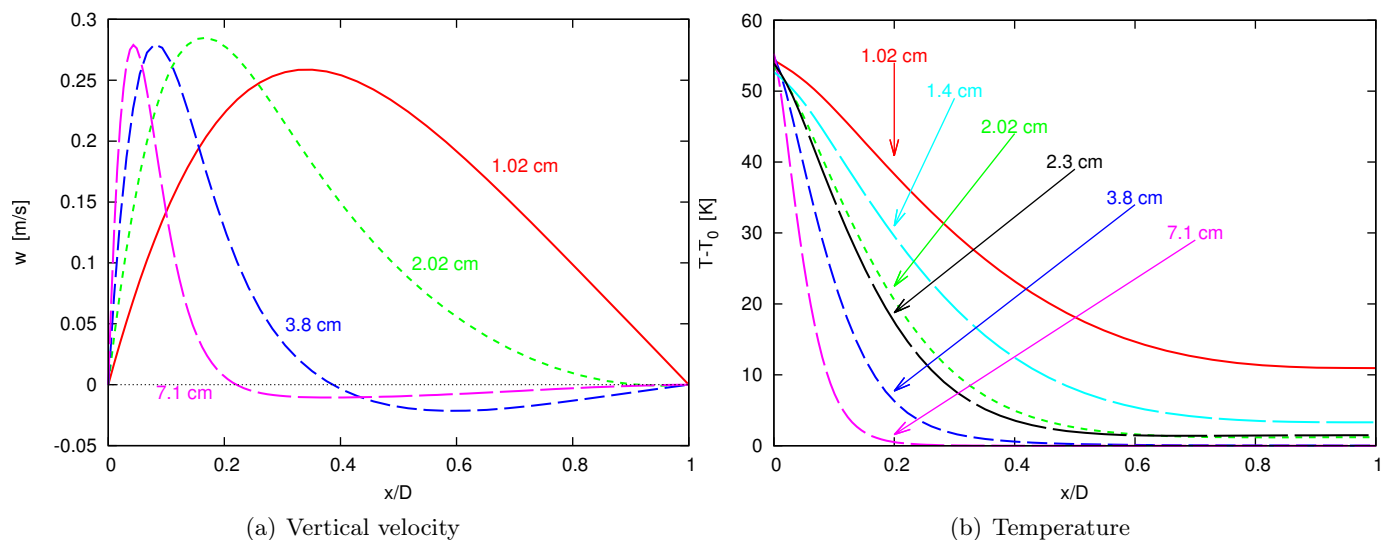
(b) Temperature

Figure 6.4 – Pure convection. (a) Vertical velocity profiles and (b) temperature at the outlet section of the heated part ($z = 3H/2$) according to the wall spacing, $q_w = 300\,W/m^2$.

other hand, negative velocities are seen for $D \geq 2.02\ cm$. That demonstrates the existence of flow reversals whose extends increase with the spacing. This pocket of downflow and recirculation was revealed experimentally for the first time by Sparrow et al. [144], with water as the working fluid. The temperature profiles reported in Fig. 6.4(b) are typical of a boundary layer flow along a single plate for $D \geq 1.4\ cm$.

At the outlet channel section, the velocity profile (Fig. 6.5(a)) are not strongly modified, except for the increase in the downflow velocities. The main changes in the flow variables

(a) Vertical velocity
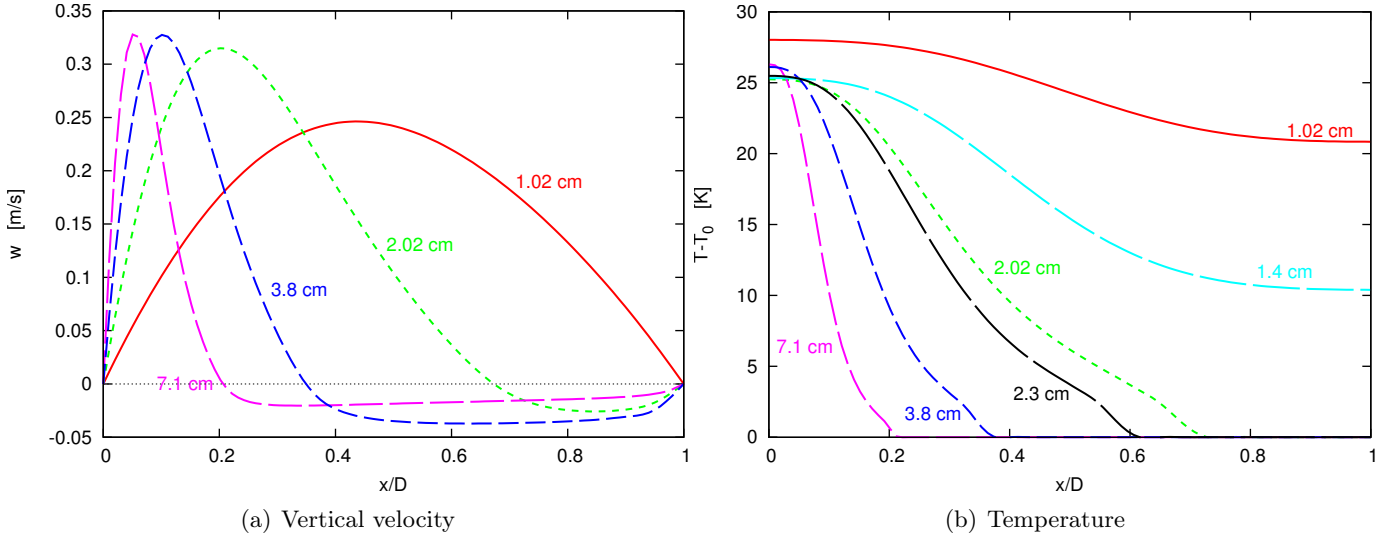
(b) Temperature

Figure 6.5 – Pure convection. (a) Vertical velocity profiles and (b) temperature at the outlet section of the channel ($z = 2H$) according to the wall spacing, $q_w = 300 \, W/m^2$.

are seen from the temperature profiles (Fig. 6.5(b)) because the flow reversal induces an abrupt transition to the surroundings temperature.

The distributions of the temperature differences from the inlet temperature T_0 along the two vertical walls are plotted in Fig. 6.6 for a heating rate of $q_w = 300 \, W/m^2$ and wall
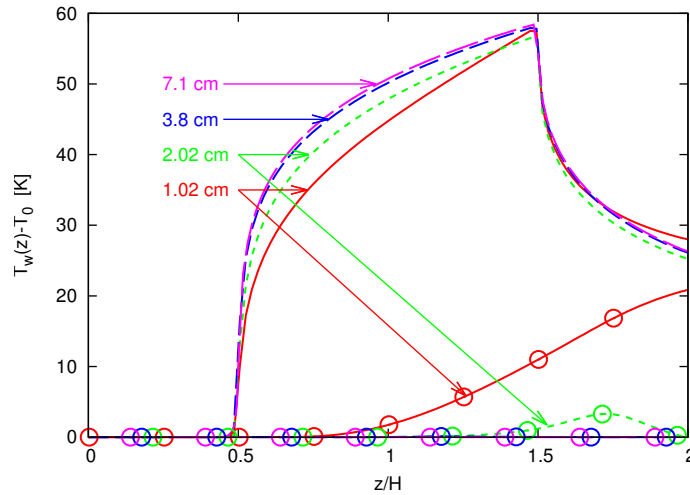
Figure 6.6 – Temperature distribution along the vertical channel walls according to the wall spacing, $q_w = 300 \, W/m^2$. The open circle symbols are for the adiabatic wall.

spacings ranging from $D = 1.02 \, cm$ to $D = 7.1 \, cm$ (i.e $945 \leq Ra^* \leq 1.54 \cdot 10^7$ with the thermophysical properties of air taken at $T_0 = 290 \, K$ for evaluating Ra^*). When the wall spacing augments, the temperatures of the heated wall increase and reach their maximum values for $D \approx 2.3 \, cm$, showing that the single-plate limit is approached. The bottom adiabatic section is almost uniformly at T_0 while the temperature of the top adiabatic section decreases abruptly from a maximum value almost independent of D provided that $D \geq 1 \, cm$: $T_{max} \approx 346 \, K$. This result indicates that the minimum heat transfer coefficient,

$h_{min} = q_w/(T_{max} - T_0)$, does not depend on D. On the other hand, the average temperature of the heated section increases first with D and reaches then an almost constant value for $D \geq 2.3\,cm$. Therefore, the mean heat transfer coefficient, calculated by using either Eq. 6.15 or Eq. 6.18, decreases at first with the wall spacing. For $1.02\,cm \leq D \leq 2.3\,cm$, the adiabatic RHS-wall is heated by the flow of hot air at its upper part, and the decrease in its temperature as D increases shows the transition to the asymptotic regime, for which the RHS-wall is uniformly at T_0.

Figure 6.7 shows the isotherms (left side) and streamlines (right side) for $D = 2.02\,cm$

<center>(a) Streamlines   (b) Isotherms</center>
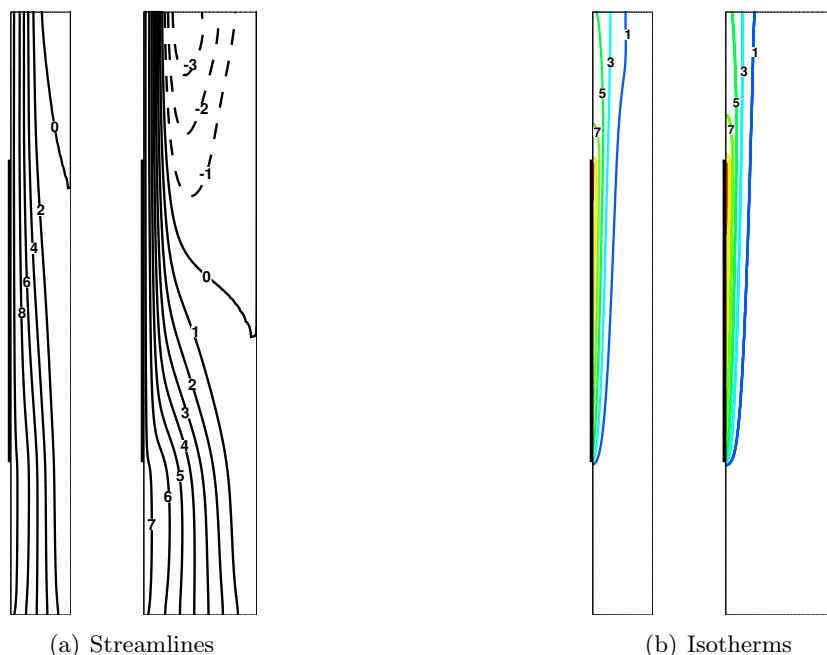
Figure 6.7 – Pure natural convection. (a) Streamlines $\psi_i/[g/(m \cdot s)] = 0.25 \times i$ and (b) isotherms $T_i/[K] = 290 + 5 \times i$ for $D = 2.02\,cm$ (left) and $D = 3.8\,cm$ (right), $q_w = 300\,W/m^2$. The horizontal scales are enlarged by 50%.

$(Ra^* = 945)$ and $D = 3.8\,cm$ $(Ra^* = 6.78 \cdot 10^5)$ in the case $q_w = 300\,W/m^2$. The dimensional steamfunction $([kg/(m \cdot s)])$ for 2D and variable density flows is calculated from its definition as

$$\rho\,u = \frac{\partial\psi}{\partial z} \quad , \quad \rho\,w = -\frac{\partial\psi}{\partial x} \tag{6.38}$$

In what follows, the plots of the streamlines are for a streamfunction value at the RHS wall arbitrarily set to zero. The dashed lines (negative ψ-values) are for the streamlines into the pocket of flow recirculation. The streamlines show boundary layer development along the heated wall and penetration of a downcoming flow along the RHS-wall. At the stagnation point located very close to the RHS-wall, the downward flow starts to merge into the flow coming from the inlet section. The formation of reversal flow results from air drawn in through the channel exit due to insufficient incoming air through the inlet. The size of the pocket-like streamlines increase with Ra^* (or D) and the penetration depth of the recirculating flow increases also. This result is in good agreement with the experimental and numerical studies by Sparrow et al. [144] for a one-sided heated vertical channel and by Kihm et al. [88] for isothermal vertical walls.

The recirculation pocket extends both downward and in width as D increases, as illustrated in Fig. 6.7. The width d_ψ of the recirculation at the outlet of the heated section ($d_\psi(3H/2)$ at $z = 3H/2$, Eq. 6.37) and at the channel outlet ($d_\psi(2H)$ at $z = 2H$, Eq. 6.36), and the

<center>111</center>

penetration length L_p are provided in Fig. 6.8 versus the wall spacing. These quantities are

(a) Recirculation widths

(b) Penetration length
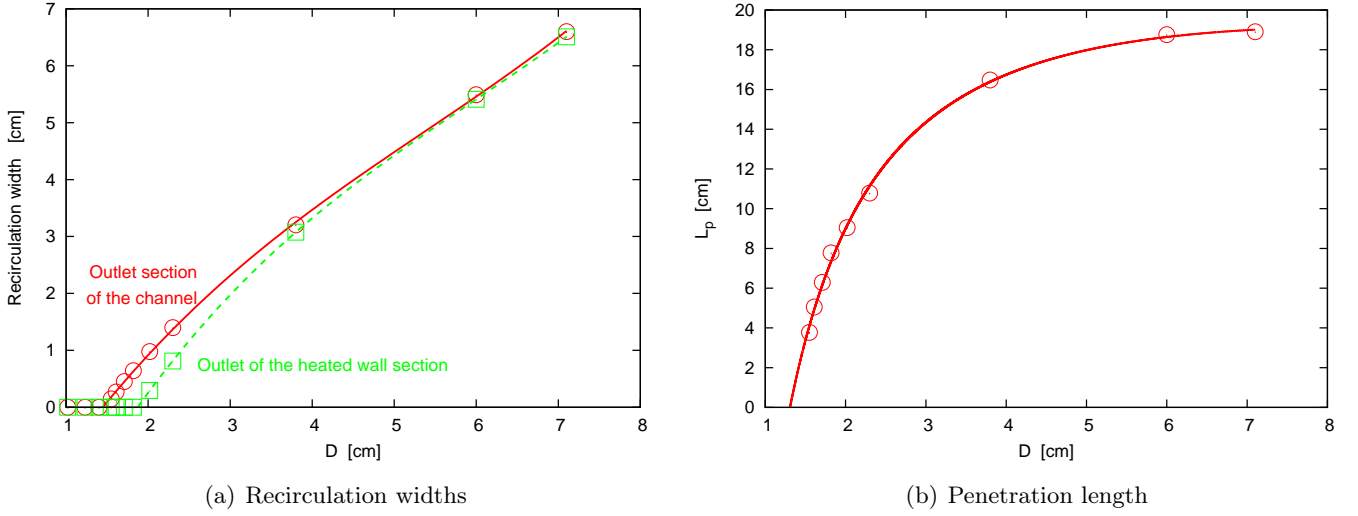
Figure 6.8 – (a) Recirculation widths and (b) penetration length (L_p) versus the channel width for $\epsilon = 0$ and $q_w = 300\,W/m^2$

based on the location of the $\psi = 0$ value of the streamfunction: the width of the circulation at any z-position is the distance between the $\psi = 0$ streamline and the RHS-wall, and the penetration length is the distance from the outlet section at which the $\psi = 0$ streamline separates from the RHS-wall (stagnation point). Figure 6.8(a) shows the increases in the recirculation width versus the wall spacing at the two aforementioned channel sections. It can be seen that the wall spacing for the onset of the recirculation appears to be very close to $D = 1.5\,cm$ and that the recirculation width increases almost linearly with D (or as $Ra^{*1/5}$), and that $d_\psi(3H/2) \approx d_\psi(2H)$ for $D \geq 4\,cm$. The penetration length (Fig. 6.8(b)) increases sharply with D just after the formation of a recirculating flow while a slow augmentation of L_p is observed for $D \geq 4\,cm$. This behavior is in fairly good agreement with that reported in Kihm et al. [88] for symmetrically isothermal walls and much smaller modified-Rayleigh numbers.

The mass flow rate ($\dot{m}_{in}$, Eq. 6.34) through the inlet section is reported in Table 6.3 as a function of the wall spacing. As can be seen, $\dot{m}_{in}$ reaches a maximum for $D \approx 2\,cm$, and decreases thereafter. An optimal plate spacing for natural convection between an array of symmetrically heated plates was first demonstrated at the same time by Bar Cohen and Rohsenow [18] and Bejan [21], and discussed in details in a recent paper by Sun et al. [150]. The present results show that such an optimum exists also for asymmetrically heated channels, but no attempt at correlating this spacing with Ra^* was done for the specific case considered, because it is clear that it depends also on the length of the adiabatic upper section (chimney effect). However, the main difference with symmetric heating is that the reduction in the mass flow rate at the inlet section occurs almost simultaneously with the onset of a flow reversal at the top part of the channel. From the present computations for $q_w = 300\,W/m^2$, it can be concluded that the optimal spacing is close to $D = 0.75\,cm$ if it is based on the D-value at which the mean and maximum temperatures of the heated section reach asymptotic values ($\overline{T} \approx 333\,K$, $T_{max} \approx 347\,K$).

From the values of the mass flow rate through the outlet section reported in Table 6.3, $\dot{m}_{out}$ (Eq. 6.35), it can be seen that $\dot{m}_{in} = \dot{m}_{out}$ up to $D = 1.4\,cm$. Since $\dot{m}_{out}$ is the sum of $\dot{m}_{in}$ plus the upward recirculating flow, the difference $\dot{m}_{out} - \dot{m}_{in}$ characterizes the onset and intensity of the recirculation. From Table 6.3, it can be seen that $\dot{m}_{out}$ is almost constant

for $D \geq 2.02\,cm$ while $\dot{m}_{in}$ decreases (see also Fig. 6.13). The effect of the recirculation is to concentrate the streamlines corresponding to the induced air flow at the entrance region ($\psi > 0$) and to provide enough cold air, suck in through the outlet section, in order to feed the boundary layer. Hence the rise in the boundary layer thickness as D increases is due to the downcoming flow through the outlet section.

The present numerical results can be well fitted by the least square method with correlation coefficients greater than $r^2 = 0.99$. The correlations turned out to be:

$$\overline{Nu}_{c,1} = 0.859 Ra^{*0.183}, \ \ \overline{Nu}_{c,2} = 0.763 Ra^{*0.188},$$
$$\overline{Nu}_{\frac{1}{2}} = 0.721 Ra^{*0.189}, \ \ \theta_{max} = 1.86 Ra^{*-0.201} \quad (6.39)$$

The agreement between the above correlations and those reported from the experimental results by Webb and Hill [161] for the same configuration could considered as rather good. Table 6.4 gives a more realistic view about the discrepancies between these corre-

	$Ra^* = 10^3$	$Ra^* = 1.5 \cdot 10^7$
$\overline{Nu}_c = 0.82 Ra^{*0.194}$ [161]	3.13	20.2
$\overline{Nu}_{c,1} = 0.859 Ra^{*0.183}$ (present)	3.04	17.7
$\overline{Nu}_{c,2} = 0.763 Ra^{*0.188}$ (present)	2.80	17.0
$\overline{Nu}_{\frac{1}{2}} = 0.58 Ra^{*0.206}$ [161]	2.41	17.4
$\overline{Nu}_{\frac{1}{2}} = 0.721 Ra^{*0.189}$ present	2.66	16.4
$\theta_{max} = 1.735 Ra^{*-0.220}$ [105]	0.380	0.0458
$\theta_{max} = 1.86 Ra^{*-0.201}$ (present)	0.464	0.0672

Table 6.4 – Comparisons between the present results with previous correlations [105, 161] for the range of channel Rayleigh numbers considered (single-plate regime).

lations for the lowest and highest Rayleigh numbers corresponding to both works. Note that the range of Ra^* considered is within the so-called single-plate regime. The first result is that the discrepancies increase with Ra^* from 2.9% to 13% for $\overline{Nu}_{c,1}$. The second result clearly indicates that the definition of the average heat transfer coefficient following Eq. 6.15 or Eq. 6.18 has a significant influence (up to 8% for $Ra^* = 10^3$). This finding was not mentioned previously. The differences between the experimentally [161] and numerically determined midheight Nusselt numbers are within the range 6.1% to 11% for $10^3 \leq Ra^* \leq 1.5 \cdot 10^7$. About the maximum heated wall temperature, the discrepancies with the experimental results from Manca et al. [105] can be attributed to different chimney effects in the two studies since the upper extension was larger than the channel width in [105].

6.4.3 Effects of surface radiation on the flow field and heat transfer

From the above result discussion (subsection 6.4.1), it is clear that radiative exchanges amongst surfaces have a significant effects on the flow field and heat transfer when the facing plates are submitted to imposed heat fluxes. Figure 6.9 shows the effect of radiation on the temperature distributions along the two vertical walls according to their emissivity, assumed equal for both walls. The selected case is $D = 3.8\,cm$ and $q_w = 300\,W/m^2$, i.e. the largest configuration experimentally studied in [161]. As can be seen, the temperature
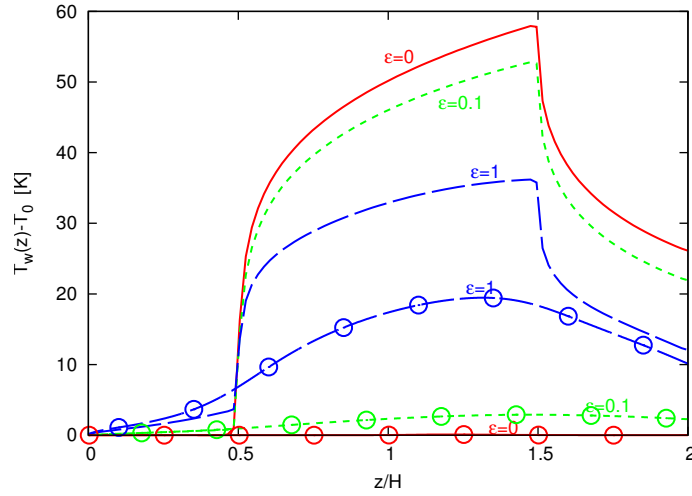
Figure 6.9 – Variation of the heated wall temperature with height according to the emissivity of the vertical walls for $D = 3.8\,cm$ and $q_w = 300\,W/m^2$. The open circle symbols are for the adiabatic wall.

of the heated surface decreases when the emissivity is increased, the opposite being predicted for the facing adiabatic surface whose temperature increases. Therefore, radiation modifies the flow field, and hence the wall convective heat transfer. This point raises some doubts about the interpretation of experimental results and derivation of Nusselt number correlations when the effects of radiation are not properly evaluated. For example, if the radiative exchanges amongst the surfaces can be calculated from the surface temperature measurements, the convective heat flux profiles can be easily obtained (provided that the conductive heat losses are accurately estimated). Nevertheless, the temperature distribution along the heated surface, used in the definition of the local heat transfer coefficient, results from the coupling between radiation and convection. Therefore, the heat transfer coefficient is overestimated for a surface cooled by radiation and underestimated if heated by radiation.

The effect of radiation on the vertical velocity profiles at three channel cross sections are seen in Figs. 6.10(a)-6.10(c). The increase in the velocities (and in flow rate because the density variations from the channel inlet are very small) with emissivity at the inlet section of the heated wall is clearly seen in Fig. 6.10(a). The reason is that the adiabatic RHS-wall becomes thermally active as soon as its temperature raises significantly under the effect of surface radiation. When the fluid proceeds upwards the boundary-layer like velocity profile along the heated wall turns into a boundary layer profile of an asymmetrically heated channel, as seen in 6.10(b) and 6.10(c) for $\varepsilon = 1$. Furthermore, the flow reversal disappears for a wall emissivity as small as $\varepsilon = 0.1$. The profiles of the temperature differences reported in Figs. 6.10(d)-6.10(f) give another view of the decrease in the heated wall temperature, and increases of the fluid and adiabatic wall temperatures.

The net radiative heat flux distribution along the LHS-heated wall and RHS-adiabatic wall are drawn in Figs. 6.11(a) and 6.11(b) for $\varepsilon = 0.1$ and $\varepsilon = 1$, respectively ($D = 2.02\,cm$, $q_w = 300\,W/m^2$). Positive $q_r(z)$-values are for radiative cooling and negative ones for radiative heating. For both cases, the RHS-wall is heated by radiation over most of its surface and the heating rate increases sharply with emissivity. The bottom adiabatic part of the LHS-wall is heated by the radiation reflected by the RHS-wall, and cooled by radiation exchanges with the cold inlet section, assumed to be a black surface at $T_0 = 290\,K$. Since

(a) Vertical velocity profile, $z = H/2$

(b) Vertical velocity profile, $z = 3H/2$

(c) Vertical velocity profile, $z = 2H$

(d) Temperature increase, $z = H/2$

(e) Temperature increase, $z = 3H/2$

(f) Temperature increase, $z = H$
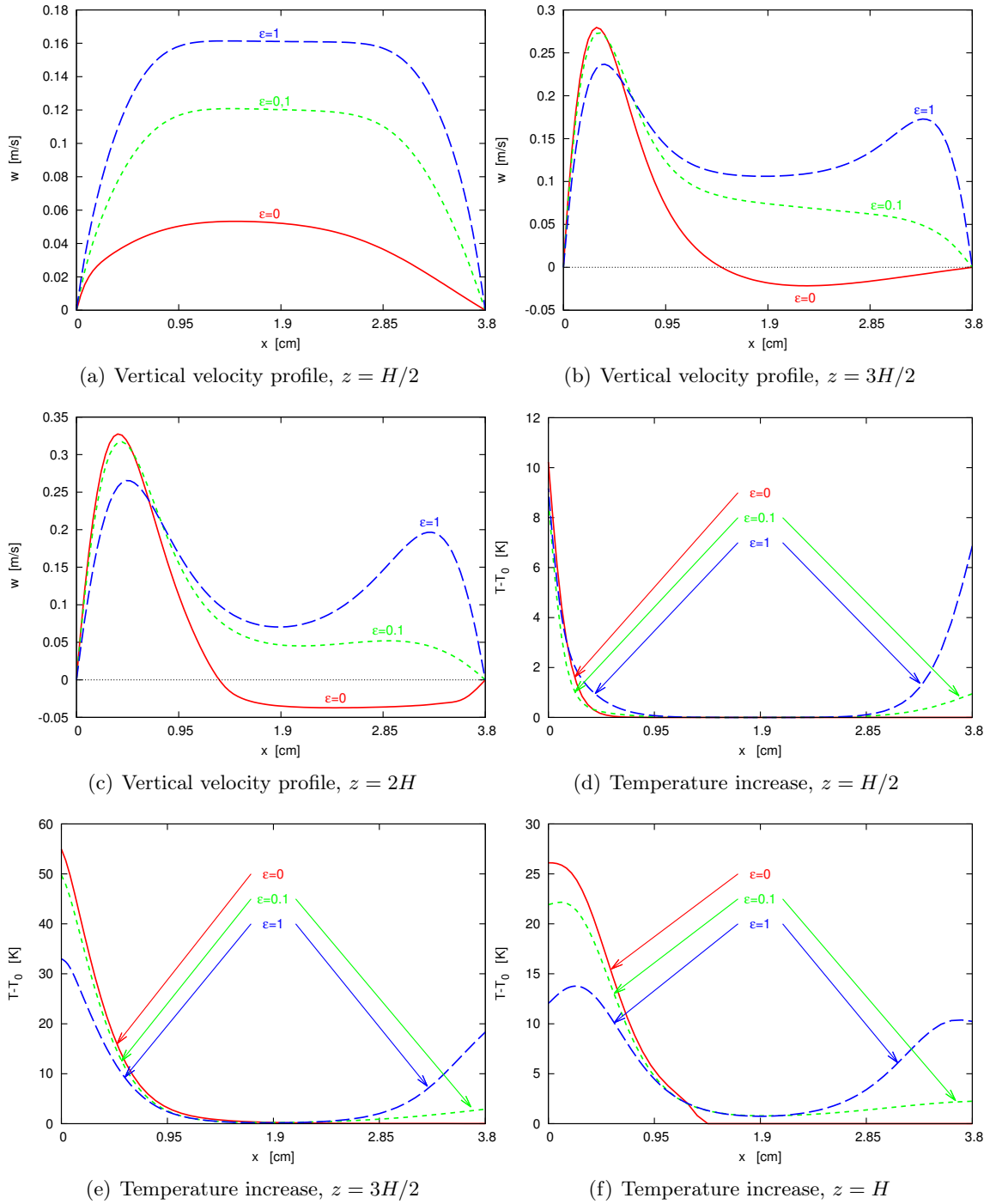
Figure 6.10 – Vertical velocity profiles (a) at the inlet of the heated wall section ($z = H/2$), (b) at the outlet of the heated wall section ($z = 3H/2$), (c) at the outlet section of the channel ($z = 2H$) and temperature gap profiles (d) at the inlet of the heated wall section ($z = H/2$), (e) at the outlet of the heated wall section ($z = 3H/2$), (f) at the outlet section of the channel ($z = 2H$) as a function of the emissivity of the vertical walls ($D = 3.8\,cm$, $q_w = 300\,W/m^2$).

the view factor between the inlet section and the bottom of the walls is rather small, the adiabatic bottom of the heated wall is always heated by radiation. This result is just specific to the small D-value considered. More significant is the relative magnitude of the
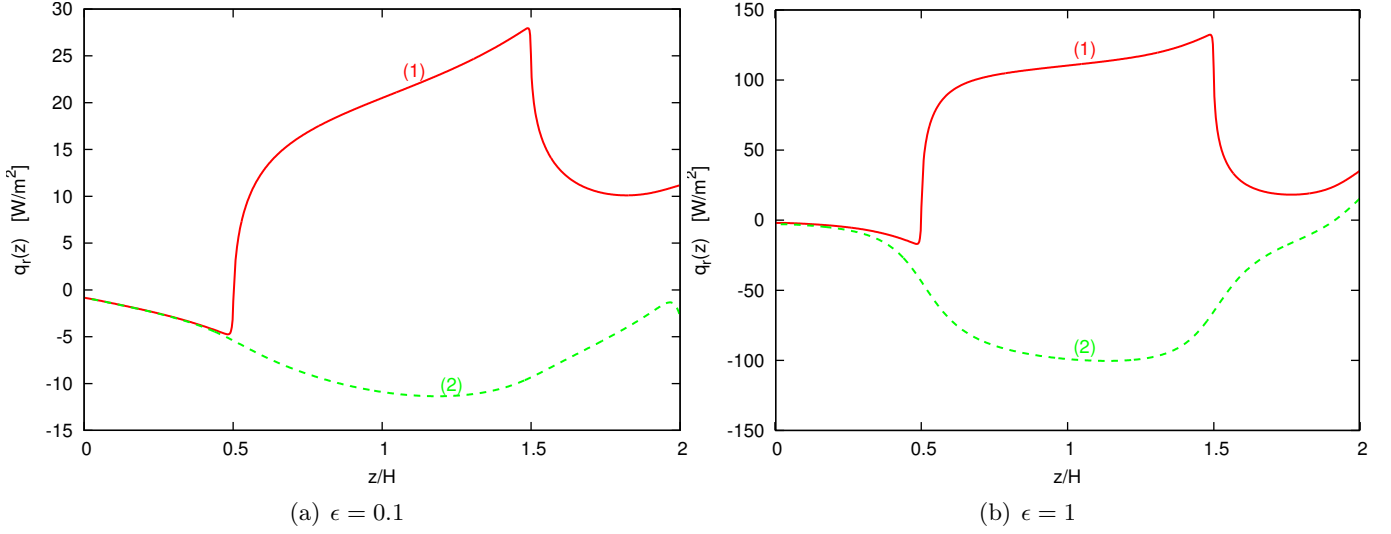
Figure 6.11 – Distribution of the net radiative heat flux densities along (1) the heated wall and (2) along the adiabatic wall, with (a) $\epsilon = 0.1$ and (b) $\epsilon = 1$, for $D = 2.02\,cm$ and $q_w = 300\,W/m^2$.

radiative heat losses, $\overline{q}_r$, to the heating flux, q_w, along the heated section. For $\varepsilon = 0.1$ (as in the experiments by Webb et Hill [161]), the average radiative heat flux is $\overline{q}_r = 23\,W/m^2$ (6% of q_w) and reaches $\overline{q}_r = 118\,W/m^2$ (more than 40% of q_w) for $\varepsilon = 1$. As expected, the peaks in $q_r(z)$ correspond to the maximum in wall temperature. The results are that, both the average and maximum temperatures of the heated section decrease under the effects of surface radiation. We will consider in what follows the effect of surface radiation on the convective Nusselt number when introducing a decoupling between convective and radiative modes, as it is usually done when maximum surface temperatures do not exceed about 10% of the inlet gas temperature (in K).

Comparisons between the isothermal and streamline patterns shown in Fig. 6.7 for $\varepsilon = 0$ and those in Fig. 6.12 for $D = 2.02\,cm$ and $3.8\,cm$ clearly exhibit the large changes in the flow topology under the effects of surface radiation for $\varepsilon = 0.1$ and $\varepsilon = 1$. These patterns demonstrate that radiation exchanges lead to a modification in the thermal conditions from a one-wall heating to an asymmetric heating, with the disappearance of the flow reversal. The insulated wall being heated by radiation, the downcoming flow from the outlet section cannot persist as soon as the temperature of that wall exceeds just a little the surrounding temperature. That happens at very low emissivity of the walls. When the radiative heating of the insulated wall is large enough, a thermal boundary layer develops along the wall, and starts at a lower z-elevation than at the heated wall. These observations may explain why flow reversal are difficult to observe experimentally if the working fluid is a gas. On the other hand, the recent experiments conducted by Ospir et al. [120] with water as the working fluid and for the same boundary conditions as in the present study provide very reliable pictures on the flow reversal.

The variation of the mass flow rate reported in Fig. 6.13 for $q_w = 300\,W/m^2$ indicates continuous increases in $\dot{m}_{in}$ with the wall spacing for $\varepsilon = 0.1$ and $\varepsilon = 1$ since any downcoming air flow is predicted for both wall emissivities. On the other hand, the flow reversal discussed previously for $\varepsilon = 0$ leads to a maximum in the flow rate at the inlet section (see Table 6.3) while the outcoming flow rate at the outlet section $\dot{m}_{out}$ (Eq. 6.35) is almost constant for $D \geq D_{opt}$, as seen in Fig. 6.13. The influence of surface radiation on

(a) $D = 2.02\,cm$, $\epsilon = 0.1$ (b) $D = 2.0216\,cm$, $\epsilon = 1$ (c) $D = 3.8\,cm$, $\epsilon = 0.1$ (d) $D = 3.8\,cm$, $\epsilon = 1$
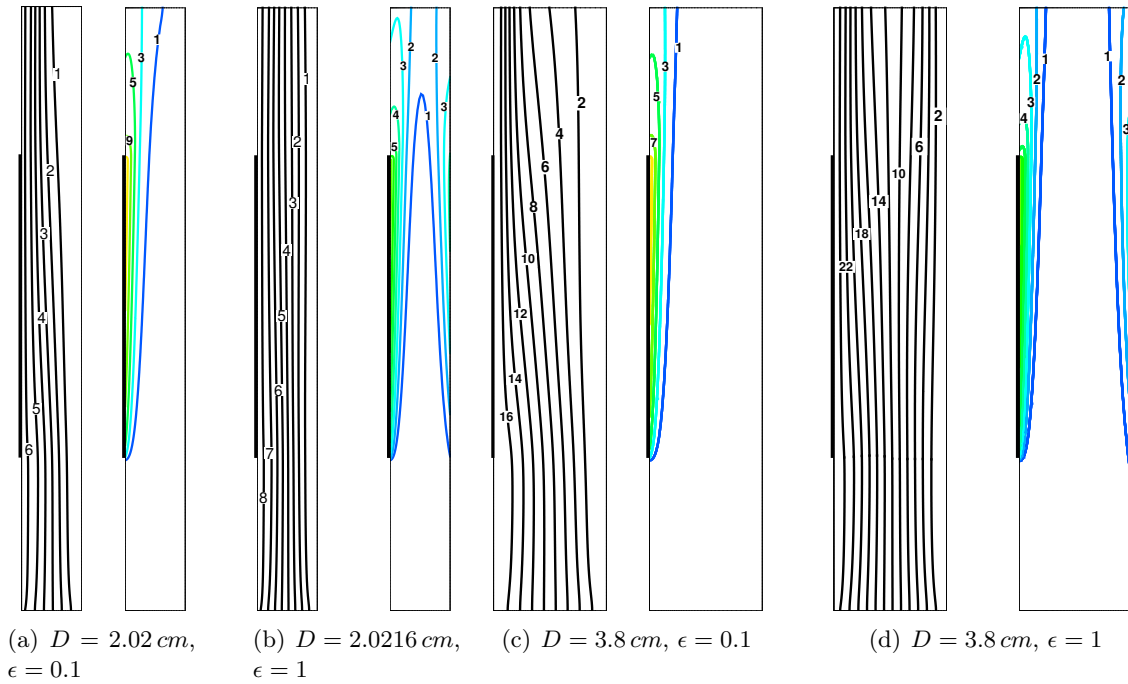
Figure 6.12 – Effect of surface radiation on streamlines $\psi_i/[g/(m \cdot s)] = 0.25 \times i$ (left) and isotherms $T_i/[K] = 290 + 5 \times i$ (right) with $q_w = 300\,W/m^2$ and for (a) $D = 2.02\,cm$, $\epsilon = 0.1$, (b) $D = 2.02\,cm$, $\epsilon = 1$, (c) $D = 3.8\,cm$, $\epsilon = 0.1$, (d) $D = 3.8\,cm$, $\epsilon = 1$. The horizontal scales are enlarged by 50%.
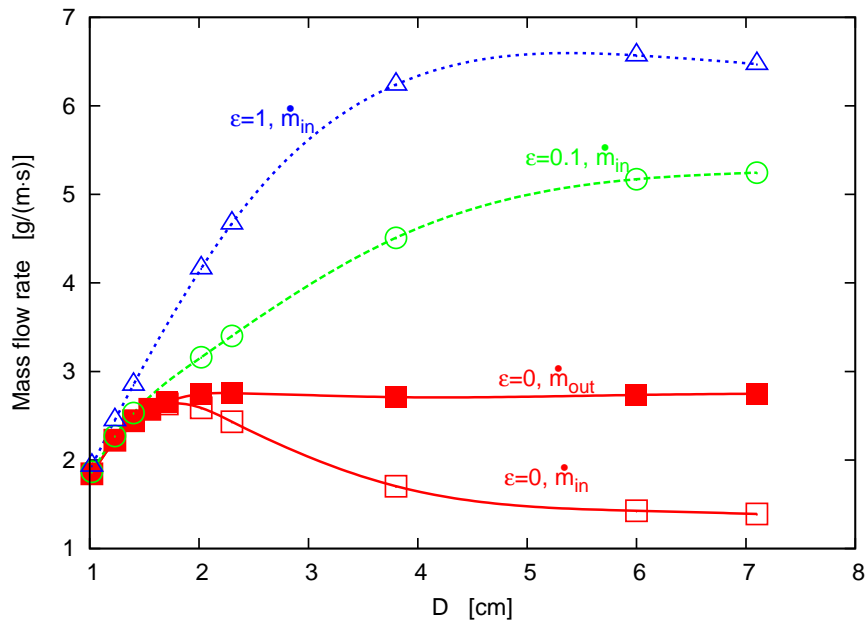
Figure 6.13 – Mass flow rate versus the wall spacing for three wall emissivities, $q_w = 300\,W/m^2$; $\dot{m}_{out} = 0$ for $\epsilon = 0.1$ and $\epsilon = 1$.

the mean and maximum temperature of the heated section is reported in Table 6.5 for the minimum and maximum plate spacings considered in the present study. The overall effect is a reduction in both $\overline{T}$ and T_{max} as ε and D increase. Such a reduction is in part

117

		$D = 1.02\,cm$	$D = 7.1\,cm$
		$(Ra^* = 945)$	$(Ra^* = 1.54 \cdot 10^7)$
$\varepsilon = 0$	$\overline{T}$	332.8	338.6
	T_{max}	347.7	347.7
$\varepsilon = 0.1$	$\overline{T}$	331.2	334.4
	T_{max}	344.9	341.4
$\varepsilon = 1$	$\overline{T}$	321.2	320.7
	T_{max}	331.7	323.5

Table 6.5 – Comparisons between the average and maximum heated wall temperatures for $q_w = 300\,W/m^2$.

due to the radiative exchanges with the outlet section assumed as a black surface at T_0. That explains why the effect of radiation is more important as the modified Rayleigh is increased. Here again, this result is specific to the cases considered because the variations in Ra^* are only due to changes in D while the channel height is kept constant. Hence, it cannot be concluded that radiation effects increase with the Rayleigh number, as it has been assumed in many papers.

Correlations

Owing to the present definition of the conduction-to-radiation parameter, the N_R-range is $N_R = 0.748$ for an inlet air temperature $T_0 = 290K$ and $q_w = 300\,W/m^2$. The radiative Nusselt is therefore of the order of magnitude of the convective Nusselt number for black surfaces. Note that the emissivity is not accounted for in the definition of N_R: the influence of surface radiation is thus much smaller for low surface emissivities than it seems, just by considering only the N_R value.

The convective and radiative Nusselt numbers defined by Eq. 6.29 are reported in Fig. 6.14. In comparison with $\varepsilon = 0$, $\overline{Nu}_{c,2}$ is slightly modified for $\varepsilon = 0.1$ while its reduction is more
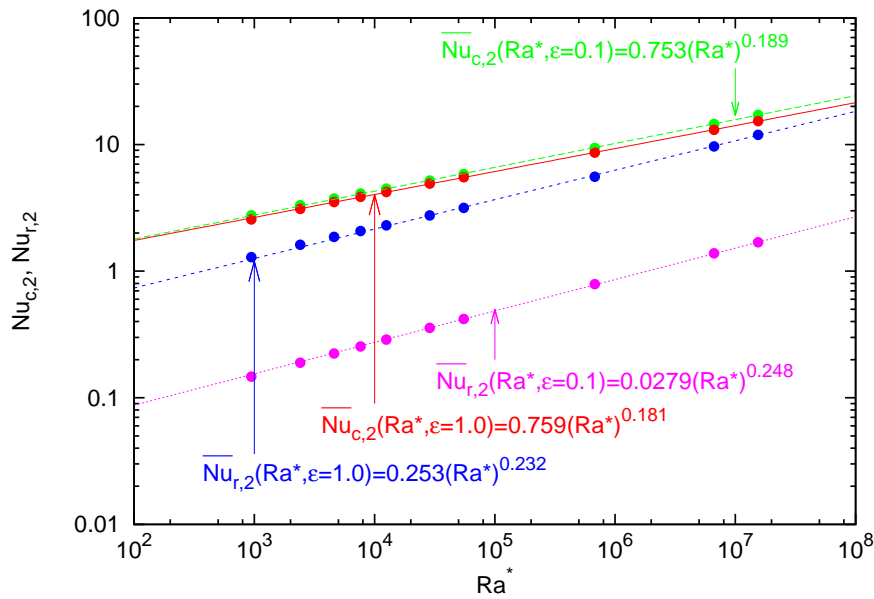
Figure 6.14 – Radiative ($\overline{Nu}_{r,2}$) and convective ($\overline{Nu}_{c,2}$) Nusselt numbers (eq. 6.30) vs the channel Rayleigh number for two emissivities of the vertical walls.

significant for $\varepsilon = 1$. In that case $\overline{Nu}_{r,2}$ is of the order of $\overline{Nu}_{c,2}$. The combined radiation convection effect produces a reduction in the maximum temperature of the heated wall, all the more large since the plate spacing and the emissivity increase. For $q_w = 300\,W/m^2$ and $\varepsilon = 1$, that reduction lies between $16.0\,K$ for $D = 1.02\,cm$ and $24.2\,K$ for $D = 7.1\,cm$. The present computations lead to the following correlations

$$\overline{Nu}_{c,2} = 0.753 Ra^{*0.189} \quad , \quad \overline{Nu}_{r,2} = 0.0279 Ra^{*0.248} \quad \text{for} \quad \varepsilon = 0.1 \tag{6.40}$$

$$\overline{Nu}_{c,2} = 0.759 Ra^{*0.181} \quad , \quad \overline{Nu}_{r,2} = 0.253 Ra^{*0.236} \quad \text{for} \quad \varepsilon = 1 \tag{6.41}$$

$$\theta_{max} = 1.88 Ra^{*-0.207} \text{ for } \varepsilon = 0.1 \,, \qquad \theta_{max} = 1.60 Ra^{*-0.226} \text{ for } \varepsilon = 1 \tag{6.42}$$

6.4.4 On the procedures used for the determination of the convective heat transfer coefficient from temperature measurements

As discussed in the previous sections, surface radiation has a strong influence on the flow field and makes difficult the observation of air flow reversals. Its effect on the total heat transfer rate at the heated wall is also significant when mirror like wall surfaces are not used in experimental set up. Since emissivities as low as $\varepsilon = 0.05$ are difficult to maintain due to oxidation produced by the air flow (except if the wall are covered with gold films), most experiments conducted for different heat fluxes prescribed to the walls are for non negligible combined effects of surface radiation and natural convection. The usual ways employed to determine the convective heat transfer coefficient are first the evaluation of the radiative heat flux from the temperature measurements along the walls. The convective heat flux is then obtained, just by subtraction, i.e $q_{cv}(z) = q_w - q_r(z)$ (provided that the conductive heat losses have been properly considered in the evaluation of q_w (i.e. $q_w = q_{Ohmic} - q_{conduction}$)).

Such a procedure has been followed, for example, by Webb and Hill [161] and more recently by Krishnan et al. [91] who used a combined experimental and numerical approach. Since we are modeling the full coupled heat transfer modes, it is easy to proceed exactly as it was done by experimentalists.

As an example, the case $D = 2.02\,cm$ and $q_w = 300\,W/m^2$ is considered (note that the effects of radiative exchanges with the cold inlet or outlet sections are rather weak in that case). The coupled solutions are displayed in Fig. 6.12(a) ($\varepsilon = 0.1$) and in Fig. 6.12(b) ($\varepsilon = 1$). The heat transfer results for the three approximate approaches are summarized in Table 6.6. The corresponding streamlines and isotherms are displayed in Figs. 6.15 and 6.16 when the radiative heat fluxes or temperature distributions computed from the coupled problem for $\varepsilon = 0.1$ and $\varepsilon = 1$, respectively, are used to generate the thermal boundary conditions on the heated section: $\overline{q}'_w$, $T_w(z)$ or $\overline{T}$.

- $\overline{q}_r$ is subtracted from q_w (rows 2a and 3a in Table 6.6).
  First, the average radiative flux at the heated section is calculated from the coupled computations: $\overline{q}_r = 19\,W/m^2$ for $\varepsilon = 0.1$ and $\overline{q}_r = 108\,W/m^2$ for $\varepsilon = 1$.

  Computations were carried out by setting $\varepsilon = 0$ and $\overline{q}'_w = q_w - \overline{q}_r$. The plots of the isotherms and streamlines reported in Figs. 6.15(a) and 6.16(a) exhibit large differences both between the true flow fields (Figs. 6.12(a) and 6.12(b)) while it resembles more or less those which are in the absence of surface radiation (i.e. for $q_w = 300\,W/m^2$, row 1 in Table 6.6). Hence it could be assumed that this procedure

		B.C. type	q_w $[W/m^2]$	Ra^*	$\overline{h}_{cv,1}$ $[W/(m^2 \cdot K)]$	$\overline{h}_{cv,2}$ $[W/(m^2 \cdot K)]$	T_{max} $[K]$
1	$\varepsilon = 0$	q_w (N.C.)	300	$2.88 \cdot 10^4$	7.06	6.59	346.5
2	$\varepsilon = 0.1$	q_w (Coupled)	300	$2.88 \cdot 10^4$	7.05	6.56	342.5
2a	$\varepsilon = 0$	$\overline{q}'_w$	281	$2.69 \cdot 10^4$	6.98	6.52	343.5
2b	–	$T_w(z)$	282*	$2.71 \cdot 10^4$	6.63	6.60	342.7
2c	–	$\overline{T}_w$	268*	$2.57 \cdot 10^4$	6.27	6.27	332.8
3	$\varepsilon = 1$	q_w (Coupled)	300	$2.88 \cdot 10^4$	6.67	6.20	327.2
3a	$\varepsilon = 0$	$\overline{q}'_w$	192	$1.85 \cdot 10^4$	6.47	6.11	329.3
3b	–	$T_w(z)$	194*	$1.86 \cdot 10^4$	6.51	6.25	327.4
3c	–	$\overline{T}_w$	186*	$1.78 \cdot 10^4$	5.99	5.99	321.0

Table 6.6 – Comparisons between the different procedures used for the convective part ($D = 2.02\,cm$). N. C.: pure natural convection, Coupled: combined radiation and natural convection, * denotes an output from the temperature distribution, Ra^* are based on the average wall heat flux given in column 4.

(a) $\overline{q}'_w = 281\,W/m^2$ and adiabatic surfaces

(b) $T_w(z)$ and average temperatures on other walls, draft=false

(c) $\overline{T}_w = 332.8\,K$ and average temperatures on other walls
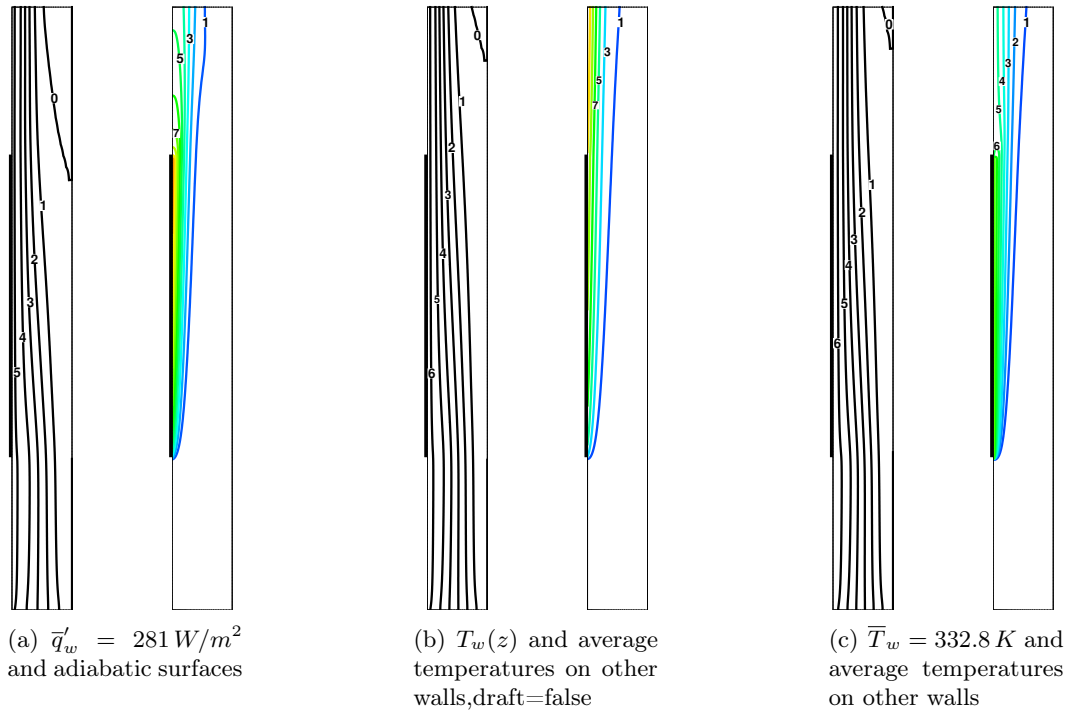
Figure 6.15 – Natural convection. Streamlines $\psi_i/[g/(m \cdot s)] = 0.5 \times i$ (left) and temperature $T_i/[K] = 290 + 5 \times i$ (right) for (a) $\epsilon = 0$, $\overline{q}'_w = 280\,W/m^2$ and adiabatic surfaces, (b) $\epsilon = 0$, $T_w(z)$ and average temperatures on other walls, (c) $\epsilon = 0$, $\overline{T}_w = 332.8\,K$ and average temperatures on other walls. The horizontal scales are enlarged by 50%.

leads to wrong calculations of the heat transfer rate. However, the overall convective heat transfer is weakly altered by the presence of a flow reversal, as it was also noted by Kihm et al. [88]. Comparisons between the $\overline{h}_{c,1}$, $\overline{h}_{c,2}$ and T_{max} reported in rows 1, 2 and 2a for $\varepsilon = 0.1$ show that the differences in the maximum wall temperature are within 1%. Therefore the procedure followed by Webb and Hill Webb et Hill [161]

(a) $\bar{q}'_w = 192\,W/m^2$ and adiabatic surfaces

(b) $T_w(z)$ and average temperatures on other walls

(c) $\bar{T}_w = 320.92\,K$ and average temperatures on other walls
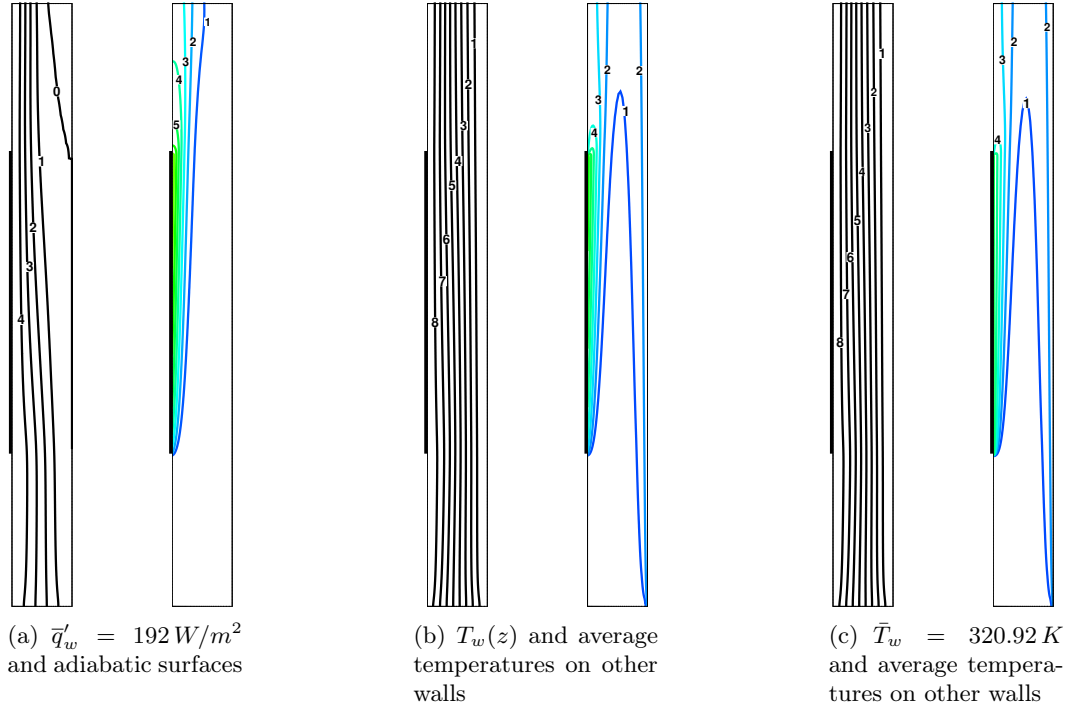
Figure 6.16 – Natural convection. Streamlines $\psi_i/[g/(m \cdot s)] = 0.5 \times i$ (left) and isotherms $T_i/[K] = 290 + 5 \times i$ (right) for (a) $\epsilon = 0$, $\bar{q}'_w = 192\,W/m^2$ and adiabatic surfaces, (b) $\epsilon = 0$, $T_w(z)$ and average temperatures on other walls, (c) $\epsilon = 0$, $\bar{T}_w = 320.92\,K$ and average temperatures on other walls. The horizontal scales are enlarged by 50%.

may be considered accurate. Similar comparisons between rows 3 and 3a for $\varepsilon = 1$ show slightly larger differences, but less than 3%. On the other hand, comparisons between rows 1, 3 and 3a demonstrate that a radiative heat flux correction is needed for black surfaces, since the departures decrease from 6% (without correction) to 3% (with correction).

– Temperatures at the heated section used as boundary conditions for the computations [91] (rows 2b-c and 3b-a in Table 6.6).
The temperature at the heated section is either the temperature distribution (Figs. 6.15(b) and 6.16(b)) or the average temperature (Figs. 6.15(c) and 6.16(c)) extracted from the coupled problem. For the four cases considered, the average temperatures of the adiabatic wall sections determined from the coupled problem are applied as boundary conditions [91]: at the RHS-wall ($\bar{T} = 292.7\,K$ and $\bar{T} = 302.5\,K$ for $\varepsilon = 0.1$ and $\varepsilon = 1$, respectively), at the bottom extension of the LHS-wall ($\bar{T} = 290.4\,K$ and $\bar{T} = 290.8\,K$ for $\varepsilon = 0.1$ and $\varepsilon = 1$, respectively), and at the top extension of the LHS-wall ($\bar{T} = 319.0\,K$ and $\bar{T} = 309.0\,K$ for $\varepsilon = 0.1$ and $\varepsilon = 1$, respectively). Note that the small increase in the average temperature of the RHS-wall for $\varepsilon = 0.1$ is enough to almost suppress the flow reversal, and that the top extension is colder for $\varepsilon = 1$ than for $\varepsilon = 0.1$.
The streamlines and isotherms displayed in Figs. 6.15(b)-(c) and Figs. 6.16(b)-(c) show a better agreement with those reported in 6.12(a) and 6.12(b) than those obtained by subtracting the average radiative flux. However, the average temperature applied at the adiabatic wall may lead to the development of a thermal boundary layer from its bottom (see the isotherms in Figs. 6.16(b)-(c)).

The results reported in rows 2b and 2c of Table 6.6 show that the mean heat transfer rate and maximum temperature do not differ much from the previous cases if the temperature distribution $(T_w(z))$ applied at the heated section is that deduced from the coupled formulation. On the other hand, the use of the average temperature leads to significant differences, both in the convective coefficient and in the maximum temperature. This result conflicts with the analysis reported in [91].

6.4.5 Non-Boussinesq effects

The influence of property variations on natural convection from a vertical isothermal, heated surface was experimentally investigated by Clausing and Kempka [50]. By using a cryogenic environment, the ratio of the absolute temperature of the wall to the ambient temperature of gaseous nitrogen was varied in the range $1 < T_w/T_0 \leq 2.6$. The experimental apparatus allowed to study parts of both laminar and turbulent regimes $(10^7 \leq Ra_H \leq 2 \cdot 10^{10})$. It was shown that variable properties have virtually no influence in the laminar regime while cause large increases in heat transfer rates in the turbulent regime. Guo and Zhao [72] used laser speckle photographic techniques for studying laminar natural convection between two isothermal vertical parallel plates in air. The surface-to-ambient temperature difference varied from $15\,K$ to $530\,K$, and the spacing of the $10\,cm$-high plates was between $3\,mm$ and $20\,mm$. The experiments showed that the effects of variable properties are much larger than on a single plate. The subsequent numerical study by Guo and Wu [71] based on a parabolic formulation indicated strongest effects for small spacings and large values of the non-Boussinesq parameter. From these two studies, it was also shown that, unlike for the constant property case, the mass flow rate exhibits a nonmonotonic change with a maximum whose amplitude depends both on the spacing and heating rate. This question was numerically revisited by Zamora and Hernández [169] who used an elliptic formulation for an asymmetric heated channel with prescribed temperature at the hot wall and unheated facing wall. They showed in particular that variable property effects produce an important reduction of the recirculation region. It should be noted that experiments and computations showing large variable property effects on the flow patterns were carried out for very high temperature differences between the inlet and wall temperatures (up to $7 \times T_0$). Hence, conclusions about large variable property effects must be cautiously taken into consideration for practical applications dealing with cooling of electronic equipments or non-concentrated solar collectors, for example.

In what follows, results obtained from the variable property formulation are compared with those derived by invoking the Boussinesq approximation. One of the reasons is that Webb et Hill [161] suggested that the use of local properties is more appropriate for correlating local heat transfer data despite the maximum measured temperature differences between the bottom and top ends of the heated section were much smaller than in the work by Clausing and Kempka [50].

For the range of Ra^* investigated, the influence of D (or A) was found negligible. The reason is that the maximum wall temperature is almost insensitive to D provided that $D \geq 1\,cm$, as shown in subsection 6.4.2. Therefore, we discuss only results obtained for $D = 2.02\,cm$. In order to focus on the influence of variable property effects, pure natural convection is considered. The wall heat flux was varied from $q_w = 375\,W/m^2$ to $q_w = 1400\,W/m^2$ ($3.56 \cdot 10^4 \leq Ra^* \leq 1.33 \cdot 10^5$).The non-Boussinesq parameter was thus in the range $1.02 \leq \gamma \leq 3.82$, and the corresponding maximal wall temperature was found

in the range $358\,K \leq T_{max} \leq 489\,K$, i.e. $\Delta T_{max}/T_0$ between 0.23 and 0.69, larger than the usual 0.1-limit for the validity of the Boussinesq approximation. The dynamical viscosity and thermal conductivity of mixtures of ideal polyatomic gases increase with temperature, roughly as the absolute temperature to the power 0.6 to 1.0, while the density decreases as T^{-1} (the pressure effects being negligibly small, see Eq. 6.4). Therefore, the opposite effects on viscous drag and buoyancy may produce nonmonotonic and unpredictable variations of the flow rate with increasing the maximum temperature difference.

Figure 6.17 shows that the non-Boussinesq effects have a weak influence on the flow

(a) $q_w = 375\,W/m^2$, Boussinesq approximation (b) $q_w = 375\,W/m^2$, low Mach number approximation (c) $q_w = 1400\,W/m^2$, Boussinesq approximation (d) $q_w = 1400\,W/m^2$, low Mach number approximation
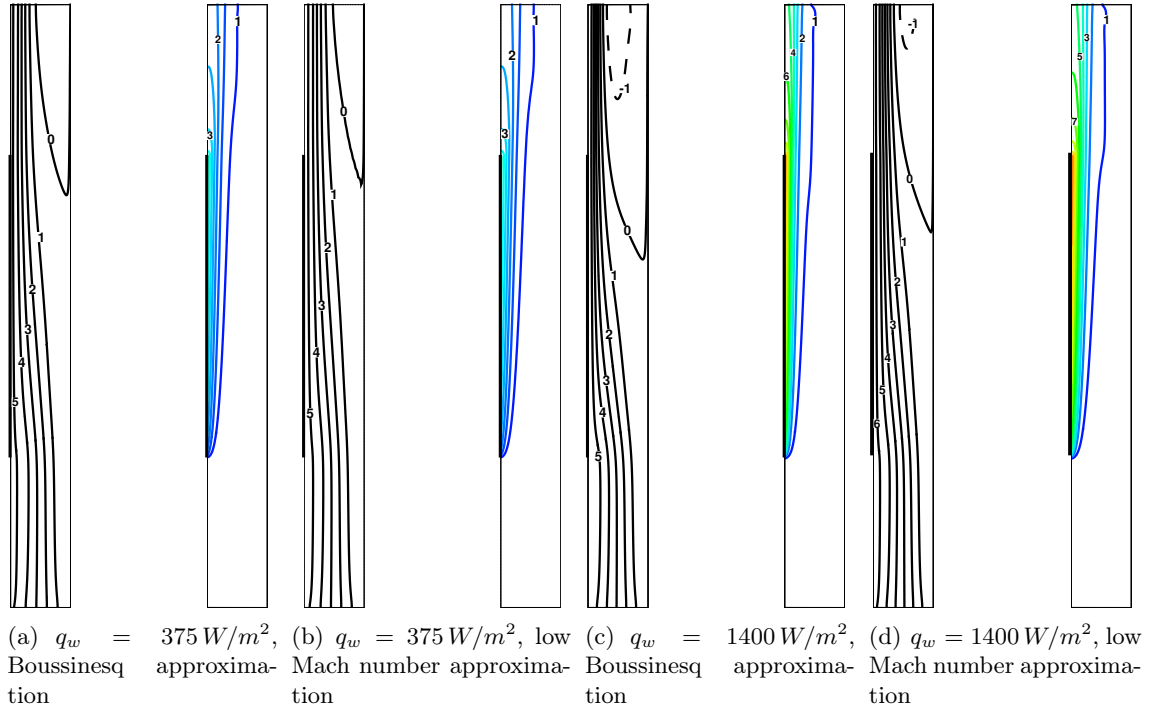
Figure 6.17 – Natural convection. Streamlines $\psi_i/[g/(m \cdot s)] = 0.5 \times i$ (left) and isotherms $T_i/[K] = 290 + 20 \times i$ (right) for (a) $q_w = 375\,W/m^2$ and the Boussinesq approximation, (b) $q_w = 375\,W/m^2$ and the low Mach number approximation, (c) $q_w = 1400\,W/m^2$ and the Boussinesq approximation, (d) $q_w = 1400\,W/m^2$ and the low Mach number approximation. The horizontal scales are enlarged by 50%.

patterns near the heated wall for $q_w = 375\,W/m^2$, and that the flow rate at the inlet section is slightly increased (about 9%) for $q_w = 1400\,W/m^2$ due to variable property effects. The most salient result is about the reduction of the size of the recirculation region (width and penetration length). This reduction and the increase in $\dot{m}_{in}$ are linked, as discused previously (Figs. 6.8 and 6.13). Concerning the heat transfer results, it has been found that the influence of variables properties is almost null for the smallest heat flux considered ($q_w = 235\,W/m^2$) while the changes in average and maximum temperatures of the heated section were about 1% for the highest q_w-value ($q_w = 1400\,W/m^2$). Hence it can be concluded that the Nusselt number correlations reported previously would have been identical if the Bousinesq approximation has been invoked. As a result, taking variable properties effects into consideration for natural convection of air is not required for maximum increase in temperature less than about $200\,K$. These trends are in general agreement with the results discussed by Zamora et Hernández [169] for asymmetric isothermal channels.

Chapter 7

Conclusions & Perspectives

7.1 Key points of this work

7.1.1 Numerical developments

An original scheme has been developed in the Finite Volume discretization framework for low Mach number approximation and its simplification for small temperature gaps, the Boussinesq approximation. The convergence properties of this numerical scheme were carefully checked by performing comparisons with analytical and benchmark solutions. The second order temporal and spatial convergences were retrieved.

7.1.2 Results

– Optimal plate spacing for mixed convection from an array of vertical isothermal plates.
  The purpose of this work was to numerically analyze the optimum spacing of a stack of symmetrically isothermal plates cooled by natural, forced or mixed convection. This idealized configuration has a number of applications in the convective cooling of electronic equipments. The governing equations were solved in their full elliptic form by assuming steady, laminar incompressible flows, constant thermophysical properties, and by invoking the Boussinesq approximation for natural and mixed convection. We implemented specific pressure boundary conditions in order to make relevant comparisons between the results obtained for the three modes of convective cooling, including very small flow rates. In these cases, it was demonstrated that axial heat conduction plays a significant role and that an appropriate modeling of the thermal boundary condition is required. The main concluding remarks are as follows:

  1. The present computations are in agreement with the optimal plate spacing predicted by using asymptotic analyses for natural convection [21],[18] and forced convection [25].

  2. The optimal plate spacing still exists for mixed convection : it is smaller than for forced convection. The maximal heat flux is increased due to the combined effects of pressure and buoyancy forces.

  3. The heat flux transferred by mixed convection is considerably higher than that by natural convection : for the specific case considered, a small pressure drop at the outlet section (i.e. $-1\ Pa$) is enough for increasing the heat flux by a factor of three.

– On the modeling of aiding mixed convection in vertical channels.
Mixed-convection for assisting flows occurring in isothermal flat-plate channels was studied by solving numerically the system of conservation equations written in elliptical form. The computations were carried out by using a finite-volume method implemented in an in-house code. The spatial order of convergence of the method and the accuracy of the results have been checked thanks to the Richardson extrapolation method and regularized inlet thermal conditions in order to properly solve cases of low flow rates linked to small plate spacing and/or small temperature differences.

As an example, we have considered air at ambient temperature flowing in vertical channels (height $H = 1\ m$ or $H = 1.5\ m$, width $D = 2\ cm$ or $D = 3\ cm$). For a maximum temperature difference compatible with the Boussinesq approximation ($\Delta T = 20\ K$), leading to $Gr_H = 2.65\ 10^9 H^3$, the entire laminar mixed-convection regime has been covered by changing either the inlet velocity or the outlet pressure drop. Re_{D_h} was varied from $Re_{D_h} \approx 200$ to $Re_{D_h} \approx 2800$. Although most of the results have been discussed in their dimensional forms, we have also analyzed the reliability of scaling predictions based on dimensionless numbers.

The results for a prescribed inlet velocity $\overline{w_0}$ show that flow recirculations may appear in the entry region when the inlet velocity is lower than that for pure natural convection. In that case, the pressure force opposes to the buoyancy force and the problem is, in fact, similar to that of opposing natural convection with a downward bulk flow. In addition, we have shown that to prescribe $\overline{w_0}$ yields no significant difference between the wall heat fluxes calculated either for forced convection or for mixed convection.

The modeling of mixed convection based on a pressure drop at the outlet section ($p_s < 0$) and a total pressure at the inlet section leads to a completely different analysis of the results, with a better accordance with the common physical sense. When imposing an outlet pressure drop, natural convection assists effectively forced convection and the flow rate as well as the wall heat.

– Effect of surface radiation on natural convective flows and onset of flow reversal in asymmetrically heated vertical channels.
The combined effects of surface radiation and air natural convection in vertical, asymmetrically heated plate channels have been numerically investigated thanks to an improved mathematical formulation in which the temperature variations of all thermophysical properties are accounted for. The present formulation does not imply excessive increases in the computational costs. Extensive comparisons with the experimental results by Webb et Hill [161] have been carried out and heat transfer correlations for pure natural convection as well as for combined effects are provided. The agreement with the experimental results is fairly good and the onset of flow reversal for pure natural convection has been revisited. The study leads to the following conclusions:
  – The onset of flow reversal is delayed upon the effect of surface radiation. Mirror like wall surfaces are required to observe experimentally flow recirculations when using air as the working fluid. The effect of the plate spacing on the formation of a recirculating flow and on the mass flow rates through both inlet and outlet sections has been analyzed in detail. The large feeding of the boundary layer along the heated wall due the penetration of a downcoming flow along the opposite wall

has been quantitatively explored.

– The radiation contribution is to increase the temperatures of the adiabatic wall facing the heated section, leading to prevent the occurrence of down flow for wall emissivity as small as $\varepsilon = 0.1$. Radiation enhances the cooling of the heated wall and its contribution to the total heat transfer rate is significant. For black surface at room temperatures, the heat transfer by radiation is of the order of that by natural convection.

– Procedures generally used which consist in subtracting the radiative contribution to the heat flux applied to the hot surface, q_w, have been examined. If the radiative heat flux distribution or the average radiative heat flux is subtracted from q_w, the coupled (i.e. $\varepsilon \neq 0$) and uncoupled (i.e. $\varepsilon = 0$) numerical solutions lead to quite accurate predictions of the average convective heat transfer coefficient and maximum wall temperature. However, a flow reversal is predicted in the uncoupled solutions while it is not for the coupled solutions. If the measured temperature distribution along the heated section is used as the thermal boundary condition in a combined experimental and numerical approach, the heat transfer predictions are also quite accurate. On the other hand, large discrepancies are found when the average temperature of the heated section is employed as thermal boundary condition.

– Since the maximum temperature of the heated wall is *a priori* unknown for pre-scribed wall heat flux, a weakly compressible formulation for ideal gas has been used in carrying out the computations. This point was raised in [161] since maximum wall temperatures $50\,K$ above the inlet temperature were measured. It could be much greater for higher wall heat fluxes or smaller plate spacing. The comparisons between the usual Boussinesq formulation and fully variable fluid properties (including density in the transport terms) showed that negligible influence of the variable property effects for surface-to-ambient temperature difference up to $200\,K$.

7.2   Works prospects

Since the natural and mixed convection flows studied in this work occur in rectangular geometries, structured grids were found more suitable than triangular meshes. But our scheme is also designed for triangle meshes, provided that the triangulation is Delaunay. Thus, a validation part should be added to ensure the numerical scheme is correctly implemented and to check the convergence properties. The discrete scheme based on unstructured control volumes cannot be directly used to three dimensional problems because all required conditions on meshes are not fulfilled by tetrahedrons any more. Therefore, modifications in some discrete operators must be done.

The main challenge in the study of natural and mixed convection flows in vertical heated channels probably relies on the inlet/outlet boundary conditions again. Indeed, fluid flows resulting from the boundary conditions presented in this work reflect well the common physical sense, but only qualitative comparisons with well designed experiments could definitively validate our approach, for example by comparing the velocity profile and temperature distributions in different sections of the channel. However, I am aware that such ideal experiments are probably hard to manage. One point which would worth to be studied is the part played by the three dimensional effects on heat transfers and fluid flows, for instance, in the simulation of natural convection produced by the cooling/heating of systems equipped by horizontal fins. Finally, further numerical development on turbulence model should be engaged to be able to simulate higher Rayleigh number values obtained

by increasing temperature gaps or the height of the channels.

Part II

Comparisons of Level-Set numerical schemes for the modeling of immiscible incompressible fluid flows

Outlines

Chapter 7 gives a brief review of the interface tracking methods by emphasizing their advantages and drawbacks.

Chapter 8 is devoted to the Level Set method. In a first step, the mathematical model of incompressible and immiscible fluid flows is presented. The level-set method is then introduced through the transport equation of a continuous function and the part played by the signed distance function is emphasized. A particular attention was paid to the spatial and temporal accuracies of the discrete transport and signed distance equations. The principles of the Essentially Non-Oscillatory (ENO) and Weighted Essentially Non-Oscillatory (WENO) schemes are reminded and their related algorithms are given. In particular, the fifth order WENO schemes are developed for regular and irregular grids. At last, two variants of the signed distance equation are presented to improve the mass conservation of each fluid.

The purpose of *chapter 9* is to study the accuracy of the different numerical schemes. We first show that the Essentially Non-Oscillatory scheme in the transport equation has a non-linear behavior, what gives rise to a deterioration of the expected convergence properties. According to previous works, this is due to the change of the stencil as a function of time. In contrast, and by construction, the Weighted Essentially Non-Oscillatory schemes does not suffer of such a problem. The second validation test concerns the signed distance equation with or without the mass conservation improvements. This consists in initializing the equation with an exact signed distance function slightly perturbed, and to measure the departure between the exact function and the signed distance solution at the steady state.

One dimensional test for the transport equation and two dimensional test are used to valid convergence properties of the ENO scheme and WENO scheme. Classical cases like 2D zalesak disc, stretching of a circular fluid element, traveling solitary wave, equilibrium elliptic bubble are applied as validations.

Chapter 1

Brief review of the interface tracking methods

Natural and industrial examples of non-miscible two-phase flows are numerous. Amongst them, we can mention bubbles rising during the water boiling, raindrops falling in the air, water and steam circulating through a nuclear reactor, crystal growing from the molten or liquid state and many others. These flows can take place in two non miscible liquids, a liquid circulating and interacting with a solid phase, a liquid and a vapor, or a solid and a vapor. Therefore, there appears a clear and discernible interface which must be determined. Unlike the single-phase flows or miscible fluid flows, the existence of an interface acts significantly on flows and transfers. Therefore, the determination and the tracking of the interface are essential tasks which require devoted methods.

Numerous methods have been developed over the last past decades. The first class is the moving-grid approach based on Lagrange-type method [59] which is firstly introduced by Hirt *et al.* [77]. It requires a buffer zone located near the interface which must be re-meshed when grids are highly distorted by large deformations. The advantage of this technique is to make the surface sharp in order to keep its position precise, and to allow mesh redistribution or refinement in particular locations near the interface. Thus, the moving-grid approach provides an accurate and efficient method for many problems concerning fluid dynamics, hydraulic, combustion and heat transfer. But frequent reconstructions are severe drawbacks for computational performances and data storage ability. Examples of this method include the two-dimensional computational of the breakup of a drop by Oran et Boris [118], the examination of the initial deformation of a buoyant bubble by Shopov *et al.* [139], the simulation of the unsteady two-dimensional motion of several particles by Feng *et al.* [58] and the axisymmetric computations of the collision of a single drop with a flat surface by Fukai *et al.* [61].

The second class is the front-tracking method also named surface-maker methods by Scardovelli et Zaleski [138]. The free surface is explicitly identified and tracked by means of pre-defined makers or interface-fitted grid cells. Firstly proposed by Glimm *et al.* [67], in the front-tracking method, a separate front marks the interface in fixed grids and is modified only near the front to follow the interface. Advantages of the use of the front-tracking method are that it allows formation of very thin liquid bridges that do no break [138]; the high degree of accuracy that may be achieved by representing the interface through high-order interpolation polynomials because they track exactly the location of the interface [138] and it can obtain the better solutions on coarser grids [66]. However, when there are more than two phases, it may become difficult to handle the complexity of triple lines (lines

in three-dimensional space where three phases meet) and other effects associated with the presence of several phases [138]. And specialized boundary integral methods should be used to the full Navier-Stokes equations. The front-tracking method was developed to combine with the front capturing method by not treating the each phase separately. A single set of governing equations for whole flow filed was solved [157]. The impressive application is that Unverdi et Tryggvason [158] used it for a bubbly flow.

The oldest and still the most popular approach to compute multifluid and multiphase flows is to capture the front directly on a regular, stationary grid. Among them, there exists the maker-and-cell (MAC) method by Harlow et Welch [75] in which marker particles are used to identify each fluid. The essence is the use of Lagrangian virtual particles, whose coordinates are stored, and which move from a cell to the next according to the latest computed velocity field. If a cell contains a particle it is deemed to contain fluid, thus providing flow visualization of the free surface. Compared with the front-tracking methods, it is able to handle the complexity of triple lines and effects associated with more than two phases but hard to avoid becoming distorted as time goes by [138].

The volume-of-fluid (VOF) method is developed by Hirt et Nichols [78], in which a maker function is used to distinguish the fractions of two fluids in each cell. An advantage of representing the free surface as a volume fraction is that we can write accurate algorithms for advecting the volume fraction so that the mass is conserved, while still maintaining a reasonably sharp representation of the free surface. On the other hand, a disadvantage of the volume of fluid approach is the fact that it is difficult to accurately compute local curvature from volume fractions [108].

A number of recent developments have been developed, including the use of "level set" to mark the fluid interface. In the level set methods, the free surface is implicitly captured by a contour of a certain scalar function. This was originally introduced by Osher et Sethian [119]. The original notion of level set methods (LSM) is to define a smooth function $\phi(\vec{x}, t)$ called level set function to represent the free surface. The level set is advected by the local velocity field. The interface can be captured at any time by locating the zero level set, which alleviates the burden of increasing grid resolution at the interface in many other numerical approaches. Usually, ϕ is defined as a signed distance function to the interface. This provides the great convenience of handling topological merging, breaking and even self-intersecting of interfaces in a natural way by taking advantage of the smoothness of the level set function. Information about the interface, such as orientation and curvature, can be conveniently obtained by examining the zero level set so that surface tension can be accurately estimated. Another advantage of LSM is that the extension from two to three dimensions is straightforward. The level set method has the main disadvantage that its approximation accumulates more numerical errors during time evolution than a front tracking method or a volume of fluid method, particularly if the free surface experiences rapid changes in curvature. The consequence is that mass is not fully conserved [108]. Applications of LSM concern incompressible fluid mechanics (Chang *et al.* [41], Foster et Fedkiw [60], Iafrati *et al.* [80], Sussman et Smereka [152], Sussman *et al.* [153] for instance), detonation shock of dynamics (Aslam *et al.* [6]), solidification (Kim *et al.* [90]), crystal growth (Smereka [143]) and many others.

Chapter 2

Level set method

2.1 Mathematical model of incompressible and non miscible fluid flows

2.1.1 Navier-Stokes equations

We consider two incompressible fluids which are flowing in a domain Ω without mixing. At any location of the fluid domain, only one phase is present. We classically denote the density and the dynamic viscosity by ρ and μ respectively and we assume that the density is constant in each phase. To distinguish the fluids, we introduce the subscripts g and l which, for example, could correspond to a gas phase and a liquid phase. By definition, we denote $\Omega_g(t)$ and $\Omega_l(t)$ the open domains containing the gas phase and the liquid phase. The shapes of these regions depend on time.

The geometric loci separating these non-miscible fluids is called interface (or free surface between a liquid and a gas) and is noted $\Gamma(t)$. This interface is mathematically defined by $\Gamma(t) = \bar{\Omega}_g \cap \bar{\Omega}_l$ where $\bar{\Omega}_g$ and $\bar{\Omega}_l$ stand for closed domains for the gas and the liquid, respectively.

For a fluid at rest, the molecules are submitted to attractive and repulsive forces of which the sum is, in mean, equal to zero in the bulk. But when the molecules are located close to the interface, the resultant force cannot vanish and it results a surface tension at the macroscopic level. This surface tension acts as a force by unit length and is noted $\sigma\,[N/m]$. The Laplace-Young equation says that the jump in the normal component of the stress $\bar{\bar{\sigma}} = -p\bar{\bar{\delta}} + 2\mu\bar{\bar{D}}$ at the interface between both fluids is balanced by surface tension:

$$(\bar{\bar{\sigma}}_l - \bar{\bar{\sigma}}_g) \cdot \vec{n} = \sigma\kappa\vec{n} \tag{2.1}$$

where $\bar{\bar{D}}$ is the rate of deformation tensor, $\vec{n}$ is the unit normal vector to the interface, and $\kappa\,[m^{-1}]$ is the local curvature of the interface $\Gamma(t)$.

When the free surface is balanced by surface tension, the two-phase flow system can be treated as a single-fluid flow system. A unified Navier-Stokes equation can be applied in the whole computational domain $\Omega = \Omega_g \cup \Omega_l \cup \Gamma$. We embed Eq. (2.1) in the momentum equation as a volume force by distributing the normal stress at the free surface using the δ-Dirac distribution

$$\int_\Omega f(\vec{x})\delta(\Gamma)\,d\vec{x} = f(\vec{x}_\Gamma) \tag{2.2}$$

with $\vec{x}_{\Gamma(t)}$ the coordinates of the interface $\Gamma(t)$. The incompressible Navier-Stokes equations are reconstructed with variable density and viscosity, and using a volume force to represent the surface tension effect [34]:

$$\nabla \cdot \vec{v} = 0 \tag{2.3a}$$

$$\frac{\partial \vec{v}}{\partial t} + \nabla \cdot (\vec{v} \otimes \vec{v}) = -\frac{1}{\rho}\nabla p + \vec{g} + \frac{1}{\rho}\nabla \cdot (\mu\nabla\vec{v}) + \frac{1}{\rho}\nabla \cdot (\mu\nabla\vec{v})^t - \frac{\sigma\kappa\delta(\Gamma)\vec{n}}{\rho} \tag{2.3b}$$

with $(\mu, \rho) = (\mu_g, \rho_g)$ in the gas phase and $(\mu, \rho) = (\mu_l, \rho_l)$ in the liquid phase.

2.1.2 Interface and fluid properties

To solve Eqs. (2.3), we need locating the position of the interface Γ as a function of time, and to determine its local characteristics, viz the curvature κ and the normal unit vector $\vec{n}$. Instead of performing a Lagrangian tracking of the interface, the interface is solved implicitly by an Eulerian method. To this end, we introduce a regular function $\phi(\vec{x}, t)$, called the level-set function. The free surface $\Gamma(t)$ is identified by a zero level set function $\phi(\vec{x}, t)$:

$$\Gamma(t) = \{\vec{x} \mid \phi(\vec{x}, t) = 0\}$$

with $\phi < 0$ in the gas region and $\phi > 0$ in the liquid region. More specifically, the level set function ϕ is initially assigned with the signed distance function,

$$\phi(\vec{x}, t) = \begin{cases} -d(\vec{x}, t), \ \vec{x} \in \Omega_g \text{ (gas phase)} \\ 0, \ \vec{x} \in \Gamma \text{ (interface)} \\ d(\vec{x}, t), \ x \in \Omega_l \text{ (liquid phase)} \end{cases} \tag{2.4}$$

where $d(\vec{x}, t)$ is the smallest distance to the interface at time t.

Thanks to the definition of the level set function, it is now easy to define the properties of the fluid. To do this, we first define the Heaviside function $H(\phi)$ such that

$$H(\phi) = \begin{cases} 0, \text{ if } \phi < 0 \text{ (gas phase)} \\ 1, \text{ if } \phi > 0 \text{ (liquid phase)} \end{cases} \tag{2.5}$$

Then, the density and the dynamic viscosity of the fluid over the whole domain Ω write:

$$\rho(\phi) = \rho_g + (\rho_l - \rho_g)H(\phi) \tag{2.6a}$$

$$\mu(\phi) = \mu_g + (\mu_l - \mu_g)H(\phi) \tag{2.6b}$$

Assuming the level set function is regular enough, the unit normal $\vec{n}$ to the interface writes:

$$\vec{n} = \left.\frac{\nabla\phi}{|\nabla\phi|}\right|_{\phi=0} \tag{2.7}$$

and the local curvature $\kappa(\phi)$ gives

$$\kappa(\phi) = \nabla \cdot \vec{n} = \left.\nabla \cdot \left(\frac{\nabla\phi}{|\nabla\phi|}\right)\right|_{\phi=0} \tag{2.8}$$

Finally, the Eulerian transport by the velocity $\vec{u}(\vec{x}, t)$ of the free surface Γ is expressed by the following level set equation:

$$\frac{\partial\phi}{\partial t} + \vec{u}(\vec{x}, t) \cdot \nabla\phi = 0$$

with the following requirement

$$\vec{u}(\vec{x}_{\Gamma(t)}, t) = \vec{v}(\vec{x}_{\Gamma(t)}, t)$$

where $\vec{v}(\vec{x}_{\Gamma(t)}, t)$ is the local velocity of the fluid at the interface. But for the purpose of extending the knowledge of the velocity field apart from the interface and at any time, we simply use the fluid velocity, solution of the Navier-Stokes equations (2.3), as a vector field for the transport of the level set function:

$$\frac{\partial \phi}{\partial t} + \vec{v}(\vec{x}, t) \cdot \nabla \phi = 0 \tag{2.9}$$

2.1.3 Thickening of the interface

Sudden variations in the fluid properties at the interface, as for example between the densities of gases $\rho_g \approx 1\,kg/m^3$ and liquids $\rho_l \approx 10^3\,kg/m^3$, may introduce numerical instabilities. A way to overcome this problem is to smear out the discontinuities in a transition zone of constant thickness 2ε [158] (Fig. 2.1). This is achieved by smearing out
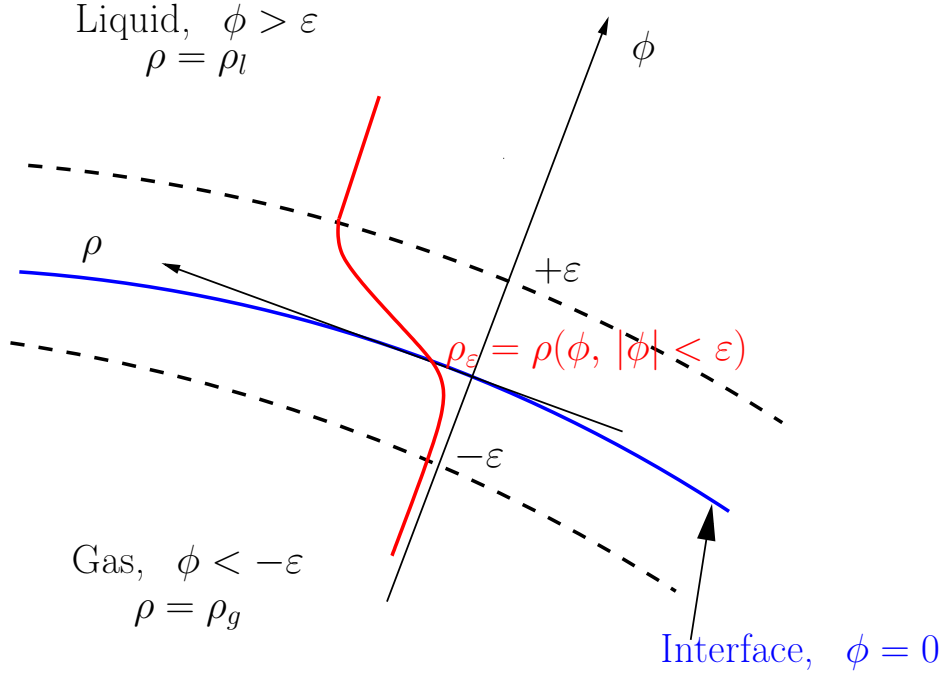
Figure 2.1 – Demonstration of density jump

the Heaviside function (2.5), $H_\varepsilon(\phi)$, defined as follows:

$$H_\epsilon(\phi) = \begin{cases} 0, & \text{if } \phi < -\varepsilon \\ \frac{1}{2}\left[1 + \frac{\phi}{\varepsilon} + \frac{1}{\pi}\sin\left(\frac{\pi\phi}{\varepsilon}\right)\right], & \text{if } |\phi| \leq \varepsilon \\ 1, & \text{if } \phi > \varepsilon \end{cases} \tag{2.10}$$

where ε is an adjustable parameter. For example, Sussman *et al.* [153] suggested a value of order of the grid size Δx, $\varepsilon = 1.5\Delta x$. Taking the thickness of the interface into account, the smeared-out density $\rho_\varepsilon(\phi)$ and viscosity $\mu_\varepsilon(\phi)$ write:

$$\rho_\varepsilon(\phi) = \rho_g + (\rho_l - \rho_g)H_\varepsilon(\phi) \tag{2.11a}$$

$$\mu_\varepsilon(\phi) = \mu_g + (\mu_l - \mu_g)H_\varepsilon(\phi) \tag{2.11b}$$

The Dirac distribution (2.2), allowing to transform the right-hand side of the Young-Laplace's surface equation (2.1) into a volume contribution (see Eq. (2.3b)), is also smeared out. The $\delta_\varepsilon(\phi)$-function is the derivative of the smooth Heaviside function (2.10):

$$\delta_\varepsilon(\phi) = \nabla_\phi H(\phi) = \begin{cases} 0, \text{ if } |\phi| > \varepsilon \\ \frac{1}{2\varepsilon}\left[1 + \cos(\frac{\pi\phi}{\varepsilon})\right], \text{ if } |\phi| \leq \varepsilon \end{cases} \qquad (2.12)$$

Thus, the surface tension is spread over the transition zone by substitution in Eq. (2.3b) $\sigma\kappa\delta(\Gamma)\vec{n}$ by

$$\sigma\kappa\delta_\varepsilon(\phi)\vec{n} \qquad (2.13)$$

2.2 Reinitialization of level set function: Equation of the signed distance

2.2.1 The transport equation and distance function

The level set function enables the tracking of the interface (Eq. (2.9)). But this is not its unique use. It also allows the calculations of the regularized fluid properties, the curvature κ and the unit normal vector $\vec{n}$ to the interface (Cf Eqs. (2.11), (2.8) and (2.7) respectively). However, these calculations have sense only if the level set function is a signed measure of the distance to the interface. Unfortunately, its transport by the fluid velocity usually alters this essential property.

As an illustration, we consider a one-dimensional problem (see Fig. 2.2). At time t, the
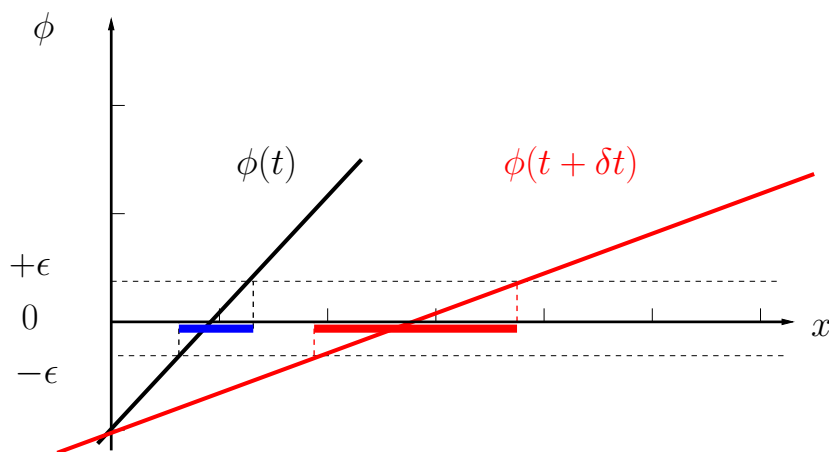
Figure 2.2 – Illustration of transport of the level set function on the distance function

gas is located at $x < 1$ whereas the liquid takes up the remaining space. The zero level set is then located at $x_0(t) = 1$ and, in accordance with Eq. (2.4), the level set function is equal to the signed distance: its analytical expression writes $\phi(x,t) = x - 1$ (black solid line in Fig. 2.2). To avoid discontinuities, the interface is stretched out on the abscissa x such that $|\phi(x)| < \varepsilon$. It results a thickening of the interface over 2ε (blue segment in Fig. 2.2). Let us now assume that the fluid velocity v_x is fixed and equal to $v_x \equiv dx/dt = x$. Then at time $t + \delta t$, the level set defined for $x(t) > 0$ ($x(t) < 0$) is moved to the right (left) such that any point $x(t)$ of this level set is translated to the abscissa $x(t + \delta t) = x(t)\exp(\delta t)$ (inclined red

line in Fig. 2.2). The new level set function writes $\phi(x, t + \delta t) = x \exp(-\delta t) - 1$ and does any more represent the distance function! As a consequence, the thickness of the interface grew from 2ε (blue segment) to $2\varepsilon \exp(\delta t)$ (red horizontal segment), but this evolution is unfortunately not desired.

If the difference between the level set function and the signed distance is too large, $\|\nabla\phi\|$ will depart significantly from unit. The quantities $\rho(\phi)$ and $\mu(\phi)$ will be greatly distorted, especially in the case of large ratios of density or viscosity. In the same way, the numerical approximations of the unit normal vector $\vec{n}$ (Eq. (2.7)) and of the deduced interface curvature κ (Eq. (2.8)) will be inaccurate. Finally, the bad evaluation of the surface tension source term Eq. (2.13) will deform substantially the free surface shape and will make significant loss or gain of mass. So maintaining the level set function ϕ as close as possible to the signed distance function is of great importance.

2.2.2 Signed distance equation

After computing the level set transport equation Eq. (2.9), a re-initialization procedure concerning ϕ may be required to satisfy $\|\nabla\phi\| = 1$. This is achieved by solving the distance equation (Eq. (2.14) here-below) at the steady state, at least in the vicinity of the interface. To distinguish the variable associated with the distance equation from the level set variable, we define the signed distance function $d(\vec{x}, \tau)$, solution of a Hamilton-Jacobi equation:

$$\frac{\partial d}{\partial \tau} + s(d^0)\left(\|\nabla d\| - 1\right) = 0 \qquad\qquad (2.14)$$
$$d(\vec{x}, 0) = d^0(\vec{x})$$

where τ is an artificial time introduced to converge to the steady state, $s(d^0)$ is the smoothed sign function defined as in [127],

$$s(d^0) = \frac{d^0}{\sqrt{d_0^2 + \left(\|\nabla d^0\|\,\epsilon\right)^2}} \qquad\qquad (2.15)$$

and $d^0(\vec{x})$ is set such that it shares the same zero as the level set $\phi(\vec{x}, t)$. In practical applications, this last condition is reduced to $d^0(\vec{x}) = \phi(\vec{x}, t)$. The parameter ϵ has the dimension of a length.

The Hamilton Jacobi equation (2.14) can be viewed as a transport equation with a source term. To this end, let us define the velocity field $\vec{w}(\vec{x}, t)$ of unit modulus, with a direction normal to iso-distance values, and pointing outward the zero distance function:

$$\vec{w}(\vec{x}, t) = s(d_0)\frac{\nabla d}{\|\nabla d\|} \qquad\qquad (2.16)$$

Then the Hamilton-Jacobi equation (2.14) simply writes :

$$\frac{\partial d}{\partial \tau} + \vec{w} \cdot \nabla d = s(d^0) \qquad\qquad (2.17)$$

To illustrate the reinitialization procedure, we are going to reconsider the example presented in Sec. 2.2.1 to achieve $\|\phi_{new}(x, t + \delta t)\| = 1$ (see Fig. 2.3). We chose $\epsilon = 0$ in (2.15) and we are only interested in solutions for the liquid phase, namely for $x \geq x_0(t + \delta t)$, and the value of the zero level set is extended to abscissa corresponding to the gas phase.
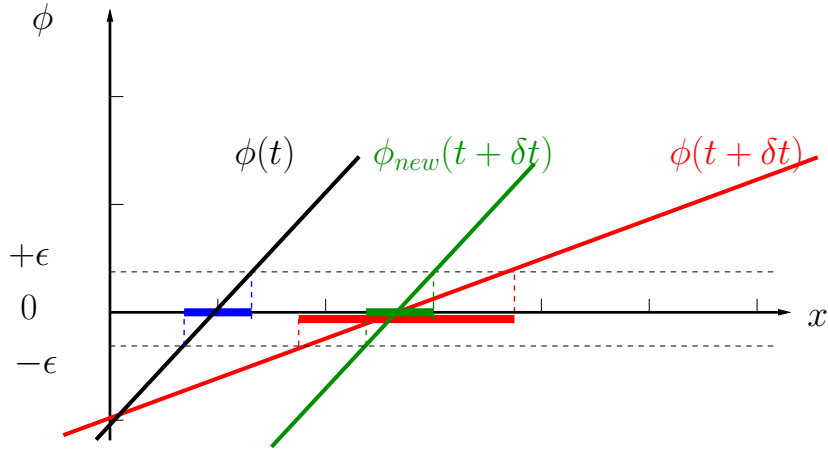
Figure 2.3 – Illustration of reinitialization method

Therefore, we have $s(d_0) = 1$ and $\vec{w} = +\vec{e}_x$. From both Eq. (2.17) and the preceding remarks, we get:

$$\forall x \geq x_0(t + \delta t), \quad \frac{\partial d}{\partial \tau} + \frac{\partial d}{\partial x} = 1 \qquad (2.18a)$$

$$\forall x \leq x_0(t + \delta t), \quad d(x, \tau) = 0 \qquad (2.18b)$$

with the initial condition:

$$\forall x \geq x_0(t + \delta t), \quad d(x, \tau = 0) = d^0(x) \equiv \phi(x, t + \delta t) \qquad (2.19)$$

where $\phi(x, t + \delta t) = x \exp(-\delta t) - 1$ (red straight line in Fig. 2.3) and $x_0(t + \delta t) = \exp(-\delta t) - 1$ the zero level set function at time $t + \delta t$. For $x \geq x_0(t + \delta t)$, the solution gives $d(x, \tau) = D(X) + x$ with $X = x - \tau$. Using the initial condition (2.19) and Eq. (2.18b), the function $D(X)$ writes:

$$\forall X \geq x_0(t + \delta t), \quad D(X) = d^0(X) - X$$
$$\forall X \leq x_0(t + \delta t), \quad D(X) = -x_0(t + \delta t)$$

since $d^0(x_0(t + \delta t)) = 0$. For $x \geq x_0(t + \delta t)$, we then get

$$\lim_{\tau \to \infty} d(x, \tau) = \lim_{\tau \to \infty} (D(x - \tau) + x) = -x_0(t + \delta t) + x$$

The steady state solution is then assigned to the reinitialized level set function: $\phi_{new}(\vec{x}, t + \delta t) = x - x_0(t + \delta t)$ (green inclined line in Fig. 2.3). As shown in Fig. 2.3, the thickness of the interface is now preserved between times t and $t + \delta t$.

2.2.3 Signed distance equation – Improvement of the volume conservation

Mathematically, the resolution of the signed distance equation (2.14) does not move the location of the interface because the smooth sign function (2.15) is then exactly zero (provided that $\epsilon > 0$). But due to numerical errors, it is hard to ensure it, and sometimes the interface shifts and loses its shape because of accumulation of numerical errors. In this document, two methods are used to improve the volume conservation.

One approach is related to "the subcell fix" method [136]. When constructing high-order schemes for the signed distance equation, we need to take several adjacent points into account to construct the discretization form. The ideal of this method is introduce explicitly the position of the interface of which the approximation is based on high order polynomial interpolation.

The second method proposed by Sussman et Fatemi [151] modifies the right-hand side of the signed distance equation (2.14) with the idea to improve the volume enclosed by the zero level set during the reinitialization process. This new method is called the "constrained distance function" method and writes [153]:

$$\frac{\partial d}{\partial \tau} + s(d^0)\left(\|\nabla d\| - 1\right) = \lambda \delta(d)\|\nabla d\| \tag{2.20}$$

where λ is a parameter which will be discussed bellow.

The expression of the parameter λ is obtained as follows. Since the liquid phase is defined by positive level set values, the fluid volume is preserved during time evolution if

$$\frac{\partial}{\partial \tau} \int_\Omega H(d(\vec{x}, \tau))\, d\vec{x} = 0$$

The left-hand side gives:

$$\begin{aligned}
\frac{\partial}{\partial \tau} \int_\Omega H(d(\vec{x}, \tau))\, d\vec{x} &= \int_\Omega H'(d)\frac{\partial d}{\partial \tau}\, d\vec{x} \\
&= \int_\Omega H'(d)\left(\lambda \delta(d)\|\nabla d\| - s(d^0)\left(\|\nabla d\| - 1\right)\right)\, d\vec{x}
\end{aligned}$$

Since this expression cancels out, we get:

$$\lambda = \frac{\displaystyle\int_\Omega H'(d)\left(s(d^0)\left(\|\nabla d\| - 1\right)\right)\, d\vec{x}}{\displaystyle\int_\Omega H'(d)\delta(d)\|\nabla d\|\, d\vec{x}}$$

And after expressing the derivative of the Heaviside function, the parameter writes:

$$\lambda = \frac{\displaystyle\int_\Omega \delta(d)\left(s(d^0)\left(\|\nabla d\| - 1\right)\right)\, d\vec{x}}{\displaystyle\int_\Omega (\delta(d))^2\|\nabla d\|\, d\vec{x}}$$

From this expression, we can see that the constraint acts only on the interface where $\lambda \leq 0$. Far from the zero level set, Eq. (2.20) is reduced to Eq. (2.14).

2.3   A variable-density projection method

2.3.1   Continuous equations

The variable-density incompressible Navier-Stokes equations read:

$$\frac{\partial \vec{v}}{\partial t} + \nabla \cdot (\vec{v} \otimes \vec{v}) = -\frac{1}{\rho}\nabla \Pi + \vec{g} + \frac{1}{\rho}\nabla \cdot (\mu \nabla \vec{v}) + \frac{1}{\rho}\nabla \cdot (\mu \nabla \vec{v})^t - \frac{\sigma \kappa \delta \vec{n}}{\rho}$$

$$\nabla \cdot \vec{v} = 0$$

Using the abbreviate notations

$$L(\vec{v}) = \frac{1}{\rho(\phi)} \nabla \cdot (\mu(\phi)\nabla\vec{v}) \qquad (2.21a)$$

$$S(\vec{v}) = \frac{1}{\rho(\phi)} \left[\nabla \cdot (\mu(\phi)\nabla\vec{v})^t - \rho(\phi)\nabla(\vec{v}\otimes\vec{v}) + \rho(\phi)\vec{g} - \sigma\kappa\delta(\phi)\vec{n} \right] \qquad (2.21b)$$

we simply get

$$\frac{\partial\vec{v}}{\partial t} = -\frac{1}{\rho(\phi)}\nabla\Pi + L(\vec{v}) + S(\vec{v}) \qquad (2.22a)$$

$$\nabla \cdot \vec{v} = 0 \qquad (2.22b)$$

2.3.2 Discrete equations

The level set and the fluid flow equations are solved successively. First we evaluate the new level set function from a known velocity field. Once ϕ is known, we calculate the surface tension, the density and viscosity as well as the normal vector to the interface. Then, the variable-density incompressible Navier-Stokes equations are solved.

The spatial and temporal discretizations are described in Chapter 2, page 19. For the time discretization of the variable-density incompressible Navier-Stokes method, we express the equations at time $t = (n+1)\Delta t$ by using the second order Euler approximation (2.6). The term $S(\vec{v})$ in (2.21b) is evaluated at time $t = (n+1)\Delta t$ using an Adams-Bashforth extrapolation $X^{(n+1)} = 2X^{(n)} - X^{(n-1)}$ for the non-linear and viscous contributions, whereas the surface tension and weight contributions are already explicitly known at time $t = (n+1)\Delta t$.

The spatial approximations rest on the finite volume scheme developed in Sec. 2.2, but for structured grids only. This section only emphasizes the decoupling between the velocity and pressure, because the projection step (the pressure Poisson equation) differs slightly from the one phase fluid flow (see Sec. 2.1.4):
  – Predictor or diffusion step:

$$\left(\frac{3}{2\Delta t} - L\right)\vec{v}^{(n+1)*} = \frac{2}{\Delta t}\vec{v}^{(n)} - \frac{1}{2\Delta t}\vec{v}^{(n-1)} + S^{(n+1)}(\vec{v}) - \frac{1}{\rho^{(n+1)}}\nabla\Pi^n \qquad (2.23)$$

  with $\vec{v}^{(n+1)*}$ the intermediate velocity.
  – Projection step, Poisson equation:

$$\nabla \cdot \left(\frac{1}{\rho^{n+1}}\nabla(\Phi^{(n+1)})\right) = \frac{3}{2\Delta t}\nabla \cdot \vec{v}^{(n+1)*}$$

  For the sake of stability (see Sec. 2.2.1.1, page 26), the approximation on cell K of the left-hand side of this equation $\nabla_K \cdot \left(\frac{1}{\rho^{n+1}}\widetilde{\nabla}_K(\Phi^{(n+1)})\right)$ is substituted by

$$\left(\nabla \cdot \left(\frac{1}{\rho^{n+1}}\nabla(\Phi^{(n+1)})\right)\right)_K$$

  whose expression is detailed in Sec. 2.2.3.1.
  – Correction step:
  The new pressure field writes

$$\Pi^{(n+1)} = \Pi^{(n)} + \Phi^{(n+1)}$$

The relationship between the intermediate velocity and the true velocity at time $t = (n+1)\Delta t$ is given by:

$$\vec{v}^{(n+1)} - \vec{v}^{(n+1)*} = -\frac{2\Delta t}{3\rho^{(n+1)}}\nabla\Phi^{(n+1)}$$

2.4 Discretization of transport equation

The spatial discretization of the transport term is based on a structured grid with faces located at coordinates $\vec{x}_{i+1/2,j+1/2} = (x_{i+1/2}, y_{j+1/2})$. By default, we assume a constant grid cell size $\Delta x = x_{i+1/2} - x_{i-1/2}$ and $\Delta y = y_{j+1/2} - y_{j-1/2}$ as well as a constant time step Δt.

Using the mass conservation equation (2.22b), the transport equation (2.9) writes in hyperbolic form as:

$$\frac{\partial\phi}{\partial t} + \frac{\partial f(\phi)}{\partial x} + \frac{\partial g(\phi)}{\partial y} = 0 \tag{2.24}$$

with $\phi(\vec{x}, 0) = \phi_0(\vec{x})$, $f(\phi) = \phi\vec{v}\cdot\vec{e}_x$ and $g(\phi) = \phi\vec{v}\cdot\vec{e}_y$. Since the fluxes $f(\phi)$ and $g(\phi)$ are linear, the numerical resolution of this hyperbolic equation can be done direction by direction. From now on, we simply consider the one-dimension problem in x-direction:

$$\frac{\partial\phi}{\partial t} + \frac{\partial f(\phi)}{\partial x} = 0 \tag{2.25}$$

2.4.1 Time discretization

A third order TVD Runge-Kutta discretisation is used:

$$\phi^0 = \phi^{(n)}$$
$$\phi^i = \sum_{k=0}^{i-1}\left[\alpha_{ik}\phi^k - \beta_{ik}\Delta t\frac{\partial f(\phi^k)}{\partial x}\right], \quad i = 1, \cdots, 3$$
$$\phi^{(n+1)} = \phi^3$$

with coefficients reported in Tab. 2.1.

α_{ik}	$k=0$	$k=1$	$k=2$		β_{ik}	$k=0$	$k=1$	$k=2$
$i=1$	1				$i=1$	1		
$i=2$	3/4	1/4			$i=2$	0	1/4	
$i=3$	1/3	0	2/3		$i=3$	0	0	2/3

Table 2.1 – Coefficients of the third-order TVD Runge-Kutta scheme

This scheme is stable under the Courant-Friedrichs-Lewy (CFL) condition:

$$\frac{\Delta t}{\Delta x} \le c_r\lambda_0$$

where c_r is CFL coefficient and λ_0 is usually inversely proportional to $\max|f'(\phi)|$. For the above mentioned third order Runge-Kutta scheme, $c_r = 1$.

The scheme is also said TVD (Total Variation Diminishing) since, provided that the CFL condition is satisfied, we have

$$TV(\phi^{(n+1)}) \le TV(\phi^{(n)})$$

with $TV(\phi) = \sum_i |\phi_i - \phi_{i-1}|$.

2.4.2 Basic idea of the spatial discretization

The Finite Volume method is based on averaged values of $\phi(x)$ on control volume. To emphasize this, we denote by $\bar{\phi}_i$ its average value on interval $I_i = [x_{i-1/2}, x_{i+1/2}]$ and by ϕ_i its approximation at point $x_i = (x_{i+1/2} + x_{i-1/2})/2$. Thus we get

$$\bar{\phi}_i = \frac{1}{\Delta x_i} \int_{x_{i-1/2}}^{x_{i+1/2}} \phi(x) dx \tag{2.27}$$

with $\Delta x_i = x_{i+1/2} - x_{i-1/2}$.

We integrate Eq. (2.25) on I_i to get

$$\frac{d\bar{\phi}_i(t)}{dt} = -\frac{1}{\Delta x_i} \left(f(\phi_{x_{i+1/2}}, t) - f(\phi_{x_{i-1/2}}, t) \right)$$

The fluxes $f(\phi_{x_{i\pm1/2}}, t)$ are undefined on cell faces. They have to be approximated, and we note $\hat{f}_{i\pm1/2}(t) \approx f(\hat{\phi}_{i\pm1/2}, t)$ this approximation. We then obtain

$$\frac{d\bar{\phi}_i(t)}{dt} = -\frac{1}{\Delta x}(\hat{f}_{i+1/2} - \hat{f}_{i-1/2}) \tag{2.28}$$

The problem is now to get a good approximation of $\phi(x_{i\pm1/2})$, from the average values $\bar{\phi}_i$. This is the aim of the ENO and WENO schemes.

2.4.3 Principle of reconstruction procedure for ENO and WENO schemes

The approximation of $\phi_{i+1/2}$ (and $\phi_{i-1/2}$) relies on either an Essentially Non-Oscillatory (ENO) scheme or a Weighted Essentially Non-Oscillatory (WENO) scheme [140]. They consist in searching different polynomial approximations of the primitive function of $\phi(x)$, and then to calculate its derivative on cell face $x_{i+1/2}$.

We note $Q(x)$ a primitive function of $\phi(x)$, defined as

$$Q(x) = \int_{x_{-1/2}}^{x} \phi(\xi) \, d\xi \tag{2.29}$$

In the expression of any primitive, the lower limit $x_{-1/2}$ is irrelevant and it can be replaced by any other fixed point. We the have

$$Q(x_{i+1/2}) = \int_{x_{-1/2}}^{x_{i+1/2}} \phi(\xi) \, d\xi = \sum_{l=0}^{i} \int_{x_{l-1/2}}^{x_{l+1/2}} \phi(\xi) \, d\xi = \sum_{l=0}^{i} \Delta x_i \bar{\phi}_l$$

It results that the knowledge of cell averages $\bar{\phi}_l$ provides a reconstruction of a primitive evaluated at the cell face $x_{i+1/2}$, whatever the cell i considered. Thanks to reconstructions $Q(x_{i+1/2})$, we are able to approximate a primitive function $Q(x)$ by interpolation polynomials $P_n(x)$ on $Q(x_{i+1/2})$. Then, the derivate $P_n'(x)$ provides good approximation of the function $\phi(x)$, all the more accurate that the polynomial degree is high.

From now on, average values are written without extra notations: the bar over the level set function is omitted.

2.4.4 Essentially Non-Oscillatory (ENO) scheme

The main challenge of solving Hamilton-Jacobi type equation is that discontinuities in derivatives are easily produced even with a smooth initial condition. Traditional low order numerical methods, such as the first order Godunov or Roe schemes can resolve the discontinuities monotonically, without spurious numerical oscillations, but often at the cost of too important diffusion. They also introduce relatively large numerical dissipation in the smooth part of the solution. Hence, many grid points are required to compute complicated smooth structures such as vortices or acoustic waves, especially for long time simulation [140]. Specific numerical schemes, which satisfies monotonicity preserving, must be applied to get a unique viscosity solution, such as TVD (total variation diminishing) with first-order accuracy, ENO (essentially non-oscillatory) or WENO (weighted ENO) with high-order accuracy. For essentially non-oscillatory scheme, the basic idea is to choose the local adaptive stencil to automatically achieve high order accuracy and the non-oscillatory property near discontinuities.

The ENO scheme was originally developed by Harten and Osher [76] for the non-oscillatory shock-capturing approximations of hyperbolic conservation laws, and then extended to Hamilton-Jacobi equations by Shu and Osher, motivated by the observation of the close relationship between conservation laws and Hamilton-Jacobi equations ([141, 142]). The ENO scheme start from the first-order upwind scheme, also named the first-order ENO scheme. Then local adaptive stencils are successively chosen to construct higher-order ENO scheme.

2.4.4.1 Algorithm

The algorithm based on Sec. 2.4.3 to evaluate $\phi_{i+1/2}$ with the ENO scheme writes:
1. Compute the divided difference table of ϕ, named H:

$$H[x_{i-1/2}, x_{i+1/2}] = \phi[x_i]$$

$$H[x_{i-1/2}, x_{i+1/2}, ..., x_{i+k+1/2}] = \frac{1}{k+1}\phi[x_i, ..., x_{i+k}], \ k = 1, 2, ..., r$$

2. Upwinding building block: Let $u_{i+1/2} \equiv \vec{v} \cdot \vec{e}_x$ the velocity on face $x_{i+1/2}$ then

$$\begin{cases} \text{If } u_{i+1/2} \geq 0, & k^{(1)}_{\min} = i \\ \text{If } u_{i+1/2} < 0, & k^{(1)}_{\min} = i+1 \end{cases}$$

and $Q^{(1)}(x) = H[x_{k^{(1)}_{\min}-1/2}, x_{k^{(1)}_{\min}+1/2}](x - x_{k^{(1)}_{\min}-1/2})$.

3. For $l > 1$,

$$a^{(l)} = H[x_{k^{(l-1)}_{\min}-1/2}, ..., x_{k^{(l-1)}_{\min}+l-1/2}]$$

$$b^{(l)} = H[x_{k^{(l-1)}_{\min}-1-1/2}, ..., x_{k^{(l-1)}_{\min}+l-1-1/2}]$$

then

$$\begin{cases} \text{If } |a^l| \geq |b^l|, & c^{(l)} = b^{(l)}, \text{ and } k^{(l)}_{\min} = k^{(l-1)}_{\min} - 1 \\ \text{If } |a^l| < |b^l|, & c^{(l)} = a^{(l)}, \text{ and } k^{(l)}_{\min} = k^{(l-1)}_{\min} \end{cases}$$

and form

$$Q^{(l)}(x) = Q^{(l-1)}(x) + c^{(l)} \prod_{k=k^{(l-1)}_{\min}}^{k^{(l-1)}_{\min}+l-1} (x - x_{k-1/2})$$

4. $Q_{i+1/2}(x) = Q^{(r+1)}(x)$.

5. We then get

$$\widehat{\phi}_{i+1/2} = \frac{d}{dx}Q_{i+1/2}(x)|_{x=x_{i+1/2}}$$

2.4.4.2 Application to the third order ENO scheme

The convection term (2.24) in x-direction is discretized in cell $[x_{i-1/2,j}, x_{i+1/2,j}] \times [y_{i,j-1/2}, y_{i,j+1/2}]$ as follows:

$$\frac{u_{i+1/2,j}\hat{\phi}_{i+1/2,j} - u_{i-1/2,j}\hat{\phi}_{i-1/2,j}}{\Delta x}$$

where the velocity component $u \equiv \vec{v} \cdot \vec{e}_x$ is known at cell faces $x_{i+1/2,j}$ and the level set function at the cell centers $x_{i,j}$(the average value) only. For an uniform grid spacing, $\hat{\phi}_{i+1/2,j}$ is approximated by the third order ENO scheme as follows.

  – We denote

$$\delta\phi_i^- = \phi_{i-1,j} - \phi_{i,j}, \quad \delta\phi_i^0 = \phi_{i+1,j} - \phi_{i,j}, \quad \delta\phi_i^+ = \phi_{i+2,j} - \phi_{i+1,j}$$

and

$$\delta^2\phi_i^- = \phi_{i-2,j} - 2\phi_{i-1,j} + \phi_{i,j}, \qquad \delta^2\phi_i^0 = \phi_{i-1,j} - 2\phi_{i,j} + \phi_{i+1,j}$$
$$\delta^2\phi_i^+ = \phi_{i,j} - 2\phi_{i+1,j} + \phi_{i+2,j}, \qquad \delta^2\phi_i^{++} = \phi_{i+1,j} - 2\phi_{i+2,j} + \phi_{i+3,j}$$

  – The first-order ENO scheme is reduced to

$$\hat{\phi}_{i+1/2,j}^{(1)} = \begin{cases} \phi_{i,j} & \text{if } u_{i+1/2,j} \geq 0 \\ \phi_{i+1,j} & \text{otherwise} \end{cases}$$

  the first-order upwind scheme.

  – The second-order ENO scheme is formulated as

$$\hat{\phi}_{i+1/2,j}^{(2)} = \hat{\phi}_{i+1/2,j}^{(1)} +$$
$$\frac{1}{2}\max[\text{sign}(u_{i+1/2,j}),0]m(\delta\phi_i^-, \delta\phi_i^0) +$$
$$\frac{1}{2}\min[\text{sign}(u_{i+1/2,j}),0]m(\delta\phi_i^0, \delta\phi_i^+)$$

  with

$$m(a,b) = \begin{cases} a & \text{if } |a| \leq |b| \\ b & \text{otherwise} \end{cases}, \qquad \text{sign}(a) = \begin{cases} 1 & \text{if } a > 0 \\ 0 & \text{if } a = 0 \\ -1 & \text{if } a < 0 \end{cases}$$

  – The third-order ENO is formulated as

$$\hat{\phi}_{i+1/2,j}^{(3)} = \hat{\phi}_{i+1/2,j}^{(2)} +$$
$$\frac{1}{3}\max[\text{sign}(u_{i+1/2,j}),0]\left\{\max[c_i^-,0]m(\delta^2\phi_i^-, \delta^2\phi_i^0) + \frac{1}{2}\min[c_i^-,0]m(\delta^2\phi_i^0, \delta^2\phi_i^+)\right\} +$$
$$\frac{1}{3}\min[\text{sign}(u_{i+1/2,j}),0]\left\{\frac{1}{2}\max[c_i^+,0]m(\delta^2\phi_i^0, \delta^2\phi_i^+) + \min[c_i^+,0]m(\delta^2\phi_i^+, \delta^2\phi_i^{++})\right\}$$

  where

$$c_i^- = c(\delta\phi_i^-, \delta\phi_i^0), \qquad c_i^+ = c(\delta\phi_i^0, \delta\phi_i^+)$$

  with

$$c(a,b) = \begin{cases} 1 & \text{if } |a| \leq |b| \\ -1 & \text{otherwise} \end{cases}$$

2.4.5 Weighted Essentially Non-Oscillatory (WENO) scheme

The Weighted Essentially Non-Oscillatory (WENO) scheme was proposed in 1994 by Liu *et al.* [103] for a third-order finite volume discretization. In 1996, third-order and fifth-order finite difference WENO schemes in multi-space dimensions was constructed by Jiang et Shu [84], with a general framework for the design of smoothness indicators and nonlinear weights. Both ENO and WENO schemes rely on the idea of adaptive stencils to automatically achieve high order accuracy and non-oscillatory property near discontinuities. The advantage of the WENO scheme is its arbitrarily high order formal accuracy in smooth regions while maintaining stable, non-oscillatory and sharp discontinuity transitions. Also this scheme are suitable for problems containing both strong discontinuities and complex smooth solution features [140].

The one-dimensional transport equation (2.28) writes

$$\frac{d\bar{\phi}_i(t)}{dt} = -\frac{1}{\Delta x}(\hat{f}_{i+1/2} - \hat{f}_{i-1/2}) \tag{2.30}$$

Let us consider one of the numerical fluxes $\hat{f}_{i\pm1/2}$, $\hat{f}_{i+1/2}$ for instance. This term is defined as follows:

$$\hat{f}_{i+1/2} = \hat{f}(\phi^-_{i+1/2}, \phi^+_{i+1/2}) \tag{2.31}$$

where $\phi^\pm_{i+1/2}$ are computed from a WENO reconstruction procedure on different stencils. The new numerical flux $\hat{f}(\phi^-, \phi^+)$ must be monotone and therefore it satisfies:

 – $\hat{f}(\phi^-, \phi^+)$ is non-decreasing in its first argument ϕ^- and non-increasing in its second argument ϕ^+;
 – $\hat{f}(\phi^-, \phi^+)$ is consistent with the physical flux $f(\phi)$, i.e. $\hat{f}(\phi, \phi) = f(\phi)$;
 – $\hat{f}(\phi^-, \phi^+)$ is Lipschitz continuous with respect to both argument.

Amongst the monotone fluxes available in the literature, we use the Godunov flux ($\hat{f}(\phi^-, \phi^+) \equiv G(\phi^-, \phi^+)$):

$$G(\phi^-_{i+1/2}, \phi^+_{i+1/2}) = \begin{cases} \displaystyle\min_{\phi^-_{i+1/2}\leq\phi\leq\phi^+_{i+1/2}} f(\phi) & \text{if } \phi^-_{i+1/2} \leq \phi^+_{i+1/2} \\ \displaystyle\max_{\phi^+_{i+1/2}\leq\phi\leq\phi^-_{i+1/2}} f(\phi) & \text{if } \phi^-_{i+1/2} > \phi^+_{i+1/2} \end{cases} \tag{2.32}$$

2.4.5.1 Basic idea of the WENO scheme

A− Local interpolation Let $\Phi_1(x)$ be the polynomial of degree at most three which interpolates the function $Q(x)$ (Eq. (2.29)) at the four points $x_{k+1/2}$, with $k = i-3, \cdots, i$, and let $\phi_1(x) = d\Phi_1/dx$ its spatial derivative. The second order polynomial $\phi_1(x)$ is unique and it reconstructs $\phi(x)$ over the range $S_1 = \{I_{i-2}, I_{i-1}, I_i\}$, where I_i designates the segment $I_i = [x_{i-1/2}, x_{i+1/2}]$, in the sense that

$$\frac{1}{x_{j+1/2} - x_{j-1/2}} \int_{x_{j-1/2}}^{x_{j+1/2}} \phi_1(x)\,dx = \bar{\phi}_j, \qquad j = i-2, \cdots, i$$

This reconstruction also provides an approximation $\phi_1(x_{i+1/2})$ of $\phi(x)$ at point $x_{i+1/2}$. If the function $\phi(x)$ is smooth over the stencil S_1, we have $\phi_1(x_{i+1/2}) - \phi(x_{i+1/2}) = O(\Delta x^3)$ what indicates that this approximation is third order accurate at point $x_{i+1/2}$.

Following the same reasoning, we get two additional reconstructions of $\phi(x)$ on the stencils $S_2 = \{I_{i-1}, I_i, I_{i+1}\}$ and $S_3 = \{I_i, I_{i+1}, I_{i+2}\}$ which provide two new approximations $\phi_2(x_{i+1/2})$ and $\phi_3(x_{i+1/2})$ of $\phi(x)$ at point $x_{i+1/2}$. If $\phi(x)$ is smooth enough over the

stencil S_j, $\phi_j(x_{i+1/2}) - \phi(x_{i+1/2}) = O(\Delta x^3)$.

B– Global interpolation If we use the large stencil $S^{(i)} = \{I_{i-2}, I_{i-1}, I_i, I_{i+1}, I_{i+2}\}$ which is the union of all three stencils S_1, S_2 and S_3, then we would be able to obtain an interpolation polynomial $\tilde{\phi}(x)$ of degree at most four, satisfying

$$\frac{1}{x_{j+1/2} - x_{j-1/2}} \int_{x_{j-1/2}}^{x_{j+1/2}} \tilde{\phi}(x)\, dx = \bar{\phi}_j, \qquad j = i-2, \cdots, i+2$$

and providing an approximation $\tilde{\phi}(x_{i+1/2})$ with a fifth order accuracy: $\tilde{\phi}(x_{i+1/2}) - \phi(x_{i+1/2}) = O(\Delta x^5)$ (provided that $\phi(x)$ is smooth enough on $S_{i+1/2}$). The fifth order accurate approximation $\tilde{\phi}(x_{i+1/2})$ can also be written as a linear convex combination of the three third order approximations $\phi_j(x_{i+1/2})$ based on the smaller stencil S_j:

$$\tilde{\phi}_{i+1/2} \equiv \tilde{\phi}(x_{i+1/2}) = \gamma_1 \phi_1(x_{i+1/2}) + \gamma_2 \phi_2(x_{i+1/2}) + \gamma_3 \phi_3(x_{i+1/2}) \tag{2.33}$$

where γ_1, γ_2, γ_3, satisfying $\gamma_1 + \gamma_2 + \gamma_3 = 1$, are usually referred to as the linear weights.

C– Linear convex combinaison and indicators The final WENO approximation $\hat{\phi}_{i+1/2}$ is another linear convex combination of the three third order approximations $\phi_{i+1/2}^{(j)}$

$$\hat{\phi}_{i+1/2} = \omega_1 \phi_1(x_{i+1/2}) + \omega_2 \phi_2(x_{i+1/2}) + \omega_3 \phi_3(x_{i+1/2}) \tag{2.34}$$

where ω_j are non-linear weights satisfying

$$\omega_j = \frac{\alpha_j}{\alpha_1 + \alpha_2 + \alpha_3}, \quad j = 1, 2, 3 \tag{2.35}$$

with $\omega_j > 0$ and $\omega_1 + \omega_2 + \omega_3 = 1$. The idea to determine the non-linear weights ω_j is that they must satisfy the following requirements:
 – $\omega_j \approx \gamma_j$ if $\phi(x)$ is smooth in the big stencil $S^{(i)} = \{I_{i-2}, I_{i-1}, I_i, I_{i+1}, I_{i+2}\}$;
 – $\omega_j \approx 0$ if $\phi(x)$ has a discontinuity in the stencil $S_j = \{I_{i+j-3}, I_{i+j-2}, I_{i+j-1}\}$, $j = 1$ or 2 or 3, but it is smooth in at least one of the two other stencils.
To ensure this, the coefficient α_j writes

$$\alpha_j = \frac{\gamma_j}{(\epsilon + \beta_j)^2} \tag{2.36}$$

with ϵ is positive real number introduced to avoid the denominator becoming zero. As suggested in [84], we chose $\epsilon = 10^{-6}$. The last coefficient β_j is the indicator which measures the smoothness of the polynomial $\phi_j(x)$ on stencil S_j:

$$\beta_j = \sum_{l=1}^{k} (\Delta x)^{2l-1} \int_{x_{i-1/2}}^{x_{i+1/2}} \left(\frac{d^l}{dx^l} \phi_j(x) \right)^2 dx \tag{2.37}$$

where k is the polynomial degree of p_j, two in our case.

2.4.5.2 Interpolation formula

The evaluation of fluxes $\hat{f}_{i+1/2}$ and $\hat{f}_{i-1/2}$ of Eq. (2.30) writes as follows:

$$\hat{f}_{i+1/2} = G(\phi^-_{i+1/2}, \phi^+_{i+1/2})$$

$$\hat{f}_{i-1/2} = G(\phi^-_{i-1/2}, \phi^-_{i-1/2})$$

with $G(\phi^-, \phi^+)$ the monotone Godunov flux (2.32). The face values $\phi^-_{i+1/2}$, $\phi^+_{i+1/2}$, $\phi^-_{i-1/2}$ and $\phi^-_{i-1/2}$ are approximated with the WENO scheme on different stencils. The superscript $\pm$ indicates WENO reconstructions from stencils one point biased to the left $(^-)$ and one point biased to the right $(^+)$ (see Tab. 2.2) Therefore, Eq. (2.34) gives

Stencil	I_{i-3}	I_{i-2}	I_{i-1}	I_i	I_{i+1}	I_{i+2}	I_{i+3}
$\phi^-(x_{i-1/2})$	+	+	+	+	+		
$\phi^+(x_{i-1/2})$		+	+	+	+	+	
$\phi^-(x_{i+1/2})$		+	+	+	+	+	
$\phi^+(x_{i+1/2})$			+	+	+	+	+

Table 2.2 – Stencils for the reconstructions

$$\phi^-(x_{i-1/2}) = \omega^{(i-1)-}_1 \phi_1(x_{i-1/2}) + \omega^{(i-1)-}_2 \phi_2(x_{i-1/2}) + \omega^{(i-1)-}_3 \phi_3(x_{i-1/2}),$$
$$\text{on } \{I_{i-3}, I_{i-2}, I_{i-1}, I_i, I_{i+1}\} \quad (2.38\text{a})$$

$$\phi^+(x_{i-1/2}) = \omega^{(i)}_0 \phi_0(x_{i-1/2}) + \omega^{(i)}_1 \phi_1(x_{i-1/2}) + \omega^{(i)}_2 \phi_2(x_{i-1/2}),$$
$$\text{on } \{I_{i-2}, I_{i-1}, I_i, I_{i+1}, I_{i+2}\} \quad (2.38\text{b})$$

$$\phi^-(x_{i+1/2}) = \omega^{(i)}_0 \phi_0(x_{i+1/2}) + \omega^{(i)}_1 \phi_1(x_{i+1/2}) + \omega^{(i)}_2 \phi_2(x_{i+1/2}),$$
$$\text{on } \{I_{i-2}, I_{i-1}, I_i, I_{i+1}, I_{i+2}\} \quad (2.38\text{c})$$

$$\phi^+(x_{i+1/2}) = \omega^{(i+1)+}_{-1} \phi_{-1}(x_{i+1/2}) + \omega^{(i+1)+}_0 \phi_0(x_{i+1/2}) + \omega^{(i+1)+}_1 \phi_1(x_{i+1/2}),$$
$$\text{on } \{I_{i-1}, I_i, I_{i+1}, I_{i+2}, I_{i+3}\} \quad (2.38\text{d})$$

A general formula is used for the second order interpolation polynomials,

$$\phi_r(x) = \sum_{j=0}^{2} B_{rj}(x) h_{3-r+j} \bar{\phi}_{i-r+j}, \text{ on stencil } \{I_{i-r}, I_{i-r+1}, I_{i-r+2}\} \quad (2.39)$$

where $r = -1, \cdots, 3$ indicates the shift of the stencil and h_m is the local grid size:

$$h_m = \Delta x_{i-3+m}, \quad m = 0, \cdots, 6 \quad (2.40)$$

The coefficient $B_{rj}(x)$ is written:

$$B_{rj}(x) = \sum_{m=j+1}^{3} \frac{\sum_{l=0, l \neq m}^{3} \Pi_{q=0, q \neq m, l}^{3} (x - x_{i-r+q+1/2})}{\Pi_{l=0, l \neq m}^{3} (x_{i-r+m+1/2} - x_{i-r+l+1/2})}, \text{ with } \begin{cases} j = 0, \cdots, 2 \\ r = -1, \cdots, 3 \end{cases} \quad (2.41)$$

We now can deduce approximations at faces $x_{i+1/2}$, $\phi_r(x_{i+1/2})$, and $x_{i-1/2}$, $\phi_r(x_{i-1/2})$:

$$\phi_r(x_{i+1/2}) = \sum_{j=0}^{2} \hat{b}_{r,j}^{(i)} h_{3-r+j} \bar{\phi}_{i-r+j}, \qquad \phi_r(x_{i-1/2}) = \sum_{j=0}^{2} b_{r,j}^{(i)} h_{3-r+j} \bar{\phi}_{i-r+j} \qquad (2.42)$$

with $\hat{b}_{r,j}^{(i)} = B_{rj}(x_{i+1/2})$, $b_{r,j}^{(i)} = B_{rj}(x_{i-1/2})$ and $j = 0, \cdots, 2$. It is easy to prove that the following equivalence yields

$$\hat{b}_{r,j}^{(i)} \equiv b_{r+1,j}^{(i-1)}$$

A– Explicit formulations of coefficients $\hat{b}_{r,j}^{(i)}$ for irregular grids

$$
\begin{cases}
\hat{b}_{2,2}^{(i)} = \dfrac{1}{h_1 + h_2 + h_3} + \dfrac{1}{h_2 + h_3} + \dfrac{1}{h_3} \\[2mm]
\hat{b}_{2,1}^{(i)} = \hat{b}_{22} - \dfrac{(h_1 + h_2 + h_3)(h_2 + h_3)}{(h_1 + h_2)h_2 h_3} \\[2mm]
\hat{b}_{2,0}^{(i)} = \hat{b}_{21} + \dfrac{(h_1 + h_2 + h_3)h_3}{h_1 h_2(h_2 + h_3)}
\end{cases}
,\quad
\begin{cases}
\hat{b}_{1,2}^{(i)} = \dfrac{(h_2 + h_3)h_3}{(h_2 + h_3 + h_4)(h_3 + h_4)h_4} \\[2mm]
\hat{b}_{1,1}^{(i)} = \hat{b}_{12} + \dfrac{1}{h_2 + h_3} + \dfrac{1}{h_3} - \dfrac{1}{h_4} \\[2mm]
\hat{b}_{1,0}^{(i)} = \hat{b}_{11} - \dfrac{(h_2 + h_3)h_4}{h_2 h_3(h_3 + h_4)}
\end{cases}
$$

$$
\begin{cases}
\hat{b}_{0,2}^{(i)} = -\dfrac{h_3 h_4}{(h_3 + h_4 + h_5)(h_4 + h_5)h_5} \\[2mm]
\hat{b}_{0,1}^{(i)} = \hat{b}_{02} + \dfrac{h_3(h_4 + h_5)}{(h_3 + h_4)h_4 h_5} \\[2mm]
\hat{b}_{0,0}^{(i)} = \hat{b}_{01} + \dfrac{1}{h_3} - \dfrac{1}{h_4} - \dfrac{1}{h_4 + h_5}
\end{cases}
,\quad
\begin{cases}
\hat{b}_{-1,2}^{(i)} = \dfrac{h_4(h_4 + h_5)}{(h_4 + h_5 + h_6)(h_5 + h_6)h_6} \\[2mm]
\hat{b}_{-1,1}^{(i)} = \hat{b}_{-12} - \dfrac{h_4(h_4 + h_5 + h_6)}{(h_4 + h_5)h_5 h_6} \\[2mm]
\hat{b}_{-1,0}^{(i)} = \hat{b}_{-11} + \dfrac{(h_4 + h_5)(h_4 + h_5 + h_6)}{h_4 h_5(h_5 + h_6)}
\end{cases}
$$

$$(2.43)$$

To get $b_{r,j}^{(i)} \equiv \hat{b}_{r-1,j}^{(i+1)}$, we have to select $\hat{b}_{r-1,j}^{(i)}$ and to substitute the all the subscript values k of the grid spacings h by the value $k - 1$. For example we obtain:

$$b_{3,2}^{(i)} \equiv \hat{b}_{2,2}^{(i+1)} = \dfrac{1}{h_0 + h_1 + h_2} + \dfrac{1}{h_1 + h_2} + \dfrac{1}{h_2}$$

B– Explicit formulation for regular grids For uniform meshes, all h_m are identical. Expressions (2.43) are greatly simplified, and the different approximations on faces (Eq. (2.42)) then write:

$$
\begin{cases}
\phi_3(x_{i-1/2}) = \frac{11}{6}\bar{\phi}_i - \frac{7}{6}\bar{\phi}_{i+1} + \frac{2}{6}\bar{\phi}_{i+2} \\[1mm]
\phi_2(x_{i-1/2}) = \frac{2}{6}\bar{\phi}_{i-1} + \frac{5}{6}\bar{\phi}_i - \frac{1}{6}\bar{\phi}_{i+1} \\[1mm]
\phi_1(x_{i-1/2}) = -\frac{1}{6}\bar{\phi}_{i-2} + \frac{5}{6}\bar{\phi}_{i-1} + \frac{2}{6}\bar{\phi}_i \\[1mm]
\phi_0(x_{i-1/2}) = \frac{2}{6}\bar{\phi}_{i-3} - \frac{7}{6}\bar{\phi}_{i-2} + \frac{11}{6}\bar{\phi}_{i-1}
\end{cases}
,\quad
\begin{cases}
\phi_2(x_{i+1/2}) = \frac{11}{6}\bar{\phi}_{i+1} - \frac{7}{6}\bar{\phi}_{i+2} + \frac{2}{6}\bar{\phi}_{i+3} \\[1mm]
\phi_1(x_{i+1/2}) = \frac{2}{6}\bar{\phi}_i + \frac{5}{6}\bar{\phi}_{i+1} - \frac{1}{6}\bar{\phi}_{i+2} \\[1mm]
\phi_0(x_{i+1/2}) = -\frac{1}{6}\bar{\phi}_{i-1} + \frac{5}{6}\bar{\phi}_i + \frac{2}{6}\bar{\phi}_{i+1} \\[1mm]
\phi_{-1}(x_{i+1/2}) = \frac{2}{6}\bar{\phi}_{i-2} - \frac{7}{6}\bar{\phi}_{i-1} + \frac{11}{6}\bar{\phi}_i
\end{cases}
$$

2.4.5.3 Smoothness measure

The non-linear weights $\omega_r^{(i)}$, $\omega_r^{(i-1)-}$ and $\omega_r^{(i+1)+}$ in Eqs. (2.38) are expressed as a function of linear weights $\gamma_r^{(i)}$, $\gamma_r^{(i-1)-}$ and $\gamma_r^{(i+1)+}$ as well as a function of smoothness

indicators $\beta_r^{(i)}$, $\beta_r^{(i-1)-}$ and $\beta_r^{(i+1)+}$ as follows:

$$\omega_r^{(i)} = \frac{\alpha_r^{(i)}}{\alpha_0^{(i)} + \alpha_1^{(i)} + \alpha_2^{(i)}}, \quad \gamma_r^{(i)} = \frac{\gamma_r^{(i)}}{\left(\epsilon + \beta_r^{(i)}\right)^2}, \qquad r = 0, \cdots, 2$$

$$\omega_r^{(i-1)-} = \frac{\alpha_r^{(i-1)-}}{\alpha_1^{(i-1)-} + \alpha_2^{(i-1)-} + \alpha_3^{(i-1)-}}, \quad \gamma_r^{(i-1)-} = \frac{\gamma_r^{(i-1)-}}{\left(\epsilon + \beta_r^{(i-1)-}\right)^2}, \qquad r = 1, \cdots, 3$$

$$\omega_r^{(i+1)+} = \frac{\alpha_r^{(i+1)+}}{\alpha_{-1}^{(i+1)+} + \alpha_0^{(i+1)+} + \alpha_1^{(i+1)+}}, \quad \gamma_r^{(i+1)+} = \frac{\gamma_r^{(i+1)+}}{\left(\epsilon + \beta_r^{(i+1)+}\right)^2}, \qquad r = -1, \cdots, 1$$

Larger is the smoothness indicator $\beta_r^{(j)}$, less smooth is the function $\phi_r(x)$ in the stencil I_j.

In this section, we focus on the smoothness indicators $\beta_r^{(i)}$, $r = 0, \cdots, 2$, in Eqs. (2.38b) and (2.38c) since the others can be deduced from these indicators. We choose a smoothness indicator $\beta_r^{(i)}$ according to Jiang et Shu [84]:

$$\beta_r^{(i)} = \sum_{l=1}^{2} (\Delta x_i)^{2l-1} \int_{x_{i-1/2}}^{x_{i+1/2}} \left(\frac{d^l}{dx^l}\phi_r(x)\right)^2 dx, \qquad r = 0, \cdots, 2$$

The other indicators in Eqs. (2.38a) and (2.38d) are deduced from relations :

$$\beta_r^{(i-1)-} \equiv \beta_{r-1}^{(i-1)}, \text{ and } \beta_r^{(i+1)+} \equiv \beta_{r+1}^{(i+1)}$$

A− Smoothness indicators for $\phi_{i-1/2}^+$ and $\phi_{i+1/2}^-$ with irregular grids Taking the variable change Eq. (2.40) into account, the indicator $\beta_r^{(i)}$ simply writes

$$\beta_r^{(i)} = \int_{x_{i-1/2}}^{x_{i+1/2}} h_3 \left(\frac{d\phi_r}{dx}\right)^2 dx + \int_{x_{i-1/2}}^{x_{i+1/2}} h_3^3 \left(\frac{d^2\phi_r}{dx^2}\right)^2 dx \qquad (2.44)$$

The two terms of the right-hand side of Eq. (2.44) are considered independently.
  – The second integral in Eq. (2.44) is easily evaluated since the second derivative of $\phi_r(x)$ is constant and $\phi_r(x)$ is defined by Eq. (2.39). We then have:

$$\int_{x_{i-1/2}}^{x_{i+1/2}} (h_3)^3 \left(\frac{d^2\phi_r}{dx^2}\right)^2 dx = (h_3)^4 \left(\sum_{j=0}^{2} B''_{rj} h_{3-r+j} \bar{\phi}_{i-r+j}\right)^2$$

where $B''_{rj}(x)$ is constant, $B''_{rj}(x) \equiv B''_{rj}$ with

$$B''_{r2} = \frac{6}{(h_{3-r} + h_{4-r} + h_{5-r})(h_{4-r} + h_{5-r})h_{5-r}}, \qquad r = 0, \cdots, 2$$

$$B''_{r1} = B''_{r2} - \frac{6}{(h_{3-r} + h_{4-r})h_{4-r}h_{5-r}}, \qquad r = 0, \cdots, 3$$

$$B''_{r0} = B''_{r1} + \frac{6}{h_{3-r}h_{4-r}(h_{4-r} + h_{5-r})}, \qquad r = 0, \cdots, 2$$

– The first right-hand side term in Eq. (2.44) involves the integration of a quadratic function. This is performed with the Simpson's quadrature:

$$\int_{x_{i-1/2}}^{x_{i+1/2}} h_3(\phi'(x))^2 dx =$$

$$\frac{(h_3)^2}{6}\left(\left(\frac{d\phi_r}{dx}(x_{i-1/2})\right)^2 + 4\left(\frac{d\phi_r}{dx}(x_i)\right)^2 + \left(\frac{d\phi_r}{dx}(x_{i+1/2})\right)^2\right)$$

Again, the derivative $\phi'(x)$ is obtained from Eq. (2.39):

$$\frac{d\phi_r}{dx}(x) = \sum_{j=0}^{2} B'_{rj}(x)h_{3-r+j}\bar{\phi}_{i-r+j}$$

The expressions $B'_{rj}(x_{i-1/2})$, $B'_{rj}(x_i)$ and $B'_{rj}(x_{i+1/2})$ are:

$$\begin{cases} B'_{22}(x_{i-1/2}) = \dfrac{2(h_1 + 2h_2)}{(h_1 + h_2 + h_3)(h_2 + h_3)h_3} \\ B'_{21}(x_{i-1/2}) = B'_{22}(x_{i-1/2}) - \dfrac{2(h_1 + 2h_2 - h_3)}{(h_1 + h_2)h_2h_3} \\ B'_{20}(x_{i-1/2}) = B'_{21}(x_{i-1/2}) + \dfrac{2(h_1 + h_2 - h_3)}{h_1h_2(h_2 + h_3)} \end{cases}$$

$$\begin{cases} B'_{12}(x_{i-1/2}) = \dfrac{2(h_2 - h_3)}{(h_2 + h_3 + h_4)(h_3 + h_4)h_4} \\ B'_{11}(x_{i-1/2}) = B'_{12}(x_{i-1/2}) - \dfrac{2(h_2 - h_3 - h_4)}{(h_2 + h_3)h_3h_4} \\ B'_{10}(x_{i-1/2}) = B'_{11}(x_{i-1/2}) + \dfrac{2(h_2 - 2h_3 - h_4)}{h_2h_3(h_3 + h_4)} \end{cases}$$

$$\begin{cases} B'_{02}(x_{i-1/2}) = -\dfrac{2(2h_3 + h_4)}{(h_3 + h_4 + h_5)(h_4 + h_5)h_5} \\ B'_{01}(x_{i-1/2}) = B'_{02}(x_{i-1/2}) + \dfrac{2(2h_3 + h_4 + h_5)}{(h_3 + h_4)h_4h_5} \\ B'_{00}(x_{i-1/2}) = B'_{01}(x_{i-1/2}) - \dfrac{2(2h_3 + 2h_4 + h_5)}{h_3h_4(h_4 + h_5)} \end{cases}$$

and

$$B'_{rj}(x_i) = B'_{rj}(x_{i-1/2}) + \frac{1}{2}h_3 B''_{rj}, \qquad j = 0, \cdots, 2$$
$$B'_{rj}(x_{i+1/2}) = B'_{rj}(x_{i-1/2}) + h_3 B''_{rj}, \qquad j = 0, \cdots, 2$$

B– Smoothness indicators for $\phi^+_{i-1/2}$ and $\phi^-_{i+1/2}$ with regular grids For the uniform meshes, we then get:

$$\beta_1^{(i)} = \frac{13}{12}(\bar{\phi}_{i-2} - 2\bar{\phi}_{i-1} + \bar{\phi}_i)^2 + \frac{1}{4}(\bar{\phi}_{i-2} - 4\bar{\phi}_{i-1} + 3\bar{\phi}_i)^2$$
$$\beta_2^{(i)} = \frac{13}{12}(\bar{\phi}_{i-1} - 2\bar{\phi}_i + \bar{\phi}_{i+1})^2 + \frac{1}{4}(\bar{\phi}_{i-1} - \bar{\phi}_{i+1})^2$$
$$\beta_3^{(i)} = \frac{13}{12}(\bar{\phi}_i - 2\bar{\phi}_{i+1} + \bar{\phi}_{i+2})^2 + \frac{1}{4}(3\bar{\phi}_i - 4\bar{\phi}_{i+1} + \bar{\phi}_{i+2})^2$$

2.4.5.4 Computation of linear weights

Using relation (2.39) on the extended stencil $\{I_{i-r}, I_{i-r+1}, I_{i-r+2}, I_{i-r+3}, I_{i-r+4}\}$, we can construct a fifth-order interpolation approximation $\tilde{\phi}_r(x)$ such that

$$\tilde{\phi}_r(x) = \sum_{j=0}^{4} \tilde{B}_{rj}(x) h_{3-r+j} \bar{\phi}_{i-r+j}$$

with

$$\frac{1}{h_{3-r+j}} \int_{x_{3-r+j-1/2}}^{x_{3-r+j+1/2}} \tilde{\phi}_r(x)\, dx = \bar{\phi}_{3-r+j}, \qquad r = 1, \cdots, 3, \text{ and } j = 0, \cdots, 4$$

The functions $\tilde{B}_{rj}(x)$ are expressed similarly to Eq. (2.41):

$$\tilde{B}_{rj}(x) = \sum_{m=j+1}^{5} \frac{\sum_{l=0, l\neq m}^{5} \Pi_{q=0, q\neq m,l}^{5} (x - x_{i-r+q+1/2})}{\Pi_{l=0, l\neq m}^{5} (x_{i-r+m+1/2} - x_{i-r+l+1/2})}$$

The convex linear combinations write:

$$\tilde{\phi}_3(x_{i-1/2}) = \sum_{j=1}^{3} \gamma_j^{3-} \phi_j(x_{i-1/2})$$

$$\tilde{\phi}_2(x_{i-1/2}) = \sum_{j=0}^{2} \gamma_j^{2+} \phi_j(x_{i-1/2}), \qquad \tilde{\phi}_2(x_{i+1/2}) = \sum_{j=0}^{2} \gamma_j^{2-} \phi_j(x_{i+1/2})$$

$$\tilde{\phi}_1(x_{i+1/2}) = \sum_{j=-1}^{1} \gamma_j^{1+} \phi_j(x_{i+1/2})$$

A− Linear weight for irregular grids   We get:

$$\begin{cases} \gamma_3^{3-} = \dfrac{h_3(h_3 + h_4)}{(h_0 + h_1 + h_2 + h_3)(h_0 + h_1 + h_2 + h_3 + h_4)} \\[2mm] \gamma_2^{3-} = \dfrac{(h_0 + h_1 + h_2)(h_3 + h_4)(h_0 + 2h_1 + 2h_2 + 2h_3 + h_4)}{(h_0 + h_1 + h_2 + h_3)(h_1 + h_2 + h_3 + h_4)(h_0 + h_1 + h_2 + h_3 + h_4)} \\[2mm] \gamma_1^{3-} = \dfrac{(h_1 + h_2)(h_0 + h_1 + h_2)}{(h_1 + h_2 + h_3 + h_4)(h_0 + h_1 + h_2 + h_3 + h_4)} \end{cases}$$

$$\begin{cases} \gamma_2^{2+} = \dfrac{(h_3 + h_4)(h_3 + h_4 + h_5)}{(h_1 + h_2 + h_3 + h_4)(h_1 + h_2 + h_3 + h_4 + h_5)} \\[2mm] \gamma_1^{2+} = \dfrac{(h_1 + h_2)(h_3 + h_4 + h_5)(h_1 + 2h_2 + 2h_3 + 2h_4 + h_5)}{(h_1 + h_2 + h_3 + h_4)(h_2 + h_3 + h_4 + h_5)(h_1 + h_2 + h_3 + h_4 + h_5)} \\[2mm] \gamma_0^{2+} = \dfrac{h_2(h_1 + h_2)}{(h_2 + h_3 + h_4 + h_5)(h_1 + h_2 + h_3 + h_4 + h_5)} \end{cases}$$

$$\begin{cases} \gamma_2^{2-} = \dfrac{h_4(h_4 + h_5)}{(h_1 + h_2 + h_3 + h_4)(h_1 + h_2 + h_3 + h_4 + h_5)} \\[2mm] \gamma_1^{2-} = \dfrac{(h_1 + h_2 + h_3)(h_4 + h_5)(h_1 + 2h_2 + 2h_3 + 2h_4 + h_5)}{(h_1 + h_2 + h_3 + h_4)(h_2 + h_3 + h_4 + h_5)(h_1 + h_2 + h_3 + h_4 + h_5)} \\[2mm] \gamma_0^{2-} = \dfrac{(h_2 + h_3)(h_1 + h_2 + h_3)}{(h_2 + h_3 + h_4 + h_5)(h_1 + h_2 + h_3 + h_4 + h_5)} \end{cases}$$

$$
\left\{
\begin{aligned}
\gamma_1^{1+} &= \frac{(h_4 + h_5)(h_4 + h_5 + h_6)}{(h_2 + h_3 + h_4 + h_5)(h_2 + h_3 + h_4 + h_5 + h_6)} \\
\gamma_0^{1+} &= \frac{(h_2 + h_3)(h_4 + h_5 + h_6)(h_2 + 2h_3 + 2h_4 + 2h_5 + h_6)}{(h_2 + h_3 + h_4 + h_5)(h_3 + h_4 + h_5 + h_6)(h_2 + h_3 + h_4 + h_5 + h_6)} \\
\gamma_{-1}^{1+} &= \frac{h_3(h_2 + h_3)}{(h_3 + h_4 + h_5 + h_6)(h_2 + h_3 + h_4 + h_5 + h_6)}
\end{aligned}
\right.
$$

B– Linear weight for regular grids

$$
\gamma_3^{3-} = \frac{1}{10}, \gamma_2^{3-} = \frac{6}{10}, \gamma_1^{3-} = \frac{3}{10}
$$

$$
\gamma_2^{2+} = \frac{3}{10}, \gamma_1^{2+} = \frac{6}{10}, \gamma_0^{2+} = \frac{1}{10}
$$

$$
\gamma_2^{2-} = \frac{1}{10}, \gamma_1^{2-} = \frac{6}{10}, \gamma_0^{2-} = \frac{3}{10}
$$

$$
\gamma_1^{1+} = \frac{3}{10}, \gamma_0^{1+} = \frac{6}{10}, \gamma_{-1}^{1+} = \frac{1}{10}
$$

2.5 Discretization of signed distance equation

The idea which governs the discretization of the signed distance function is very similar to what was applied for the transport of the level set function. We use the third order TVD Runge-Kutta discretization:

$$
d^0 = d^{(n)} \tag{2.45a}
$$

$$
d^i = \sum_{k=0}^{i-1} \left[\alpha_{ik} d^k - \beta_{ik} \Delta t\, f(d^k) \right], \quad i = 1, \cdots, 3 \tag{2.45b}
$$

$$
d^{(n+1)} = d^3 \tag{2.45c}
$$

with $f(d^k) = s(d^0)(\|\nabla d^k\| - 1)$ and coefficients α_{ik} and β_{ik} given in Tab. 2.1.

The spatial discretization cannot be achieved with a finite volume method; a finite difference method is used instead. The issue is the computation the first order derivatives $\partial d/\partial x$ and $\partial d/\partial y$ at the cell center (x_i, y_j). This is performed with either second-order ENO or fifth-order WENO reconstruction methods, both of these approaches being based on the monotone Godunov flux.

The main reconstruction of the derivatives is succinctly explained. Let us consider the derivative in x direction. Then, its average value is known at $x_{i\pm1/2}$:

$$
\overline{\frac{\partial d}{\partial x}}(x_{i\pm1/2}, y_j) \equiv d_x^{(1)\pm} = \frac{1}{x_i - x_{i\pm1}} \int_{x_{i\pm1}}^{x_i} \frac{\partial d}{\partial x}\, dx = \frac{d_{i,j} - d_{i\pm1,j}}{x_i - x_{i\pm1}} \tag{2.46}
$$

Since the average values are known on cell faces, the ENO or WENO reconstructions provide approximates at the cell center (x_i, y_j), $\frac{\partial d}{\partial x}(x_i, y_j)^\pm$. In the ENO algorithm for the transport equation of the level set function (Sec. 2.4.4.1), the upwind approximation allows to select one of the two approximations on each face. For the signed distance function, such a choice is unclear. To overcome this difficulty, the monotone Godunov flux (2.32) is used.

2.5.1 ENO scheme

The following second-order ENO scheme is applied for the signed distance function $d(x, y)$ (Eq. (2.14)) for a regular grid spacing Δx and Δy :

1. Approximations of x-derivatives (similar relations hold for y-derivatives)

   (a) First-order approximations:

   $$d_x^{(1)-} = \frac{d_{i,j} - d_{i-1,j}}{\Delta x}, \qquad d_x^{(1)+} = \frac{d_{i+1,j} - d_{i,j}}{\Delta x}$$

   (b) Second-order approximations:

   $$d_x^{(2)-} = d_x^{(1)-} + \frac{\Delta x^-}{2} \frac{\delta^2 d^-}{\delta x^2}, \qquad d_x^{(2)+} = d_x^{(1)+} - \frac{\Delta x^+}{2} \frac{\delta^2 d^+}{\delta x^2}$$

   where

   $$\frac{\delta^2 d^-}{\delta x^2} = \text{minmod}(d(1), d(2)), \qquad \frac{\delta^2 d^+}{\delta x^2} = \text{minmod}(d(2), d(3))$$

   $$\text{minmod}(a, b) = \begin{cases} \text{sign}(a) \ \text{minmod}(|a|, |b|) & \text{if } a \times b > 0 \\ 0 & \text{otherwise} \end{cases}$$

   and $d(1)$, $d(2)$ and $d(3)$ are the central difference approximation of $\partial^2 d/\partial x^2$ on stencils $(x_{i-2,j}, x_{i-1,j}, x_{i,j})$, $(x_{i-1,j}, x_{i,j}, x_{i+1,j})$, and $(x_{i,j}, x_{i+1,j}, x_{i+2,j})$, respectively:

   $$d(l) = \frac{d_{i+l-1,j} - 2d_{i+l-2,j} + d_{i+l-3,j}}{(\Delta x)^2}, \quad l = 1, \cdots, 3$$

2. Computation of $\|\nabla d\|$.
   Let

   $$a = d_x^{(2)-}, b = d_x^{(2)+}$$
   $$c = d_y^{(2)-}, d = d_y^{(2)+}$$

   The computation of $\|\nabla d\|$ is performed by Godunov's method [153]:

   $$\|\nabla d\| = \begin{cases} D^+ & \text{if } s(d^0) > 0 \\ D^- & \text{if } s(d^0) < 0 \\ 0 & \text{otherwise} \end{cases} \tag{2.47}$$

   with

   $$D^+ = \sqrt{\max(a_+^2, b_-^2) + \max(c_+^2, d_-^2)} \qquad D^- = \sqrt{\max(a_-^2, b_+^2) + \max(c_-^2, d_+^2)}$$

   where

   $$\begin{aligned} a_+ &= \max(a, 0), & a_- &= \min(a, 0) \\ b_+ &= \max(b, 0), & b_- &= \min(b, 0) \\ c_+ &= \max(c, 0), & c_- &= \min(c, 0) \\ d_+ &= \max(d, 0), & d_- &= \min(d, 0) \end{aligned}$$

Therefore, the function $f(d^k)$ in the Runge-Kutta method (2.45) writes

$$f(d^k) \equiv s(d^0)(\|\nabla d^k\| - 1) = \max\left[s(d^0), 0\right](D^+ - 1) + \min\left[s(d^0), 0\right](D^- - 1) \tag{2.48}$$

2.5.2 WENO scheme

Like the ENO scheme, the reconstruction is based on average values (See Eq. (2.46)):

$$\bar{d}^{(1)}_{i+k+1} = \frac{1}{x_{i+k+1} - x_{i+k}} \int_{x_{i+k}}^{x_{i+k+1}} \frac{\partial d}{\partial x}\, dx = \frac{d_{i+k+1,j} - d_{i+k,j}}{x_{i+k+1} - x_{i+k}}$$

where $\{x_{i+k},\ k = -3, ..., 2\}$ stands for the left-biased stencil (Fig. 2.4(a)), and $\{x_{i+k},\ k = -2, ..., 3\}$ corresponds to the right-biased stencil (Fig. 2.4(b)). Using the grid spacing

(a) Left biased stencil (b) Right biased stencil
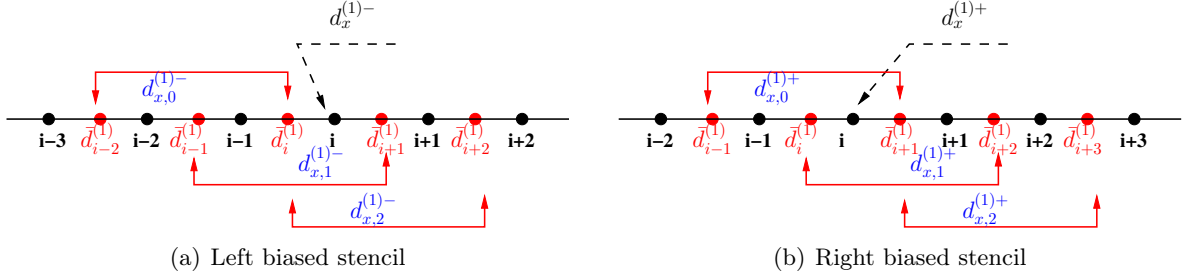
Figure 2.4 – Left and right biased stencils for the signed distance equation

$$h_j \equiv x_{i-3+j} - x_{i-4+j}, \quad j = 1, ..., 6$$

we get:

$$\bar{d}^{(1)}_{i+k+1} = \frac{d_{i+k+1,j} - d_{i+k,j}}{h_{4+k}}$$

The left- and right-biased approximations $d_x^{(1)-}$ and $d_x^{(1)+}$ of $(\partial d/\partial x)(x_i, y_j)$ write:

$$d_x^{(1)\pm} = \omega_0^\pm d_{x,0}^{(1)\pm}(x_i) + \omega_1^\pm d_{x,1}^{(1)\pm}(x_i) + \omega_2^\pm d_{x,2}^{(1)\pm}(x_i)$$

with $d_{x,j}^{(1)\pm}(x_i)$, $j = 0, \cdots, 2$, defined in Tab. 2.3. The coefficients $\omega_j^\pm$, $j = 0, \cdots, 2$, of the linear convex combination are expressed as follows:

$$\omega_j^\pm = \frac{\alpha_j^\pm}{\alpha_0^\pm + \alpha_1^\pm + \alpha_2^\pm}, \quad j = 0, \cdots, 2$$

with

$$\alpha_j^\pm = \frac{\gamma_j^\pm}{\left(\epsilon + \beta_j^\pm\right)^2}$$

and $\epsilon = 10^{-6}$, for instance. The linear weights $\gamma_j^\pm$, $j = 0, \cdots, 2$, are reported in Tab. 2.5. The smoothness indicators $\beta_j^\pm$ are indicated in Tab. 2.4 for a regular grid size. For irregular grids the indicators $\beta_j^\pm$, $j = 0, \cdots, 2$ are computed according to the formula:

$$\beta_j^- = \frac{(h_3)^2}{6}\left[\left(\sum_{k=0}^{2} B'^-_{jk}(x_{i-1})h_{3-j+k}\bar{d}^{(1)}_{i-j+k-1}\right)^2 + \right.$$

$$4\left(\sum_{k=0}^{2} B'^-_{jk}(x_{i-1/2})h_{3-j+k}\bar{d}^{(1)}_{i-j+k-1}\right)^2 + \left(\sum_{k=0}^{2} B'^-_{jk}(x_i)h_{3-j+k}\bar{d}^{(1)}_{i-j+k-1}\right)^2 \left.\right] +$$

$$(h_3)^4\left(\sum_{k=0}^{2} B''^-_{jk}h_{3-j+k}\bar{d}^{(1)}_{i-j+k-1}\right)^2$$

and

$$\beta_j^+ = \frac{(h_4)^2}{6} \left[\left(\sum_{k=0}^{2} B_{jk}^{'+}(x_i) h_{4-j+k} \bar{d}_{i-j+k}^{(1)} \right)^2 + \right.$$

$$4 \left(\sum_{k=0}^{2} B_{jk}^{'+}(x_{i+1/2}) h_{4-j+k} \bar{d}_{i-j+k}^{(1)} \right)^2 + \left. \left(\sum_{k=0}^{2} B_{jk}^{'+}(x_{i+1}) h_{4-j+k} \bar{d}_{i-j+k}^{(1)} \right)^2 \right] +$$

$$(h_4)^4 \left(\sum_{k=0}^{2} B_{jk}^{''+} h_{4-j+k} \bar{d}_{i-j+k}^{(1)} \right)^2$$

where coefficients $B_{jk}^{'\pm}$ and $B_{jk}^{''\pm}$ are provided by Tab. 2.4.

Table 2.3: Local approximations on substencils of the fifth-order WENO scheme for uniform and non-uniform grids ($h_j \equiv x_{i-3+j} - x_{i-4+j}$, $j = 1,...,6$)

	Non-uniform grid	Uniform grid	Coefficients
$d_{x,0}^{(1)-}(x_i)$	$\hat{b}_{20}b_1 d_{i-3}^{(1)} + \hat{b}_{21}h_2 b_2 d_{i-2}^{(1)} + \hat{b}_{22}h_3 d_{i-1}^{(1)}$	$\frac{1}{3}d_{i-3}^{(1)} - \frac{7}{6}d_{i-2}^{(1)} + \frac{11}{6}d_{i-1}^{(1)}$	$\hat{b}_{22} = \dfrac{1}{h_1+h_2+h_3} + \dfrac{1}{h_2+h_3} + \dfrac{1}{h_3}$
			$\hat{b}_{21} = \hat{b}_{22} - \dfrac{(h_1+h_2+h_3)(h_2+h_3)}{(h_1+h_2)h_2 h_3}\,h_3$
			$\hat{b}_{20} = \hat{b}_{21} + \dfrac{(h_1+h_2+h_3)h_3}{h_1 h_2(h_2+h_3)h_3}$
$d_{x,1}^{(1)-}(x_i)$	$\hat{b}_{10}h_2 d_{i-2}^{(1)} + \hat{b}_{11}h_3 d_{i-1}^{(1)} + \hat{b}_{12}h_4 d_i^{(1)}$	$-\frac{1}{6}d_{i-2}^{(1)} + \frac{5}{6}d_{i-1}^{(1)} + \frac{1}{3}d_i^{(1)}$	$\hat{b}_{12} = \dfrac{(h_2+h_3)h_3}{(h_2+h_3+h_4)(h_3+h_4)h_4}$
			$\hat{b}_{11} = \hat{b}_{12} + \dfrac{1}{h_2+h_3} + \dfrac{1}{h_3} - \dfrac{1}{h_4}$
			$\hat{b}_{10} = \hat{b}_{11} - \dfrac{(h_2+h_3)h_4}{h_2 h_3(h_3+h_4)h_4}$
$d_{x,2}^{(1)-}(x_i)$	$\hat{b}_{00}h_3 d_{i-1}^{(1)} + \hat{b}_{01}h_4 d_i^{(1)} + \hat{b}_{02}h_5 d_{i+1}^{(1)}$	$\frac{1}{3}d_{i-1}^{(1)} + \frac{5}{6}d_i^{(1)} - \frac{1}{6}d_{i+1}^{(1)}$	$\hat{b}_{02} = -\dfrac{h_3 h_4}{(h_3+h_4+h_5)(h_4+h_5)h_5}$
			$\hat{b}_{01} = \hat{b}_{02} + \dfrac{(h_3+h_4)h_4 h_5}{h_3(h_4+h_5)}$
			$\hat{b}_{00} = \hat{b}_{01} + \dfrac{1}{h_3} - \dfrac{1}{h_4} - \dfrac{1}{h_4+h_5}$
$d_{x,0}^{(1)+}(x_i)$	$\hat{b}_{-10}h_4 d_i^{(1)} + \hat{b}_{-11}h_5 d_{i+1}^{(1)} + \hat{b}_{-12}h_6 d_{i+2}^{(1)}$	$\frac{11}{6}d_i^{(1)} - \frac{7}{6}d_{i+1}^{(1)} + \frac{1}{3}d_{i+2}^{(1)}$	$\hat{b}_{-12} = -\dfrac{(h_4+h_5+h_6)(h_5+h_6)h_6}{h_4(h_4+h_5+h_6)}$
			$\hat{b}_{-11} = \hat{b}_{-12} + \dfrac{(h_4+h_5)h_5 h_6}{(h_4+h_5)(h_4+h_5+h_6)}$
			$\hat{b}_{-10} = \hat{b}_{-11} + \dfrac{(h_4+h_5)(h_4+h_5+h_6)}{h_4 h_5(h_5+h_6)}$
$d_{x,1}^{(1)+}(x_i)$	$\hat{b}_{00}h_3 d_{i-1}^{(1)} + \hat{b}_{01}h_4 d_i^{(1)} + \hat{b}_{02}h_5 d_{i+1}^{(1)}$	$\frac{1}{3}d_{i-1}^{(1)} + \frac{5}{6}d_i^{(1)} - \frac{1}{6}d_{i+1}^{(1)}$	
$d_{x,2}^{(1)+}(x_i)$	$\hat{b}_{10}h_2 d_{i-2}^{(1)} + \hat{b}_{11}h_3 d_{i-1}^{(1)} + \hat{b}_{12}h_4 d_i^{(1)}$	$-\frac{1}{6}d_{i-2}^{(1)} + \frac{5}{6}d_{i-1}^{(1)} + \frac{1}{3}d_i^{(1)}$	

Coefficients of the smoothness indicators $\beta_{j,k}$

	B'_{jk}	B''_{jk}	Uniform grids
$d^{(1)-}_{x,2}(x_i)$	$B'_{22}(x_{i-1}) = \dfrac{2(h_1+2h_2)}{(h_1+h_2+h_3)(h_2+h_3)h_3}$	$B''_{22} = \dfrac{6}{(h_1+h_2+h_3)(h_2+h_3)h_3}$	$\beta^-_{j,2} = \dfrac{13}{12}(\bar{d}^{(1)}_{i-3} - 2\bar{d}^{(1)}_{i-2} + \bar{d}^{(1)}_{i-1})^2 +$
	$B'_{21}(x_{i-1}) = B'_{22}(x_i) - \dfrac{2(h_1+2h_2-h_3)}{(h_1+h_2)h_2h_3}$	$B''_{21} = B''_{22} - \dfrac{(h_1+h_2)h_2h_3}{6}$	$\dfrac{1}{4}(\bar{d}^{(1)}_{i-3} - 4\bar{d}^{(1)}_{i-2} + 3\bar{d}^{(1)}_{i-1})^2$
	$B'_{20}(x_{i-1}) = B'_{21}(x_i) + \dfrac{2(h_1+h_2-h_3)}{h_1h_2(h_2+h_3)}$	$B''_{20} = B''_{21} + \dfrac{(h_1+h_2)h_2h_3}{h_1h_2(h_2+h_3)}$	
$d^{(1)-}_{x,1}(x_i)$	$B'_{12}(x_{i-1}) = \dfrac{2(h_2-h_3)}{(h_2+h_3+h_4)(h_3+h_4)h_4}$	$B''_{12} = \dfrac{6}{(h_2+h_3+h_4)(h_3+h_4)h_4}$	$\beta^-_{j,1} = \dfrac{13}{12}(\bar{d}^{(1)}_{i-2} - 2\bar{d}^{(1)}_{i-1} + \bar{d}^{(1)}_{i})^2 +$
	$B'_{11}(x_{i-1}) = B'_{12}(x_i) - \dfrac{2(h_2-h_3-h_4)}{(h_2+h_3)h_3h_4}$	$B''_{11} = B''_{12} - \dfrac{(h_2+h_3)h_3h_4}{6}$	$\dfrac{1}{4}(\bar{d}^{(1)}_{i-2} - \bar{d}^{(1)}_{i})^2$
	$B'_{10}(x_{i-1}) = B'_{11}(x_i) + \dfrac{2(h_2-2h_3-h_4)}{h_2h_3(h_3+h_4)}$	$B''_{10} = B''_{11} + \dfrac{(h_2+h_3)h_3h_4}{h_2h_3(h_3+h_4)}$	
$d^{(1)-}_{x,0}(x_i)$	$B'_{02}(x_{i-1}) = -\dfrac{2(2h_3+h_4)}{(h_3+h_4+h_5)(h_4+h_5)h_5}$	$B''_{02} = \dfrac{6}{(h_3+h_4+h_5)(h_4+h_5)h_5}$	$\beta^-_{j,0} = \dfrac{13}{12}(\bar{d}^{(1)}_{i-1} - 2\bar{d}^{(1)}_{i} + \bar{d}^{(1)}_{i+1})^2 +$
	$B'_{01}(x_{i-1}) = B'_{02}(x_i) + \dfrac{2(2h_3+h_4+h_5)}{(h_3+h_4)h_4h_5}$	$B''_{01} = B''_{02} - \dfrac{(h_3+h_4)h_4h_5}{6}$	$\dfrac{1}{4}(3\bar{d}^{(1)}_{i-1} - 4\bar{d}^{(1)}_{i} + \bar{d}^{(1)}_{i+1})^2$
	$B'_{00}(x_{i-1}) = B'_{01}(x_i) - \dfrac{2(2h_3+2h_4+h_5)}{h_3h_4(h_4+h_5)}$	$B''_{00} = B''_{01} + \dfrac{(h_3+h_4)h_4h_5}{h_3h_4(h_4+h_5)}$	

$$B'^-_{jk}(x_{i-1/2}) = B'^-_{jk}(x_{i-1}) + \frac{h_3}{2}B''^-_{jk}, \qquad j=0,\cdots,2, \quad k=0,\cdots,2$$

$$B'^-_{jk}(x_i) = B'^-_{jk}(x_{i-1}) + h_3 B''^-_{jk}, \qquad j=0,\cdots,2, \quad k=0,\cdots,2$$

Table 2.4: Smoothness indicators of the fifth-order WENO scheme for uniform and non-uniform grids

Coefficients of the smoothness indicators $\beta_{j,k}$

B'_{jk}	B''_{jk}	Uniform grids

$d^{(1)+}_{x,2}(x_i)$

$$B'^+_{22}(x_i) = \frac{2(h_2+2h_3)}{(h_2+h_3+h_4)(h_3+h_4)h_4}$$

$$B'^+_{21}(x_i) = B'^+_{22}(x_i) - \frac{2(h_2+2h_3-h_4)}{(h_2+h_3)h_3h_4}$$

$$B'^+_{20}(x_i) = B'^+_{21}(x_i) + \frac{2(h_2+h_3-h_4)}{h_2h_3(h_3+h_4)}$$

$$B''^+_{22} = \frac{6}{(h_2+h_3+h_4)(h_3+h_4)h_4}$$

$$B''^+_{21} = B''^+_{22} - \frac{6}{(h_2+h_3)h_3h_4}$$

$$B''^+_{20} = B''^+_{20} + \frac{6}{h_2h_3(h_3+h_4)}$$

$$\beta^+_{j,2} = \frac{13}{12}(\bar{d}^{(1)}_{i-2} - 2\bar{d}^{(1)}_{i-1} + \bar{d}^{(1)}_i)^2 + \frac{1}{4}(\bar{d}^{(1)}_{i-2} - 4\bar{d}^{(1)}_{i-1} + 3\bar{d}^{(1)}_i)^2$$

$d^{(1)+}_{x,1}(x_i)$

$$B'^+_{12}(x_i) = \frac{2(h_3-h_4)}{(h_3+h_4+h_5)(h_4+h_5)h_5}$$

$$B'^+_{11}(x_i) = B'^+_{12}(x_i) - \frac{2(h_3-h_4-h_5)}{(h_3+h_4)h_4h_5}$$

$$B'^+_{10}(x_i) = B'^+_{11}(x_i) + \frac{2(h_3-2h_4-h_5)}{h_3h_4(h_4+h_5)}$$

$$B''^+_{12} = \frac{6}{(h_3+h_4+h_5)(h_4+h_5)h_5}$$

$$B''^+_{11} = B''^+_{12} - \frac{6}{(h_3+h_4)h_4h_5}$$

$$B''^+_{10} = B''^+_{11} + \frac{6}{h_3h_4(h_4+h_5)}$$

$$\beta^+_{j,1} = \frac{13}{12}(\bar{d}^{(1)}_{i-1} - 2\bar{d}^{(1)}_i + \bar{d}^{(1)}_{i+1})^2 + \frac{1}{4}(\bar{d}^{(1)}_{i-1} - \bar{d}^{(1)}_{i+1})^2$$

$d^{(1)+}_{x,0}(x_i)$

$$B'^+_{02}(x_i) = -\frac{2(2h_4+h_5)}{(h_4+h_5+h_6)(h_5+h_6)h_6}$$

$$B'^+_{01}(x_i) = B'^+_{02}(x_i) + \frac{2(2h_4+h_5+h_6)}{(h_4+h_5)h_5h_6}$$

$$B'^+_{00}(x_i) = B'^+_{01}(x_i) - \frac{2(2h_4+2h_5+h_6)}{h_4h_5(h_5+h_6)}$$

$$B''^+_{02} = \frac{6}{(h_4+h_5+h_6)(h_5+h_6)h_6}$$

$$B''^+_{01} = B''^+_{02} - \frac{6}{(h_4+h_5)h_5h_6}$$

$$B''^+_{00} = B''^+_{01} + \frac{6}{h_4h_5(h_5+h_6)}$$

$$\beta^+_{j,0} = \frac{13}{12}(\bar{d}^{(1)}_i - 2\bar{d}^{(1)}_{i+1} + \bar{d}^{(1)}_{i+2})^2 + \frac{1}{4}(3\bar{d}^{(1)}_i - 4\bar{d}^{(1)}_{i+1} + \bar{d}^{(1)}_{i+2})^2$$

$$B'^+_{jk}(x_{i+1/2}) = B'^+_{jk}(x_i) + \frac{h_4}{2}B''^+_{jk}, \qquad j=0,\cdots,2, \quad k=0,\cdots,2$$

$$B'^+_{jk}(x_{i+1}) = B'^+_{jk}(x_i) + h_4 B''^+_{jk}, \qquad j=0,\cdots,2, \quad k=0,\cdots,2$$

Table 2.4: (continued)

		Non-uniform grid	Uniform grid
$d_x^{(1)+}$	$\gamma_2^+ =$	$\dfrac{(h_3+h_4)(h_3+h_4+h_5)}{(h_1+h_2+h_3+h_4)(h_1+h_2+h_3+h_4+h_5)}$	$\dfrac{3}{10}$
	$\gamma_1^+ =$	$\dfrac{(h_1+h_2)(h_3+h_4+h_5)(h_1+2h_2+2h_3+2h_4+h_5)}{(h_1+h_2+h_3+h_4)(h_2+h_3+h_4+h_5)(h_1+h_2+h_3+h_4+h_5)}$	$\dfrac{6}{10}$
	$\gamma_0^+ =$	$\dfrac{h_2(h_1+h_2)}{(h_2+h_3+h_4+h_5)(h_1+h_2+h_3+h_4+h_5)}$	$\dfrac{1}{10}$
$d_x^{(1)-}$	$\gamma_2^- =$	$\dfrac{h_3(h_3+h_4)}{(h_0+h_1+h_2+h_3)(h_0+h_1+h_2+h_3+h_4)}$	$\dfrac{1}{10}$
	$\gamma_1^- =$	$\dfrac{(h_0+h_1+h_2)(h_3+h_4)(h_0+2h_1+2h_2+2h_3+h_4)}{(h_0+h_1+h_2+h_3)(h_1+h_2+h_3+h_4)(h_0+h_1+h_2+h_3+h_4)}$	$\dfrac{6}{10}$
	$\gamma_0^- =$	$\dfrac{(h_1+h_2)(h_0+h_1+h_2)}{(h_1+h_2+h_3+h_4)(h_0+h_1+h_2+h_3+h_4)}$	$\dfrac{3}{10}$

Table 2.5: Linear weights of the fifth-order WENO scheme for uniform and non-uniform grids

2.6 Some improvements of the signed distance equation

Although the continuous signed distance equation does not move the zero level function (the interface), this property is more or less lost at the discrete level. This issue is the subject of the following subsections.

2.6.1 Constrained signed distance equation

As mentioned in Sec. 2.2.3, the right-hand side of the signed distance equation may be modified in order the volume enclosed in the level-set function is better preserved. This is performed by substituting the signed distance equation by the constraint signed distance equation (2.20):

$$\frac{\partial d}{\partial \tau} + s(d^0)\left(\|\nabla d\| - 1\right) = \lambda \delta(d)\|\nabla d\|$$

with

$$\lambda = -\frac{\displaystyle\int_\Omega \delta(d)\left(s(d^0)\left(1 - \|\nabla d\|\right)\right)\,d\vec{x}}{\displaystyle\int_\Omega (\delta(d))^2\|\nabla d\|\,d\vec{x}}$$

From the numerical point of view, we follow the approach given by Sussman et Fatemi [151]. We first solve the signed distance equation (see Sec. 2.5) on cell $\Omega_{i,j}$, of center $\vec{x}_{i,j} = (x_i, y_j)$, what is written in an abridged version (first order time discretization):

$$\tilde{d}_{i,j}^{(n+1)} = d_{i,j}^{(n)} + \Delta t L_{i,j}(d^{(0)}, d^{(n)})$$

where $L_{i,j}(d^{(0)}, d^{(n)})$ stands for $s(d_{i,j}^{(0)})\left(1 - \|\nabla_{i,j}d^{(n)}\|\right)$. Then, the intermediate signed distance function $\tilde{d}_{i,j}^{(n+1)}$ is updated to get the constrained signed distance $d^{(n+1)}$:

$$d_{i,j}^{(n+1)} = \tilde{d}_{i,j}^{(n+1)} + \Delta t \lambda_{i,j}\delta_\varepsilon(d_{i,j}^{(0)})\|\nabla_{i,j}d^{(0)}\|$$

The local coefficient $\lambda_{i,j}$ writes:

$$\lambda_{i,j} = \frac{-\displaystyle\int_{\Omega_{i,j}} \delta_\varepsilon(d_{i,j}^0)\frac{\tilde{d}_{i,j}^{(n+1)} - d_{i,j}^{(0)}}{\Delta t}}{\displaystyle\int_{\Omega_{i,j}} \left[\delta_\varepsilon(d_{i,j}^{(0)})\right]^2 \|\nabla_{i,j} d^{(0)}\|} \tag{2.49}$$

with $\delta_\varepsilon(d)$ is a smoothed representation of the Dirac "function" (see Eq. (2.12)). The numerical integrations on $\Omega_{i,j} = [x_{i-1/2}, x_{i+1/2}] \times [y_{j-1/2}, y_{j+1/2}]$ are performed using a nine-points stencil:

$$\int_{\Omega_{i,j}} g \approx \frac{h^2}{24}\left(16 g_{i,j} + \sum_{\substack{m,n=-1 \\ (m,n)\neq(0,0)}}^{1} g_{i+m,j+n}\right)$$

This constraint signed distance method usually provides a better mass conservation than its non-constraint counterpart. However, and as it will be shown later, it often results a interface shape significantly distorted.

2.6.2   Subcell fix method

As noted here-above, the discrete signed distance equation may displace the interface and thus damage the fluid volume conservation. Russo et Smereka [136] introduced the so-called subcell fix method in order to limit the lose of accuracy of the zero-level set. The main idea relies on the explicit accounting of an approximation of the interface location for the calculation of the signed distance equation.

The use of the fifth-order ENO reconstruction leads to use five points for the average values $\bar{d}_k^{(1)}$ on each stencil, and six points when considering the local values $d_k^{(1)}$. For example, the right-biased stencil for the average values concerns "faces" positions $(x_{i-3/2}, x_{i-1/2}, x_{i+1/2}, x_{i+3/2}, x_{i+5/2})$ whereas the corresponding local values are located at cells center $(x_{i-2}, x_{i-1}, x_i, x_{i+1}, x_{i+2}, x_{i+3})$. If the interface passes through any of two adjacent points among these six cell centers, its position x_{int} is searched through a third-order polynomial interpolation. Assuming $x_i < x_{int} < x_{i+1}$, then the basic six-points stencil becomes $(x_{i-2}, x_{i-1}, x_i, x_{int}, x_{i+1}, x_{i+2})$ and the corresponding distance values are $(d_{i-2}, d_{i-1}, d_i, 0, d_{i+1}, d_{i+2})$. It is worth to notice that it is essential the scheme handles irregular grids, since the interface location will always break the eventual regularity of the basic mesh.

The approximation of the zero-level set abscissa x_{int} rests on a third-order interpolation method. The main issue is to choose the four points giving rise to a good approximation of the interface. If the solution is locally smooth, any choice should give an equivalent result. But the signed distance function has not necessarily continuous derivatives in the vicinity of the interface. Therefore, it can result an erroneous evaluation of x_{int}. We now discuss how the four points are chosen.

Once the product between two adjacent level set values are negative, a zero-level set is expected. Let us assume this occurs between x_i and x_{i+1}, for example. The linear approx-

imation $p_1(x)$ simply writes:

$$p_1(x) = d(x_i) + d[x_i, x_{i+1}](x - x_i)$$

where $d[x_i, x_{i+1}]$ is the first divided difference of d between points x_i and x_{i+1}. Starting from $p_1(x)$, the polynomial $p_3(x)$ is constructed recursively on points $\{x_{i-r_n}, \cdots, x_{i-r_n+n}\}$, with $0 \leq r_n \leq n - 1$ and n the degree of the polynomial $p_n(x)$. The main question now raised concerns the choice of the integer value r_n (function of n), or in other words, do we consider the left or right node of the current stencil as a new interpolation point? The idea developed in our subcell fix method is to keep the point which provides the smallest divided difference. Thus, starting from $r_1 = 0$, by induction we get:

– do:
If $|d[x_{i-r_n-1}, x_{i-r_n}, \cdots, x_{i-r_n+n}]| < |d[x_{i-r_n}, x_{i-r_n}, \cdots, x_{i-r_n+n+1}]|$ then $r_{n+1} = r_n - 1$, otherwise $r_{n+1} = r_n$, and

$$p_{n+1}(x) = p_n(x) + d[x_{i-r_{n+1}}, x_{i-r_n}, \cdots, x_{i-r_n+n}] \prod_{k=1}^{n+1}(x - x_{i-r_n})$$

Once the polynomial is determined, a Newton-Raphson method is used to achieve the root x_{int} lying between x_i and x_{i+1} of the third-order polynomial $p_3(x)$:

1. The value x_{int}^0 is set such that $p_2(x_{int}^0) = 0$, with $x_i < x_{int}^0 < x_{i+1}$.
2. do for $k \geq 0$,

$$\delta x = -\frac{p_3(x_{int}^k)}{\dfrac{dp_3}{dx}(x_{int}^k)}$$
$$x_{int}^{k+1} = x_{int}^{k+1} + \delta x$$

if $|\delta x|/|x_{i+1} - x_i| < 10^{-6}$ or $k > 3$ stop
3. if $k \leq 3$, $x_{int} = x_{int}^{k+1}$, otherwise $x_{int} = x_{int}^0$.

The rate of convergence of the Newton-Raphson method being second-order, a very accurate solution is expected within at most 3 iterations, otherwise, the interface location is kept to its initialization value.

2.7 Restriction on the discrete time step

Since, the source term $S(\vec{v})$ (Eq. (2.21b)) in Eq. (2.23) consists of explicit contributions (convection, surface tension, gravity and the subsidiary viscous terms), the time step must be restricted to enforce the stability of the numerical schemes. According to [34],
– the limit time step for the surface tension writes

$$\Delta t_\sigma = \min_{\Omega_\delta} \sqrt{\frac{(\rho_l + \rho_g)\Delta h^3}{4\pi\sigma}}$$

where $\Delta h = \min(\Delta x, \Delta y)$ and Ω_δ represents the transition zone where $\delta(\phi) > 0$.
– the limit time step for the convective terms must fulfill the Courant-Friedrichs-Lewy (CFL) condition:

$$\Delta t_u = \min_{\Omega} \frac{C\Delta x}{|u| + |v|}$$

where $C = 0.5$ and Ω represents the whole computational domain.

– the limit time step associated with the gravity is expressed by

$$\Delta t_g = \min_{\Omega} \sqrt{\frac{\Delta y}{g}}$$

– and limit time step based on the subsidiary viscous terms are

$$\Delta t_\mu = \min_{\Omega_\delta} \frac{\rho \Delta h^2}{2\mu}$$

We then get the restriction on the time step for the overall scheme:

$$\Delta t^{n+1} = \min(\Delta t_u, \Delta t_\sigma, \Delta t_g, \Delta t_\mu)$$

Chapter 3

Validation

This chapter presents numerical studies with the aim at validating the different numerical schemes and implementation choices described in the previous chapter. The Essentially Non Oscillatory (ENO) and Weighted Essentially Non Oscillatory (WENO) discretizations are first examined for the transport equations. Then, solutions of the signed distance equation are studied by comparing the results achieved using the basic method and its two variants, namely the constraint and subcell fix methods. Afterwards, the coupling between the transport equation and the signed distance equation is considered by studying, first the classical Zalesak problem and then the stretching of a circular fluid element. At last, this chapters ends with dealing immiscible fluid flows.

3.1 Definition and measure of errors

3.1.1 Relative volume conservation error

The relative error on the volume conservation, defined by Yue *et al.* [168], measures the difference between volumes V delimited by the computed interface and the exact interface. This is defined as follows:

$$L_1(V) = \frac{\left| \int_\Omega H(\phi_{\text{exact}}) \, d\Omega - \int_\Omega H(\phi_{\text{computed}}) \, d\Omega \right|}{\int_\Omega H(\phi_{\text{exact}}) \, d\Omega} \tag{3.1}$$

where Ω is the computational domain.

If necessary, continuous integrals are substituted by numerical quadratures. Usually, the exact contribution in Eq. (3.1) is calculated exactly whereas the approximated mass is numerically evaluated. This is performed by the following algorithm.
Let $\vec{x}_K$ the coordinates of the cell center of any rectangular cell K and $\vec{x}_K(i)$, $i = 1, \cdots, 4$, its four vertices.
   – Set the variable *Int* to zero;
   – For all control volumes K, do
      – If the euclidean distance between x_K and any vertex $x_K(i)$, $i = 1, \cdots, 4$, is larger than ϕ_K, the numerical interface cuts the cell K. Then, divide the cell K into tiny pieces K_j, e.g. $j = 1, \cdots, 1000 \times 1000$. For each sub-rectangle K_j, do
         – Evaluate the numerical values ϕ onto newly created pieces K_j, namely ϕ_{K_j}, by using bi-quadratic interpolations based on cell K and its eight neighboring cells;

– Use the one-point Gauss quadrature method on cell K_j to compute an approximation Int_j:

$$\int_{K_j} H(\phi_{\text{computed}})\, d\Omega \approx m_{K_j} \times \text{sign}(\max(\phi_{K_j}, 0)) \equiv Int_j$$

with m_{K_j} the size of the tiny sub-cell K_j and $\text{sign}(x) = 1$ if $x > 0$, otherwise $\text{sign}(x) = 0$

– $Int \leftarrow Int + Int_j$;
– End do;
– End do;
– Int provides an approximation of the requested integral.

It is worth noticing that the one-point Gauss method is only one order accurate because the integrand is discontinuous.

3.1.2 Level Set error in L_2-norm

The volume conservation error is not the only standard to measure the accuracy of schemes. Indeed, this error can remain weak whereas the shape of the computed interface may greatly differ from the expected one. So, in addition to the volume conservation error, we monitor the relative error of the discrete level set function in L_2-norm. This calculation is performed on the sub-domain Ω_{test} which can correspond to the whole computation domain or just a part of it centered around the interface. The discrete expression of the Level Set error in L_2-norm writes at time $t^{(n)}$:

$$L_2(\phi, \Omega_{\text{test}}) = \sqrt{\frac{\displaystyle\sum_{K \in \mathcal{M}, \vec{x}_K \in \Omega_{\text{test}}} m_K (\phi_K^{(n)} - \phi(\vec{x}_K, t^{(n)}))^2}{\displaystyle\sum_{K \in \mathcal{M}, \vec{x}_K \in \Omega_{\text{test}}} m_K \phi(\vec{x}_K, t^{(n)})^2}} \tag{3.2}$$

with $\phi_K^{(n)}$ the discrete approximation of the exact solution $\phi(\vec{x}_K, t^{(n)})$.

3.1.3 Curvature error in L_2-norm

In Sun et Tao [146], the accuracy of the scheme is evaluated by the measure of the error on the interface curvature (see (2.8) page 136 for its mathematical definition).

Since this error is only applied for circular interfaces of radius R, the L_2 discrete curvature error computed on a sub-domain Ω_{test} centered on the interface is defined as:

$$L_2(\kappa, \Omega_{\text{test}}) = \sqrt{\frac{\displaystyle\sum_{K \in \mathcal{M}, \vec{x}_K \in \Omega_{\text{test}}} m_K \left(\kappa_K^{(n)} \times R - 1\right)^2}{\displaystyle\sum_{K \in \mathcal{M}, \vec{x}_K \in \Omega_{\text{test}}} m_K}} \tag{3.3}$$

with $\kappa_K^{(n)}$ the approximated curvature on cell K. Obviously, this error is expected to increase when the sub-domain of calculation Ω_{test} get thicker.

3.2 One dimensional test problem for transport equation

The discrete initial condition of the level-set ϕ on cell center $\vec{x}_K$ is defined by computing the mean value of the analytical initial condition on cell K

$$\phi_K = \frac{1}{m_K} \int_K \phi(x, t = 0) \, d\vec{x}$$

The numerical tests presented in this section consist of the transport at unit velocity of different initial conditions. The level-set function $\phi(x, t)$ is then solution of Eq. (2.9), with $\vec{v}(\vec{x}, t) \equiv \vec{e}_x$. The computational domain length is fixed to 100 and the number of regular control volumes ranges from 50 up to 12800. Therefore, the mesh size h extends from $1/128$ to 2. The time step is related to the Courant-Friedrichs-Lewy condition fixed to $CFL = 0.1$.

3.2.1 Smooth initial conditions

The first study is devoted to periodic initial conditions:

$$\phi(x, t = 0) = \sin(4\pi x/100), \quad 0 \le x \le 100 \tag{3.4}$$

Figure 3.1 shows the $L_2(\phi, \Omega)$ error at time $t = 10\,s$ as the function of grid size h, for the

(a) ENO scheme   (b) WENO scheme
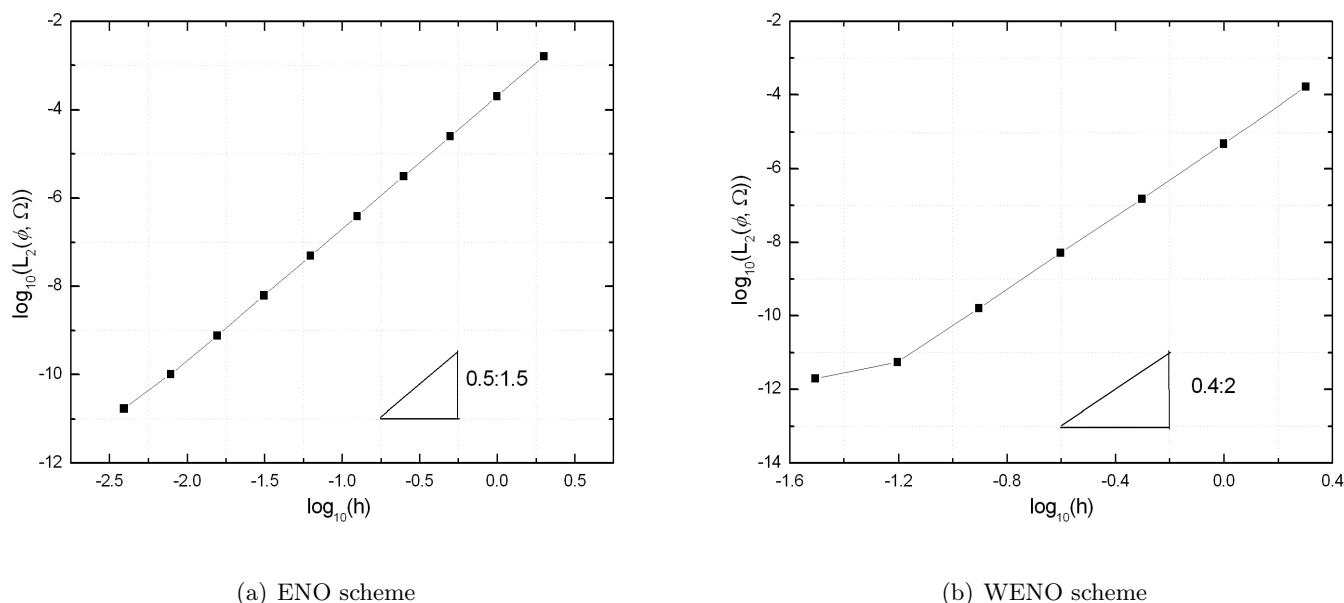
Figure 3.1 – One dimensional test problem for transport equation. $L_2(\phi, \Omega)$ errors for ENO and WENO schemes. Initial condition (3.4).

Essentially Non Oscillatory (ENO) and Weighted Essentially Non Oscillatory discretizations. As expected, the discrete approximations converge to the exact solution with third- and fifth-order accuracies for ENO and WENO schemes.

Another simulation is performed using the ENO scheme, but with the new initial condition

$$\phi(x, t = 0) = \sin^4(\pi x/100), \quad 0 \le x \le 100, \tag{3.5}$$
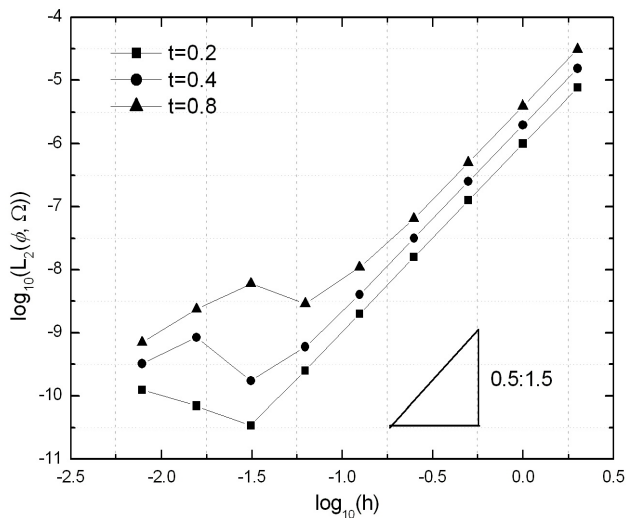
(a) Sensitivity to the grid size h (b) Sensitivity to the number of temporal iterations n
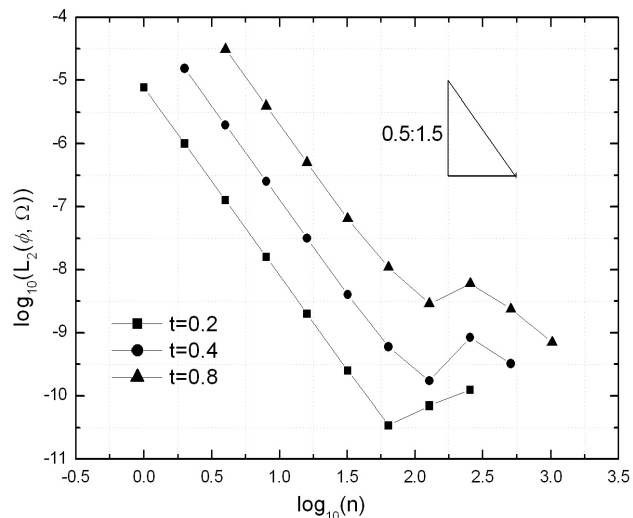
Figure 3.2 – One dimensional test problem for transport equation. $L_2(\phi, \Omega)$ errors for ENO discretization. Initial condition (3.5).

Figure 3.2 presents the $L_2(\phi, \Omega)$ errors at three instants $t = 0.2$, $t = 0.4$ and $t = 0.8$, and for different meshes. Figure 3.2(a) shows that solution converges at third-order on a grid size interval all the more extended that the computational time is small. Afterwards, the error begins to increase dramatically what indicates that the ENO scheme does not converge to the exact solution for the finest grids. The break in the convergence behavior appears, for the three integration times studied, for different grid sizes h_l: roughly speaking, $h_l = 1/32$ for $t = 0.2$, $h_l = 1/16$ for $t = 0.4$ and $h_l = 1/8$ for $t = 0.8$. Accounting for the value of the CFL number ($CFL = 0.1$), this correspond to the same number of total temporal iterations (64 iterations). This result is illustrated in Fig. 3.2(b) which presents the $L_2(\phi, \Omega)$ errors as a function of the number of time iterations n necessary to reach time $t_{max} = 0.2$, 0.4 or 0.8. This number of time iterations n is related to the grid size h by relation $n = t_{max}/\Delta t = t_{max}/(CFL \times h)$. Reducing the CFL number by an order of magnitude does not lead to a significant improvement. In this example, the spatial ENO discretization seems to become unstable with time iterations, and that independently from the CFL number.

The two preceding numerical tests lead to either a convergence or a non-convergence of the ENO scheme, depending on the initial condition. However, the initial condition (3.5) can be rewritten as:

$$\sin^4\left(\frac{\pi x}{100}\right) = \frac{1}{8}\left[\sin\left(4\frac{\pi x}{100} + \frac{\pi}{2}\right) - 4\sin\left(2\frac{\pi x}{100} + \frac{\pi}{2}\right) + 3\right] \qquad (3.6)$$

In this expression, the first term of the right-hand side corresponds to the initial condition (3.4) with a different phase. Moreover, we have verified (but not presented) that the ENO scheme converges also when the initial condition is set to the second term of the right-hand side of Eq. (3.6). Therefore, the sum of two initial conditions, satisfying for each of them the third-order convergence properties, produces a solution whose convergence fails. This result highlights the non-linear behavior of the Essentially Non Oscillatory scheme.

The non-linear aspect comes from the choice of the computation stencil used by the ENO method to reconstruct the level set function on cell faces. Indeed, Rogerson et Meiburg [134] showed that the selected stencil may be unsuited, what produces temporal instabilities. The Weighted Essentially Non Oscillatory (WENO) discretization scheme is less subjected to such problem, since the stencil is fixed: only the weights of the interpolations on sub-stencils evolve with the local smoothness of the solution. Figure 3.3 clearly con-
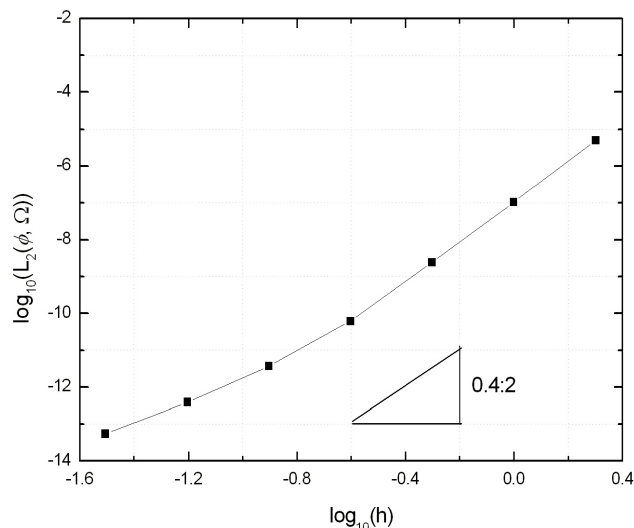
Figure 3.3 – One dimensional test problem for transport equation. $L_2(\phi, \Omega)$ errors for WENO discretization. Initial condition (3.5) and $t = 0.8$.

firms that the WENO discretization scheme converges with a fifth-order accuracy, except for smallest grid sizes where the order in slightly reduced, probably due to computation accuracy.

3.2.2 Smooth solution on irregular grid

The next test case aims at validating the transport equation with WENO discretization on an irregular grid. Boundary conditions are set to analytical solution. The initial condition writes:

$$\phi(x, t = 0) = \arctan(0.2(x - 10)), \quad 0 \leq x \leq 100, \tag{3.7}$$

In Fig. 3.4 is drawn $\phi(x, t = 0)$, $\phi(x, t = 50)$ and the nodes location. The L_2 error, represented in Fig. 3.5 for regular and irregular grid size distribution, shows that the fifth-order WENO scheme is well recovered.

3.2.3 Initial condition with discontinuous derivative

The purpose of this section is to study the transport of a continuous function characterized by a local jump in derivatives, abusively called shock in this report. The initial condition

$$\phi(x, t = 0) = |x - 10|, \quad 0 \leq x \leq 100$$

169
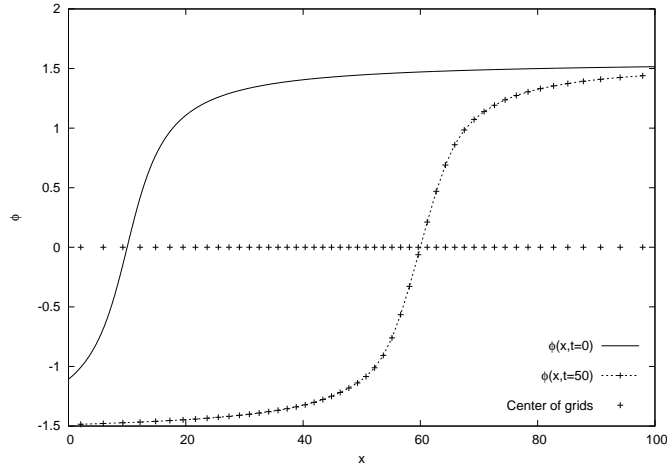
Figure 3.4 – Initial condition (3.7), $\phi(x, t = 50)$ and nodes location for irregular grid.
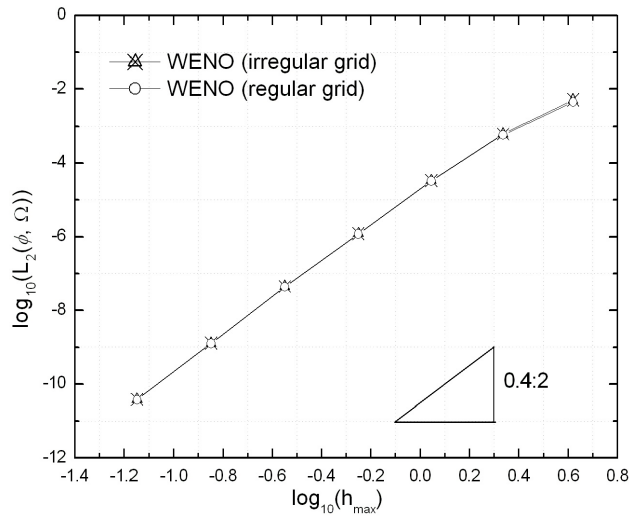
Figure 3.5 – Initial condition (3.7), $\phi(x, t = 50)$ and nodes distribution for regular and irregular grids.

is continuous but the derivatives are not defined at $x_s(t = 0) = 10$. Figure 3.6 illustrates the initial condition and $\phi(x, t = 50)$ for two grid sizes $h = 2$ and $h = 1/8$. The numerical solution is clearly smoothed around $x_s(t = 50) = 60$, and this regularization is all the more pronounced since the grid is coarse. To evaluate the effect of shock on the numerical solution, we have considered three sub-domains. One is centered on the shock location x_s and extends from $x_s - 6$ to $x_s + 6$, and the two others are located upstream ($[0; x_s - 6]$) and downstream ($[x_s + 6; 100]$). Table 3.1 collects the relative errors of the level set function at $t = 50$ and local orders of convergence of the numerical methods. We see

170
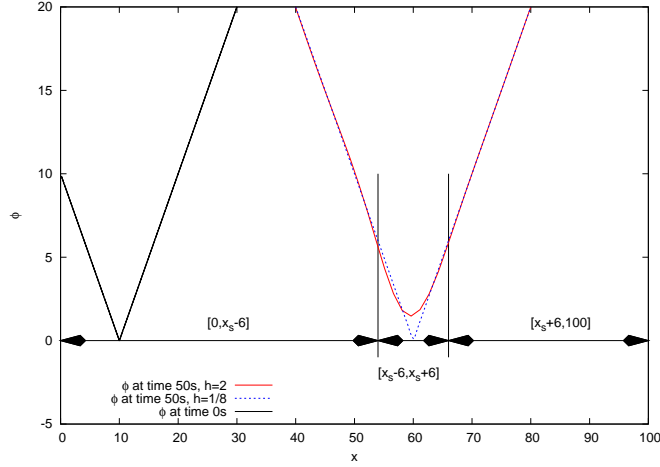
Figure 3.6 – Transport of the initial condition (3.2.3). Initial solution and $\phi(x, t = 50)$ for two grid sizes $h = 2$ and $h = 1/8$. WENO scheme.

	ENO scheme					
Grid	$L_2(\phi, [x_s + 6; 100])$		$L_2(\phi, [0; x_s - 6])$		$L_2(\phi, [x_s - 6; x_s + 6])$	
	error	Order	error	Order	error	Order
50	3.5E-03	NA	2.3E-03	NA	2.0E-01	NA
100	3.2E-04	3.4	1.8E-04	3.7	9.7E-02	1.0
200	2.8E-06	6.9	3.1E-06	5.9	4.5E-02	1.1
400	6.9E-10	12	2.9E-09	10	2.1E-02	1.1
800	3.5E-13	11	1.7E-13	14	9.6E-03	1.1

	WENO scheme					
Grid	$L_2(\phi, [x_s + 6; 100])$		$L_2(\phi, [0; x_s - 6])$		$L_2(\phi, [x_s - 6; x_s + 6])$	
	error	Order	error	Order	error	Order
50	1.2E-03	NA	1.0E-03	NA	1.4E-01	NA
100	1.1E-04	3.4	1.7E-04	2.5	6.1E-02	1.2
200	2.6E-06	5.4	1.7E-05	3.3	2.7E-02	1.2
400	1.1E-08	7.8	2.5E-07	6.1	1.1E-02	1.2
800	8.6E-13	14	4.4E-10	9.2	4.9E-03	1.2

Table 3.1 – Relative errors (Eq. 3.2) of $\phi(x, t = 50)$ and local order of convergence as a function of the grid size for the initial condition (3.2.3), $x_s = 60$.

that the convergence orders of the numerical solution obtained with the ENO scheme in the upstream and downstream sub-domains are at least 3, a value in accordance with the expected order. For the WENO scheme, the order ranges from approximatively 3 to more than 5. This result is in accordance with the theory [140] since the fifth-order accuracy is obtained only for smooth solutions. If some discontinuity is located into one or two of the WENO sub-stencils used for interpolations, the accuracy is reduced to third-order. Both in Fig. 3.6 and in Tab. 3.1 for the WENO scheme, we observe that the errors are slightly larger after the shock occurrence ($x < x_s$) than before ($x > x_s$) [140]. At last, nearby the derivative discontinuity x_s, the high-order ENO and WENO schemes fail to achieve the

desired order of accuracy: the three sub-stencils of the WENO reconstruction contain the discontinuity point. Therefore, the solution is only first order accurate.

3.3 Two dimensional test problem for signed distance equation

Mathematically, the resolution of the signed distance equation (2.14) (page 139) preserves the zero-level curve with time. Indeed, this is essential not to move the interface during the reinitialization of the level set function. However at the discrete level, this is unfortunately not guaranteed because the initial signed distance function may be too flat or too steep close to the zero-level curve. It then results an inaccurate evaluation of $\|\nabla d\|$ and perturbations of the interface location. This section aims at studiyng solutions obtained with the ENO or WENO discretizations, but also to investigate the expected improvements provided by of the constraint version (see Sec. 2.6.1 page 161) and the subcell fix method (see Sec. 2.6.2 page 162).

Computations are carried out up to the steady state on regular grids. In order that the temporal accuracy remains negligible compared to the spatial one, the CFL number must be reduced with the decrease of the mesh size. With 25^2, 50^2, 100^2 and 200^2 cells, the CFL number decreases from 0.125 to 0.0625, 0.03125 and 0.015625. The small parameter ϵ in the sign function (2.15) is set to $2\Delta x$.

The signed distance equation (2.14) is initialized by an analytic signed distance function weakly disturbed and defined from a circle of radius 0.5 and located at the center of a square box of side 2:

$$d_0(x, y, \tau = 0) = \begin{cases} b + \dfrac{\epsilon}{16\pi} \sin\left(\dfrac{4\pi b \sin(5\theta)}{\delta}\right) & \text{if } |b| \leq \delta \\ b & \text{otherwise.} \end{cases}$$

with $b = \sqrt{(x-1)^2 + (y-1)^2} - 0.5$, $\theta = \arctan((y-1)/(x-1))$ and $\delta = 0.2$ [83]. Figure 3.7(a) shows iso-levels of the signed distance which consist of concentric circles very few disturbed. The draw of the local curvatures of the signed distance function $d(\vec{x}, \tau = 0)$, $\kappa(d(\vec{x}, \tau)) = \nabla \cdot (\nabla d/\|\nabla d\|)$ (see Eq. (2.8) page 136), is also presented in Fig. 3.7(b). It is worth noticing that the expected curvature function at the steady state is:

$$\kappa_{\text{stationary}}(x, y) = \frac{1}{\sqrt{(x-1)^2 + (y-1)^2}}$$

Numerous figures and tables illustrate the results. The drawings show the curvatures of the steady state solutions obtained with the different schemes on a 100×100 grid and quantitative results are provided in tables as a function of the computation mesh. The indicators are the relative volume accuracy ($L_1(V)$, Eq. (3.1)) and the relative errors of the signed distance ($L_2(d, \Omega_\epsilon)$ Eq. (3.2)) and curvature ($L_2(\kappa, \Omega_\epsilon)$ Eq. (3.3)), both computed on the reduced domain $\Omega_\epsilon = \{(x,y)/ |\sqrt{(x-1)^2 + (y-1)^2} - 0.5| \leq 0.2\}$. The columns labeled "Order" give the accuracy of the scheme between two successive errors.

Figure 3.8 presents the curvatures of signed distance functions at the steady state, using the ENO discretization scheme. Two results are presented: on the left part of this figure, the solution is achieved by the basic signed distance equation whereas on the right part, the

(a) Signed distance   (b) Curvature
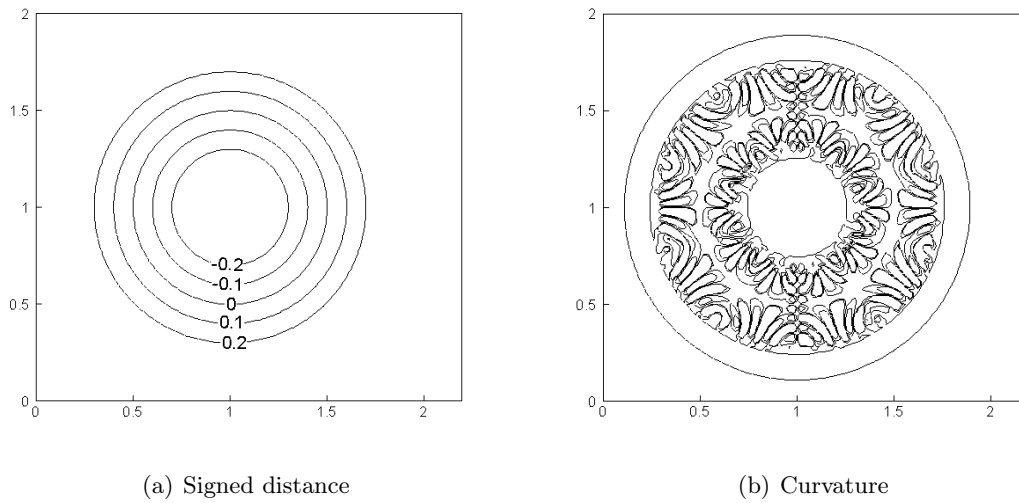
Figure 3.7 – Signed distance equation. Iso-levels at $\tau = 0$ and with 100×100 cells

(a) Basic scheme   (b) Constraint scheme
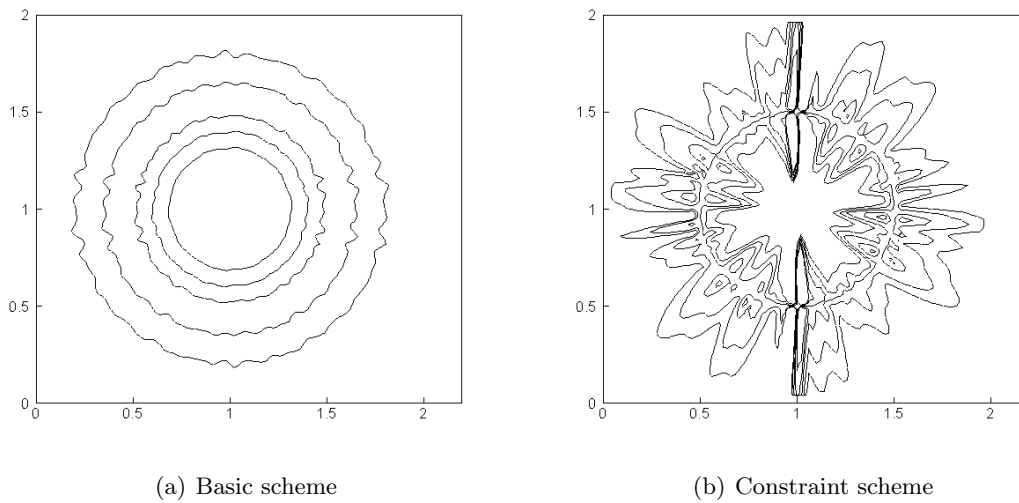
Figure 3.8 – Curvature of the signed distance function at the steady state using the ENO discretization scheme

constraint version of this equation is applied. It clearly appears that the constraint signed distance equation worsens the curvatures deeply in comparison with the basic method. This observation is confirmed by considering the last two columns of Tab. 3.2. Whereas the curvatures obtained by the basic signed distance equation converge with the grid refinement, those computed with the constraint equation do not. Similar remarks may be done for the distance field d. In contrast, the relative mass error $L_1(V)$ is smaller when computations are carried out with the constraint signed distance equation. This improvement is all the more obvious that the mesh is coarse. At last, the third-order ENO scheme is recovered for the basic scheme, except for the curvature variable. For the curvature, the accuracy is at best second-order since its calculation requires discrete operators which are consistent

Basic scheme							
Grid	CFL	$L_1(V)$ (Eq. 3.1)		$L_2(d, \Omega_\epsilon)$ (Eq. 3.2)		$L_2(\kappa, \Omega_\epsilon)$ (Eq. 3.3)	
		error	Order	error	Order	error	Order
25^2	0.125	1.9E-02	NA	5.0E-02	NA	7.1E-02	NA
50^2	0.0625	3.7E-03	2.4	1.0E-02	2.3	2.8E-02	1.3
100^2	0.03125	4.2E-04	3.1	1.4E-03	2.9	2.1E-02	0.45
200^2	0.015625	3.5E-05	3.6	1.8E-04	2.9	7.0E-03	1.5

Constraint version							
Grid	CFL	$L_1(V)$ (Eq. 3.1)		$L_2(d, \Omega_\epsilon)$ (Eq. 3.2)		$L_2(\kappa, \Omega_\epsilon)$ (Eq. 3.3)	
		error	Order	error	Order	error	Order
25^2	0.125	3.6E-04	NA	1.4E-02	NA	9.2E-02	NA
50^2	0.0625	9.7E-05	1.9	1.7E-02	-0.32	1.6E-01	-0.84
100^2	0.03125	1.8E-05	2.4	1.8E-02	-0.0060	3.3E-01	-1.0
200^2	0.015625	1.1E-05	0.76	1.4E-02	0.30	6.1E-01	-0.88

Table 3.2 – Convergence properties for the signed distance equation at the steady state using the ENO discretization scheme.

at second-order only.

The same tests are performed for the WENO discretization scheme. Figure 3.9 clearly shows that the constraint approach provides the worst curvatures and the subcell fix the best ones. In this latter method, the exact zero-level curve is used instead of an interpolation procedure. Interpolation of the interface leads to a small deterioration of results, but they still remain the bests in comparison with the two other methods. Again, the graphic results are confirmed by the quantitative data reported in Tab. 3.3. For the three indicators

Basic scheme							
Grid	CFL	$L_1(V)$ (Eq. 3.1)		$L_2(d, \Omega_\epsilon)$ (Eq. 3.2)		$L_2(\kappa, \Omega_\epsilon)$ (Eq. 3.3)	
		error	Order	error	Order	error	Order
25^2	0.125	3.4E-03	NA	1.3E-02	NA	8.0E-02	NA
50^2	0.0625	8.2E-04	2.0	2.7E-03	2.2	4.5E-02	0.83
100^2	0.03125	1.8E-05	5.5	1.1E-04	4.6	1.0E-02	2.1
200^2	0.015625	2.8E-07	6.0	2.3E-06	5.6	8.1E-04	3.7

Constraint version							
Grid	CFL	$L_1(V)$ (Eq. 3.1)		$L_2(d, \Omega_\epsilon)$ (Eq. 3.2)		$L_2(\kappa, \Omega_\epsilon)$ (Eq. 3.3)	
		error	Order	error	Order	error	Order
25^2	0.125	3.0E-04	NA	1.4E-02	NA	9.4E-02	NA
50^2	0.0625	1.6E-04	0.92	1.5E-02	-0.081	1.6E-01	-0.72
100^2	0.03125	1.4E-05	3.5	2.1E-02	-0.53	4.2E-01	-1.4
200^2	0.015625	1.2E-05	0.15	1.5E-02	0.51	7.2E-01	-0.78

Subcell fix method							
Grid	CFL	$L_1(V)$ (Eq. 3.1)		$L_2(d, \Omega_\epsilon)$ (Eq. 3.2)		$L_2(\kappa, \Omega_\epsilon)$ (Eq. 3.3)	
		error	Order	error	Order	error	Order
25^2	0.125	1.1E-04	NA	1.4E-02	NA	3.6E-02	NA
50^2	0.0625	1.7E-06	6.0	5.1E-04	4.8	8.3E-03	2.1
100^2	0.03125	4.3E-09	8.6	3.2E-06	7.3	1.9E-03	2.1
200^2	0.015625	1.6E-08	-1.9	1.3E-09	11	4.9E-04	2.0

Table 3.3 – Convergence properties for distance equation

(a) Basic scheme

(b) Constraint scheme

(c) Subcell fix method
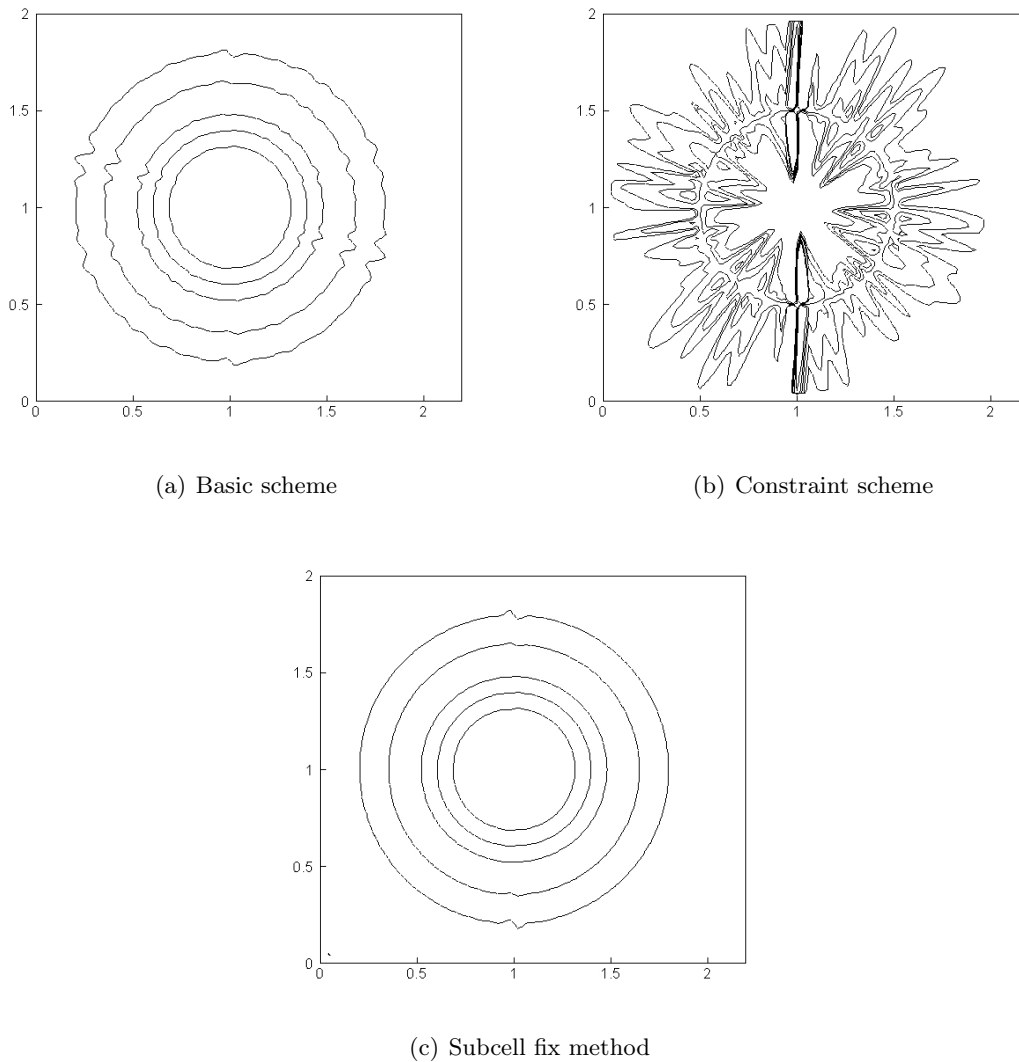
Figure 3.9 – Curvature of the signed distance function at the steady state using the WENO discretization scheme.

recorded, the best results are given by the subcell fix method. It is interesting to remark that solutions provided by the basic signed distance equation with WENO discretizations are much accurate than those obtained with the ENO approach. But this remark does not apply to the constraint method since errors are not significantly modified by changing the spatial discretization.

3.4   Solid transport of a slotted disk: Zalesak's problem

The Zalesak's problem refers to a slotted disk rotating around a fixed center with a steady angular velocity. The notched disk, of radius of 15 with a slot width 6, is initially located at coordinates $(50, 75)$ in a square (100×100) domain. The advection velocity is

stationary and writes

$$u(x, y) = \frac{\pi}{314}(50 - y)$$
$$v(x, y) = \frac{\pi}{314}(x - 50)$$

The initial level set function $\phi(x, y, t = 0)$ is set to the exact signed distance from the slotted disk. The disk returns to its original position past a period of $200\pi (\approx 628)$ time units. After one turn, the diffusion on the numerical scheme is evaluated by checking the degree of distortion of the slotted disk. The volume conservation is also an important indicator of the accuracy of the numerical method. The grid size is constant and ranges from $\Delta x = 1$ to $\Delta x = 1/3$. The time step Δt is equal to Δx: the resulting maximum CFL number is equal to 0.5. The small parameter ϵ involved in the sign function (2.15) of the signed distance equation (2.14) is fixed to $2\Delta x$.

3.4.1   Study without the distance equation

Since the transport velocity corresponds to a solid rotation, the reinitialization by the signed distance equation turns out to be useless. In this section, we focus on spatial discretizations by using second- and third-order ENO schemes and the fifth order WENO scheme with $\Delta x = 1$. Figure 3.10 shows that the slot is totally smeared-out at sharp corners

Black -- Initial
Red -- 2rd ENO
Green -- 3rd ENO
Blue -- WENO
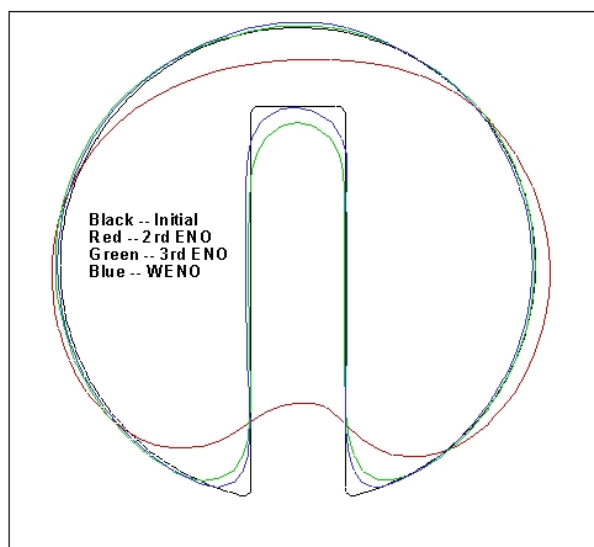
Figure 3.10 – Zalesak's problem. Comparison of interfaces computed with second- and third-order ENO schemes, and fifth-order WENO schemes when the notched disc rotates without the reinitialization step. Grid size: $\Delta x = 1$.

after one complete rotation. The circular boundary is also crushed slightly with the second-order ENO discretization. The third-order ENO and fifth WENO schemes preserve better the slot shape and circular boundary. However, the left part of the slot deviates from its original position to a very small angle, slightly larger with the WENO scheme. Despite

the diffusion which smooths the sharp angles, the WENO method provides the best form even near the slot. This remark worths also when we calculate the volume conservation of the notched disc after one turn. The relative error $L_1(V)$ (Eq. (3.1)) is reduced from 13.34% to 2.93% and to 0.316% with the increase in the order of the spatial discretization. We then conclude that the fifth-order Weighted Essentially Non-Oscillatory scheme is the most accurate. This method is then retained for all further computations of the transport equation.

3.4.2 Study the time step in the signed distance equation

We study the time step in the signed distance equation. Fig. 3.11 and fig. 3.12 show

<div align="center">(a) Standard   (b) The volume constraint</div>
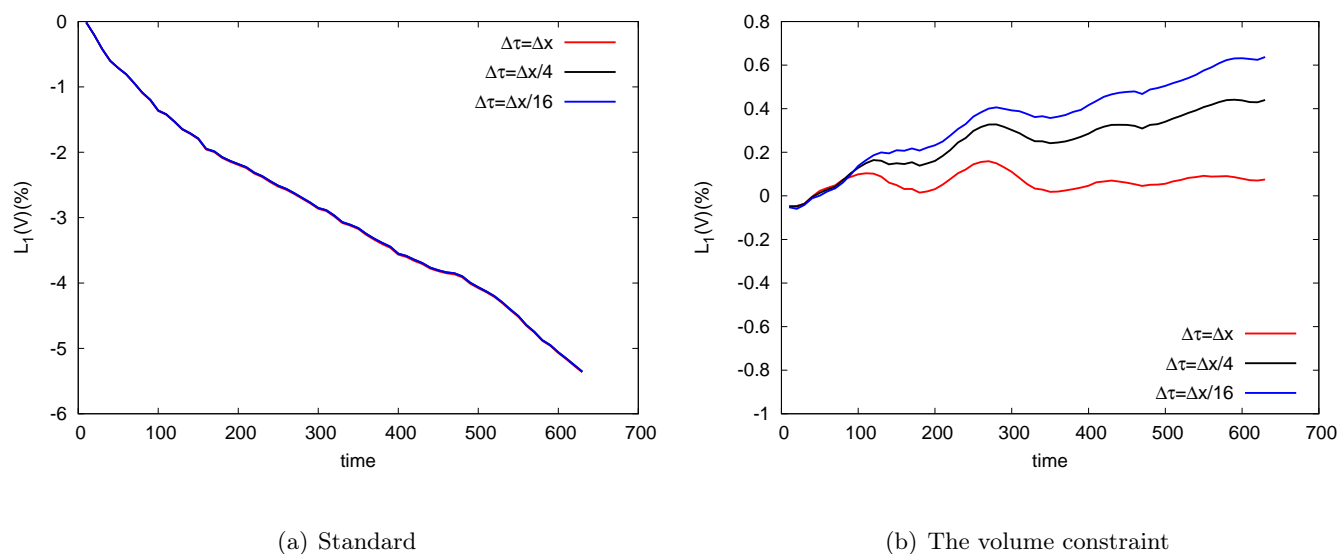
Figure 3.11 – Variation of $L_1(V)$ with $\Delta\tau$ with 100×100 cells; the ENO scheme

variations of relative volume conservation error $L_1(V)$ (Eq. (3.1) page 165) with the time step $\Delta\tau$ in the same grid size $\Delta x = 1$. In different schemes for the signed distance function, $\Delta\tau$ decreases from 1 to 0.0625; the number of iteration of the signed distance function should increase proportionally from 4 to 64 in order to make sure that the signed distance function propagates and smooths at last four cells in each side of interface.

Results demonstrate the small time step doesn't make the mass conservation better in the standard ENO scheme. The standard WENO scheme and the WENO scheme with subcell fix method do not depend on the time step as soon as $\Delta\tau \leq \Delta x/4$. The schemes with the volume constraint is still sensitive to $\Delta\tau$, even if $\Delta\tau < \Delta x/4$. The best result is given by the WENO subcell fix method since the mass error evolution keeps almost constant and relatively small.

3.4.3 Reinitialization with the signed distance function

In this section, we study the spatial discretization of the signed distance equation (2.14) and the eventual improvements brought by the constraint approach (Sec. 2.6.1 page 161) and the subcell fix method (Sec. 2.6.2 page 162). In all cases the spatial discretization of the transport equation is always based on the fifth-order WENO scheme. The signed distance equation is invoked at the end of each transport iteration. The time step is $\Delta\tau = 0.0625$
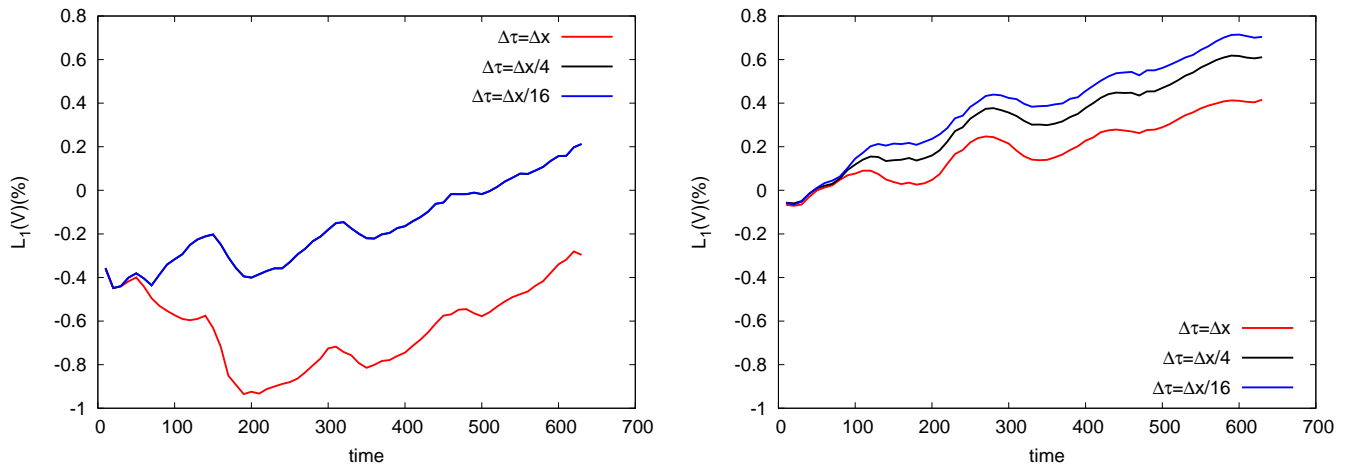
(a) Standard

(b) The volume constraint
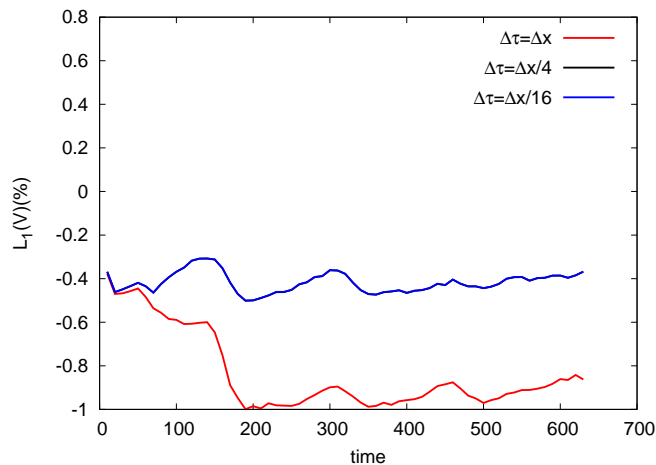
(c) The subcell fix

Figure 3.12 – Variations of $L_1(V)$ with $\Delta\tau$ with 100×100 cells; WENO scheme

and the number of iterations is fixed to 64.

Figure 3.13 presents the notched disc after one rotation, for three grid sizes and the third-order ENO discretization. For the coarsest grid, the constraint method improves significantly the shape of the interface. In comparison with the pure transport problem of Fig. 3.10, we observe that the shape of the notched disk gets worse by using the standard signed distance equation: sharp corners are considerably smoothed and the depth of the slot is reduced. For finer grids, the difference between the constraint and non-constraint methods is reduced. Table 3.4 gathers the relative errors on volume conservation for the basic and constraint signed distance methods, as well as referenced values by Sussman et Fatemi [151]. Improvement in the mass conservation is obvious as soon as the constraint approach is chosen. Comparison of our values with those by [151] shows some differences which are probably explained by the spatial discretization of the transport equation. In-

(a) $\Delta x = 1$

(b) $\Delta x = 1/2$

(c) $\Delta x = 1/3$
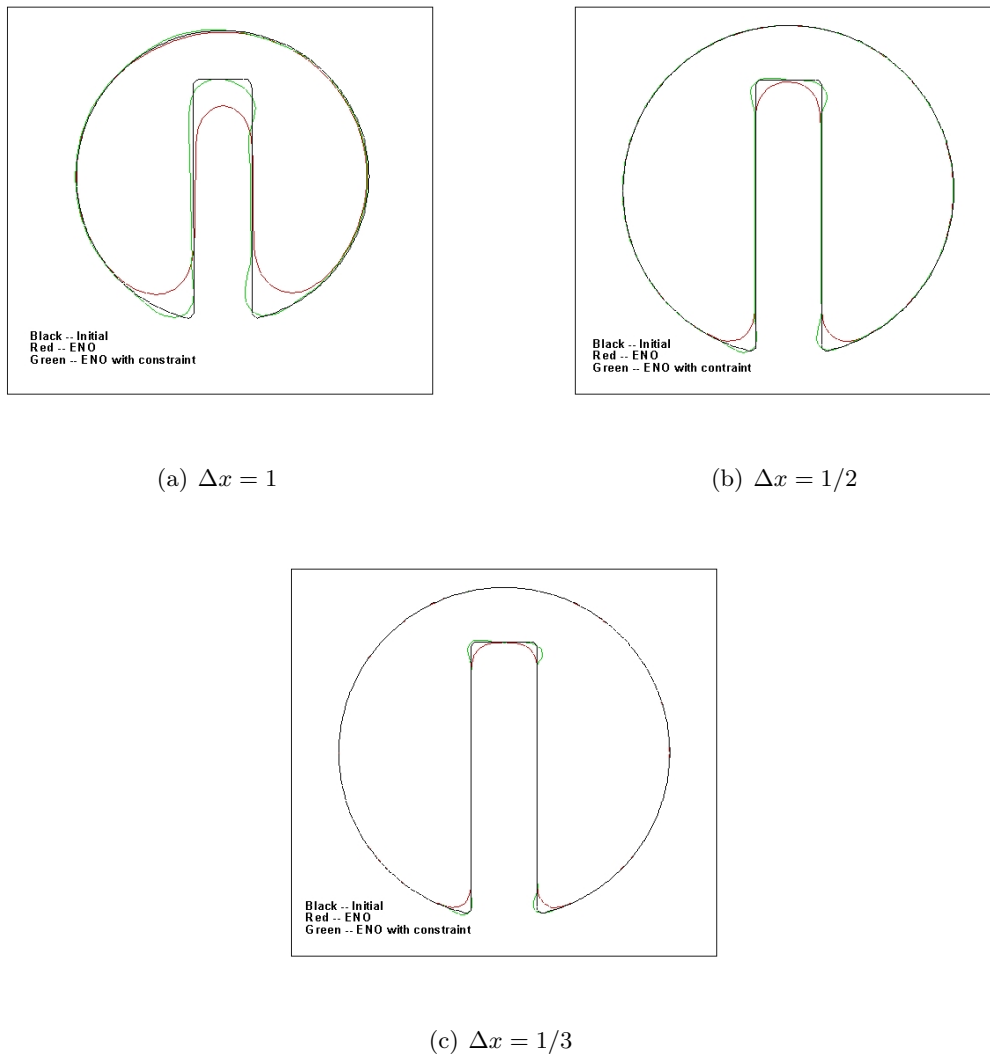
Figure 3.13 – Zalesak problem. Comparison of interfaces computed with standard and constrained signed distance equations for the third-order ENO discretization and different grid sizes.

Δx		Basic method (%)	Constraint method (%)
1		2.5	5.3E-01
	Ref[151]	–	1.3
1/2		4.7E-01	8.9E-02
	Ref[151]	–	0.20
1/3		1.5E-01	6.2E-02
	Ref[151]	–	0.11

Table 3.4 – Zalesak problem. Relative volume conservation $L_1(V)$ for the standard and constraint signed distance methods with ENO discretization.

deed, we chose the fifth-order WENO scheme whereas the referenced work is based on a third order ENO scheme only.

Figure 3.14 illustrates the notched disc after one turn, for three grid sizes and the fifth-

(a) $\Delta x = 1$

(b) $\Delta x = 1/2$

(c) $\Delta x = 1/3$
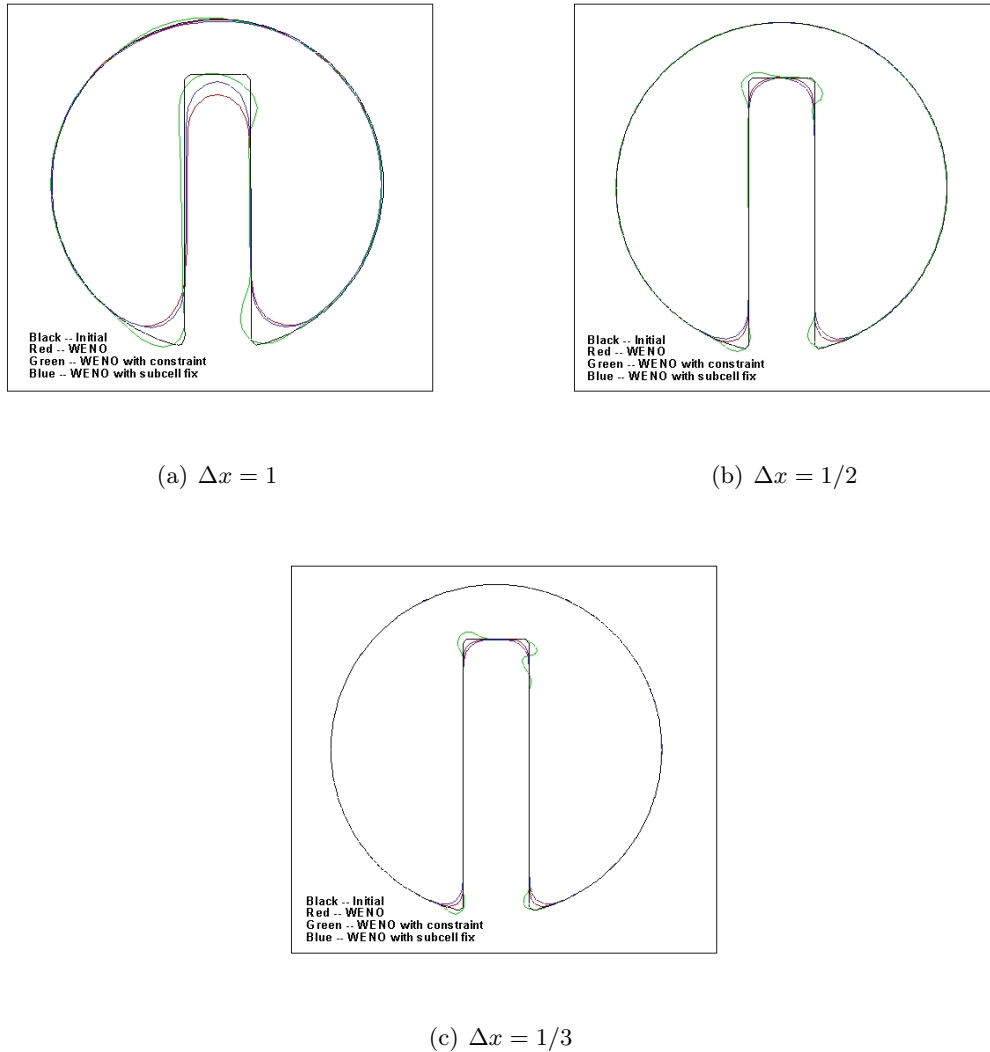
Figure 3.14 – Zalesak problem. Comparison of interfaces computed with standard and constrained signed distance equations for the fifth-order WENO discretization and different grid sizes.

order WENO discretization. The constraint method clearly reduces diffusion near the sharp corners at the expense of spurious oscillations. These oscillations are more pronounced with the fifth-order WENO scheme than with the third-order ENO discretization, since this latter one is more diffusive. The subcell fix approach preserves better the deep of the slot in comparison with the basic signed distance method, at least for the coarsest grid. Table 3.5, which collects the volume conservation errors for the different methods, clearly shows that the improvement in the slot shape entails a deterioration of the volume measure. Therefore considering the volume indicator, the standard signed distance method provides the best results.

Δx	Basic method (%)	Constraint method (%)	Subcell fix method(%)
1	2.1E-01	5.8E-01	1.7
1/2	8.2E-02	1.3E-01	2.9E-01
1/3	5.5E-03	6.7E-02	1.3E-01

Table 3.5 – Zalesak problem. Relative volume conservation $L_1(V)$ for the standard, constraint and sub-cell fix signed distance methods with WENO discretization.

3.4.4 Partial conclusions

From the above analysis concerning the ENO/WENO discretization schemes and the standard, constraint and subcell fix methods for the signed distance equation, we can drawn some conclusions about the Zaleska problem. First, the constraint method reduces the diffusion at sharp corners but produces spurious oscillations. For low order spatial discretization, this approach improves the volume balance. The subcell fix approach may lead to a better representation of the slotted disc for coarse grids but the accuracy on the volume conservation is quite bad. Finally, the better compromise between the error on volume conservation and the shape of the solution is probably to use the high-order Weighted Essentially Non-Oscillatory (WENO) discretization method with the basic signed distance equation.

3.5 Analytical stretching of a circular fluid element

The stretching of a circular fluid element is a classical test for validating the interface tracking methods [132, 135, 168]. In a 100×100 square domain, a circular fluid element of center $(50, 75)$ and radius of 15 is placed into a swirling shear flow field and then stretched into a thin filament.

3.5.1 Steady flow field

The swirling shear flow field is steady and it is given by the stream function φ:

$$\varphi = -\frac{100}{\pi} \sin^2 \left(\frac{\pi x}{100} \right) \sin^2 \left(\frac{\pi y}{100} \right)$$

The solenoïdal velocity field then writes

$$
\begin{aligned}
u &= \frac{\partial \varphi}{\partial y} = -\sin^2 \left(\frac{\pi x}{100} \right) \sin \left(\frac{\pi y}{50} \right) \\
v &= -\frac{\partial \varphi}{\partial x} = \sin^2 \left(\frac{\pi y}{100} \right) \sin \left(\frac{\pi x}{50} \right)
\end{aligned}
\tag{3.8}
$$

Periodic conditions are assumed on boundaries. The WENO discretization schemes is applied for the transport equation. Computations are carried out without the reinitialization.

Figure 3.15 shows four snapshots of the fluid element computed on a 200×200 regular grid and with a time step $\Delta t = 0.25$. The fluid interfaces are in quite good agreement with previous studies [168]. Starting from a circle, the fluid element is stretched into a convergent spiral. During the stretching process, a filament wraps inward its orbit and gets thinner with time increasing. At the time $t = 300$, a significant breakup of the filaments happens. During the stretching, one cell ($t = 100$ and $t = 200$) or less ($t = 300$) is contained in the tail of the filament. This explains the break up of the filament at long times.
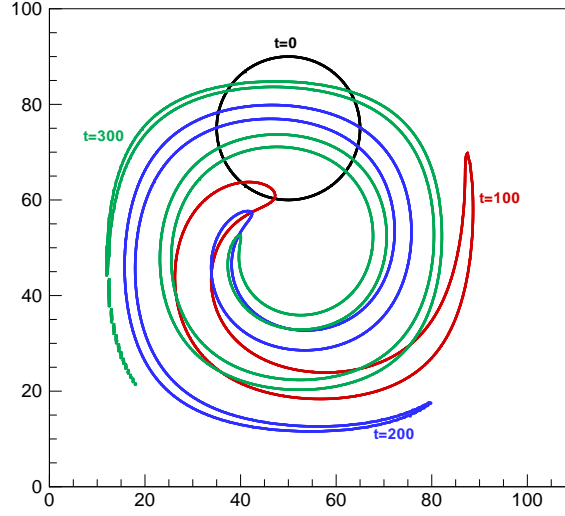
Figure 3.15 – Stretching of a circular fluid element with velocity field (3.8).

3.5.2 Periodic flow field

To evaluate the errors of area preserving and the accuracy of interface advection and deformation, the velocity field of Eq. (3.8) is multiplied by $\cos(\pi t/T)$, so that the stretching process is time-reversed [98, 168] after half period of time $T/2$. Since the third-order TVD Runge-Kutta scheme is used for the advection equation of level set function, it is better to impose the velocity field at the right time in each step. We list the three steps of TVD Runge-kutta scheme:

$$\phi^{(1)} = \phi^{(n)} - \Delta t \vec{v}^n R(\phi^{(n)})$$

$$\phi^{(2)} = \frac{3}{4}\phi^{(n)} + \frac{1}{4}\phi^{(1)} - \frac{\Delta t}{4}\vec{v}^{n+1}R(\phi^{(1)}) = \phi^{(n)} - \frac{\Delta t}{2}\frac{\vec{v}^n R(\phi^{(n)}) + \vec{v}^{n+1}R(\phi^{(1)})}{2}$$

$$\phi^{(3)} = \frac{1}{3}\phi^{(n)} + \frac{2}{3}\phi^{(2)} - \frac{2\Delta t}{3}\vec{v}^{n+1/2}R(\phi^{(2)}) = \phi^{(n)} - \Delta t\frac{\vec{v}^n R(\phi^{(n)}) + \vec{v}^{n+1}R(\phi^{(1)}) + 4\vec{v}^{n+1/2}R(\phi^{(2)})}{6}$$

where $R(\phi) = \nabla\phi$. In the first step, the velocity field at time n is used; in the second step, we apply it at time $n + 1$; in the third step, we take it at time $n + 1/2$.

Fig. 3.16 shows stretching processes ($0 < t < T/2$) at different times for two periods, $T = 250$ and $T = 500$, computed on a 200×200 regular grid and with a time step $\Delta t = 0.25$. Starting from circles at $t = 0$, the flow elements are stretched out by the swirling shear flow during $0 < t < T/2$. Compared with the stretching process in $T = 250$, the circle is deformed seriously in the long period $T = 500$ and the tail of filament gets thinner. In subsequent shrinking processing (during $T/2 \leq t < T$), following the same orbits, it will reverse the direction and shrink back to its initial shape at $t = T$.

Fig.3.17 shows the mass evolutions with time. We take time steps $\Delta t = 0.5$ and $\Delta t = 0.06225$ for grids 100×100 and 800×800 respectively. The time step of signed distance equation keeps $\Delta\tau = 0.0625$ and the number of iterations is fixed to 64.

(a) T=250

(b) T=500
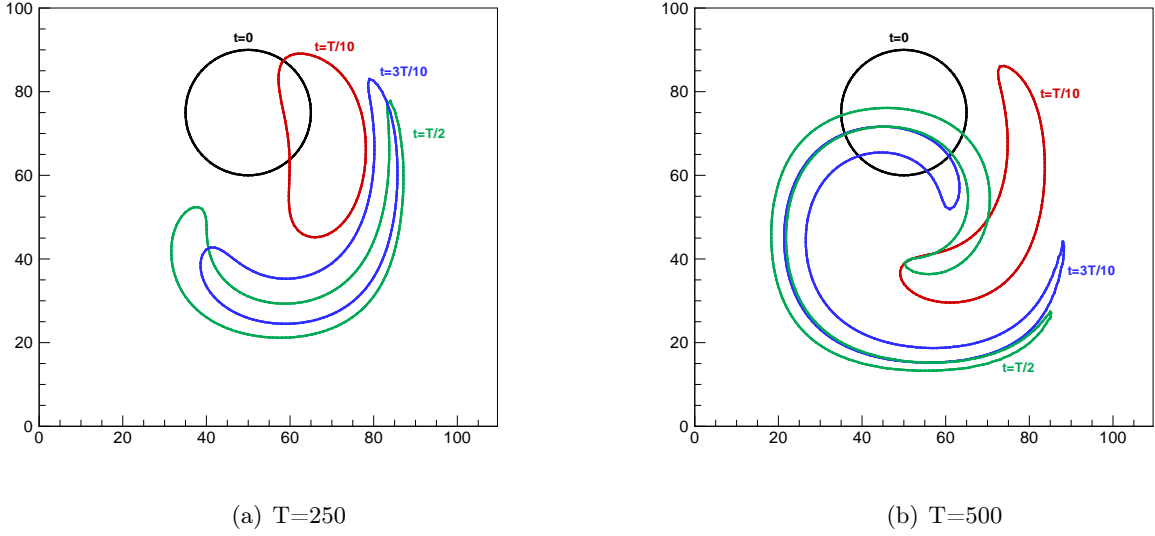
Figure 3.16 – Stretching process during $0 <= t <= T/2$ with 100×100 cells; without signed distance equation

The calculation without the signed distance equation generates the smallest mass error but with the irregular lost and gains of mass during the evolution process. In contrast, smooth curves of mass error are obtained with the redistance step. Among them, some schemes with signed distance equation work well in one case but not in another. For example, as shown in Fig. 3.17(a) and (c), the calculations performed by the volume constraint approach have small mass error for the short period but not for the long period; the opposite behavior is observed with the ENO scheme.

This result is in accordance with the theory [140] since the fifth-order accuracy is obtained only for smooth solutions. In this problem, since the circle is stretched more seriously in the long period $T = 500$ as shown in Fig. 3.16(b), few cells are contained between two zero level interfaces in the filament tail (for instance, only 1 or 2 cells with 100×100 cells and $T = 500$). Therefore, when constructing the high order schemes, we are forced to select cells with discontinuous derivatives in ϕ. If some discontinuity is located into one or two of the WENO sub-stencils used for interpolations, the accuracy is reduced to third-order. But if this discontinuity occurs in all sub-stencils the accuracy tumbles dramatically to first-order. For finer grids, more cells are located in filament tail. It results a smooth solution and more accurate mass balance (Fig. 3.17(c) and (d)).

This can either explain why the standard third order ENO scheme does better in the long period and the good performance of the calculation without the signed distance equation since the discontinuous $\|\nabla d\|$ is not used any more. Despite of this, the signed distance function plays an important part in simulation of real fluid flows. Amongst schemes for the signed distance equation, the WENO scheme with subcell fix method gives quite good convergence properties. The above conclusions can also be verified by measurements of time average relative volume conservation errors defined by

$$\frac{1}{T} \int_0^T \left| \frac{\int_\Omega H(\phi_{\text{computed}}, t)\, d\Omega - \int_\Omega H(\phi_{\text{exact}})\, d\Omega}{\int_\Omega H(\phi_{\text{exact}})\, d\Omega} \right| dt$$

183
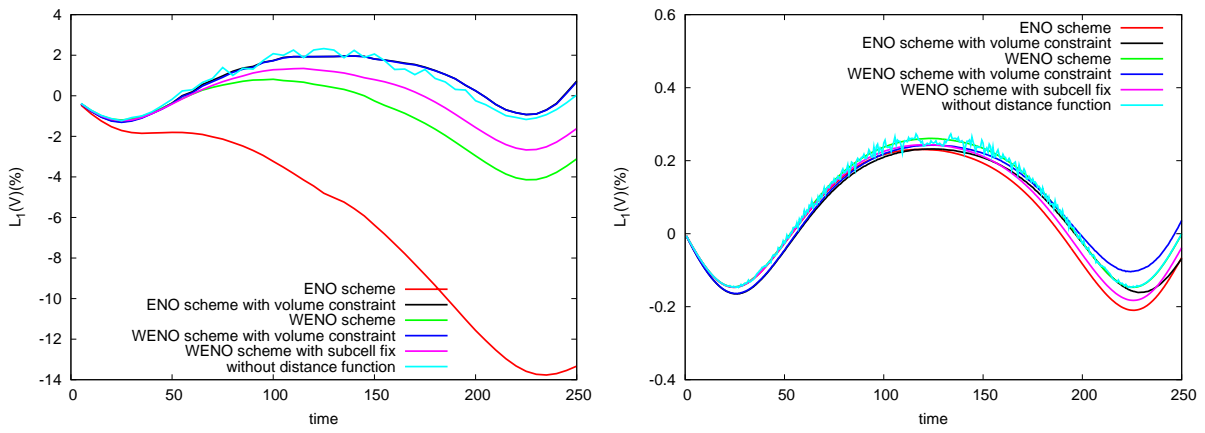
(a) T=250 with 100×100 cells

(b) T=250 with 800×800 cells
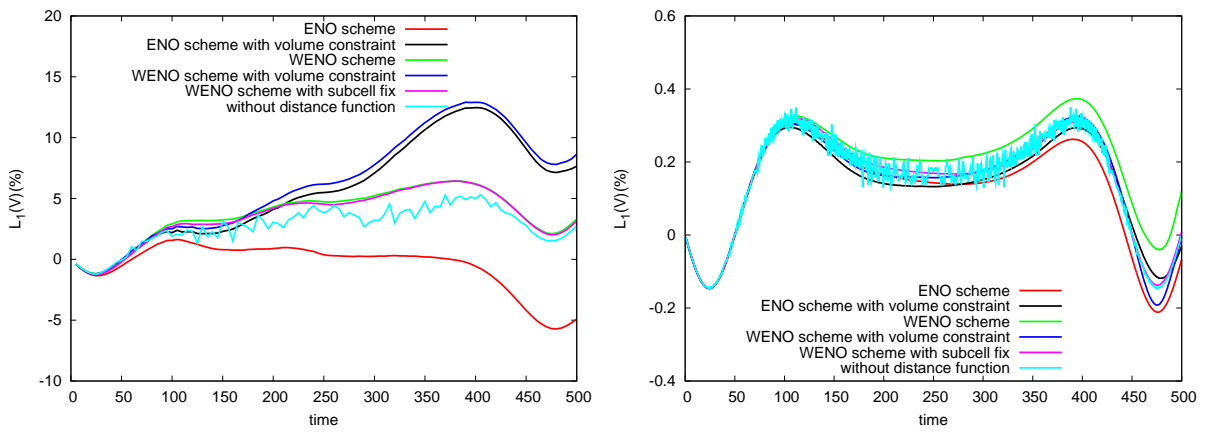
(c) T=500 with 100×100 cells

(d) T=500 with 800×800 cells

Figure 3.17 – Mass evolutions over complete periods

and presented in Tab. 3.6 and Tab. 3.7, and by the curvature errors presented in Tab. 3.8

Grid	w/o d (%)	ENO scheme(%)		WENO scheme(%)		
		standard	volume constraint	standard	volume constraint	subcell fix
100^2	1.12E+00	6.08E+00	1.10E+00	1.39E+00	1.10E+00	1.11E+00
200^2	2.74E-01	1.26E-01	2.78E-01	2.52E-01	2.80E-01	2.37E-01
400^2	4.17E-02	4.31E-02	4.69E-02	4.15E-02	4.74E-02	4.23E-02
800^2	1.30E-02	1.31E-02	1.45E-02	1.30E-02	1.44E-02	1.31E-02

Table 3.6 – Time average relative volume conservation errors for different schemes with the signed distance equation; T=250

and Tab. 3.9 where the negative aspects of the volume constraint method, deforming the

Grid	w/o d (%)	ENO scheme(%)		WENO scheme(%)		
		standard	volume constraint	standard	volume constraint	subcell fix
100^2	1.05E+00	4.55E-01	1.24E+00	1.38E+00	1.42E+00	1.31E+00
200^2	1.71E-01	1.55E-01	1.70E-01	1.82E-01	1.80E-01	1.73E-01
400^2	2.15E-02	2.15E-02	2.22E-02	2.14E-02	2.18E-02	2.14E-02
800^2	6.49E-03	6.52E-03	6.53E-03	6.50E-03	6.57E-03	6.52E-03

Table 3.7 – Time average relative volume conservation errors for different schemes with the signed distance equation; T=500

Grid	w/o d (%)	ENO scheme(%)		WENO scheme(%)		
		standard	volume constraint	standard	volume constraint	subcell fix
100^2	4.3	59	57	43	70	38
200^2	9.7E-01	27	30	19	61	15
400^2	7.7E-02	13	23	9.2	77	9.3
800^2	1.2E-02	6.8	21	11	93	5.1

Table 3.8 – Curvature error $L_2(\kappa, \Omega_\varepsilon), |\varepsilon| < 2$ for different schemes with the signed distance equation at t=T; T=250

Grid	w/o d(%)	ENO scheme(%)		WENO scheme(%)		
		standard	volume constraint	standard	volume constraint	subcell fix
100^2	25	197	233	236	244	232
200^2	13	131	330	250	386	250
400^2	2.2	79	173	252	246	146
800^2	1.1E-01	42	105	602	185	105

Table 3.9 – Curvature error $L_2(\kappa, \Omega_\varepsilon), |\varepsilon| < 2$ for different schemes with the signed distance equation at t=T; T=500

interface and ruining the smoothness of curvature of circle, are shown again.

3.6 Immiscible fluid flows

3.6.1 Traveling solitary wave

Propagating of a solitary wave is used to ascertain if our numerical scheme can predict the viscous damping and run-up on a vertical wall of a traveling solitary wave in a enclosed domain. As shown in Fig.3.18, the size of the enclosure is $20h$ width and $2h$ height. Half of the domain is filled by still water. To generate a solitary wave, we release an additional water volume, initially at rest, from the left vertical wall; its maximal amplitude is A_0. The wave then escapes from the influence of left wall and gradually becomes a solitary wave before reaching the right wall with a maximal height A_{run-up}. The amplitude of the wave at mid-distance $x = 10h$ is noted A_c.

Making use of Laitone's analytical approximation [129], the initially still water surface
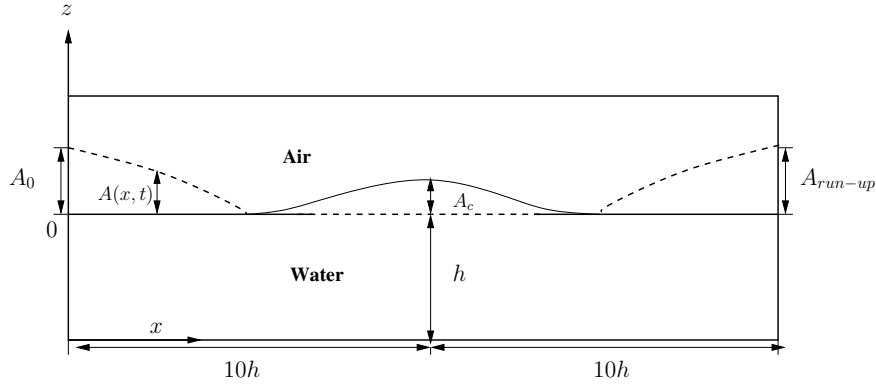
Figure 3.18 – Illustration of the formation and traveling of a solitary wave in an enclosure.

in hydrostatic balance can be predicted by

$$A(x, t = 0) = A_0 / \cosh^2\left(\frac{\sqrt{3A_0}}{2} x\right) \tag{3.9}$$

where A_0 is the initial amplitude. The physical parameters are chosen so that the theoretically predicted wave speed is $C_w = \sqrt{gh} = 1.0\,m/s$ and the Reynolds number gives $Re = C_w\,h/\nu_w = 5 \times 10^4$. For the simulation, the viscosity ratio $\nu_a/\nu_w = 15$, and the density ratio $\rho_a/\rho_w = 1.2 \times 10^{-3}$ where subscripts a and w denote air and water, respectively. Theoretically, after $t' = 6.0\,s$, the wave has escaped totally from the left wall and may be regarded as a solitary wave. For studying the solitary wave, $t' = 6\,s$ is set as initial time, $t = t' - 6$.

The regular grid used for simulations is 200×120. We assume no-slip boundary conditions for velocity and symmetry conditions for the level-set function at walls. The time step is related to the CFL number, fixed to $CFL = 0.1$. The basic signed distance equation is used with the WENO spatial discretization.

For $A_0 = 0.4h$, the profiles of solitary waves from time $t = 0\,s$ until $t = 14\,s$ are demonstrated in Fig. 3.19(a). The solitary wave propagates from the left to the right and at last climbs at the right vertical wall. There exists a slight damping of the wave amplitude due to the viscous effects. The wave speed measured from Fig. 3.19(a) is $1.03\,m/s$ between $t = 0\,s$ and $t = 10\,s$ which is close to the theoretical value. Figure 3.19(b) shows a typical velocity field at $t = 4.0\,s$. A vortex centered at the wave top is observed.

To quantify the viscous damping characteristic of the wave, we compute three waves with different initial amplitudes, and compare the results with those predicted by Mei perturbation theory [109]

$$A_{\max}^{-1/4}(t) = A_{0\,\max}^{-1/4} + 0.08356\left(\frac{\nu_w}{C_w^{1/2} h^{3/2}}\right)^{1/2} \frac{C_w t}{h} \tag{3.10}$$

where $A_{\max}(t)$ is the instantaneous amplitude of the solitary wave, and $A_{0\,\max}$ is the amplitude at the initial state, $t = 0\,s$. Figure 3.20(a) shows the computation agrees better with the perturbation theory all the more $A_{0\,\max} \equiv A_{\max}(t = 0)$ is small. That is because Eq. (3.19(b)) is valid only for $A_{0\,\max} \leq 0.1$.

Another point for comparison is the wave run-up (the highest point) at the right vertical wall. To this end, we compute nine cases $A_0/h = 0.1, \cdots, 0.9$ and measure the run-ups
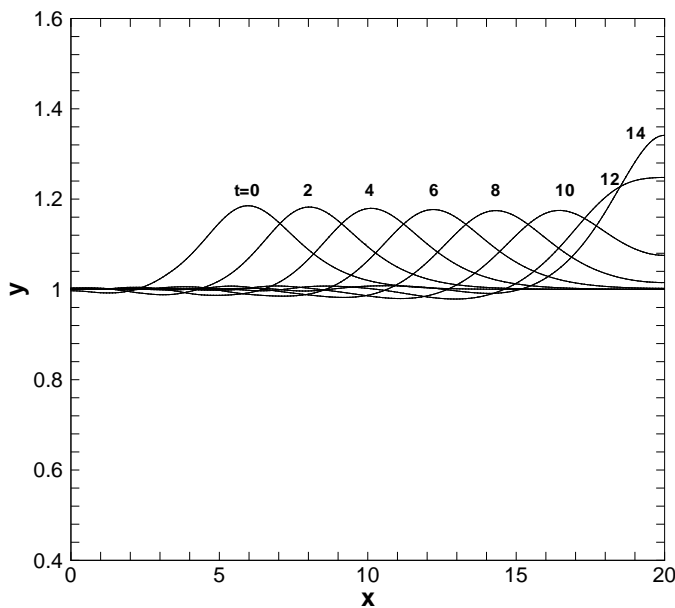
(a) Traveling trains of a solitary wave.
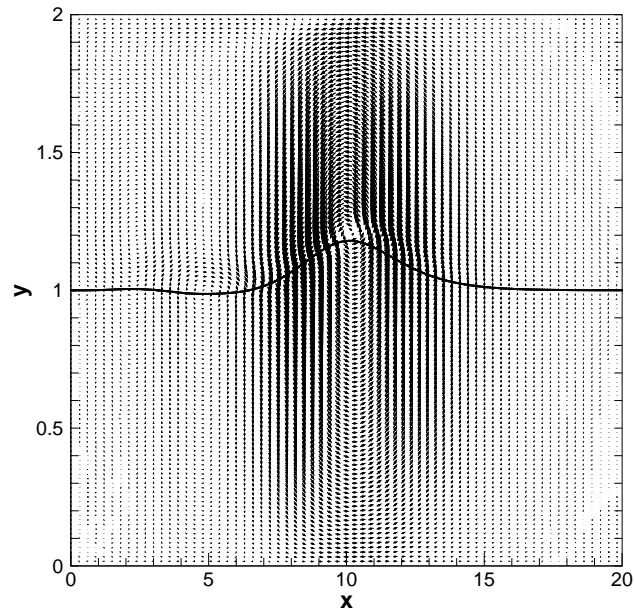
(b) A typical velocity field of a solitary wave at 4.0s.

Figure 3.19 – Solitary wave and velocity field in reduced coordinates.
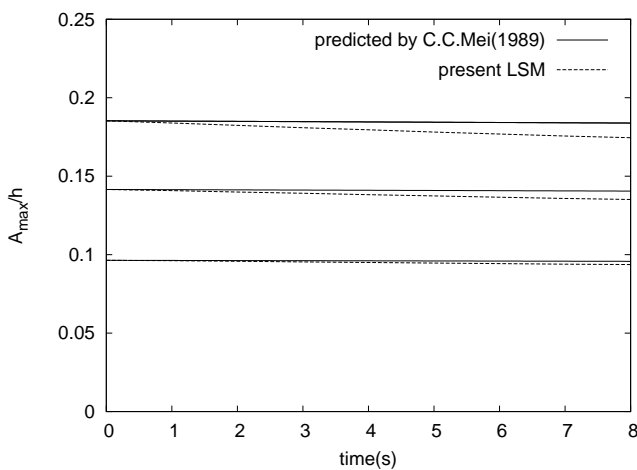
(a) Damping rate of solitary waves.
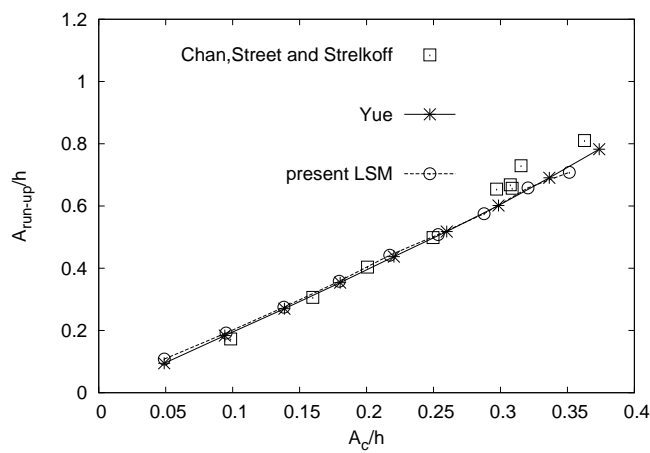
(b) Wave run-up versus incident wave amplitude.

Figure 3.20 – Properties of the solitary wave. References: Mei [109], Chan et Street [40], Yue *et al.* [168]

at the right wall boundary. The computational results are compared with the experimental data by Chan et Street [40] and numerical data by Yue *et al.* [168] (Fig. 3.20(b)). In this figure, the label A_c in the x-axis stands for the amplitude of the solitary wave at the middle of the horizontal distance of the computational domain. Our results agree well with numerical data by [168]. The agreement between computations and experiments is very good for

$A_c/h < 0.3$. Beyond this value, the experimental data exhibit some scatter. Overall, these results demonstrate that the Level-Set Method (LSM) can accurately predict the viscous damping characteristic without introducing significant numerical damping effects.

To evaluate the volume (or mass) conservation of the liquid phase, we computed the evolution of the relative volume variation $(V(t) - V(t=0))/\Delta V$ (Fig. 3.21), with ΔV the
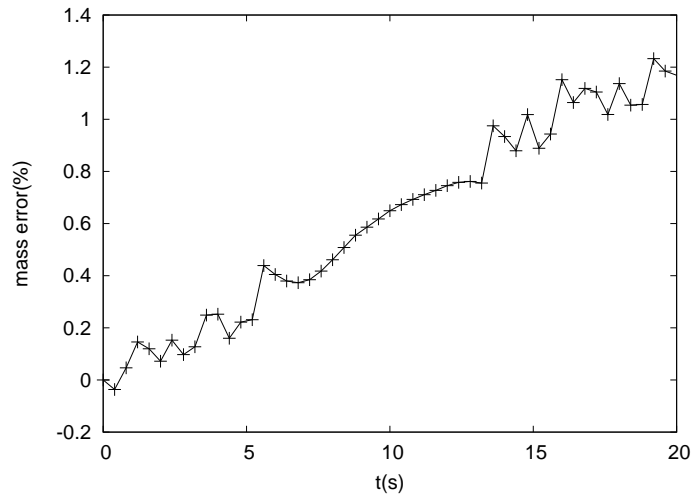
Figure 3.21 – Mass (volume) error during propagation.

additional volume corresponding to the initial wave ($\Delta V = V(t=0) - 20 \times h^2$). As can be seen, the relative error is at most of 1.4%.

3.6.2 Bubble problems

3.6.2.1 Equilibrium-elliptic bubble

The problem of equilibrium elliptic bubble is a simple but challenging problem to test the accuracy of curvature and the smoothness of discontinuous physical quantities near surfaces. In absence of gravitational force, the circle bubble will be static and keep its original form by the force of surface tension. Physically, velocity fields do not exist if the circle bubble does not move at all. Numerically, when the surface tension force becomes the dominant force, the accuracy and the stability of surface tension force critically affect the dynamics of fluid flow. The inaccuracy of surface tension force is one of the important reasons leading to parasitic currents.

Consider a $0.04\,m$ square computational domain initially filled with water except a circular air bubble of radius $0.01\,m$ centered in the middle of the domain (Fig. 3.22). The properties of water are $\rho_{\text{water}} = 1000\,kg/m^3$ and $\mu_{\text{water}} = 1.137 \times 10^{-3}\,kg/ms$ and those of air are $\rho_{\text{air}} = 1.226\,kg/m^3$ and $\mu_{\text{air}} = 1.78 \times 10^{-5}\,kg/ms$. The coefficient of surface tension is $\sigma = 0.0728\,kg/s^2$. The gravity $g = 0$. The CFL number is set to 0.1 and the WENO discretization scheme is used for the transport and the signed distance equations in the regular mesh.
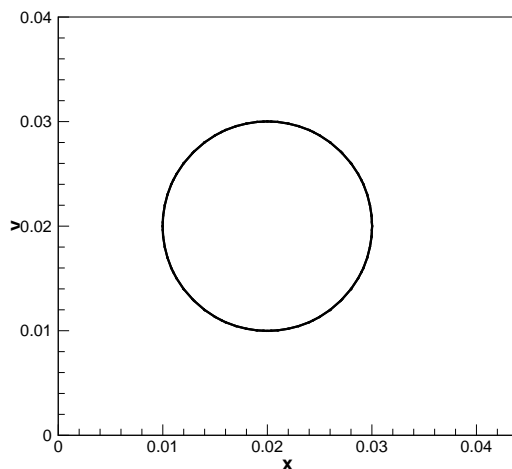
Figure 3.22 – Air bubble at $t = 0.05\,s$

Grid	ε	$L_2(\kappa, \Omega_{\text{test}})$ (%)	$L_{2,\text{exact}}(\kappa, \Omega_{\text{test}})$ (%)	$L_1(V)$ (%)	$v_{\max}$ (m/s)
20^2	$2\Delta x$	27.9	28.4	0.69	0.196
40^2	$2\Delta x$	12.2	10.94	0.709	0.27
	$4\Delta x$	24.6	24.4	0.237	0.13
80^2	$2\Delta x$	7.34	5.80	0.984	0.35
	$4\Delta x$	11.7	11.5	0.083	0.14
	$8\Delta x$	24.5	24.5	0.126	0.035
160^2	$2\Delta x$	7.10	2.93	1.10	0.24
	$4\Delta x$	5.92	5.85	0.074	0.14
	$8\Delta x$	11.7	11.6	0.031	0.04
	$16\Delta x$	24.4	24.4	0.048	0.009
320^2	$2\Delta x$	6.03	1.59	0.92	0.21
	$4\Delta x$	3.08	2.90	0.07	0.10
	$8\Delta x$	5.81	5.80	0.01	0.04
	$16\Delta x$	11.7	11.7	0.01	0.01
	$32\Delta x$	24.3	24.3	0.009	0.002

Table 3.10 – Errors $L_2(\kappa, \Omega_{\text{test}})$ (Eq. 3.3 page 166) and $L_1(V)$ (Eq. 3.1 page 165) and maximal velocity $v_{\max}$ as a function of the grid size and the half-thickness of interface ε (see Fig. 2.1 page 137) at $t = 0.05s$. The sub-domain Ω_{test} is defined such that $|\phi(\vec{x})| < \varepsilon$. The column $L_{2,\text{exact}}(\kappa, \Omega_{\text{test}})$ is the numerical measure of the curvature at $t = 0$.

Table 3.10 shows the influences of the grid size and interface thickness on mass conservation, interface curvature and maximum velocities at $t = 0.05s$.

First, the $L_2(\kappa, \Omega_{\text{test}})$ errors of different grids are compared with the a constant half-thickness of transition zone ε. To do this, we have to multiply ε by two when the grid becomes double. For example, we must compare the following lines: $\varepsilon = 2\Delta x$ with grid 20^2, $\varepsilon = 4\Delta x$ with grid 40^2, $\varepsilon = 8\Delta x$ with grid 80^2, $\varepsilon = 16\Delta x$ with grid 160^2 and $\varepsilon = 32\Delta x$ with grid 320^2. With this approach, Tab. 3.10 clearly indicates that the error on the curvature does not change. But it is interesting to compare the values $L_2(\kappa, \Omega_{\text{test}})$ to the smallest expected errors defined as the relative errors of the interface curvatures without parasitic currents $L_{2,\text{exact}}(\kappa, \Omega_{\text{test}})$, that is at $t = 0$. Such comparison seems to

prove that the curvatures are well preserved during time iterations. In contrast, the error on the volume conservation is greatly improved with mesh refinement. This improvement is due to the reduction in the maximal magnitude of the spurious velocities $v_{\max}$ which occur in the thick interface.

For a fixed grid, the variation of $L_2(\kappa, \Omega_{\text{test}})$ errors depends on two parameters. On the one hand, the decrease in the parasitic current magnitude leads to an improvement of the interface shape and volume. On the other hand, the thickening of the interface region, measured by ε, worsens the value of the average curvature error since the reference curvature is kept to exact bubble radius R (see Eq. (3.3), page 166). This antagonistic variation is clearly shown for the finest mesh, 320×320. Indeed, $L_2(\kappa, \Omega_{\text{test}})$ decreases from $\varepsilon = 2\Delta x$ to $\varepsilon = 4\Delta x$, and then increases beyond $\varepsilon = 4\Delta x$. When we consider $L_{2,\text{exact}}(\kappa, \Omega_{\text{test}})$ errors, spurious velocities do no exist. It results that the variation of the 'exact' curvature error is only sensitive to the interface thickening, and then $L_{2,\text{exact}}(\kappa, \Omega_{\text{test}})$ augments with ε.

The maximum value of velocity field $v_{\max}$ can be an estimation of parasitic currents which correspond to the accuracy and stability of surface tension force (Tab. 3.10). The maximum velocity converges, both for a fixed interface thickness (ε) with mesh refinement, and for a fixed grid with increase in ε. In these two situations, the density, viscosity and surface tension are smoothed by reducing their numerical gradients on cells located in the transition zone $|\phi(\vec{x})| < \varepsilon$. It is worth noticing that the parasitic currents may be greatly reduced by substituting the interface thickening by an alternative approach, called the 'Ghost method': for a 40×40 grid, the maximum velocity falls from $0.27\,m/s$ to $0.1\,m/s$ with such method [85].

The relative volume conservation error $L_1(V)$ follows essentially the same behavior as the maximum velocity $v_{\max}$. However, for fixed grids and the largest interface thicknesses, $L_1(V)$ becomes almost constant because the calculation of the volume conservation is affected by spatial accuracy.

3.6.2.2 Non-equilibrium elliptic bubble

An elliptic bubble with a long axis radius $R_l = 0.01\,m$ and a short axis radius $R_s = 0.005\,m$ is centered into a $0.05\,m$ square box [146]. The properties of water are $\rho_{\text{water}} = 1000\,kg/m^3$ and $\mu_{\text{water}} = 1.137 \times 10^{-3}\,kg/ms$ and those of air are $\rho_{\text{air}} = 1.226\,kg/m^3$ and $\mu_{\text{air}} = 1.78 \times 10^{-5}\,kg/ms$. The coefficient of surface tension is $\sigma = 7.28 \times 10^{-2}\,kg/s^2$. The gravitational force is disregarded.

The small time step $\Delta t = 10^{-4}$ is taken. The WENO discretization scheme is used for the transport and the basic signed distance equations for regular meshes ranging from 80×80 to 320×320. The half interface thickness is set to $\varepsilon = 2\Delta x$.

The air bubble in a water box starts from a slightly stretched state in x-direction. When we remove the tensile stress, the elliptic bubble begins to relax toward its equilibrium circle state by oscillating with decreasing magnitude (Fig. 3.23). From $t = 5\,s$, the surface tension force is exactly balanced by the pressure drop on both sides of the bubble interface so that the bubble is steady.

The evolution of the relative volume conservation error $L_1(V)$ is presented in Fig. 3.24. The volume of the bubble grows with time, and all the more that the mesh is coarse. For example at time $t = 5\,s$, the volume error augments from 8% to 21% when the mesh shrinks from 320×320 to 80×80. That is related to the maximum velocity in the flow field which increases from $0.017\,m/s$ to $0.037\,m/s$, whereas a stationary state is expected.

(a) t=0 s   (b) t=0.02 s   (c) t=0.3 s

(d) t=0.6 s   (e) t=5 s
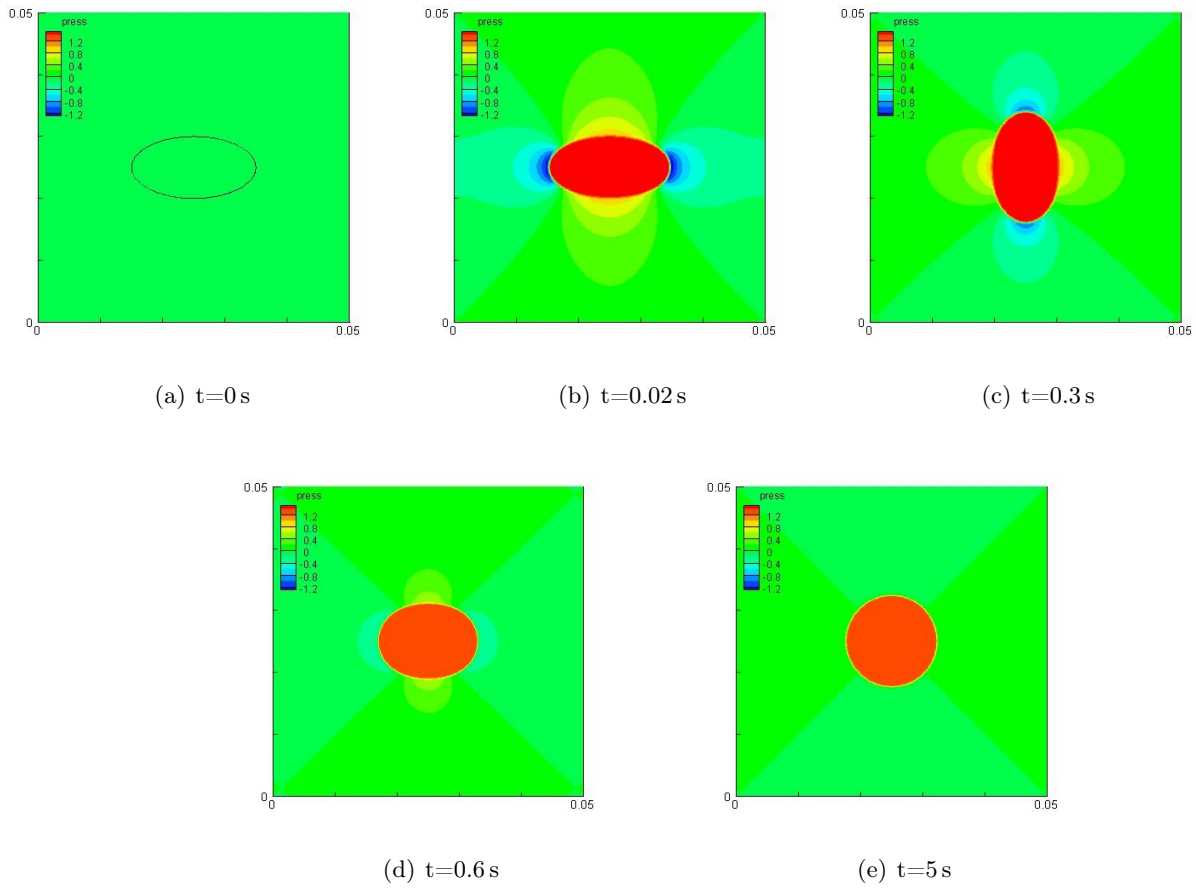
Figure 3.23 – Pressure fields of bubbles at different times with cells 320×320
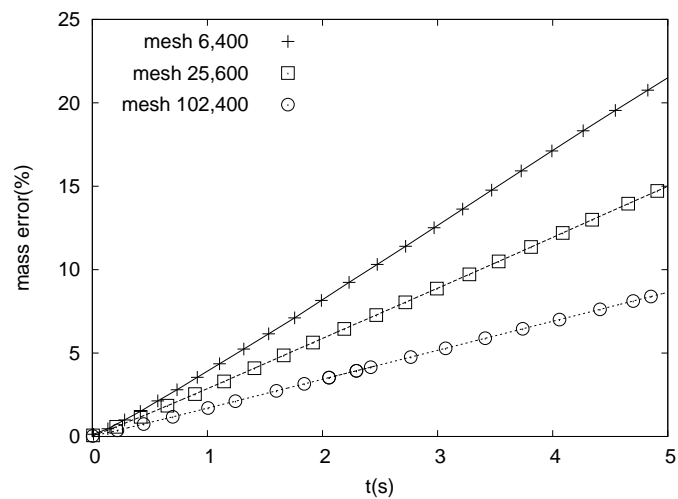
Figure 3.24 – Variation curve of mass (volume) error with time in the non-equilibrium bubble problem

191

Chapter 4

Conclusions & perspectives

4.1   Key points of this work

An interface tracking method was developed using the level-Set approach. A particular care was taken to explain the principles of the level set method and the part played by the signed distance function in the Navier-Stokes equations. High-order approximations were retained to discretize temporal and spatial derivatives. The spatial discretizations, based on essentially non oscillatory schemes, were presented in details. Modifications in the signed distance equation were considered to improve the fluid mass conservation.

Validation steps and comparisons between the different versions of the level-set methods were carried out. The Weighted Essentially Non-Oscillatory (WENO) scheme seems to have a better convergence property in the transport equation than the Essentially Non-Oscillatory (ENO) scheme, since ENO solutions may diverge with time increasing and grid refinement. Final conclusion cannot be drawn on the real improvements of the numerical solutions when one modifies the signed distance equation. However, some remarks can be performed:
  – It appears that the "volume constraint" method generally ameliorates the fluid mass conservation, especially for coarse meshes, but always at the cost of deformation of the zero level curve. Therefore, it results a deterioration of the curvature of the interface when one applies too many iterations to solve the signed distance equation.
  – The "subcell fix" method seems to be more efficient to preserve the curvature of the interface.

4.2   Works prospects

One of the main issues of the Level-Set method is that mass conservations of each fluid are not fully respected. As an example, this leads to difficulties when forces involved in the physical problems evolve slowly. In that case, improvements in the numerical scheme must be taken into account. One way to do this could be to suppress the spurious flows which appear in the interface thickness by explicitly introducing into the discrete equations the jumps of fluid properties and stresses across two immiscible fluids. Another improvement in the mass conservation should be to refine the mesh locally around the interface. Physical validations must also be added, for instance to study natural convection induced by surface tension variations.

Conclusions

The aim of my research is to develop and investigate the natural convection for immiscible fluid flows. To answer this purpose, I developed numerical models under low Mach number and Boussinesq approximations. These schemes were then programmed and carefully validated. These tools allowed us to investigate natural and mixed convection flows in vertical channel partially or fully heated at walls. Simultaneously, I worked on interface tracking methods. After a bibliography study, I selected the level-Set method. An important work was done to understand this method and to familiarize myself to the new numerical schemes which are classically applied for discretizing the hyperbolic equations of transport and signed distance. Then a validation step was conducted to compare the convergence properties to the ones expected.

List of Figures

I

Part II: Comparisons of Level-Set numerical schemes for the modeling of immiscible incompressible fluid flows   129

List of Tables

Bibliography

[1] N. ANAND, S. KIM et L. FLETCHER : The effect of plate spacing on free convection between heated parallel plates. *Journal of Heat Transfer (Transactions of the ASME (American Society of Mechanical Engineers), Series C);(United States)*, 114(2), 1992.

[2] J. ANDERSON et J. WENDT : *Computational fluid dynamics*, vol. 206. McGraw-Hill, 1995.

[3] A. ANDREOZZI, B. BUONOMO et O. MANCA : Numerical study of natural convection in vertical channels with adiabatic extensions downstream. *Numerical Heat Transfer, Part A*, 47(8):741–762, 2005.

[4] A. ANDREOZZI, B. BUONOMO et O. MANCA : Thermal and fluid dynamic behaviors in symmetrical heated channel-chimney systems. *International Journal of Numerical Methods for Heat & Fluid Flow*, 20(7):811–833, 2010.

[5] A. ANDREOZZI, O. MANCA et V. NASO : Natural convection in vertical channels with an auxiliary plate. *International Journal of Numerical Methods for Heat & 38; Fluid Flow*, 12(6):716–734, 2002.

[6] T. ASLAM, J. BDZIL et D. STEWART : Level set methods applied to modeling detonation shock dynamics. *Journal of Computational Physics*, 126(2):390–409, 1996.

[7] A. AULETTA et O. MANCA : Heat and fluid flow resulting from the chimney effect in a symmetrically heated vertical channel with adiabatic extensions. *International Journal of Thermal Sciences*, 41(12):1101–1111, 2002.

[8] W. AUNG : Fully developed laminar free convection between vertical plates heated asymmetrically. *International Journal of Heat and Mass Transfer*, 15(8):1577–1580, 1972.

[9] W. AUNG : Mixed convection in internal flow. *Handbook of Single-Phase Convective Heat Transfer*, p. 1–15, 1987.

[10] W. AUNG, L. FLETCHER et V. SERNAS : Developing laminar free convection between vertical flat plates with asymmetric heating. *International Journal of Heat and Mass Transfer*, 15(11):2293–2304, 1972.

[11] W. AUNG et G. WORKU : Developing flow and flow reversal in a vertical channel with asymmetric wall temperatures. *Journal of Heat Transfer*, 108(2):229–304, 1986.

[12] W. AUNG et G. WORKU : Theory of fully developed, combined convection including flow reversal. *Journal of Heat Transfer*, 108(2):485–488, 1986.

[13] W. AUNG et G. WORKU : Mixed convection in ducts with asymmetric wall heat fluxes. *Journal of Heat Transfer*, 109(4):947–951, 1987.

[14] I. Babuška : The finite element method with Lagragian multipliers. *Numeri Math.*, 20:179–192, 1973.

[15] C. Balaji et S. Venkateshan : Interaction of surface radiation with free convection in a square cavity. *International Journal of Heat and Fluid Flow*, 14(3):260–267, 1993.

[16] C. Balaji et S. Venkateshan : Correlations for free convection and surface radiation in a square cavity. *International Journal of Heat and Fluid Flow*, 15(3):249–251, 1994.

[17] B. Balunov, A. Babykin, R. Rybin, V. Krylov, V. Tanchuk et S. Grigoriev : Heat transfer at mixed convection in vertical and inclined flat channels of the vacuum chamber of the iter international thermonuclear reactor. *High Temperature*, 42(1):126–133, 2004.

[18] A. Bar-Cohen et W. Rohsenow : Thermally optimum spacing of vertical, natural convection cooled, parallel plates. *Journal of Heat Transfer*, 106(1):116–123, 1984.

[19] A. Barletta et E. Zanchini : On the choice of the reference temperature for fully-developed mixed convection in a vertical channel. *International Journal of Heat and Mass Transfer*, 42(16):3169–3181, 1999.

[20] R. Beam et R. Warming : An implicit finite-difference algorithm for hyperbolic systems in conservation-law form. *Journal of Computational Physics*, 22(1):87–110, 1976.

[21] A. Bejan : *Convection heat transfer.* John Wiley and Sons Inc., New York, NY, 1984.

[22] A. Bejan : *Convection heat transfer 3rd.* John Wiley & Sons Inc, 2004.

[23] A. Bejan et G. Ledezma : Thermodynamic optimization of cooling techniques for electronic packages. *International Journal of Heat and Mass Transfer*, 39(6):1213–1221, 1996.

[24] A. Bejan et S. Lorente : *Design with constructal theory.* Wiley Online Library, 2008.

[25] A. Bejan et E. Sciubba : The optimal spacing of parallel plates cooled by forced convection. *International Journal of Heat and Mass Transfer*, 35(12):3259–3264, 1992.

[26] T. Bello-Ochende et A. Bejan : Optimal spacings for mixed convection. *Journal of Heat Transfer*, 126:956–962, 2004.

[27] M. Bernier et B. Baliga : Visualization of upward mixed-convection flows in vertical pipes using a thin semitransparent gold-film heater and dye injection. *International Journal of Heat and Fluid Flow*, 13(3):241–249, 1992.

[28] N. Bianco, L. Langellotto, O. Manca et S. Nardini : Radiative effects on natural convection in vertical convergent channels. *International Journal of Heat and Mass Transfer*, 53(17):3513–3524, 2010.

[29] R. Bird, W. Stewart et E. Lightfoot : *Transport phenomena.* J. Wiley & Sons (ASIA), 2004.

[30] J. Bodoia et J. Osterle : The development of free convection between heated vertical plates. *Journal of Heat Transfer*, 84:40–44, 1962.

[31] S. Boetcher et E. Sparrow : Buoyancy-induced flow in an open-ended cavity: Assessment of a similarity solution and of numerical simulation models. *International Journal of Heat and Mass Transfer*, 52(15-16):3850–3856, 2009.

[32] H. Bouali, A. Mezrhab, H. Amaoui et M. Bouzidi : Radiation¡ªnatural convection heat transfer in an inclined rectangular enclosure. *International Journal of Thermal Sciences*, 45(6):553–566, 2006.

[33] J. Boussinesq : Théorie analytique de la chaleur, volume 2. gauthier-villars, paris (france), 1903. *Reproduction Bibliotheque Nationale de France*, 1995.

[34] J. Brackbill, D. Kothe et C. Zemach : A continuum method for modeling surface tension* 1. *Journal of Computational Physics*, 100(2):335–354, 1992.

[35] F. Brezzi : On the existence, uniqueness and approximation of saddle-point problems arising for Lagrangian multipliers. *R.A.I.R.O. Anal. Numér.*, 8(R2):129–151, 1974.

[36] B. Buonomo et O. Manca : Natural convection slip flow in a vertical microchannel heated at uniform heat flux. *International Journal of Thermal Sciences*, 49(8):1333–1344, 2010.

[37] B. Buonomo et O. Manca : Transient natural convection in a vertical microchannel heated at uniform heat flux. *International Journal of Thermal Sciences*, 56:35–47, 2012.

[38] A. Campo : Bounds for the optimal conditions of forced convective flows inside multiple channels whose plates are heated by a uniform flux. *International Communications in Heat and Mass Transfer*, 26(1):105–114, 1999.

[39] J. Carpenter, D. Briggs et V. Sernas : Combined radiation and developing laminar free convection between vertical flat plates with asymmetric heating. *Journal of Heat Transfer*, 98:95–100, 1976.

[40] R. Chan et R. Street : A computer study of finite-amplitude water waves. *Journal of Computational Physics*, 6(1):68–94, 1970.

[41] Y. Chang, T. Hou, B. Merriman et S. Osher : A level set formulation of eulerian interface capturing methods for incompressible fluid flows. *Journal of Computational Physics*, 124(2):449–464, 1996.

[42] T. Chen, B. Armaly et W. Aung : Natural Convection:Fundamentals and Applications. p. 669–725, 1985.

[43] Y. Chen et J. Chung : The linear stability of mixed convection in a vertical channel flow. *Journal of Fluid Mechanics*, 325:29–52, 1996.

[44] C. Cheng, S. Huang et W. Aung : Enhancement of flare method for predicting buoyancy-induced flow reversal in vertical ducts via parabolic model. *Numerical Heat Transfer*, 31(3):327–345, 1997.

[45] C. Cheng, H. Kou et W. Huang : Flow reversal and heat transfer of fully developed mixed convection in vertical channels. *Journal of Thermophysics and Heat Transfer*, 4(3):375–383, 1990.

[46] E. Chénier, R. Eymard, R. Herbin et O. Touazi : Collocated finite volume schemes for the simulation of natural convective flows on unstructured meshes. *International Journal for Numerical Methods in Fluids*, 56(11):2045–2068, 2008.

[47] E. Chénier, R. Eymard et O. Touazi : Numerical results using a colocated finite volume scheme on unstructured grids for incompressible fluid flows. *Numerical Heat Transfer Part B*, 49(3):259–276, 2006. URL http://letem.univ-mlv.fr/ chenier/BIBLIOGRAPHIE/chenier2006.pdf.

[48] A. Chorin : The numerical solution of the navier-stokes equations for an incompressible fluid. *Bull. Amer. Math. Soc*, 73(928-931):17, 1967.

[49] M. Christon, P. Gresho et S. Sutton : Computational predictability of time-dependent natural convection flows in enclosures (including a benchmark solution). *International Journal for Numerical Methods in Fluids*, 40(8):953–980, 2002.

[50] A. Clausing et S. Kempka : The influences of property variations on natural convection from vertical surfaces. *Journal of Heat Transfer*, 103:609–612, 1981.

[51] G. Colomer, M. Costa, R. Consul et A. Oliva : Three-dimensional numerical simulation of convection and radiation in a differentially heated cavity using the discrete ordinates method. *International Journal of Heat and Mass Transfer*, 47 (2):257–269, 2004.

[52] A. da Silva et A. Bejan : Constructal multi-scale structure for maximal heat transfer density in natural convection. *International Journal of Heat and Fluid Flow*, 26(1):34–44, 2005.

[53] G. De Vahl Davis : Natural convection of air in a square cavity: A bench mark numerical solution. *International Journal for Numerical Methods in Fluids*, 3(3):249–264, 1983. ISSN 1097-0363. URL http://dx.doi.org/10.1002/fld.1650030305.

[54] B. Delaunay : Sur la sphère vide. *Bul. Acad. Sci. URSS, Class. Sci. Nat.*, p. 793–800, 1934.

[55] G. Desrayaud et G. Lauriat : A numerical study of natural convection in partially open enclosures with a conducting side-wall. *Journal of Heat Transfer*, 126:76–83, 2004.

[56] G. Desrayaud et G. Lauriat : Flow reversal of laminar mixed convection in the entry region of symmetrically heated, vertical plate channels. *International Journal of Thermal Sciences*, 48(11):2036–2045, 2009.

[57] W. Elenbaas : Heat dissipation of parallel plates by free convection. *Physica*, 9 (1):1–28, 1942.

[58] J. Feng, H. Hu et D. Joseph : Direct simulation of initial value problems for the motion of solid bodies in a newtonian fluid. part 1. sedimentation. *Journal of Fluid Mechanics*, 261:95–134, 1994.

[59] J. Floryan et H. Rasmussen : Numerical methods for viscous flows with moving boundaries. *Applied Mechanics Reviews*, 42:323, 1989.

[60] N. Foster et R. Fedkiw : Practical animation of liquids. *In Proceedings of the 28th annual conference on Computer graphics and interactive techniques*, p. 23–30. ACM, 2001.

[61] J. Fukai, Y. Shiiba, T. Yamamoto, O. Miyatake, D. Poulikakos, C. Megaridis et Z. Zhao : Wetting effects on the spreading of a liquid droplet colliding with a flat surface: experiment and modeling. *Physics of Fluids*, 7:236, 1995.

[62] M. Gad et C. Balaji : Effect of surface radiation on rbc in cavities heated from below. *International Communications in Heat and Mass Transfer*, 37(10):1459–1464, 2010.

[63] C. Gau, Y. K. et W. Aung : Measurements of heat transfer and flow structure in heated vertical channels with buoyancy assisted and opposed flows. *AIAA J. Thermophys. Heat Transfer*, 6:707–712, 1992.

[64] C. Gau, Y. K. et W. Aung : Reversed flow structure and heat transfer measurements for buoyancy-assisted convection in a heated vertical duct. *ASME J. Heat Transfer*, 114:928–935, 1992.

[65] B. Gebhart, Y. Jaluria, R. Mahajan et B. Sammakia : *Buoyancy-induced flows and transport.* New York, NY (USA); Hemisphere Publishing, 1988.

[66] J. Glimm, J. Grove, X. Li, K. Shyue, Y. Zeng et Q. Zhang : Three dimensional front tracking. *SIAM Journal on Scientific Computing*, 19(3):703–727, 1998.

[67] J. Glimm, O. McBryan, R. Menikoff et D. Sharp : Front tracking applied to rayleigh–taylor instability. *SIAM Journal on Scientific and Statistical Computing*, 7:230, 1986.

[68] K. Goda : A multistep technique with implicit difference schemes for calculating two- or three-dimensional cavity flows. *Journal of Computational Physics*, 30:76 – 95, 1979.

[69] D. D. Gray et A. Giorgini : The validity of the boussinesq approximation for liquids and gases. *International Journal of Heat and Mass Transfer*, 19(5):545 – 551, 1976.

[70] C. Guillet, T. Mare et C. Nguyen : Application of a non-linear local analysis method for the problem of mixed convection instability. *International Journal of Non-Linear Mechanics*, 42(8):981–988, 2007.

[71] Z. Guo et X. Wu : Thermal drag and critical heat flux for natural convection of air in vertical parallel plates. *Journal of Heat Transfer*, 115(1):124–129, 1993.

[72] Z. Guo, S. Y.Z. et X. Zhao : Experimental investigation on natural convection in channel by laser speckle photography. *Experimental Thermal and Fluid Science*, 4 (5):594–600, 1991.

[73] P. Haldenwang, G. Labrosse, S. Abboudi et M. Deville : Chebyshev 3-d spectral and 2-d pseudospectral solvers for the Helmholtz equation. *J. Comp. Phys.*, 55:115–128, 1984.

[74] Z. Hammou, B. Benhamou, N. Galanis et J. Orfi : Laminar mixed convection of humid air in a vertical channel with evaporation or condensation at the wall. *International Journal of Thermal Sciences*, 43(6):531–539, 2004.

[75] F. Harlow et J. Welch : Numerical study of large-amplitude free-surface motions. *Physics of Fluids*, 9:842, 1966.

[76] A. HARTEN et S. OSHER : Uniformly high-order accurate nonoscillatory schemes. i. *SIAM Journal on Numerical Analysis*, p. 279–309, 1987.

[77] C. HIRT, A. AMSDEN et J. COOK : An arbitrary lagrangian-eulerian computing method for all flow speeds* 1. *Journal of Computational Physics*, 14(3):227–253, 1974.

[78] C. HIRT et B. D. NICHOLS : Volume of fluid method for the dynamics of free boundaries. *Journal of Computational Physics*, 39(1):201–225, 1981.

[79] T. HUANG, C. GAU et W. AUNG : Mixed convection flow and heat transfer in a heated vertical convergent channel. *International Journal of Heat and Mass Transfer*, 38(13):2445–2456, 1995.

[80] A. IAFRATI, A. DI MASCIO et E. CAMPANA : A level set technique applied to unsteady free surface flows. *International Journal for Numerical Methods in Fluids*, 35(3):281–297, 2001.

[81] D. INGHAM, D. KEEN, P. HEGGS et B. MORTON : Recirculating pipe flows. *J. Fluid Mech*, 213:443–464, 1990.

[82] Y. JENG, J. CHEN et W. AUNG : On the reynolds-number independence of mixed convection in a vertical channel subjected to asymmetric wall temperatures with and without flow reversal. *International Journal of Heat and Fluid Flow*, 13(4):329–339, 1992.

[83] G. JIANG et D. PENG : Weighted eno schemes for hamilton-jacobi equations. *SIAM Journal on Scientific Computing*, 21(6):2126–2143, 2000.

[84] G. JIANG et C. SHU : Efficient implementation of weighted eno schemes. Rap. tech., DTIC Document, 1995.

[85] M. KANG, R. FEDKIW et X. LIU : A boundary condition capturing method for multiphase incompressible flow. *Journal of Scientific Computing*, 15(3):323–360, 2000.

[86] K. KHANAFER et K. VAFAI : Buoyancy-driven flow and heat transfer in open-ended enclosures: elimination of the extended boundaries. *International Journal of Heat and Mass Transfer*, 43(22):4087–4100, 2000.

[87] K. KHANAFER et K. VAFAI : Effective boundary conditions for buoyancy-driven flows and heat transfer in fully open-ended two-dimensional enclosures. *International Journal of Heat and Mass Transfer*, 45(12):2527–2538, 2002.

[88] K. KIHM, J. KIM et L. FLETCHER : Onset of flow reversal and penetration length of natural convective flow between isothermal vertical walls. *Transactions American Society of Mechanical Engineers Journal of Heat Transfer*, 117:776–776, 1995.

[89] J. KIM et P. MOIN : Application of a fractional-step method to incompressible Navier-Stokes equations. *Journal of Computational Physics*, 59(2):308–323, 1985. ISSN 0021-9991.

[90] Y. KIM, N. GOLDENFELD et J. DANTZIG : Computation of dendritic microstructures using a level set method. *Physical Review E*, 62(2):2471, 2000.

[91] A. Krishnan, B. Premachandran, C. Balaji et S. Venkateshan : Combined experimental and numerical approaches to multi-mode heat transfer between vertical parallel plates. *Experimental Thermal and Fluid Science*, 29(1):75–86, 2004.

[92] N. Laaroussi, G. Lauriat et G. Desrayaud : Effects of variable density for film evaporation on laminar mixed convection in a vertical channel. *International Journal of Heat and Mass Transfer*, 52(1):151–164, 2009.

[93] G. Lauriat et G. Desrayaud : Effect of surface radiation on conjugate natural convection in partially open enclosures. *International Journal of Thermal Sciences*, 45(4):335–346, 2006.

[94] P. Le Quéré : Accurate solutions to the square thermally driven cavity at high rayleigh number. *Computers Fluids*, 20(1):29–41, 1991.

[95] P. Le Quéré : Onset of unsteadiness, routes to chaos and simulations of chaotic flows in cavities heated from the side: a review of present status. *In Proceedings of the Tenth International Heat Transfer Conference, Brighton, UK Hewitt GF(ed.). Rugby, Warwickshire, UK: Institution of Chemical Engineers*, p. 281–296, 1994.

[96] P. Le Quéré et T. T.Alziary De Roquefort : Computation of natural convection in two-dimensional cavities with chebyshev polynomials. *Journal of Computational Physics*, 57(2):210 – 228, 1985. ISSN 0021-9991. URL `http://www.sciencedirect.com/science/article/pii/0021999185900439`.

[97] P. Le Quéré, C. Weisman, H. Paillère, J. Vierendeels, E. Dick, R. Becker, M. Braack et J. Locke : Modelling of natural convection flows with large temperature differences: A benchmark problem for low mach number solvers. part 1. reference solutions. *ESAIM: Mathematical Modelling and Numerical Analysis*, 39(3):609–616, 2005. URL `http://dx.doi.org/10.1051/m2an:2005027`.

[98] R. Le Veque : High-resolution conservative algorithms for advection in incompressible flow. *SIAM Journal on Numerical Analysis*, p. 627–665, 1996.

[99] K. Lee, H. Tsai et W. Yan : Mixed convection heat and mass transfer in vertical rectangular ducts. *International Journal of Heat and Mass Transfer*, 40(7):1621–1631, 1997.

[100] R. Leveque et J. Oliger : Numerical analysis project. *Manuscript NA-81-16, Computer Science Department, Stanford University, Stanfbrd, Calif*, 1981.

[101] R. Li, M. Bousetta, E. Chénier et G. Lauriat : Effect of surface radiation on natural convective flows and onset of flow reversal in asymmetrically heated vertical channels. *Submitted to International Journal of Thermal Sciences*, Ref: THESCI-D-12-00606, 2012.

[102] D. Lide et H. Kehiaian : *CRC handbook of thermophysical and thermochemical data*, vol. 1. CRC, 1994.

[103] X. Liu, S. Osher et T. Chan : Weighted essentially non-oscillatory schemes. *Journal of Computational Physics*, 115(1):200–212, 1994.

[104] Q. Lu, S. Qiu, G. Su, W. Tian et Z. Ye : Experimental research on heat transfer of natural convection in vertical rectangular channels with large aspect ratio. *Experimental Thermal and Fluid Science*, 34(1):73–80, 2010.

[105] O. Manca, M. Musto et V. Naso : Experimental analysis of asymmetrical isoflux channel-chimney systems. *International Journal of Thermal Sciences*, 42(9):837–846, 2003.

[106] O. Manca et S. Nardini : Experimental investigation of radiation effects on natural convection in horizontal channels heated from above. *Journal of Heat Transfer*, 131 (6), 2009.

[107] O. Manca et V. Naso : Experimental analysis of natural convection and thermal radiation in vertical channels. *ASME HTD*, 145:13–21, 1990.

[108] S. McKee, M. Tomé, V. Ferreira, J. Cuminato, A. Castelo, F. Sousa et N. Mangiavacchi : The mac method. *Computers and Fluids*, 37:907–930, 2008.

[109] C. Mei : *The applied dynamics of ocean surface waves*. World Scientific (Singapore and River Edge, NJ), 1989.

[110] S. Mereu, E. Sciubba et A. Bejan : The optimal cooling of a stack of heat generating boards with fixed pressure drop, flowrate or pumping power. *International Journal of Heat and Mass Transfer*, 36(15):3677–3686, 1993.

[111] A. Mezrhab, H. Bouali, H. Amaoui et M. Bouzidi : Computation of combined natural-convection and radiation heat-transfer in a cavity having a square body at its center. *Applied Energy*, 83(9):1004–1023, 2006.

[112] M. Modest : *Radiative heat transfer*. Academic Press, 2nd ed. édn, 2003.

[113] B. Mondal et X. Li : Effect of volumetric radiation on natural convection in a square cavity using lattice boltzmann method with non-uniform lattices. *International Journal of Heat and Mass Transfer*, 53(21-22):4935–4948, 2010.

[114] B. Morrone, A. Campo et O. Manca : Optimum plate separation in vertical parallelplate channels for natural convective flows: incorporation of large spaces at the channel extremes. *International Journal of Heat and Mass Transfer*, 40(5):993–1000, 1997.

[115] B. Morton, D. Ingham, D. Keen et P. Heggs : Recirculating combined convection in laminar pipe flow. *Journal of Heat Transfer*, 111(1):106–113, 1989.

[116] D. Naylor, J. Floryan et J. Tarasuk : A numerical study of developing free convection between isothermal vertical plates. *Journal of Heat Transfer (Transactions of the ASME (American Society of Mechanical Engineers), Series C);(United States)*, 113(3):620–626, 1991.

[117] C. Olsson : Prediction of Nusselt number and flow rate of buoyancy driven flow between vertical parallel plates. *Journal of Heat Transfer*, 126:97–104, 2004.

[118] E. Oran et J. Boris : Numerical simulation of reactive flow. 1987.

[119] S. Osher et J. Sethian : Fronts propagating with curvature-dependent speed: algorithms based on hamilton-jacobi formulations. *Journal of Computational Physics*, 79(1):12–49, 1988.

[120] D. Ospir, C. Popa, C. Chereches, G. Polidori et S. Fohanno : Flow visualization of natural convection in a vertical channel with asymmetric heating. *International Communications in Heat and Mass Transfer*, 39(4):486–493, 2012.

[121] C. Padet, E. M. Mladin, J. Padet et A. Dobrovicescu : Minimization of entropy production in fully developed mixed thermal convection. *In Int. Symp. on Convective Heat and Mass Transfer in Sustainable Energy*, 2009.

[122] J. Padet, R. Cotta, N. Chereches et N. El Wakil : Convection laminaire interne: critères de sélection pour distinguer les régimes de convection naturelle, mixte ou forcée. *In Congrès Français de Thermique, SFT*, vol. 5, p. 209–214, 2005.

[123] J. Padet, R. Cotta et E. Mladin : Un autre regard sur la convection mixte. *COFRET Conference, Proceedings CD-ROM, paper n° 35, Iasi (Roumanie)*, 10, 2010.

[124] H. Paillère, P. Le Quéré, C. Weisman, J. Vierendeels, E. Dick, M. Braack, F. Dabbene, A. Beccantini, E. Studer, T. Kloczko, C. Corre, V. Heuveline, M. Darbandi et S. F. Hosseinizadeh : Modelling of natural convection flows with large temperature differences: A benchmark problem for low Mach number solvers. *ESAIM: Mathematical Modelling and Numerical Analysis*, 39(3):617–621, 2005.

[125] S. Paolucci : Filtering of sound from the navier-stokes equations. Rap. tech., 1982.

[126] S. Paolucci et D. Chenoweth : Transition to chaos in a differentially heated vertical cavity. *Journal of Fluid Mechanics*, 201:379–410, 1989.

[127] D. Peng, B. Merriman, S. Osher, H. Zhao et M. Kang : A pde-based fast local level set method. *Journal of Computational Physics*, 155(2):410–438, 1999.

[128] V. Polezhaev : Numerical solution of the system of two-dimensional unsteady naver-stokes equations for a compressible gas in a closed region. *Fluid Dynamics*, 2 (2):70–74, 1967.

[129] B. Ramaswamy : Numerical simulation of unsteady viscous free surface flow. *Journal of Computational Physics*, 90(2):396–430, 1990.

[130] N. Ramesh et S. Venkateshan : Effect of surface radiation on natural convection in a square enclosure. *Journal of Thermophysics and Heat Transfer*, 13(3):299–301, 1999.

[131] C. Rhie et W. Chow : Numerical study of the turbulent flow past an airfoil with trailing edge separation. *AIAA Journal(ISSN 0001-1452)*, 21:1525–1532, 1983.

[132] W. Rider et D. Kothe : Reconstructing volume tracking. *Journal of Computational Physics*, 141(2):112–152, 1998.

[133] E. Ridouane, M. Hasnaoui et A. Campo : Effects of surface radiation on natural convection in a rayleigh-benard square enclosure: steady and unsteady conditions. *Heat and Mass Transfer*, 42(3):214–225, 2006.

[134] A. Rogerson et E. Meiburg : A numerical study of the convergence properties of eno schemes. *Journal of Scientific Computing*, 5(2):151–167, 1990.

[135] M. Rudman : Volume-tracking methods for interfacial flow calculations. *International Journal for Numerical Methods in Fluids*, 24(7):671–691, 1997.

[136] G. Russo et P. Smereka : A remark on computing distance functions. *Journal of Computational Physics*, 163(1):51–67, 2000.

[137] H. Sadat et P. Salagnac : Calcul des flux aux parois présentant des singularités. *International Journal of Heat and Mass Transfer*, 40(18):4255–4262, 1997.

[138] R. Scardovelli et S. Zaleski : Direct numerical simulation of free-surface and interfacial flow. *Annual Review of Fluid Mechanics*, 31:567–603, 1999.

[139] P. Shopov, P. Minev, I. Bazhekov et Z. Zapryanov : Interaction of a deformable bubble with a rigid wall at moderate reynolds numbers. *J. Fluid Mech*, 219:241–271, 1990.

[140] C. Shu : High order weighted essentially nonoscillatory schemes for convection dominated problems. *SIAM review*, 51(1):82, 2009.

[141] C. Shu et S. Osher : Efficient implementation of essentially non-oscillatory shock-capturing schemes. *Journal of Computational Physics*, 77(2):439–471, 1988.

[142] C. Shu et S. Osher : Efficient implementation of essentially non-oscillatory shock-capturing schemes, ii. *Journal of Computational Physics*, 83(1):32–78, 1989.

[143] P. Smereka : Spiral crystal growth. *Physica D: Nonlinear Phenomena*, 138(3-4):282–301, 2000.

[144] E. Sparrow, G. Chrysler et L. Azevedo : Observed flow reversals and measured-predicted nusselt numbers for natural convection in a one-sided heated vertical channel. *Journal of Heat Transfer*, 106:325–332, 1984.

[145] L. Spradley et S. Churchill : Pressure-and buoyancy-driven thermal convection in a rectangular enclosure. *Journal of Fluid Mechanics*, 70(04):705–720, 1975.

[146] D. Sun et W. Tao : A coupled volume-of-fluid and level set (voset) method for computing incompressible two-phase flows. *International Journal of Heat and Mass Transfer*, 53(4):645–655, 2010.

[147] H. Sun, E. Chénier et G. Lauriat : Effect of surface radiation on the breakdown of steady natural convection flows in a square, air-filled cavity containing a centered inner body. *Applied Thermal Engineering*, 31(6-7):1252–1262, 2011.

[148] H. Sun, G. Lauriat et X. Nicolas : Natural convection and wall condensation or evaporation in humid air-filled cavities subjected to wall temperature variations. *International Journal of Thermal Sciences*, 50(5):663–679, 2011.

[149] H. Sun, R. Li, E. Chénier et G. Lauriat : On the modeling of aiding convection in vertical channels. *Heat Mass Transfer*, 48(7):1125–1134, 2012.

[150] H. Sun, R. Li, E. Chénier, G. Lauriat et J. Padet : Optimal plate spacing for mixed convection from an array of vertical isothermal plates. *Int. J. Therm. Sci.*, 55:16–30, 2012.

[151] M. Sussman et E. Fatemi : An efficient, interface-preserving level set redistancing algorithm and its application to interfacial incompressible fluid flow. *SIAM Journal on Scientific Computing*, 20(4):1165–1191, 1999.

[152] M. Sussman et P. Smereka : Axisymmetric free boundary problems. *Journal of Fluid Mechanics*, 341(1):269–294, 1997.

[153] M. Sussman, P. Smereka et S. Osher : *A level set approach for computing solutions to incompressible two-phase flow.* Thèse de doctorat, UCLA, 1994.

[154] R. Temam : *Navier-Stokes equations: theory and numerical analysis*, vol. 2. Amer Mathematical Society, 2001.

[155] O. Touazi, E. Chénier et R. Eymard : Simulation of natural convection with the collocated clustered finite volume scheme. *Computers & Fluids*, 37:1138–1147, 2008.

[156] E. Tric, G. Labrosse et M. Betrouni : A first incursion into the 3D structure of natural convection of air in a differentially heated cubic cavity, from accurate numerical solutions. *International Journal of Heat and Mass Transfer*, 43:4043–4056, 2000.

[157] G. Tryggvason, B. Bunner, A. Esmaeeli, N. Juric, W. Tauber, J. Han, S. Nas et Y. Jan : A front-tracking method for the computations of multiphase flow. *Journal of Computational Physics*, 169(2):708–759, 2001.

[158] S. Unverdi et G. Tryggvason : A front-tracking method for viscous, incompressible, multi-fluid flows. *Journal of Computational Physics*, 100(1):25–37, 1992.

[159] J. Watson, N. Anand et L. Feltcher : Mixed convective heat transfer between a series of vertical parallel plates with planar heat sources. *Journal of Heat Transfer*, 118(4):984–990, 1996.

[160] S. W.D. et J. Tong : *Engineering Thermodynamics.* Higher Education publishing set, 2007.

[161] B. Webb et D. Hill : High Rayleigh number laminar natural convection in an asymmetrically heated vertical channel. *Journal of Heat Transfer*, 111:649–656, 1989.

[162] E. Weinan et J. Liu : Projection method i: convergence and numerical boundary layers. *SIAM Journal on Numerical Analysis*, 32(4):1017–1057, 1995.

[163] R. Wirtz et R. Stutzman : Experiments on free convection between vertical plates with symmetric heating. *Journal of Heat Transfer*, 104:501–507, 1982.

[164] S. Xin et P. Le Quéré : An extended chebyshev pseudo-spectral benchmark for the 8: 1 differentially heated cavity. *International Journal for Numerical Methods in Fluids*, 40(8):981–998, 2002.

[165] Y. Yamada : Combined radiation and free convection heat transfer in a vertical channel with arbitrary wall emissivities. *International Journal of Heat and Mass Transfer*, 31(2):429–440, 1988.

[166] C. Yang, D. Jeng, K. Yih, C. Gau et W. Aung : Numerical and analytical study of reversed flow and heat transfer in a heated vertical duct. *Journal of Heat Transfer*, 131(7), 2009.

[167] L. Yao : Free and forced convection in the entry region of a heated vertical channel. *International Journal of Heat and Mass Transfer*, 26(1):65–72, 1983.

[168] W. Yue, C. Lin et V. Patel : Numerical simulation of unsteady multidimensional free surface motions by level set method. *International Journal for Numerical Methods in Fluids*, 42(8):853–884, 2003.

[169] B. Zamora et J. Hernández : Influence of variable property effects on natural convection flows in asymmetrically-heated vertical channels. *International Communications in Heat and Mass Transfer*, 24(8):1153–1162, 1997.

[170] Z. Zhang : *Nano/microscale heat transfer*. McGraw-Hill Incorporated, 2007.

**Numerical simulations of natural or mixed convection in vertical channels –
Comparisons of Level-Set numerical schemes for the modeling of immiscible
incompressible fluid flows**

The aim of this research dissertation is at studying natural and mixed convections of fluid
flows, and to develop and validate numerical schemes for interface tracking in order to
treat incompressible and immiscible fluid flows, later. In a first step, an original numerical
method, based on Finite Volume discretizations, is developed for modeling low Mach num-
ber flows with large temperature gaps. Three physical applications on air flowing through
vertical heated parallel plates were investigated. We showed that the optimum spacing
corresponding to the peak heat flux transferred from an array of isothermal parallel plates
cooled by mixed convection is smaller than those for natural or forced convections when
the pressure drop at the outlet keeps constant. We also proved that mixed convection flows
resulting from an imposed flow rate may exhibit unexpected physical solutions; alternative
model based on prescribed total pressure at inlet and fixed pressure at outlet sections gives
more realistic results. For channels heated by heat flux on one wall only, surface radiation
tends to suppress the onset of recirculations at the outlet and to unify the walls tempera-
ture. In a second step, the mathematical model coupling the incompressible Navier-Stokes
equations and the Level-Set method for interface tracking is derived. Improvements in
fluid volume conservation by using high order discretization (ENO-WENO) schemes for
the transport equation and variants of the signed distance equation are discussed.

Keywords: Finite Volume method, natural convection, mixed convection, vertical chan-
nels, Level-Set method, ENO-WENO schemes

**Simulations numériques de la convection naturelle ou mixte dans des canaux
verticaux – Comparaisons de schémas numériques Level-Set pour la modélisa-
tion d'écoulements de fluides immiscibles et incompressibles**

Le but de ce mémoire de recherche est d'étudier les convections naturelle et mixte d'écou-
lements fluides, et de développer et valider des méthodes numériques pour le suivi d'in-
terfaces afin de traiter plus tard des écoulements incompressibles de fluides immiscibles.
Dans une première étape, une méthode numérique originale, basée sur des discretisations
Volumes Finis, est développée pour modéliser les écoulements à faible nombre de Mach
et grands écarts de température. Trois applications physiques, portant sur l'écoulement
d'air à travers des plaques verticales parallèles chauffées, sont étudiées. Nous avons montré
que l'espacement optimal, correspondant au pic de flux de chaleur transféré d'un réseau
de plaques parallèles isothermes refroidies par convection mixte, est plus faible que ceux
obtenus en convections naturelle ou forcée lorsque la chute de pression à la sortie est con-
stante. Nous avons également prouvé que les écoulements de convection mixte à débit
imposé peuvent présenter des solutions physiques inattendues ; un modèle alternatif basé
sur une pression totale imposée à l'entrée et une pression fixée à la sortie donne de meilleurs
résultats. Pour des canaux soumis un flux de chaleur sur une paroi seule, le rayonnement
de surface tend à supprimer l'apparition des recirculations à la sortie et à uniformiser les
températures des parois. Dans une seconde étape, le modèle mathématique couplant les
équations de Navier-Stokes incompressibles et la méthode Level-Set pour le suivi d'inter-
faces est développé. Des améliorations de la conservation du volume fluide par l'utilisation
de schémas de discrétisation d'ordres élevés (ENO-WENO) pour l'équation de transport
et des variantes de l'équation de la distance signée sont discutées.

Mots clefs : Méthodes de Volumes Finis, convection naturelle, convection mixte, canaux
verticaux, méthode Level-Set, schémas ENO-WENO.